

HU ISSN 1586–2070

JOURNAL OF COMPUTATIONAL AND APPLIED MECHANICS

A Publication of the University of Miskolc

VOLUME 6, NUMBER 2 (2005)



MISKOLC UNIVERSITY PRESS

HU ISSN 1586–2070

JOURNAL OF COMPUTATIONAL AND APPLIED MECHANICS

A Publication of the University of Miskolc

VOLUME 6, NUMBER 2 (2005)



MISKOLC UNIVERSITY PRESS

EDITORIAL BOARD

- István PÁCZELT, Editor in Chief, Department of Mechanics, University of Miskolc, 3515 MISKOLC, Hungary, mechpacz@uni-miskolc.hu
- László BARANYI, Department of Fluid and Heat Engineering, University of Miskolc, 3515 MISKOLC, Hungary, aramb1@uni-miskolc.hu
- Edgár BERTÓTI, Department of Mechanics, University of Miskolc, 3515 MISKOLC, Hungary, mechber@uni-miskolc.hu
- Tibor CZIBERE, Department of Fluid and Heat Engineering, University of Miskolc, 3515 MISKOLC, Hungary, aramct@uni-miskolc.hu
- István ECSEDI, Department of Mechanics, University of Miskolc, 3515 MISKOLC, Hungary, mechecs@uni-miskolc.hu
- Wolfram FRANK, Institut für Fluid- und Thermodynamik, Universität Siegen, Paul-Bonatz-Strasse 9-11, 57076 SIEGEN, Germany, frank@ift.mb.uni-siegen.de
- Ulrich GABBERT, Institut für Mechanik, Otto-von-Guericke-Universität Magdeburg, Universitätsplatz 2, 39106 MAGDEBURG, Germany, ulrich.gabbert@mb.uni-magdeburg.de
- Zolt GÁSPÁR, Department of Structural Mechanics, Budapest University of Technology and Economics, Műegyetem rkp. 3, 1111 BUDAPEST, Hungary, gaspar@ep-mech.me.bme.hu
- Robert HABER, Department of Theoretical and Applied Mechanics, University of Illinois at Urbana-Champaign, 216 Talbot Lab., 104 S. Wright Str., URBANA, IL 61801, USA, r-haber@uiuc.edu
- Gábor HALÁSZ, Department of Hydraulic Machines, Budapest University of Technology and Economics, Műegyetem rkp. 3, 1111 BUDAPEST, Hungary, HALASZ@vizgep.bme.hu
- Ji Huan HE, Department of Mathematics, College of Basic Science, Shanghai Donghua University, No. 1882 Yan'anxilu Road, 200051 SHANGHAI, China, jhhe@dhu.edu.cn
- Károly JÁRMAI, Department of Materials Handling and Logistics, University of Miskolc, 3515 MISKOLC, Hungary, altjar@gold.uni-miskolc.hu
- László KOLLÁR, Department of Strength of Materials and Structures, Budapest University of Technology and Economics, Műegyetem rkpt. 1-3. K.II.42., 1521 BUDAPEST, Hungary, lkollar@goliat.eik.bme.hu
- Vladimir KOMPIŠ, Department of Mechanics, University of Žilina, ŽILINA, Slovakia, Vladimir_Kompis@kmpp.utc.sk
- Imre KOZÁK, Department of Mechanics, University of Miskolc, 3515 MISKOLC, Hungary, mechkoz@uni-miskolc.hu
- József KÖVECSÉS, Department of Mechanical Engineering, McGill University, 817 Sherbrooke Street West, MD163, Montreal, Quebec H3A 2K6, jozsef.kovecses@mcgill.ca
- Márta KURUTZ, Department of Structural Mechanics, Budapest University of Technology and Economics, Műegyetem rkp. 3, 1111 BUDAPEST, Hungary, kurutzm@eik.bme.hu
- R. Ivan LEWIS, Room 2-16 Bruce Building, Newcastle University, NEWCASTLE UPON TYNE, NE1 7RU, UK, R.I.Lewis@NCL.AC.UK
- Gennadij LVOV, Department of Mechanics, Kharkov Polytechnical Institute, 2 Frunze Str., 310002 KHARKOV, Ukraine, lvovgi@kpi.kharkov.ua
- Herbert MANG, Institute for Strength of Materials, University of Technology, Karlsplatz 13, 1040 VIENNA, Austria, Herbert.Mang@tuwien.ac.at
- Zenon MROZ, Polish Academy of Sciences, Institute of Fundamental Technological Research, Swietokrzyska 21, WARSAW, Poland, zmroz@ippt.gov.pl
- Tibor NAGY, Department of Physics, University of Miskolc, 3515 MISKOLC, Hungary, fiznagyt@uni-miskolc.hu
- Gyula PATKÓ, Department of Machine Tools, University of Miskolc, 3515 MISKOLC, Hungary, mechpgy@uni-miskolc.hu
- Jan SLADEK, Ústav stavbenictva a architektúry, Slovenskej akadémie vied, Dubróvska cesta 9, 842 20 BRATISLAVA, Slovakia, usarslad@savba.sk
- Gábor STÉPÁN, Department of Mechanics, Budapest University of Technology and Economics, Műegyetem rkp. 3, 1111 BUDAPEST, Hungary, stepan@mm.bme.hu
- Barna SZABÓ, Center for Computational Mechanics, Washington University, Campus Box 1129, St. LOUIS, MO63130, USA, szabo@ccm.wustl.edu
- Szilárd SZABÓ, Department of Fluid and Heat Engineering, University of Miskolc, 3515 MISKOLC, Hungary, aram2xsz@uni-miskolc.hu
- György SZEIDL, Department of Mechanics, University of Miskolc, 3515 MISKOLC, Hungary, Gyorgy.SZEIDL@uni-miskolc.hu

LOCAL EDITORIAL COUNCIL

T. CZIBERE, I. KOZÁK, I. PÁCZELT, G. PATKÓ, G. SZEIDL

GENERALIZED MINDLIN'S METHOD FOR THE DETERMINATION OF CONSTITUTIVE EQUATIONS OF SOLIDS

GYULA BÉDA

Department of Applied Mechanics
Budapest University of Technology and Economics
Műegyetem rkp. 3, 1111 BUDAPEST, Hungary
beda@math.uni-potsdam.de

[Received: December 14, 2004]

Dedicated to István Páczelt on the occasion of his 65th birthday

Abstract. For solid bodies the principle of virtual work can often be written as the variation of a functional. This fact can be applied to determine constitutive equations. Mindlin utilized this idea in the determination of higher order constitutive equations. Mindlin's method can be generalized into a few directions. Such generalizations result in that the first order constitutive equations contain first derivatives of strain and stress with respect to time and space coordinates in a linear form only.

Mathematical Subject Classification: 74A20, 74A35

Keywords: Lagrange's derivative, evolution equation, Lagrange's derivative with condition, constitutive equation

1. Introduction

The variational principles of solids contain expressions

$$\int_{t_0}^{t_1} \int_V \boldsymbol{\sigma} \cdot \cdot \delta \boldsymbol{\varepsilon} \, dV dt \quad \text{or} \quad \int_{t_0}^{t_1} \int_V \boldsymbol{\varepsilon} \cdot \cdot \delta \boldsymbol{\sigma} \, dV dt.$$

Remaining at the first expression the identity

$$\int_{t_0}^{t_1} \int_V \boldsymbol{\sigma} \cdot \cdot \delta \boldsymbol{\varepsilon} \, dV dt \equiv \delta \int_{t_0}^{t_1} \int_V W(\cdot) \, dV dt$$

is frequently encountered. This expression can also be written in the generalized form

$$\int_{t_0}^{t_1} \int_V \boldsymbol{\sigma} \cdot \cdot \delta \boldsymbol{\varepsilon} \, dV dt = \int_{t_0}^{t_1} \int_V [\delta U(\cdot) + \mathbf{D}(\cdot) \cdot \cdot \delta \boldsymbol{\varepsilon}] \, dV dt.$$

Function \mathbf{D} is not known generally and it will be abandoned in the following.

The stresses, strains and the variation of strains are denoted by $\boldsymbol{\sigma}$, $\boldsymbol{\varepsilon}$ and $\delta \boldsymbol{\varepsilon}$, respectively. Double dots stand for the double scalar product.

Mindlin [2] investigated equation

$$\int_V \boldsymbol{\sigma} \cdots \delta \boldsymbol{\varepsilon} \, dV = \delta \int_V W(\boldsymbol{\varepsilon}, \boldsymbol{\varepsilon} \nabla, \boldsymbol{\varepsilon} \nabla \nabla) \, dV,$$

where the function W depends on the strains $\boldsymbol{\varepsilon}$, the strain gradient $\boldsymbol{\varepsilon} \nabla$ and the gradient of the strain gradient $\boldsymbol{\varepsilon} \nabla \nabla$. The variables of the scalar function W are second, third and fourth order tensors.

The present paper generalizes Mindlin's idea making use of time derivatives and the existence of acceleration waves in solids [1] (*first condition*). In order to simplify the problem small deformations will be assumed and uniaxial stress and strain states will be investigated.

2. Lagrange derivative

In case of uniaxial problems the strain ε and the stress σ depend on the space and time coordinates x and t . Dash and dot denote the spatial and time derivatives.

For the uniaxial case we shall assume that the function W takes the following form

$$W(\varepsilon, \sigma, \dot{\varepsilon}, \dot{\sigma}, \varepsilon', \sigma').$$

It follows from this representation that

$$\begin{aligned} \int_{t_0}^{t_1} \int_{x_0}^{x_1} \sigma \delta \varepsilon \, dx \, dt &= \delta \int_{t_0}^{t_1} \int_{x_0}^{x_1} W(\varepsilon, \sigma, \dot{\varepsilon}, \dot{\sigma}, \varepsilon', \sigma') \, dx \, dt \\ &\equiv \int_{t_0}^{t_1} \int_{x_0}^{x_1} \mathcal{L}_\varepsilon(W) \delta \varepsilon \, dx \, dt, \end{aligned} \quad (1)$$

where \mathcal{L}_ε denotes the Lagrange derivative of W with respect to ε , that is,

$$\mathcal{L}_\varepsilon(W) = \frac{\partial W}{\partial \varepsilon} - \left(\frac{\partial W}{\partial \dot{\varepsilon}} \right)' - \left(\frac{\partial W}{\partial \varepsilon'} \right)'.$$

Similarly, the Lagrange's derivative of W with respect to σ , reads

$$\mathcal{L}_\sigma(W) = \frac{\partial W}{\partial \sigma} - \left(\frac{\partial W}{\partial \dot{\sigma}} \right)' - \left(\frac{\partial W}{\partial \sigma'} \right)'.$$

Formula (1) yields that

$$\sigma = \mathcal{L}_\varepsilon(W), \quad (2)$$

and similarly

$$\varepsilon = \mathcal{L}_\sigma(W). \quad (3)$$

Mindlin has determined the stress for finite deformation [2]. If the strains are small and $W = W(\varepsilon, \varepsilon', \varepsilon'')$, we have

$$\sigma = \mathcal{L}_\varepsilon(W) = \frac{\partial W}{\partial \varepsilon} - \left(\frac{\partial W}{\partial \varepsilon'} \right)' - \left(\frac{\partial W}{\partial \varepsilon''} \right)''$$

or in detail

$$\begin{aligned} \sigma = & \frac{\partial W}{\partial \varepsilon} - \frac{\partial^2 W}{\partial \varepsilon' \partial \varepsilon} \varepsilon' - \frac{\partial^2 W}{\partial \partial \varepsilon'^2} \varepsilon'' - \frac{\partial^2 W}{\partial \varepsilon' \partial \varepsilon''} \varepsilon''' \\ & + \frac{\partial^2 W}{\partial \varepsilon'' \partial \varepsilon} \varepsilon'' + \frac{\partial^2 W}{\partial \varepsilon'' \partial \varepsilon'} \varepsilon''' + \frac{\partial^2 W}{\partial \varepsilon''^2} \varepsilon^{iv} . \end{aligned} \tag{4}$$

Supposing that the formulation (4) does not contain higher derivatives, i.e., it involves first derivatives only then the derivatives of W are zero with respect to ε'' and ε'^2 (second condition). Therefore W assumes the form

$$W = U(\varepsilon) + D(\varepsilon) \varepsilon' .$$

The stress σ can be derived from the function W as

$$\sigma = \frac{\partial U}{\partial \varepsilon} + \frac{\partial D}{\partial \varepsilon} \varepsilon' - \frac{\partial D}{\partial \varepsilon} \varepsilon' = \frac{\partial U}{\partial \varepsilon} ,$$

which means that the body is Green's elastic body.

3. Generalizations of Mindlin's method

3.1. **The variables extension.** We shall seek the constitutive equation in the following form

$$f(\varepsilon, \sigma, \dot{\varepsilon}, \dot{\sigma}, \varepsilon', \sigma') = 0 . \tag{5}$$

(a) Let us set

$$W = A(\varepsilon) \varepsilon' + B(\varepsilon) \dot{\varepsilon} .$$

Since the Lagrange derivative of W is equal to zero, that is

$$\sigma = \mathcal{L}_\varepsilon(W) = 0 ,$$

it follows that there exists no constitutive equation.

(b) If

$$W_1 = A_1(\varepsilon, \sigma) + B_1(\varepsilon, \sigma) \varepsilon'$$

is given, then the stress is

$$\sigma = \mathcal{L}_\varepsilon(W) = \frac{\partial A_1}{\partial \varepsilon} - \frac{\partial B_1}{\partial \sigma} \sigma' .$$

Similarly, if W is equal to

$$A_2(\varepsilon, \sigma) + B_2(\varepsilon, \sigma) \dot{\varepsilon} ,$$

the stress is of the form

$$\sigma = \mathcal{L}_\varepsilon(W) = \frac{\partial A_2}{\partial \varepsilon} - \frac{\partial B_2}{\partial \sigma} \dot{\sigma} .$$

The two constitutive equations are $f_1(\varepsilon, \sigma, \sigma') = 0$ and $f_2(\varepsilon, \sigma, \dot{\sigma}) = 0$. However neither the first equation nor the second one are constitutive equations because the first condition is not satisfied [1].

- (c) The second condition also excludes equation (5) from the set of possible constitutive equations. Namely the function W in this case reads

$$W = A(\varepsilon, \sigma) + B(\varepsilon, \sigma) \dot{\varepsilon} + C(\varepsilon, \sigma) \varepsilon' + D(\varepsilon, \sigma) \dot{\sigma} + E(\varepsilon, \sigma) \sigma' .$$

Consequently, the corresponding stress has the form

$$\sigma = \mathcal{L}_\varepsilon(W) = \frac{\partial A}{\partial \varepsilon} + \left(\frac{\partial D}{\partial \varepsilon} - \frac{\partial B}{\partial \sigma} \right) \dot{\sigma} + \left(\frac{\partial E}{\partial \varepsilon} - \frac{\partial C}{\partial \sigma} \right) \sigma' .$$

This equation does not satisfy the first condition, that is there exist no acceleration wave.

The results of these investigations have led to the conclusion that the function σ depends on either the strain ε or $\dot{\varepsilon}$ and also on the first or the second or the higher derivatives of the strain and stress. The present paper does not deal with higher order constitutive equations of this type.

3.2. Internal variables. Another way to generalize Mindlin's method is the introduction of an internal variable or internal variables. For example, assume that function W depends on $\varepsilon, \dot{\varepsilon}, \varepsilon'$ and the internal variable g . That is $W = W(\varepsilon, \dot{\varepsilon}, \varepsilon', g)$. An evolution equation should be written for the internal variable. Let the evolution equation be

$$G(\varepsilon, \sigma) \frac{\partial g}{\partial \dot{\sigma}} + \frac{\partial g}{\partial \dot{\varepsilon}} = 0 . \quad (6)$$

Equation (6) is the necessary condition of the existence of acceleration waves.

The Lagrange derivative of function W is

$$\mathcal{L}_\varepsilon(W) = \frac{\partial W}{\partial \varepsilon} - \left(\frac{\partial^2 W}{\partial \dot{\varepsilon} \partial \varepsilon} \dot{\varepsilon} + \frac{\partial^2 W}{\partial \varepsilon' \partial \varepsilon} \varepsilon' + \frac{\partial^2 W}{\partial \dot{\varepsilon} \partial g} \dot{g} + \frac{\partial^2 W}{\partial \varepsilon' \partial g} g' + (()) \right), \quad (7)$$

where $(())$ contains the higher derivatives of the variables ε and g . Term $(())$ will be omitted in view of the second condition. Evolution equation (6) implies that internal variable g depends on $\varepsilon, \sigma, \dot{\varepsilon}, \dot{\sigma}$, that is,

$$g = g(\varepsilon, \sigma, \dot{\varepsilon}, \dot{\sigma}) .$$

Now the following equation can be written

$$W = A(\varepsilon, g) + B(\varepsilon, g) \dot{\varepsilon} + C(\varepsilon, g) \varepsilon' .$$

Equation (6) is satisfied if

$$g = \sigma \quad \text{and} \quad G(\varepsilon, \sigma) \frac{\partial B}{\partial \sigma} + \frac{\partial B}{\partial \varepsilon} = 0 .$$

Finally, the stress σ is of the form (see equation (7))

$$\sigma = \frac{\partial A}{\partial \varepsilon} - \frac{\partial B}{\partial \varepsilon} \dot{\varepsilon} - \frac{\partial B}{\partial \sigma} \dot{\sigma} - \frac{\partial C}{\partial \varepsilon} \varepsilon' - \frac{\partial C}{\partial \sigma} \sigma' .$$

3.3. Conditional Lagrange derivative. A further generalization of the method can be made if we define a conditional Lagrange derivative. Then the Lagrange derivative of function W should be formed in such a way that equation $K = 0$ is also satisfied. Then we can calculate the Lagrange derivative of function $F = W + \lambda K$: Here λ is an arbitrary function, which depends on x and t .

Assume that the equation $K = 0$ coincides with equation (6). Then the function F reads

$$F = W(\varepsilon, \sigma, \dot{\varepsilon}, \varepsilon', \dot{\sigma}, \sigma') + \lambda(x, t) K(\varepsilon, \sigma, \dot{\varepsilon}, \dot{\sigma}),$$

where

$$K = G(\varepsilon, \sigma) \frac{\partial g}{\partial \dot{\sigma}} + \frac{\partial g}{\partial \dot{\varepsilon}} = 0.$$

After all that has been said, we get

$$\sigma = \mathcal{L}_\varepsilon(W) + \lambda \mathcal{L}_\varepsilon(K), \quad \text{if } K = 0. \quad (8)$$

Since now the second condition is satisfied, the function W is of the form

$$W = A(\varepsilon, \sigma) + B(\varepsilon, \sigma) \dot{\varepsilon} + C(\varepsilon, \sigma) \varepsilon' + D(\varepsilon, \sigma) \dot{\sigma} + E(\varepsilon, \sigma) \sigma'.$$

From this expression one can determine the derivative $\mathcal{L}_\varepsilon(W)$. As is well known, the derivative $\mathcal{L}_\varepsilon(K)$ is

$$\mathcal{L}_\varepsilon(K) = \frac{\partial K}{\partial \varepsilon} - \left(\frac{\partial^2 K}{\partial \dot{\varepsilon} \partial \varepsilon} \dot{\varepsilon} + \frac{\partial^2 K}{\partial \dot{\varepsilon} \partial \sigma} \dot{\sigma} \right).$$

The stress σ follows from equation (8), that is

$$\begin{aligned} \sigma = & \frac{\partial A}{\partial \varepsilon} + \lambda \frac{\partial K}{\partial \varepsilon} - \left(\frac{\partial D}{\partial \varepsilon} - \frac{\partial B}{\partial \sigma} + \lambda \frac{\partial^2 K}{\partial \dot{\varepsilon} \partial \sigma} \right) \dot{\sigma} \\ & - \lambda \frac{\partial^2 K}{\partial \dot{\varepsilon} \partial \varepsilon} \dot{\varepsilon} - \left(\frac{\partial E}{\partial \varepsilon} - \frac{\partial C}{\partial \sigma} \right) \sigma'. \end{aligned}$$

The sufficient condition for the existence of an acceleration wave in continua is [1]

$$\frac{\lambda \frac{\partial^2 K}{\partial \dot{\varepsilon} \partial \varepsilon}}{\frac{\partial D}{\partial \varepsilon} - \frac{\partial B}{\partial \sigma} + \lambda \frac{\partial^2 K}{\partial \dot{\varepsilon} \partial \sigma}} < 0.$$

The necessary condition that satisfies it is equation (6).

4. Conclusions

Mindlin's method for the determination of constitutive equations can be generalized in several directions. The method of extension of the variables does not lead to new constitutive equation if the first derivatives of stress and strain can occur in the constitutive equations. This investigation directs attention to higher order constitutive equations. The other two generalizations can lead to possible constitutive equations.

Acknowledgement. This work was supported by the National Scientific Research Fund of Hungary (under contract OTKA T037715). This support is gratefully acknowledged.

References

1. BÉDA, GY.: Die Differentialgleichungen der möglichen Stoffgesetze des dynamischen plastischen Zuges. *Publications of the Technical University of Miskolc*, **25**, (1965), 194-204.
2. MINDLIN, R.D.: Second gradient of strain and surface-tension in linear elasticity. *International Journal of Solids Structures*, **1**, (1965), 417-438.

EVOLUTION METHODS FOR DISCRETE MINIMAL WEIGHT DESIGN OF SPACE TRUSSES WITH STABILITY CONSTRAINTS

ANIKÓ CSÉBFALVI

Department of Structural Engineering

University of Pécs

Boszorkány u. 2., 7624 Pécs, Hungary

csebfalv@witch.pmmf.hu

[Received: January 14, 2005]

Dedicated to István Páczelt on the occasion of his 65th birthday

Abstract. This paper provides a comparative study of evolution methods for minimal weight design of space trusses. Recently used genetic algorithms (GA), simulated annealing (SA) and tabu search (TS) methods are observed for metal structures where the truss member profiles are selected from available catalogue values. In this paper, global and local stability problems are considered using a path-following method for non-linear stability investigation. The results of the comparative study are presented for the commonly known numerical test problems. A twenty-four-member shallow dome structure was presented where structural instability constraints and member buckling are considered as well as using linear elastic material property. The effect of the nonlinear material law is compared in optimal design of the ten-bar truss structure and the twenty-five-bar transmission tower using an inverse Ramberg-Osgood material law.

Mathematical Subject Classification: 74P05

Keywords: evolution methods, minimal weight design of space trusses

1. Introduction

One of the most important practical considerations in the optimal design of steel structures is the best selection of design variables from available catalogue values. Therefore, the design is formulated as a discrete optimization problem, searching for global or local optimal solution. However, most optimization methods are suited and developed for continuous design variables. A few procedures [1, 3, 4, 5, 9, 13] have been considered for discrete optimization including e.g. enumeration techniques, integer programming, branch and bound algorithms.

This paper provides a comparative study where simulated annealing (SA), genetic algorithms (GA), and tabu search methods (TS) are considered for discrete minimal weight design problems of shallow space trusses with stability constraints.

Simulated annealing as a heuristic algorithm is associated with its original use for solving metal models as they heat and cool. Kirkpatrick et al. [10] introduced it first for discrete optimization problems. In this paper a new SA algorithm is presented for shallow space trusses with stability constraints. The SA algorithm has proven to be a good technique [6, 11] for solving combinatorial optimization problems in particular for large flexible space structures. However, it seems sometimes less useful than some conventional algorithms. Consequently, simulated annealing has not been widely accepted in engineering optimization. In order to accelerate the overall convergence, it is proposed to use the best solution for a starting point every time that the temperature is reduced. The results show that simulated annealing algorithm provides a computationally efficient tool to find near optimal solutions to otherwise computationally intractable problems.

GA methods are search algorithms that are based on the concepts of natural selection and natural genetics. Recently GA methods are very popular and have been used for sizing, shape, and topology optimization of structures, e.g. [8, 12]. The core characteristics of GAs are based on the principles of survival of the fittest and adaptation. GA methods operate on population of design variable sets, with each design variable set defining a potential solution called a string. Each string is made up of series of characters as binary numbers, representing the discrete variables for a particular solution. The fitness of each string is a measure of performance of design variables defined by the objective function and constraints. GA methods consist of a series of three processes: coding and decoding design variables into strings, evaluating the fitness of each solution string, and applying genetic operators to generate the next generation of solution strings. Most GA methods are variations of the simple GA proposed by Goldberg [8], which consists of three basic genetic operators: reproduction, crossover, and mutation. By varying these parameters, the convergence of the problem may be altered. Much attention has been focused on finding the theoretical relationships between these parameters. Rajeev and Krishnamoorthy [12] applied GA for optimal truss design. They presented all the computations for three successive generations in the form of tables for easy understanding of the problem. In this study a GA method is proposed for minimal weight design of trusses. According to the shallow space form, the instability consideration is required. The general procedure is described in subsection 3.2.

Tabu search (TS) is a computational process which attempts to solve difficult combinatorial optimization problems through controlled randomization. In other words, TS is a metaheuristic method designed to find near optimal solutions of combinatorial optimization problems. Basically it consists of several elements called the move, neighborhood, initial solution, searching strategy, intensification, diversification and stopping rules. For obtaining near optimum solutions of such problems, a better minimum of an objective function should be searched for among a huge number of local minimums, since it is almost impossible to find an exact optimum. 'Intensification' means decreasing of the objective function value to find a better solution closer to the local minimum. 'Diversification' means a jump from a searching region to other

regions to avoid getting trapped in a single local minimum. The details of the TS process are presented in paper [7] and in subsection 3.3.

2. Structural optimization problem

The basic, initial equation system of discrete minimal weight design is the total potential energy function of the geometrically nonlinear truss structure.

$$V(u_i, a_q, \lambda) = U(u_i(a_q)) - \lambda p_i u_i, \quad i = 1, 2, \dots, n \quad q = 1, 2, \dots, e \quad (1)$$

The total potential energy function is formulated in terms of load intensity parameter λ , applied external load vector p_i , nodal displacement vector u_i , and vector of the member sizing a_q , where n is the number of nodes, e is the number of elements, and $U(u_i(a_q))$ is the non-linear strain energy function. In this study nonlinear material is supposed in comparison with the results obtained by using the linear elastic material law. In the case of the nonlinear (Ramberg-Osgood) material law, the strain energy function $U(u_i(a_q))$ is replaced by the following expression:

$$U(u_i) = \frac{\sigma_y^2 \sqrt{\left(1 + \frac{E^2 \varepsilon_q^2(u_i)}{\sigma_y^2}\right)}}{E} - \frac{\sigma_y^2}{E}, \quad (2)$$

where E is the elasticity modulus, ε_q is the member strain, and σ_y is the yield stress of the materials applied.

The design variables are selected from a discrete set of the predetermined cross-sectional areas, such that minimize the total weight of the structure:

$$V(a_q) \longrightarrow \min \quad (3)$$

subject to

$$V_{,i} = 0 \quad (4)$$

$$\lambda(a_q) = 1 \quad (5)$$

$$i = 1, 2, \dots, n \quad q = 1, 2, \dots, e$$

where $V_{,i} = 0$ is the equilibrium criterion, $\lambda(a_q) = 1$ the maximal locally and globally stable and stress feasible load intensity. The path-following procedure of instability investigation is terminated when the unit load intensity is reached without any constraint violation.

The proposed instability investigation [2] is based on the perturbation technique of the stability theory and on the non-linear modification of the classical linear homotopy method. With the help of the higher-order predictor-corrector algorithm, we are able to compute an arbitrary load deflection path and detect the different types of stability points. Within the predictor step, we compute the solution of an implicit ODE problem and the corrector phase is the solution of a nonlinear equation system. The first-order derivatives are obtained from the equation system by null-space computation of the augmented Hessian matrix. The higher order derivatives are obtained from the inhomogeneous equations using the Moor-Penrose pseudo-inverse.

The basic function of the stability investigation is the total potential energy function. The equilibrium equation system is obtained from the total potential energy function. Starting from the zero point of the equilibrium path assuming that the Hessian is positive definite, the solution is obtained in terms of the arch-length parameter of the equilibrium path t .

The stability investigation is based on the eigenvalue computation of the Hessian matrix $V_{,ij}$. In every step of the path-following process we get information about the displacement, stresses, local, and global stability of the structure. This higher order predictor-corrector method provides an accurate computation of the singular points. It is capable of computing not only points but also segments of the equilibrium path. The curve segment approximation is the basis for the identification of the singular points. Since we are concerned with finding feasible designs we must define a certain appropriate measure of performance. In the proposed path-following approach the applied measure of design infeasibility $\lambda(a_q)$ is defined as the solution of the following system:

$$\lambda(a_q, t) \longrightarrow \max \quad (6)$$

$$0 \leq \lambda(a_q, t) \leq 1 \quad (7)$$

$$\eta_i(a_q, t) > 0 \quad (8)$$

$$\underline{s} \leq s_q(a_q, t) \leq \bar{s} \quad (9)$$

$$i = 1, 2, \dots, n \quad q = 1, 2, \dots, e$$

where t is the arch-length parameter of the equilibrium path, η_i is the vector of eigenvalues of Hessian matrix $V_{,ij}$, and \underline{s} , \bar{s} are the lower and upper bounds of the stress constraints.

The path-following process is terminated at the first constraint violation.

3. Discrete optimization methods

In this study tree heuristic techniques are considered: simulated annealing, a genetic algorithm and a tabu search method to find a solution for the discrete minimal weight design problem of shallow space trusses.

3.1. Simulated annealing. Simulated annealing is a computational process, which attempts to solve difficult combinatorial optimization problems through controlled randomization. Simulated annealing emulates the physical process of annealing which attempts to force a system to its lowest energy state through controlled cooling.

In general, the annealing process involves the following steps:

- The temperature of the system is raised to a sufficient level.
- The temperature of the system is maintained at the level for a prescribed amount of time.
- The system is allowed to cool under controlled conditions until the desired energy-state is attained.

The initial temperature the time system remains at and the rate at which the system is cooled are referred to as the annealing schedule. If the system is allowed to cool too fast it may freeze at an undesirable high-energy state. In simulated annealing the process starts at a given feasible or unfeasible solution. To avoid freezing at a local optimum the algorithm walks very slowly through the solution space.

The general procedure for the simulated annealing algorithm can be described as follows:

```

MaxStep = 1000
MaxNode = 150
MaxNeighbourhoodSearch = 10
Call ProblemDefinition
Temperature = 1
CoolingRatio = 0.95
n = 0
Call RandomInitialStructure
Call PathFollowingMethod
Call CurrentNodeUpdate
Call BestSolutionUpdate
Call BestFeasibleSolutionUpdate
For s = 1 To MaxStep
  ParentSolution = BestSolution
  For m = 1 To MaxNeighbourhoodSearch
    If RandomNeighbourStructure(ParentSolution)
  Then
    Call PathFollowingMethod
    If AcceptedSolution(Temperature) then
      n = n + 1
      Call CurrentNodeUpdate
      Call BestSolutionUpdate
      Call BestFeasibleSolutionUpdate
    Endif
  Else
    Exit
  End If
  Next m
  Call TemperatureUpdate: If Temperature < 0.001
  Then Exit
  Next s

```

3.2. Genetic algorithm. The genetic algorithm (GA) is an efficient and widely applied global search procedure based on a stochastic approach. All of the recently applied genetic algorithms for structural optimization have demonstrated that genetic algorithms can be powerful design tools [8, 12]. The crossover operation creates variations in the solution population by producing new solution strings that consist of parts taken from selected parent solution strings. The mutation operation introduces

random changes in the solution population. In GA, the mutation operation can be beneficial in reintroducing diversity in a population. In this study, a pair of parent solutions is randomly selected, with a higher probability of selection being ascribed to superior solutions. The two parents are combined using a crossover scheme that attempts to merge the strings representing them in a suitable fashion to produce an offspring solution. Offspring can also be modified by some random mutation perturbation. The algorithm selects the fittest solution of the current solution set, i.e. those with the best objective function values. Each pair of strings reproduces two new strings using a crossover process and then dies.

The steps of the algorithm:

```

PopulationSize = 50
NumberOfNewGenerations=50
CrossoverProbability=0.5
SwapProbability=0.1
MutationProbability=0.1
Call ProblemDefinition
Call RandomInitialPopulationGeneration
Call BestFeasibleSolutionUpdate
For  $n = 1$  to NumberOfNewGenerations
   $\{i, j\} \leftarrow$  Call RandomFittestParentPairSelection
  Call Crossover
  For Each Child: Call Mutation
    Call PathFollowingMethod
    Call BestFeasibleSolutionUpdate
   $\{i, j\} \leftarrow$  Call OffspringPairUpdate
Next  $n$ 

```

3.3. Tabu search algorithm. In the case of tabu search, diversification is introduced as follows: if there are no improving moves, the move that least degrades the objective function is chosen. In order to avoid returning to the local optimum just visited, the reverse moves are forbidden. This is realized by storing those moves in a data structure called the tabu list. This contains s elements, which define forbidden moves, where s is the tabu list size. Once a move is stored in the tabu list, it will become available s iterations later.

The steps of the algorithm:

```

MaxStep = 1000
MaxNode=150
MaxNeighbourhoodSearch = 10
MaxTabuListSize=50
Call ProblemDefinition
 $n = 0$ 
Call RandomInitialStructure

```

```

Call CurrentNodeUpdate
Call BestFeasibleSolutionUpdate
Call BestNodeUpdate
For s= 1 To MaxStep
    ParentSolution = BestSolution
    For m = 1 To MaxNeighbourhoodSearch
        If RandomNeighbourStructure(ParentSolution)
            Then
                n=n+1
                Call PathFollowingMethod
                Call BestFeasibleSolutionUpdate
                Call CurrentNodeUpdate
                Call BestNodeUpdate
                If n = MaxNode then Exit
            Else
                Exit
            End If
        Next m
    Next s

```

4. Numerical example

4.1. **The 24-member dome structure.** In this paper, one of the frequently used test examples is considered. The geometry of the 24-member is shown in Figure 1 and Table 1. According to the requirement of the symmetrical structure, the truss members were partitioned into linking groups. Group 1 includes bars 1-6, group 2 includes bars 7-12, and group 3 includes bars 13-24.

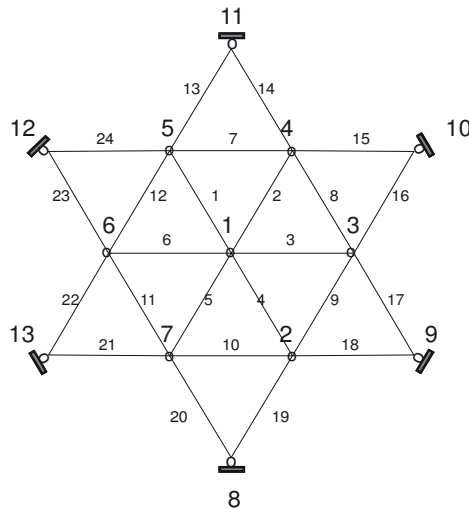


Figure 1. Layout of the 24-member dome structure

Nodal Points	X [m]	Y [m]	Z [m]
1	0.0	0.00	0.000
3	25.0	0.00	2.000
4	12.5	21.65	2.000
10	43.3	25.00	8.216
11	0.0	50.00	8.216

Table 1. Geometry of the 24-member dome structure

The elasticity modulus is $E = 7 \times 10^{10} \text{N/m}^2$. The stress constraints for tension and compression are $25 \times 10^6 \text{N/m}^2$. The density is 27500N/m^3 .

The cross-sectional areas of the truss-members with circular sections are selected from an available catalogue:

$$A_i = \{12.00; 12.25; 12.50; 12.75; 13.00; 13.25; 13.50; 13.75; 15.75\} * 10^{-4} \text{m}^2$$

The applied loads of the 24-member dome structure are $P_1 = 6 \text{kN}$ at the nodal point 1, and $P_{2-7} = 12 \text{kN}$ at the nodal points 2-7, which causes a bifurcation instability phenomenon. The results of the optimization process are shown in Tables 2-4.

Run	Weight	Cross-sections (catalogue values)	Relative error
1	258.506	{12.75,15.75,13.50}	1.408
2	258.013	{12.25,15.50,13.75}	1.215
3	256.994	{13.25,14.25,13.75}	0.815
4	256.940	{13.50,15.25,13.25}	0.794
5	256.549	{12.00,13.50,14.50}	0.641
6	256.447	{13.00,15.00,13.50}	0.601
7	256.440	{12.50,15.50,13.50}	0.598
8	256.440	{12.50,15.50,13.50}	0.598
9	255.953	{12.50,14.75,13.75}	0.407
10	255.953	{12.50,14.75,13.75}	0.407
11	255.950	{12.25,15.00,13.75}	0.406
12	255.899	{12.75,15.75,13.25}	0.386
13	255.463	{12.25,14.25,14.00}	0.215
14	255.409	{12.50,15.25,13.50}	0.193
15	255.406	{12.25,15.50,13.50}	0.192
16	255.406	{12.25,15.50,13.50}	0.192
17	255.402	{12.00,15.75,13.50}	0.191
18	254.916	{12.00,15.00,13.75}	0.000
19	254.916	{12.00,15.00,13.75}	0.000
20	254.916	{12.00,15.00,13.75}	0.000

Table 2. Results of genetic algorithm (GA)

Run	Weight	Cross-sections (catalogue values)	Relative error
1	260.697	{13.75,12.75,14.50}	2.268
2	260.044	{14.25,15.25,13.25}	2.012
3	259.557	{14.25,14.50,13.50}	1.821
4	258.526	{14.25,14.25,13.50}	1.416
5	258.468	{14.25,15.50,13.00}	1.393
6	258.465	{14.00,15.75,13.00}	1.392
7	258.084	{13.25,13.25,14.25}	1.243
8	257.978	{14.00,15.00,13.25}	1.201
9	257.536	{13.00,14.00,14.00}	1.028
10	257.488	{13.75,14.50,13.50}	1.009
11	257.488	{13.75,14.50,13.50}	1.009
12	257.430	{13.75,15.75,13.00}	0.986
13	257.046	{12.75,13.50,14.25}	0.836
14	257.036	{12.00,14.25,14.25}	0.832
15	256.991	{13.00,14.50,13.75}	0.814
16	256.978	{12.00,15.50,13.75}	0.809
17	256.450	{13.25,14.75,13.50}	0.602
18	259.557	{14.25,14.50,13.50}	1.821
19	255.950	{12.25,15.00,13.75}	0.406
20	255.406	{12.25,15.50,13.50}	0.192

Table 3. Results of simulated annealing method (SA)

Run	Weight	Cross-sections (catalogue values)	Relative error
1	264.304	{15.75,12.25,14.25}	3.683
2	263.807	{15.00,12.25,14.50}	3.488
3	262.232	{15.00,12.50,14.25}	2.870
4	262.228	{14.75,12.75,14.25}	2.868
5	262.228	{14.75,12.75,14.25}	2.868
6	260.697	{13.75,12.75,14.50}	2.268
7	260.598	{15.00,14.00,13.50}	2.229
8	260.540	{15.00,15.25,13.00}	2.206
9	259.701	{12.00,13.00,15.00}	1.877
10	259.615	{14.25,13.25,14.00}	1.843
11	259.016	{14.50,14.75,13.25}	1.608
12	259.016	{14.50,14.75,13.25}	1.608
13	258.577	{13.75,13.50,14.00}	1.436
14	258.125	{12.00,13.25,14.75}	1.259
15	258.125	{12.00,13.25,14.75}	1.259
16	258.032	{13.75,14.00,13.75}	1.222
17	256.994	{13.25,14.25,13.75}	0.815
18	256.450	{13.25,14.75,13.50}	0.602
19	255.460	{12.00,14.50,14.00}	0.213
20	254.916	{12.00,15.00,13.75}	0.000

Table 4. Results of tabu search method (TS)

The results obtained using simulated annealing (SA), genetic algorithm (GA), and tabu search (TA) methods have been illustrated in Tables 2-4.

The total number of the cross-sectional combinations for three member groups is 4096. The global optimal solution of the problem: $GW = 254.916$ the weight of the structure; $GC = \{12.00; 15.00; 13.75\}$. Using a standard implicit enumeration algorithm, 1615 node evaluations were needed to obtain this solution and to prove its global optimality. To compare the standard local search methods, we ran each method 20 times from a randomly selected design (population). In each case we stopped the searching process after 150 design evaluations.

4.2. The 10-bar truss. In this comparative study, according to the widely used dimension in the literature we adopted the same values and the same dimension system in our computation.

Load condition: $P = 100000 \text{ lb}$; Material density: $\rho = 0,1 \text{ lb/in}^2$;

Young modulus: $E = 10^7 \text{ psi}$; Yield stress: $\sigma = 40000 \text{ psi} \pm$.

The following conversion table gives us the International System of Units (SI):

1 inch (in) = 25,4 mm ;

1 pound (lb) = 0,4536 kg ;

1 pound per square in (lb/in^2) = 6895 N/m^2 ;

1 $kips$ = 4448 N .

In this example, a genetic algorithm was applied for both cases using One-Point Crossover. The cross-sectional areas are selected from the given set of the catalogue values of $\{ 36; 27; 19; 12; 7; 4; 2; 1 \}$.

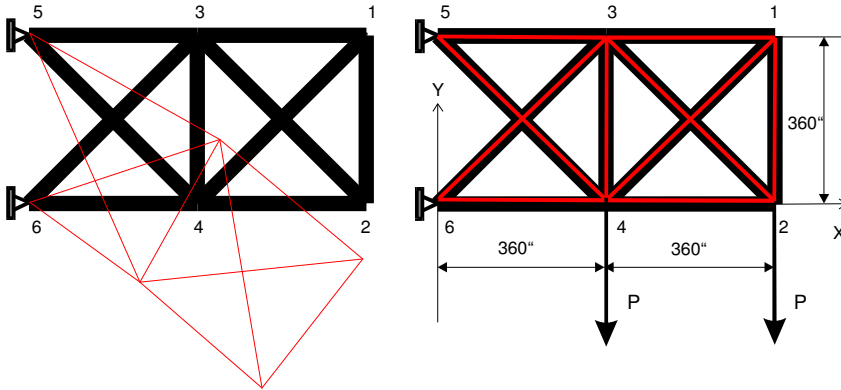


Figure 2. Layout and load condition of the 10-bar truss

The results of the ten-bar truss example (Table 5 and Table 6) demonstrate that the efficiency of GA strongly depends on the choices of population size and the crossover size. Using the nonlinear material law, we obtained much a lighter structure in both cases than in the case of a linear elastic material in the *paper quoted [3]* (see Table 10).

However we have to note that the discrete solution method proposed was different in paper [3].

Population	Crossover	Best weight	Cross-sections
50	50	3028.06	{19,4.,19,2,7,2,7,4,4,7}
50	50	5833.94	{7, 27, 19, 36, 1, 7, 4, 19, 19, 4}
50	50	3819.00	{12, 2, 19, 19, 2, 4, 7, 7, 19, 1}
50	50	3552.09	{19, 4, 19, 7, 2, 1, 2, 12, 12, 7}
50	50	4154.29	{12, 4, 19, 7, 12, 2, 4, 12, 7, 19}
50	50	3727.41	{4, 12, 7, 1, 2, 4, 12, 2, 19, 19}
50	50	3466.23	{12, 27, 19, 7, 2, 1, 4, 7., 7, 2}
50	50	3682.23	{19, 12, 7, 7, 2, 27, 7, 2, 4, 7}
50	50	3725.91	{7, 7, 12, 12, 12, 4, 19, 2, 7, 7}
50	50	4841.91	{7, 12, 19, 4, 7, 36, 12, 19, 2, 2}

Table 5. Results of ten-bar truss

Population	Crossover	Best weight	Cross-sections
100	100	3045.53	{12, 2, 19, 4, 1, 7, 7, 12, 7, 2}
100	100	2823.35	{7, 7, 7, 7, 4, 4, 7, 12, 4, 7}
100	100	4539.00	{7, 7, 19, 7, 2, 36, 7, 1, 7, 19}
100	100	3343.32	{12, 12, 19, 4, 12, 7, 12, 1, 4, 2}
100	100	3708.44	{36, 4, 7, 12, 2, 1, 4, 12, 12, 1}
100	100	3930.62	{7, 7, 19, 27, 7, 4, 12, 4, 7, 4}
100	100	3750.62	{27, 1, 12, 12, 12, 2, 7, 4, 4, 12}
100	100	3908.47	{12, 4, 19, 4, 1, 12, 27, 2, 4, 7}
100	100	4588.41	{4, 19, 27, 12, 36, 4, 12, 1, 1, 4}
100	100	3157.15	{4, 2, 12, 2, 2, 36, 12, 4, 1, 4}

Table 6. Results for ten-bar truss

4.3. **The 25-bar truss.** Material density, Young modulus, and yield stress constraints are the same as for the ten-bar truss. The loads are given in Table 7. The relationship between the indices and the cross-sections is given in Table 8. The results obtained by using the nonlinear material law (see Table 9) are approximately half of the optimal weight obtained using the linear elastic material law (see Table 10).

In this example a genetic algorithm was also applied. The cross-sectional areas are selected from the given set of the catalogue values of

$$\{ 3,5 \ 3,4 \ 3,3 \ \dots \ 1,0 \ 0,9 \ \dots \ 0,2 \ 0,1 \ 0,01 \} .$$

Nodal points	X [kips]	Y [kips]	Z [kips]
1	-	20	-5
2	-	-20	5

Table 7. Applied loads of 25-bar truss

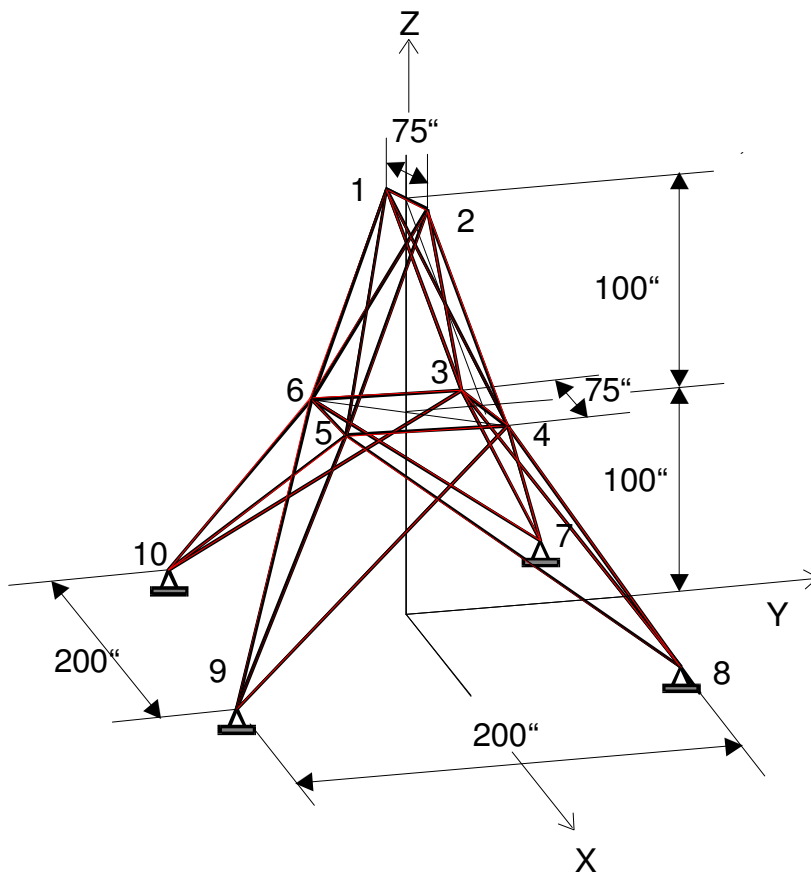


Figure 3. Geometry of the 25-bar truss

[1]=0.01	[2]= 0.1	[3]= 0.2	[4]= 0.3	[5]= 0.4	[6]= 0.5
[7]= 0.6	[8]= 0.7	[9]= 0.8	[10]= 0.9	[11]= 1.0	[12]= 1.1
[13]= 1.2	[14]= 1.3	[15]= 1.4	[16]= 1.5	[17]= 1.6	[18]= 1.7
[19]= 1.8	[20]= 1.9	[21]= 2.0	[22]= 2.1	[23]= 2.2	[24]= 2.3
[25]= 2.4	[26]= 2.5	[27]= 2.6	[28]= 2.7	[29]= 2.8	[30]= 2.9
[31]= 3.0	[32]= 3.1	[33]= 3.2	[34]= 3.3	[35]= 3.4	[36]= 3.5

Table 8. Relationship between the indices and cross-sections

Population	Crossover	Best weight	Cross-sections
50	50	201.678	{12, 5, 3, 14, 17, 5, 7, 10}
50	50	165.837	{3, 6, 12, 15, 13, 3, 4, 4}
50	50	204.183	{10, 11, 16, 3, 17, 3, 5, 3}
50	50	260.231	{15, 15, 10, 8, 3, 6, 11, 4}
50	50	188.972	{30, 8, 9, 5, 11, 5, 3, 7}
50	50	153.736	{27, 4, 4, 12, 15, 3, 4, 7}
50	50	166.926	{13, 3, 6, 6, 15, 5, 9, 3}
50	50	228.348	{8, 4, 13, 23, 16, 3, 7, 9}
50	50	160.656	{27, 4, 9, 3, 7, 3, 7, 5}
50	50	157.644	{15, 6, 4, 7, 13, 6, 5, 4}

Table 9. Results of 25-bar truss

Results of ten-bar truss			Results of twenty-five-bar truss		
Variables	Continuous solution	Discrete method	Variables	Continuous solution	Discrete method
1	30.4015	36.0	1	0.3	0.3
2	0.1	0.1	2	2.03572	2.00
3	23.1041	27.0	3	2.75761	2.80
4	15.2160	19.0	4	0.01	0.01
5	0.1	0.5	5	0.01778	0.01
6	0.6623	0.1	6	0.33511	0.40
7	7.5049	7.0	7	1.9	1.90
8	20.9631	19.0	8	0.1	0.20
9	21.5409	19.0			
10	0.1	0.1			
weight [lb]	5056.15	5273.32		394.027	403.897

Table 10. The optimum cross-sectional areas [in^2] using linear elastic material law

The optimal weight of the 25-bar truss structure is $153.736 lb$ using the nonlinear material law instead of the linear elastic rod members resulting in $403.897 lb$ for discrete design variables and resulting in $394.027 lb$ in the case of continuous solution methods.

5. Conclusions

In this work, three different solution techniques are discussed and compared, simulated annealing (SA), genetic algorithm (GA), and tabu search (TS) methods, for solving a discrete minimal weight design problem for shallow space trusses. In each case we stopped the searching process after 150 design evaluations. The computational results reveal the fact that the GA method produces high quality results when the solution time is limited. Obviously, the performance of SA, TA, and GA depends on various parameter choices, such as the cooling parameter for SA, and the population

size, frequency of mutation for GA. The TA and the SA methods are very sensitive to the starting (initial) design. When the solution time is limited, the likelihood that the TA and SA methods provide near optimal solutions is very low.

We compared the numerical results of two frequently used test problems obtained by using the linear and nonlinear material law. We obtained much lighter structure in both cases but we have to note that the solution method was different in the quoted paper [3] (see Table 7) and in the present study. In contradiction with paper [3], here nodal displacement constraints were not considered. However, the large deflection in the behavior of the initial structure might be significant. In the last two examples, a genetic algorithm (GA) was adopted for the discrete optimal design problem. In each case we stopped the searching process after 150 (300) design evaluations related to a population size of 50 (100).

References

1. ARORA, J. S., HUANG, M. W. and HSICH C. C.: Methods for optimization of nonlinear problems with discrete variables: a review. *Structural Optimization*, **8**, (1994), 69-85.
2. CSÉBFALVI, A.: A non-linear path-following method for computing the equilibrium curve of structures. *Annals of Operation Research* **81**, (1998), 15-23.
3. CSÉBFALVI A. and CSÉBFALVI, G.: A new discrete optimization procedure for geometrically non-linear space trusses, in: Proceedings of Third World Congress of Structural and Multidisciplinary Optimization (WCSMO-3), May 17-21, 1999, Buffalo, New York, 1, 1999, On-line publication:
<http://www.eng.buffalo.edu/Research/MODEL/wcsmo3/proceedings/30SMD/30SMD6.pdf>
4. CSÉBFALVI, A.: Discrete optimal weight design of geometrically nonlinear truss-structures. *Computer Assisted Mechanics and Engineering Sciences*, **6**, (1999), 313-320.
5. CSÉBFALVI, A.: Discrete optimization of shallow trusses with stability constraints, in: Proceedings of the Third International Conference on Coupled Instabilities in Metal Structures (CIMS'2000), eds. D. Camotim, D. Dubina, J. Rondal, September 21-23, 2000, Lisbon, Portugal, Imperial College Press, 635-642, 2000.
6. CSÉBFALVI, A.: A simulated annealing algorithm for discrete minimal weight design of shallow space trusses with stability constraints, WCCM-V Fifth World Congress on Computational Mechanics, July 7-12, 2002, Vienna, Austria, eds. H. A. Mang, F. G. Rammerstorfer, J. Eberhardsteiner, On-line publication (ISBN 3 9501554-0-6) Paper-ID: 81234, Session: RS 207.4, 2002.
7. CSÉBFALVI, A.: Optimal Design of Space Structures with Stability Constraints, in: System-based Vision for Strategic and Creative Design, ed. Bontempi, Swets & Zeitlinger, Lisse, ISBN 90 5809 599 1, 493-497, 2003.
8. GOLDBERG, D. E. and SAMTANI, M. P.: Engineering Optimization via Genetic Algorithms, 9th Conference on Electronic Computation, ASCE, New York, 471-482, 1986.
9. JOHN, K. V. and RAMAKRISHNAN C. V.: Optimum design of trusses from available section - use of sequential linear programming with branch and bound algorithm. *Engineering Optimization*, **13**, (1988), 119-145.
10. KIRKPATRIK, S., GELATT, C. and VECCHI, M.: Optimization by simulated annealing. *Science*, 220, (1983), 671-680.

11. LEITE, J. P. B. and TOPPING, B. H. V.: Parallel simulated annealing for structural optimization. *Computers & Structures*, **73**, (1999), 545-564.
12. RAJEEV, S. and KRISHNAMOORTY C. S.: Discrete optimization of structures using genetic algorithms. *Journal of Structural Engineering ASCE*, **118**(5), (1992), 1233-1250.
13. SALAJEGHEH, E. and SALAJEGHEH, J.: Optimum design of structures with discrete variables using higher order approximation. *Computer Methods in Applied Mechanics and Engineering*. **191**, (2002), 1395-1419.

A RECIPROCAL THEOREM FOR STEADY-STATE HEAT CONDUCTION PROBLEMS

ISTVÁN ECSEDI AND KORNÉL DLUHI
Department of Mechanics, University of Miskolc
3515 Miskolc-Egyetemváros, Hungary
mechecs@uni-miskolc.hu, mechdk@uni-miskolc.hu

[Received: October 8, 2004]

Dedicated to István Páczelt on the occasion of his 65th birthday

Abstract. This paper presents a reciprocal theorem for steady-state heat conduction problems. Some examples illustrate the applications of the reciprocal relation formulated. The method applied is based on the analogy which exists between linear elasticity and heat conduction.

Mathematical Subject Classification: 80A20

Keywords: heat conduction, reciprocal theorem, steady-state, thermal energy

1. Introduction

Consider a 3D solid body B occupying a closed and limited region \bar{V} for which the steady-state heat condition is defined. The set of inner points V is denoted by V and the set of points on the boundary of \bar{V} is denoted by ∂V , $\bar{V} = V \cup \partial V$. Point P of \bar{V} is indicated by the vector $\vec{OP} = \mathbf{p} = x\mathbf{e}_x + y\mathbf{e}_y + z\mathbf{e}_z$ in a given orthogonal Cartesian coordinate system $Oxyz$ with the unit vectors \mathbf{e}_x , \mathbf{e}_y , \mathbf{e}_z . The volume element in V is denoted by dv and the surface element defined on ∂V is da .

The temperature difference field [7, 1] in the body \bar{V} is denoted by $T = T(x, y, z)$. Following Wojnar [7] and the thermal intensity vector field is introduced by the definition

$$\mathbf{t} = -\nabla T, \quad (1)$$

where

$$\nabla = \frac{\partial}{\partial x}\mathbf{e}_x + \frac{\partial}{\partial y}\mathbf{e}_y + \frac{\partial}{\partial z}\mathbf{e}_z \quad (2)$$

is the gradient operator [4, 5]. The field equations of the steady-state heat conduction problem are the heat balance equation [1, 6]

$$-\nabla \cdot \mathbf{q} + R = 0, \quad \text{in } V \quad (3)$$

and the Fourier law of heat conduction [6, 7], which takes the form

$$\mathbf{q} = \mathbf{K} \cdot \mathbf{t}, \quad (4)$$

and the thermal intensity vector–temperature difference field relation (1). In equations (3), (4) the dot denotes the scalar product according to Malvern [5] and Lurje [4]

and in equation (4) $\mathbf{K} = \mathbf{K}(x, y, z)$ is the heat conductivity tensor field, which is symmetric and positive definit [1, 7]. The distributed heat source in B is denoted by $R = R(x, y, z)$. On the boundary surface ∂V the heat flux q is defined at every regular points of ∂V as

$$q = \mathbf{q}(x, y, z) \cdot \mathbf{n} \quad (x, y, z) \in \partial V, \quad (5)$$

where \mathbf{n} is the outward unit normal vector to ∂B at point (x, y, z) .

We say that an ordered array $s = [T, \mathbf{t}, \mathbf{q}]$ is an admissible state if T , \mathbf{t} and \mathbf{q} are sufficiently smooth in \bar{V} and they satisfy equations (1) and (4). The admissible state corresponds to internal heat source R and boundary surface heat flux q if equations (3) and (5) are satisfied. The ordered array of R and q is denoted by p as $p = [R, q]$.

2. Reciprocal theorem

Theorem 1. *Let $s = [T, \mathbf{t}, \mathbf{q}]$ and $\tilde{s} = [\tilde{T}, \tilde{\mathbf{t}}, \tilde{\mathbf{q}}]$ be two admissible states of the stationary heat conduction in body B corresponding to the internal heat sources and surface heat fluxes $p = [R, q]$ and $\tilde{p} = [\tilde{R}, \tilde{q}]$, respectively, then we have*

$$\begin{aligned} \int_V \mathbf{t} \cdot \tilde{\mathbf{q}} \, dv &= \int_V \tilde{\mathbf{t}} \cdot \mathbf{q} \, dv \\ &= - \int_{\partial V} T \tilde{q} \, da + \int_V T \tilde{R} \, dv = - \int_{\partial V} \tilde{T} q \, da + \int_V \tilde{T} R \, dv. \end{aligned} \quad (6)$$

Proof. The validity of equation (6) follows from the equations

$$\begin{aligned} \int_V \mathbf{t} \cdot \tilde{\mathbf{q}} \, dv &= \int_V \mathbf{t} \cdot \mathbf{K} \cdot \tilde{\mathbf{t}} \, dv, \quad \int_V \tilde{\mathbf{t}} \cdot \mathbf{q} \, dv = \int_V \tilde{\mathbf{t}} \cdot \mathbf{K} \cdot \mathbf{t} \, dv, \\ \int_V \tilde{\mathbf{t}} \cdot \mathbf{K} \cdot \mathbf{t} \, dv &= \int_V \mathbf{t} \cdot \mathbf{K} \cdot \tilde{\mathbf{t}} \, dv, \end{aligned} \quad (7)$$

$$\begin{aligned} \int_V \tilde{\mathbf{t}} \cdot \mathbf{K} \cdot \mathbf{t} \, dv &= \int_V \tilde{\mathbf{q}} \cdot \mathbf{t} \, dv = - \int_V \tilde{\mathbf{q}} \cdot \nabla T \, dv = \\ &= - \int_V \nabla \cdot (\tilde{\mathbf{q}} T) \, dv + \int_V T \nabla \cdot \tilde{\mathbf{q}} \, dv = - \int_{\partial V} \mathbf{n} \cdot \tilde{\mathbf{q}} T \, da + \int_V T \tilde{R} \, dv = \\ &= - \int_{\partial V} T \tilde{q} \, dv + \int_V T \tilde{R} \, dv. \end{aligned} \quad (8)$$

Here, the rule for derivation of a product function and the divergence theorem have been used. \square

3. Energy theorems

In [7], Wojnar introduced the thermal energy U corresponding to a continuous thermal intensity field \mathbf{t} defined on \bar{V} by

$$U\{\mathbf{t}\} = \frac{1}{2} \int_V \mathbf{t} \cdot \mathbf{K} \cdot \mathbf{t} \, dv. \quad (9)$$

Theorem 2. Let $s = [T, \mathbf{t}, \mathbf{q}]$ and $\tilde{s} = [\tilde{T}, \tilde{\mathbf{t}}, \tilde{\mathbf{q}}]$ be admissible states corresponding to internal heat sources and boundary surface heat fluxes $p = [R, q]$ and $\tilde{p} = [\tilde{R}, \tilde{q}]$, respectively. Then

$$U\{\mathbf{t}\} \leq U\{\tilde{\mathbf{t}}\} \tag{10}$$

provided

$$-\int_{\partial V} T(\tilde{q} - q) \, da + \int_V T(\tilde{R} - R) \, dv \geq 0, \tag{11}$$

or

$$-\int_{\partial V} q(\tilde{T} - T) \, da + \int_V R(\tilde{T} - T) \, dv \geq 0. \tag{12}$$

Thus, if ∂V_1 and ∂V_2 are complementary surface segments of ∂V ($\partial V = \partial V_1 \cup \partial V_2$, $\partial V_1 \cap \partial V_2 = \{\emptyset\}$), then we have

$$\left. \begin{array}{l} T = \tilde{T} \quad \text{on} \quad \partial V_1 \\ q = 0 \quad \text{on} \quad \partial V_2 \\ R = 0 \quad \text{in} \quad V \end{array} \right\} \Rightarrow U\{\mathbf{t}\} \leq U\{\tilde{\mathbf{t}}\}, \tag{13}$$

or

$$\left. \begin{array}{l} T = 0 \quad \text{on} \quad \partial V_1 \\ q = \tilde{q} \quad \text{on} \quad \partial V_2 \\ R = \tilde{R} \quad \text{in} \quad V \end{array} \right\} \Rightarrow U\{\mathbf{t}\} \leq U\{\tilde{\mathbf{t}}\}. \tag{14}$$

Proof. From the definition of thermal energy U it follows that

$$U\{\tilde{\mathbf{t}}\} = U\{\mathbf{t} + (\tilde{\mathbf{t}} - \mathbf{t})\} = U\{\mathbf{t}\} + U\{\tilde{\mathbf{t}} - \mathbf{t}\} + \int_V \mathbf{t} \cdot \mathbf{K} \cdot (\tilde{\mathbf{t}} - \mathbf{t}) \, dv. \tag{15}$$

On the other hand the application of Theorem 1 to the admissible states $s = [T, \mathbf{t}, \mathbf{q}]$ and $\hat{s} = [\hat{T} = T - \tilde{T}, \hat{\mathbf{t}} = \mathbf{t} - \tilde{\mathbf{t}}, \hat{\mathbf{q}} = \mathbf{q} - \tilde{\mathbf{q}}]$ were $\hat{p} = [\hat{R} = R - \tilde{R}, \hat{q} = q - \tilde{q}]$ yields

$$\begin{aligned} \int_V \mathbf{t} \cdot \mathbf{K} \cdot (\tilde{\mathbf{t}} - \mathbf{t}) \, dv &= -\int_{\partial V} T(\tilde{q} - q) \, da + \int_V T(R - \tilde{R}) \, dv \\ &= -\int_{\partial V} q(\tilde{T} - T) \, da + \int_V R(\tilde{T} - T) \, dv. \end{aligned} \tag{16}$$

We have

$$U\{\tilde{\mathbf{t}} - \mathbf{t}\} \geq 0, \tag{17}$$

since \mathbf{K} is a positive definite symmetric tensor field. From equations (15), (16) and inequality relation (17) we immediately obtain the statements formulated in Theorem 2. \square

Theorem 3. *If the admissible states $s = [T, \mathbf{t}, q]$ and $\tilde{s} = [\tilde{T}, \tilde{\mathbf{t}}, \tilde{q}]$ corresponding to $p = [R, q]$ and $\tilde{p} = [\tilde{R}, \tilde{q}]$ satisfy the following conditions*

$$R = \tilde{R} \qquad \text{in } V, \qquad (18)$$

$$T = \text{arbitrary constant} \qquad \text{on } \partial V_1, \qquad (19)$$

$$q = \tilde{q} \qquad \text{on } \partial V_2, \qquad (20)$$

where ∂V_1 and ∂V_2 are complementary surface segments of ∂V such that $\partial V = \partial V_1 \cup \partial V_2$ and $\partial V_1 \cap \partial V_2 = \{\emptyset\}$, then

$$U\{\mathbf{t}\} \leq U\{\tilde{\mathbf{t}}\}. \qquad (21)$$

Proof. We have, according to the global heat balance equation,

$$\int_{\partial V_1} q \, da = \int_V R \, dv - \int_{\partial V_2} q \, da, \qquad \int_{\partial V_1} \tilde{q} \, da = \int_V \tilde{R} \, dv - \int_{\partial V_2} q \, da. \qquad (22)$$

From equations (18), (20) and (22) it follows that

$$\int_{\partial V_1} (\tilde{q} - q) \, da = 0. \qquad (23)$$

By the use of equations (20) and (23) we can write

$$\int_{\partial V} T(\tilde{q} - q) \, da = T \int_{\partial V_1} (\tilde{q} - q) \, da + \int_{\partial V_2} T(\tilde{q} - q) \, da = 0. \qquad (24)$$

Substitution of equations (20) and (24) into relation (11) we obtain that the statement formulated in Theorem 3 is a direct consequence of Theorem 2. \square

4. Mean heat flux vector

We define the mean heat flux vector $\langle \mathbf{q} \rangle$ corresponding to an admissible state $s = [T, \mathbf{t}, \mathbf{q}]$ and $p = [R, q]$ as

$$\langle \mathbf{q} \rangle = \frac{1}{V} \int_V \mathbf{q} \, dv. \qquad (25)$$

Theorem 4. *The mean heat flux vector of the admissible state corresponding to internal heat source field R and surface heat flux q can be expressed as*

$$\langle \mathbf{q} \rangle = \frac{1}{V} \left(\int_{\partial V} \mathbf{p}q \, da - \int_V \mathbf{p}R \, dv \right). \qquad (26)$$

Proof. Be

$$\tilde{T} = \boldsymbol{\alpha} \cdot \mathbf{p} \qquad (27)$$

in equation (6) where $\boldsymbol{\alpha}$ is a constant vector. A simple computation gives

$$\tilde{R} = -\nabla \cdot \mathbf{K} \cdot \boldsymbol{\alpha} \qquad \text{in } V, \qquad (28)$$

$$\tilde{q} = -\mathbf{n} \cdot \mathbf{K} \cdot \boldsymbol{\alpha} \qquad \text{on } \partial V, \qquad (29)$$

$$\int_{\partial V} \tilde{T}q \, da - \int_V \tilde{T}R \, dv = \boldsymbol{\alpha} \cdot \left(\int_{\partial V} \mathbf{p}q \, da - \int_V \mathbf{p}R \, dv \right), \qquad (30)$$

$$\begin{aligned} \int_{\partial V} T\tilde{q} \, da - \int_V T\tilde{R} \, dv &= - \int_{\partial V} T\mathbf{n} \cdot \mathbf{K} \cdot \boldsymbol{\alpha} \, da + \int_V T\nabla \cdot \mathbf{K} \cdot \boldsymbol{\alpha} \, dv \\ &= - \int_{\partial V} T\mathbf{n} \cdot \mathbf{K} \cdot \boldsymbol{\alpha} \, da + \int_{\partial V} T\mathbf{n} \cdot \mathbf{K} \cdot \boldsymbol{\alpha} \, dv + \int_V \boldsymbol{\alpha} \cdot \mathbf{K} \cdot \mathbf{t} \, dv \\ &= \boldsymbol{\alpha} \cdot \int_V \mathbf{q} \, dv . \end{aligned} \tag{31}$$

In the derivation of equation (31) we have used the rule of differentiation of product function, divergence theorem and equation (4). Combination of equation (30) with equation (31) gives the formula of mean heat flux vector.

We note that formula (26) can be derived only by the use of equations (3) and (5). It is not necessary for $\mathbf{q} = \mathbf{q}(x, y, z)$ in (26) to be the solution of a heat conductance problem [2]. If $\mathbf{q} = \mathbf{q}(x, y, z)$ is a solution of a steady-state heat conduction problem, then it satisfies

$$\nabla \times \mathbf{R} \cdot \mathbf{q} = \mathbf{0} \qquad \text{in } V \tag{32}$$

where \mathbf{R} is the inverse tensor of \mathbf{K} (the thermal resistivity tensor [7, 1] $\mathbf{R} \cdot \mathbf{K} = \mathbf{1}$, $\mathbf{1}$ is the unit tensor). The cross between two vectors in equation (32) denotes their vectorial product according to Lurje [4] and Malvern [5]. Compatibility conditions for \mathbf{q} given by (32) are obtained from equations (1), (4). \square

5. Heat conduction on non-homogeneous curved beam

Consider a curved beam (Figure 1) which is an incomplete torus in the 3D space. A torus-like body is generated by the rotation of a plane figure about axis z whose inner and boundary points are taken from the sets A and ∂A , respectively. The domain $\bar{A} = A \cup \partial A$ is bounded and called the cross-section of curved beam. The curved beam occupies the region $\bar{V} = V \cup \partial V$; $V = \{(r, \varphi, z) | (r, z) \in A, 0 < \varphi < \alpha\}$, $\partial V = A_1 \cup A_2 \cup A_3$, $A_i = \{(r, \varphi, z) | (r, z) \in A \quad \varphi = \varphi_i \quad (i = 1, 2) \quad \varphi_1 = 0, \varphi_2 = \alpha\}$, $A_3 = \{(r, \varphi, z) | (r, z) \in \partial A \quad 0 \leq \varphi \leq \alpha\}$, which is referred to a given cylindrical coordinate system $Or\varphi z$. Unit vectors of the cylindrical coordinate system $Or\varphi z$ are $\mathbf{e}_r = \mathbf{e}_x \cos \varphi + \mathbf{e}_y \sin \varphi$, $\mathbf{e}_\varphi = \mathbf{e}_z \times \mathbf{e}_r$ and \mathbf{e}_z . The polar coordinates r and φ are defined as $r = \sqrt{x^2 + y^2}$, $\tan \varphi = y/x$. The incomplete torus-like body (curved beam) is isotropic and φ -homogeneous. This means that

$$\mathbf{K} = k(r, z) \mathbf{1} , \tag{33}$$

where $k = k(r, z)$ is the thermal conductivity of curved beam (incomplete torus, $0 < \alpha < 2\pi$), which may depend upon the cross-sectional coordinates r and z . The following boundary-value problem of the steady-state heat conduction is analysed:

$$T(r, 0, z) = \vartheta_1(r, z) \qquad \text{on } A_1 \qquad (\vartheta_1(r, z) \text{ is given function on } A_1) , \tag{34}$$

$$T(r, \alpha, z) = \vartheta_2(r, z) \qquad \text{on } A_2 \qquad (\vartheta_2(r, z) \text{ is given function on } A_2) , \tag{35}$$

$$\mathbf{q} \cdot \mathbf{n} = q_3(r, \varphi, z) \qquad \text{on } A_3 \qquad (q_3(r, \varphi, z) \text{ is given function on } A_3) , \tag{36}$$

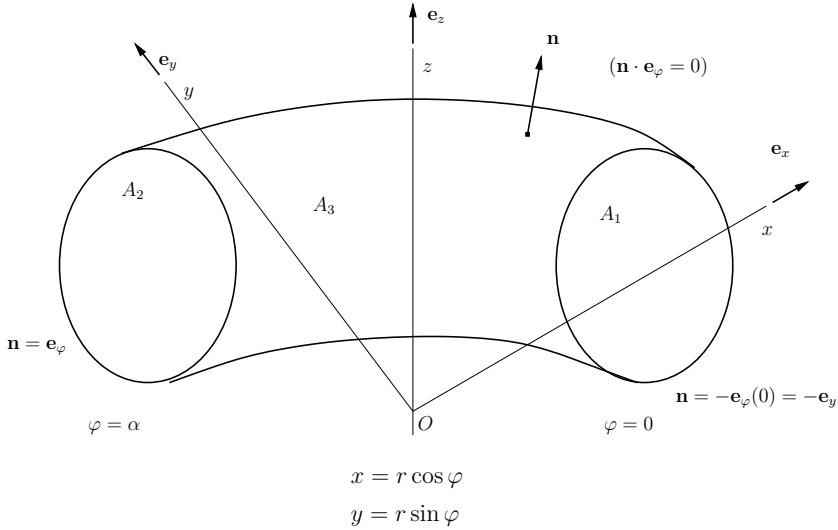


Figure 1. Incomplete non-homogeneous torus (curved beam)

furthermore $R = R(r, \varphi, z)$ is specified in V . Our aim is to obtain the values of heat flux resultants Q_1 and Q_2 which are defined as

$$Q_1 = \int_{A_1} \mathbf{q} \cdot \mathbf{n}_1 \, da = - \int_{A_1} \mathbf{q} \cdot \mathbf{e}_\varphi \, da, \quad (37)$$

$$Q_2 = \int_{A_2} \mathbf{q} \cdot \mathbf{n}_2 \, da = \int_{A_2} \mathbf{q} \cdot \mathbf{e}_\varphi \, da. \quad (38)$$

Here, we note (Figure 1) $\mathbf{n} = \mathbf{n}_1 = -\mathbf{e}_\varphi$ on A_1 , $\mathbf{n} = \mathbf{n}_2 = \mathbf{e}_\varphi$ on A_2 and $\mathbf{n} = \mathbf{n}_3$ on A_3 , $\mathbf{n}_3 \cdot \mathbf{e}_\varphi = 0$. The global heat balance equation for the incomplete torus is formulated as

$$Q_1 + Q_2 + Q_3 - Q_v = 0, \quad (39)$$

where

$$Q_3 = \int_{A_3} q_3 \, da = \int_0^\alpha \left(\oint_{\partial A} r q_3 \, d\sigma \right) d\varphi, \quad (40)$$

$$Q_v = \int_0^\alpha \left(\int_A r R \, dA \right) d\varphi. \quad (41)$$

In equation (40), σ is the arc-length defined on the boundary curve of A . The first equation, which we will use to determine the heat flux resultants Q_1 and Q_2 , is equation (39) and the second one will be derived from the reciprocal relation (6). Let the state $s = [T, \mathbf{t}, \mathbf{q}]$ be the solution of the heat conduction problem of the curved beam specified by boundary conditions (34), (35), (36) with the prescribed internal heat source $R = R(r, \varphi, z)$. The second state of steady heat conduction for the curved

beam shown in Figure 1 is given by the following equations

$$\begin{aligned} \tilde{T} &= C\varphi, & \tilde{\mathbf{t}} &= -\frac{C}{r}\mathbf{e}_\varphi, & \tilde{\mathbf{q}} &= -C\frac{\lambda(r,z)}{r}\mathbf{e}_\varphi, \\ \tilde{R} &= \nabla \cdot \tilde{\mathbf{q}} = 0, & \tilde{q} &= -C\frac{\lambda(r,z)}{r}\mathbf{e}_\varphi \cdot \mathbf{n} & \text{on } A &= A_1 \cup A_2 \cup A_3, \end{aligned}$$

where C is a constant different from zero. It is very easy to show that

$$\int_{\partial V} \tilde{T}q \, da - \int_V \tilde{T}R \, dV = C(I_1 - I_2 + \alpha Q_2), \tag{42}$$

$$\begin{aligned} \int_{\partial V} T\tilde{q} \, da - \int_V T\tilde{R} \, dV \\ = -C \left(\int_{A_2} \frac{\lambda(r,z)}{r} \vartheta_2(r,z) \, da - \int_{A_1} \frac{\lambda(r,z)}{r} \vartheta_1(r,z) \, da \right). \end{aligned} \tag{43}$$

Here,

$$I_1 = \int_{A_3} \varphi q_3 \, da = \int_0^\alpha \oint_{\partial A} r\varphi q_3 \, d\sigma \, d\varphi, \tag{44}$$

$$I_2 = \int_V \varphi R \, dV = \int_0^\alpha \oint_{\partial A} r\varphi R \, da \, d\varphi. \tag{45}$$

Substitution of equations (42) and (43) into reciprocal relation (6) yields

$$Q_2 = -\frac{1}{\alpha} \left(\int_{A_2} \frac{\lambda(r,z)}{r} \vartheta_2(r,z) \, da - \int_{A_1} \frac{\lambda(r,z)}{r} \vartheta_1(r,z) \, da \right) + \frac{I_2 - I_1}{\alpha}. \tag{46}$$

Formula (46) gives the value of heat flux resultant Q_2 without knowing the solution of the corresponding 3D heat conduction problem of the incomplete torus.

6. Mean temperature

Let B be a homogeneous solid sphere. The domain \bar{V} occupied by B is

$$\bar{V} = \{\mathbf{p} = x\mathbf{e}_x + y\mathbf{e}_y + z\mathbf{e}_z \mid p^2 - \varrho^2 \leq 0\},$$

where ϱ is the radius of the bounding spherical surface. The following boundary value problem of heat conduction is considered:

$$R(x, y, z) = R(\mathbf{p}) \quad \text{is prescribed in } V, \tag{47a}$$

$$T(x, y, z) = \vartheta(x, y, z) \quad \text{on } \partial V \quad (\vartheta(x, y, z) \text{ is given function on } \partial V). \tag{47b}$$

It is obvious that equation (47b) formulates a Dirichlet's type boundary condition. The position vector of a point on the spherical surface ∂V is denoted by $\boldsymbol{\varrho}$. Our purpose is to compute the mean value of the temperature field of a solid sphere without knowing the solution of the boundary value problem determined by the prescriptions mentioned above. We use the reciprocal relation (6). The first admissible state is the

solution of the heat conduction problem specified by equations (47a) and (47b). The second admissible state is given by the following equations

$$\tilde{T} = \frac{C}{2}(\varrho^2 - p^2), \quad \tilde{\mathbf{t}} = C\mathbf{p} \quad \text{on } \bar{V}, \quad (48)$$

$$\tilde{\mathbf{q}} = C\mathbf{K} \cdot \mathbf{p} \quad \text{on } \bar{V}, \quad (49)$$

$$\tilde{q} = C k(\varrho) \quad \text{on } \partial V \quad \tilde{R} = CK_I \quad \text{in } V. \quad (50)$$

Here,

$$k(\varrho) = \frac{\varrho \cdot \mathbf{K} \cdot \varrho}{\varrho} \quad \text{defined on } \partial V, \quad K_I = \mathbf{K} \cdot \cdot \mathbf{1}, \quad (51)$$

K_I is the first scalar invariant of the conductivity tensor and the double dot denotes the double dot product of \mathbf{K} and $\mathbf{1}$ according to Malvern [5] and Lurje [4], and we note that \mathbf{K} is constant tensor. Substitution of the fields of two chosen admissible states into formula (6) gives the result

$$\langle T \rangle = \frac{3}{4\pi K_I \varrho^3} \left[\int_{\partial V} k(\varrho) \vartheta(\varrho) \, da + \frac{\varrho^2}{2} \int_V R(\varrho) \, dV - \frac{1}{2} \int_V p^2 R(\mathbf{p}) \, dV \right]. \quad (52)$$

In equation (52) the mean temperature field $\langle T \rangle$ in the sphere is defined as

$$\langle T \rangle = \frac{3}{4\pi \varrho^3} \int_V T(\mathbf{p}) \, dV. \quad (53)$$

7. Conclusions

In this paper, a reciprocal theorem is formulated by the use of the analogy which exists between linear elasticity and heat conduction. The formalism of applied analogy follows Wojnar's approach [7]. The theorems proven are analogous to those obtained in linear elasticity theory by Gurtin [3].

Acknowledgement. The support provided by the Hungarian National Research Foundation within the framework of projects T049115 and T037759 is gratefully acknowledged.

References

1. CARLSON, D. E.: Linear thermoelasticity. [in:] S. FLÜGGE [Ed.], *Handbuch der Physik*, Vol. VIa/2, Mechanics of Solids II. 297–345, Springer, Berlin 1972.
2. ECSEDI, I.: Mean value and bounding formulae for heat conduction. *Archives of Mechanics*, **54**(2), (2002), 127–140.
3. GURTIN, M. E.: The linear theory of elasticity. [in:] S. FLÜGGE [Ed.], *Handbuch der Physik*, Vol. VIa/2, Mechanics of Solids II. pp. 1–295, Springer, Berlin 1972.
4. LURJE, A. I.: *Theory of elasticity*. Nauka, Moscow 1970. (in Russian)
5. MALVERN, L. E.: *Introduction to the mechanics of a continuous medium*. Prentice-Hall, New York 1969.
6. ÖZISIK, M. N.: *Boundary value problems of heat conduction*. Dover Publications, New York 1989.
7. WOJNAR, R.: Upper and lower bounds on heat flux. *Journal of Thermal Stresses*, **21**, (1998), 381–403.

ECONOMY OF WELDED STIFFENED STEEL PLATES AND CYLINDRICAL SHELLS

JÓZSEF FARKAS

Department of Materials Handling and Logistics, University of Miskolc
3515 Miskolc-Egyetemváros, Hungary
altfar@uni-miskolc.hu

[Received: April 12, 2004]

Dedicated to István Páczelt on the occasion of his 65th birthday

Abstract. The main requirements for modern load-carrying structures are safety, producibility and economy. Economy is characterized by cost. We have developed a structural optimization system which assures the safety and producibility by fulfillment of design and fabrication constraints, and economy is achieved by minimization of a cost function. Using this system it is possible to make realistic comparisons between different structural versions. This is based on a cost calculation method which is developed mainly for welded structures. The thickness of plates and shells can be decreased by stiffening. Stiffened structures are economic, when the cost difference caused by thickness reduction is higher than the additional cost of stiffening material and welding. It is shown by numerical problems that stiffening is economic only in case when the sensitivity of plates and shells to buckling or transverse deformation can effectively be eliminated by it.

The economy of stiffened structures depends on the type of load and stiffening. Since plates are very sensitive to buckling and transverse deformation, their stiffening is always effective and economic. Cylindrical shells are sensitive to buckling in the case of external pressure thus ring-stiffening is economic in this case. On the other hand, they are not very sensitive to buckling in the case of axial compression or bending, thus ring-stiffening is uneconomic for these loads and stringer-stiffening is economic only in cases when the transverse deformation of the whole shell is limited.

Mathematical Subject Classification: 74K20, 74K25, 74P10

Keywords: stiffened plates and shells, welded structures, buckling, minimum cost design, structural optimization, fabrication cost calculation, economy

1. Introduction

One of the most important characteristics of welded structures is cost for welding is an expensive fabrication process. Cost is a realistic basis for the comparison of different structural versions. Optimization is needed to decrease the cost in order to develop competitive structures.

The most effective method to decrease the structural mass is to decrease thickness. Thin-walled structures show the following problems: large deformations, large residual welding stresses and distortions, buckling, vibration, sensitivity to torsion,

fatigue due to large stress concentrations. To avoid these problems, stiffening can be used. Stiffening enables thickness to be decreased, but it incurs the additional cost of stiffener material and welding. Therefore stiffening is economic only in cases when the cost difference caused by thickness reduction is higher than the additional cost of stiffening material and welding.

In our research we have worked out several minimum mass or cost design problems related to stiffened plates and shells [1]. Our experience is that cost savings due to stiffening are different, in some cases the cost of an unstiffened structure is lower than that of the stiffened one. The aim of the present study is to give an overview of these optimization results.

In order to give realistic comparisons between stiffened and unstiffened structures, both structural versions should be optimized. Since optimization processes are complicated, only numerical treatments are possible. Therefore the conclusions of these comparisons cannot be general. In spite of this disadvantage, the results of this study can be useful for designers in selecting the most suitable structural versions.

The main components of an optimum design process are as follows: design constraints, fabrication aspects, cost function and mathematical algorithms of constrained function minimization. These components affect the comparisons, thus, it is important to use realistic aspects mainly in cost calculation. Therefore we try to formulate the cost function as realistically as possible.

For the design constraints the rules of API [2], ECCS [3] or DNV [4] can be used.

2. A welded stiffened plate subject to uniaxial compression

The plate is stiffened by ribs of three types as follows: flat, L-shape and trapezoidal shapes – see Figure 1. For the buckling stress constraint the Mikami-Niwa formulae [5] are used which consider the effect of residual welding stresses and initial imperfections. The unknowns are the number of stiffeners, thickness of the base plate (t_F) and stiffener dimensions (in the case of trapezoidal stiffeners the thickness is t_3 , Figure 2).

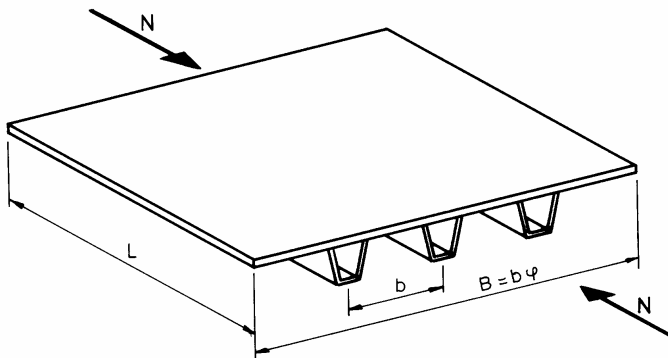


Figure 1. Uniaxially compressed plate with trapezoidal stiffeners

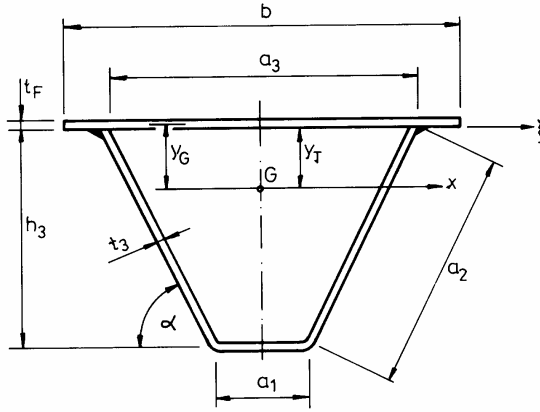


Figure 2. Dimensions of a trapezoidal stiffener

The overall buckling constraint is expressed in function of the reduced slenderness

$$\lambda = (f_y / \sigma_{cr})^{1/2} \tag{1}$$

where σ_{cr} is the classical critical buckling stress, which does not contain the above mentioned effects and, f_y is the yield stress.

The classical critical buckling stress for a uniaxially compressed longitudinally stiffened plate (Figure 1) is

$$\sigma_{cr} = \frac{\pi^2 D}{h B^2} \left(\frac{1 + \gamma_S}{\alpha_R^2} + 2 + \alpha_R^2 \right) \quad \text{for} \quad \alpha_R = L/B < \alpha_{R0} = (1 + \gamma_S)^{1/4} \tag{2}$$

$$\sigma_{cr} = \frac{2\pi^2 D}{h B^2} \left[1 + (1 + \gamma_S)^{1/2} \right] \quad \text{for} \quad \alpha_R \geq \alpha_{R0} \tag{3}$$

where, with

$$\nu = 0.3, \quad D = \frac{E t_F^3}{12(1 - \nu^2)} = \frac{E t_F^3}{10.92} \tag{4}$$

we have

$$h = t_F + \frac{A_S}{b}, \quad b = \frac{B}{\varphi}, \tag{5a}$$

$$A_S = (a_1 + 2a_2) t_3, \quad I_S = a_1 h_3^3 t_3 + \frac{2}{3} a_2^3 t_3 \sin^2 \alpha. \tag{5b}$$

According to the Stahlbau Handbuch [6] $a_1 = 90$, $a_3 = 300$ mm, thus

$$h_3 = (a_2^2 - 105^2)^{1/2}, \quad \sin^2 \alpha = 1 - \left(\frac{105}{a_2} \right)^2. \tag{5c}$$

Here A_S is the cross-sectional area of a stiffener, $\varphi - 1$ is the number of stiffeners,

$$\gamma_S = \frac{E I_S}{b D} \tag{6}$$

and I_S is the moment of inertia of a stiffener about the ξ axis.

Local buckling of a trapezoidal stiffener is defined as

$$a_2/t_3 \leq 38\varepsilon . \quad (7)$$

This constraint is treated as active.

Single panel buckling. This constraint eliminates the local buckling of the base plate parts between the stiffeners. From the classical buckling formula for a simply supported uniformly compressed bar we obtain

$$\sigma_{crP} = \frac{4\pi^2 E}{10.92} \left(\frac{t_F}{b} \right)^2 \quad (8)$$

the reduced slenderness is

$$\lambda_P = \left(\frac{4\pi^2 E}{10.92 f_y} \right)^{1/2} \frac{b}{t_F} = \frac{b/t_F}{56.8\varepsilon} , \quad \varepsilon = \left(\frac{235}{f_y} \right)^{1/2} \quad (9)$$

and the actual local buckling stress considering the initial imperfections and residual welding stresses is

$$\sigma_{UP}/f_y = 1 \quad \text{for } \lambda_P \leq 0.526 , \quad (10a)$$

$$\frac{\sigma_{UP}}{f_y} = \left(\frac{0.526}{\lambda_P} \right)^{0.7} \quad \text{for } \lambda_P \geq 0.526 . \quad (10b)$$

Then the factor ρ_P is as follows:

$$\rho_P = \begin{cases} 1 & \text{if } \sigma_{UP} > \sigma_U , \\ \sigma_{UP}/f_y & \text{if } \sigma_{UP} \leq \sigma_U . \end{cases} \quad (11)$$

Knowing the reduced slenderness (1) the actual global buckling stress can be calculated as follows:

$$\sigma_U/f_y = \begin{cases} 1 & \text{for } \lambda \leq 0.3 , \\ 1 - 0.63(\lambda - 0.3) & \text{for } 0.3 \leq \lambda \leq 1 , \\ 1/(0.8 + \lambda^2) & \text{for } \lambda > 1 . \end{cases} \quad (12)$$

The global buckling constraint is defined by

$$\frac{N}{A} \leq \sigma_U^* = \sigma_U \frac{\rho_P + \delta_S}{1 + \delta_S} \quad (13)$$

where

$$A = Bt_F + (\varphi - 1) A_S \quad (14)$$

and

$$\delta_S = \frac{A_S}{bt_F} . \quad (15)$$

Here ρ_P can be determined considering the single panel buckling of the base plate parts between the stiffeners. The factor $(\rho_P + \delta_S)/(1 + \delta_S)$ expresses the effect of the effective width of the base plate parts.

The cost function is given by

$$\frac{K}{k_m} = \rho V + \frac{k_f}{k_m} \left(\Theta_{dW} \sqrt{\kappa \rho V} + 1.3T_2 \right) , \quad (16)$$

in which V is the structural volume.

For fillet welds using GMAW-M (gas metal arc welding with mixed gas)

$$V = BLt_F + (\varphi - 1) LA_S; \quad \kappa = \varphi; \quad T_2 = 0.3258x10^{-3}a_W^2(\varphi - 1)2L. \quad (17)$$

Here $a_W = 0.5t_3$ but $a_{Wmin} = 4$ mm.

Numerical example. Given data: $B = 6000$ mm, $L = 3000$ mm, $N = 1.974 \times 10^7$ [N], $f_y = 235$ MPa, $E = 2.1 \times 10^5$ MPa, $G = E/2.6$, $\rho = 7.85 \times 10^{-6}$ kg/mm³, $\Theta_{dW} = 3$.

The results of the optimization can be seen in Figure 3. The optimal dimensions are as follows: $t_F = 11$, $t_3 = 8$ mm.

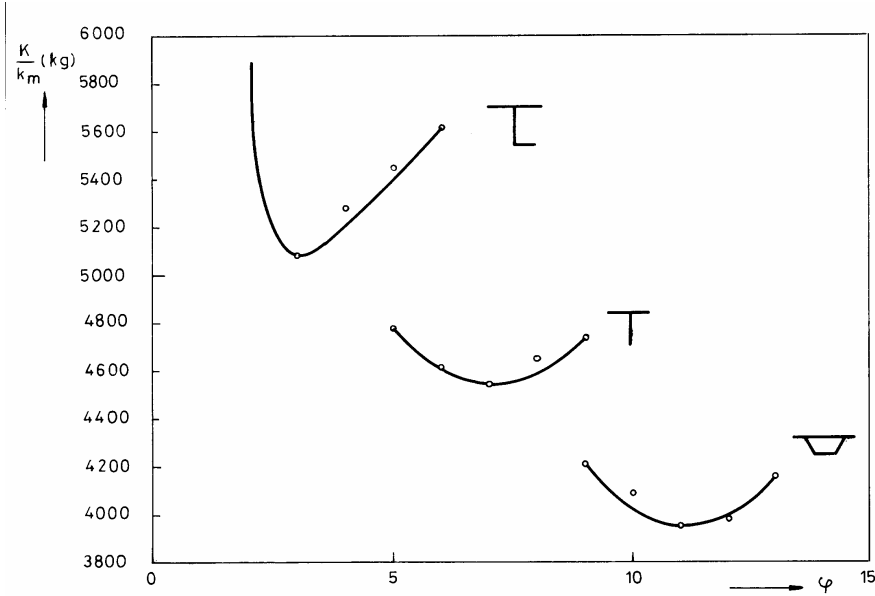


Figure 3. Cost curves in the region of the optimum number of flat, L- and trapezoidal stiffeners for $k_f/k_m = 2$ kg/min

For an unstiffened plate we have

$$\gamma_S = 0, \quad \alpha_{R0} = 1, \quad \alpha_R = 0.5, \quad h = t_F, \quad D = Et_F^3/10.92$$

and

$$\sigma_{cr} = \frac{6.25\pi^2 Et_F^2}{10.92B^2}; \quad \lambda = \frac{84.45}{t_F}. \quad (18)$$

The buckling constraint

$$\frac{N}{A} = \frac{1.974x10^7}{6x10^3 t_F} \leq \sigma_U \quad (19)$$

is fulfilled with $t_F = 51$ mm ($64.5 < 66.4$ MPa).

The cost of the unstiffened plate is

$$\frac{K}{k_m} = \rho BLt_F = 7206 \text{ kg.}$$

It can be seen that the cost of the optimized stiffened plate with trapezoidal ribs (3940 kg) is by 82% cheaper than the unstiffened one. Thus, in this case the economy of the stiffened structural version is evident.

3. An orthogonally stiffened square plate loaded by bending

A square plate with simply supported edges, loaded by uniformly distributed normal load is considered [1, 7]. The plate is stiffened by flat ribs in two directions (Figure 4). The ribs are continuous in one direction, in the other direction they are interrupted and welded to the others by double fillet welds. The size of a fillet weld is $a_W = 0.4t_S$, but $a_{Wmin} = 4\text{mm}$.

Data: $b = 6\text{ m}$, $p_0 = 5 \times 10^{-3}\text{ N/mm}^2$, the yield stress for steel is 235 MPa, the admissible stress is $\sigma_{adm} = 120\text{ MPa}$, the elastic modulus is $E = 2.1 \times 10^5\text{ MPa}$, $\rho = 7.85 \times 10^{-6}\text{ kg/mm}^3$.

In the optimization procedure we search for the optimum values of the following variables: t_F , h , t_S and φ . The number of stiffeners is $\varphi - 1$.

It is assumed that the base plate is welded with butt welds from 4 strips of dimensions $6\text{m} \times 1.5\text{m}$. Then the stiffeners are welded to the base plate by double fillet welds. Finally the interrupted ribs are welded to the other ribs by double fillet welds.

For the butt welds GMAW-M technology is used, thus, the welding time depends on the thickness of the base plate as follows [1]:

$$T_2' = \begin{cases} 3b \times 0.1861 \times 10^{-3} t_F^2 & \text{for } t_F \leq 15\text{ mm} \\ 3b \times 0.1433 \times 10^{-3} t_F^{1.9035} & \text{for } t_F > 15\text{ mm} \end{cases} \quad (20)$$

For longitudinal fillet welds the GMAW-M technology is used, thus, the welding time is

$$T_2'' = 4b(\varphi - 1) \times 0.3258 \times 10^{-3} a_W^2, \quad (21)$$

for transverse fillet welds the SMAW (shielded metal arc welding) technology is assumed, thus

$$T_2''' = 4h(\varphi - 1)^2 \times 0.7889 \times 10^{-3} a_W^2. \quad (22)$$

The volume of the structure is

$$V = b^2 t_F + 2(\varphi - 1) b h t_S. \quad (23)$$

The number of assembled elements is $\kappa = 3 + \varphi^2$. The cost function can be formulated as

$$\frac{K}{k_m} = \rho V + \frac{k_f}{k_m} \left[\Theta_{dW} (\kappa \rho V)^{0.5} + 1.3 (T_2' + T_2'' + T_2''') \right], \quad (24)$$

where $\Theta_{dW} = 3$.

Constraint on compressive stress in the central faceplate element is expressed by

$$\sigma_{\max} = \sigma_{\max.1} + \sigma_{f.\max} \leq \sigma_{adm}. \quad (25)$$

Here $\sigma_{\max.1}$ is caused by the bending of the whole plate, $\sigma_{f.\max}$ is the normal stress due to local bending of the plate elements, σ_{adm} is the admissible stress:

$$\sigma_{\max.1} = \frac{c_M p b^2}{I_x / a} y_G. \quad (26)$$

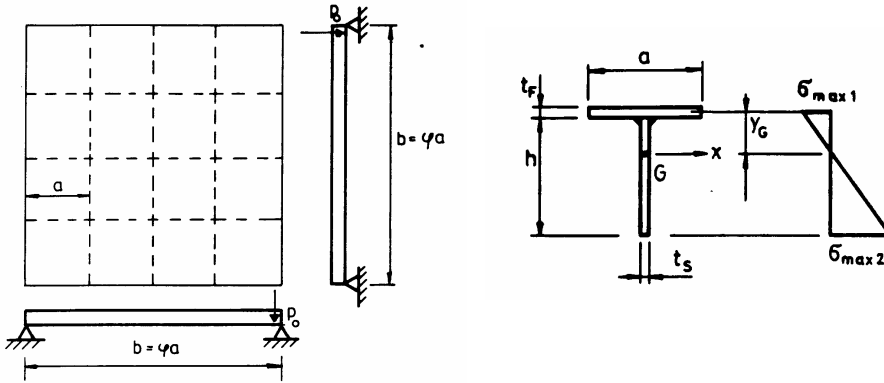


Figure 4. A simply supported transversely uniformly loaded square plate stiffened by flat ribs

The uniformly distributed normal load p contains also the self weight, approximately $p = 1.1p_0$. Since the torsional stiffness of the open section ribs is very small, the stiffened plate can be calculated as an orthotropic one having zero torsional stiffness. Schade [8] calculated for this case $c_M = 0.1102$.

As shown in Figure 4, the distance of the centroidal axis y_G can be calculated as

$$y_G = \frac{h}{2} \frac{1}{1 + \alpha}, \quad \alpha = \frac{at_F}{ht_S} = \frac{bt_F}{\varphi ht_S} \quad (27)$$

and the moment of inertia is

$$I_x = \frac{h^3 t_S}{12} \frac{1 + 4\alpha}{1 + \alpha}. \quad (28)$$

It should be noted that the admissible stress is selected so low that it is not necessary to calculate with an effective width of the face plate, thus $a = b/\varphi$.

The local bending stress can be calculated by means of formulae valid for isotropic square plates with clamped edges (Timoshenko [9])

$$\sigma_{f, \max} = \frac{5.13 \times 10^{-2} p_0 a^2}{t_F^2 / 6} = \frac{0.3078 p_0 b^2}{\varphi^2 t_F^2}. \quad (29)$$

Constraint on the maximum tensile stress in the central ribs can be written as

$$\sigma_{\max, 2} = \sigma_{\max, 1}(1 + 2\alpha) \leq \sigma_{adm}. \quad (30)$$

Constraint on local buckling of the central face plate element compressed from both sides (Farkas & Jármai [10], Volmir [11]). For a plate compressed on one side the buckling factor is $k = 4$. Instead of this value we calculate with $k = 2$. For $k = 4$ Eurocode 3 [12] gives for the limiting slenderness

$$(a/t_F)_{\lim} = 42\varepsilon, \quad \varepsilon = (235/f_y)^{0.5}, \quad (31)$$

f_y is the yield stress, but instead of using the yield stress we can calculate with the maximum stress. Thus, for $k = 2$ the buckling constraint can be written as

$$a/t_F \leq 42\varepsilon_1/\sqrt{2} \approx 30\varepsilon_1, \quad \varepsilon_1 = (235/\sigma_{\max.1})^{0.5}. \quad (32)$$

Constraint on local buckling of ribs (it is assumed that $\sigma_{\max.2}$ can also be compressive)

$$h/t_S \leq 14\varepsilon_2, \quad \varepsilon_2 = (235/\sigma_{\max.2})^{0.5}. \quad (33)$$

Constraint on shear buckling of ribs at the plate edges can be formulated as

$$\tau = \frac{0.42pb^2}{ht_S\varphi} \leq \frac{\tau_{ub}}{\gamma_b} = \frac{5.34\pi^2 E}{12(1-\nu^2)\gamma_b} \left(\frac{t_S}{h}\right)^2 \quad \text{for} \quad \frac{\tau_{ub}}{\gamma_b} \leq \tau_{adm} \quad (34)$$

and

$$\tau \leq \tau_{adm} \quad \text{for} \quad \frac{\tau_{ub}}{\gamma_b} \geq \tau_{adm}. \quad (35)$$

The factor 0.42 is considered, since the distribution of edge reactions is not uniform along the edges (Timoshenko [9]). $\tau_{adm} = \sigma_{adm}/\sqrt{3}$ is the admissible shear stress, ν is the Poisson ratio.

Constraint on residual distortion due to shrinkage of welds is formulated as follows.

Although the stiffeners are welded along two directions, we do not multiply residual deflection by 2. A multiplying factor of 1.5 is used considering the fact that the longitudinal double fillet welds are intermittent due to interruption of ribs and the residual plastic zones of the continuous welds affect the deflection caused by intermittent welds. Thus the distortion constraint is formulated as

$$f = 1.5Cb^2/8 \leq f_{adm}, \quad (36)$$

where the admissible deflection is assumed to be $f_{adm} = b/1000 = 6$ mm.

The orthotropic plate bending theory is valid only in the case when the number of stiffeners is more than 3, thus

$$\varphi \geq 4. \quad (37)$$

It can be seen that the objective function and the design constraints are highly nonlinear. For the constrained function minimization Rosenbrock's hillclimb mathematical programming method is used (a detailed description can be found in Farkas & Jármai [10]) complemented by an additional discretization of the continuous optima considering rounded dimensions and integer numbers of stiffeners.

The optimization results in the following values: for $k_F/k_m = 2$, $t_F = 11$, $h = 250$, $t_S = 14$ mm, $\varphi = 4$ and the corresponding cost is $K/k_m = 9317$ kg. The maximum deflection in the center due to the normal load is

$$w_{\max} = 0.0083 \frac{p_0 b^4}{B_x} = 6.06 < \frac{b}{300} = 20 \text{ mm}, \quad (38)$$

where

$$B_x = \frac{EI_x}{a} = 8.8684 \times 10^9 \text{ Nmm}, \quad I_x = \frac{h^3 t_S}{12} \frac{1 + 4\alpha}{1 + \alpha} = 6.3346 \times 10^7 \text{ mm}^4, \quad (39)$$

$$\alpha = \frac{at_F}{ht_S} = 4.7143.$$

The thickness required for an unstiffened plate to fulfil the deflection constraint of

$$w_{\max} = 0.065 \frac{p_0 b^4}{Et_F^3/10.92} \leq w_{adm} = 20 \text{ mm} \quad (40)$$

is $t_{F0} = 103 \text{ mm}$ and the corresponding cost is $K/k_m = \rho b^2 t_{F0} = 29108 \text{ kg}$.

It can be seen that the stiffened plate which fulfils the stress and deflection constraints is much cheaper (9317 kg) than the unstiffened one (29108 kg). It can be concluded that a plate subject to normal load is very weak against deflection, thus stiffening in this case is also economic.

From the above cases of stiffened plates it can be concluded that their stiffening is economic, since they are very sensitive to buckling as well as to large transverse deformation and stiffening eliminates these sensitivities.

4. A ring-stiffened cylindrical shell subject to external pressure

The design constraints are formulated according to API rules [2].

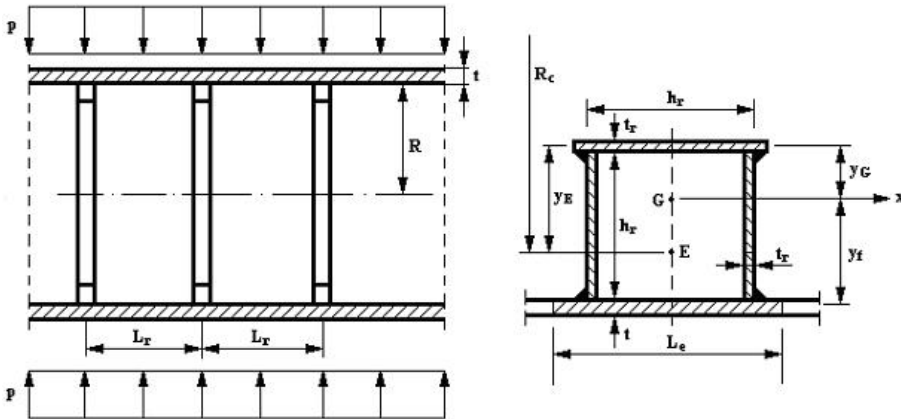


Figure 5. Ring-stiffened cylindrical shell

Geometric characteristics. Data: length of shell $L_b = 15 \text{ m}$, welded from 5 m long segments, radius of shell $R = 1850 \text{ mm}$, intensity of the external pressure $p = 0.5 \text{ MPa}$, yield stress of steel $f_y = 355 \text{ MPa}$. To avoid tilting of the ring-stiffeners, the welded square box section is used, which is characterized by height h_r and thickness t_r . Considering the local buckling constraint of the stiffener flange active, we use the following correlation between height and thickness

$$t_r = \delta_r h_r; \delta_r = 1/42\varepsilon; \varepsilon = \sqrt{235/f_y}; \delta_r = 1/34. \quad (41)$$

The cross-sectional area of a stiffener is

$$A_r = 3h_r t_r = 3\delta_r h_r^2. \quad (42)$$

The distances of centroid G are as follows (Figure 5)

$$y_G = \frac{h_r}{3}, \quad y_r = \frac{2h_r}{3} + \frac{t}{2}, \quad (43)$$

$$y_E = \frac{L_e t (h_r + \frac{t}{2}) + \delta_r h_r^3}{3\delta_r h_r^2 + L_e t}, \quad (44)$$

$$L_e = \begin{cases} 1.1\sqrt{2Rt} & \text{if } M_x = \frac{L_r}{\sqrt{Rt}} > 1.56, \\ L_r & \text{if } M_x \leq 1.56. \end{cases} \quad (45)$$

The distance of the centroid E of the cross-section consisting of the stiffener and the effective part of the shell is characterized by

$$R_C = R - \left(h_r - y_E + \frac{t}{2} \right). \quad (46)$$

The moment of inertia of the stiffener and the effective part of shell is

$$I_{er} = \frac{\delta_r h_r^4}{6} + A_r y_r^2 K_G + \frac{L_e t^2}{12}; \quad K_G = \frac{L_e t}{A_r + L_e t}, \quad (47a)$$

where

$$K_G = \frac{L_e t}{A_r + L_e t}. \quad (47b)$$

Design constraints

Constraint on local shell buckling

$$\gamma_b p \frac{R}{t} \leq \eta_L \sigma_{UL}, \quad (48)$$

where $\gamma_b = 1.5$ is the safety factor and the plasticity reduction factor η_L is calculated in function of $\delta_L = \sigma_{UL}/f_y$ as follows

$$\eta_L = \begin{cases} 1 & \text{if } \delta_L \leq 0.55, \\ \frac{0.45}{\delta_L} + 0.18 & \text{if } 0.55 < \delta_L \leq 1.6, \\ \frac{1.31}{1 + 1.15\delta_L} & \text{if } 1.6 < \delta_L < 6.25, \\ \frac{1}{\delta_L} & \text{if } \delta_L \geq 6.25. \end{cases} \quad (49)$$

The ultimate local buckling strength is

$$\sigma_{UL} = \alpha_L p_{eL} \frac{R}{t} K_L, \quad (50)$$

where $\alpha_L = 0.8$ is the imperfection factor, and for our numerical example $K_L = 1$.

$$p_{eL} = \begin{cases} \frac{1.27E}{A^{1.18} + 0.5} \left(\frac{t}{R}\right)^2 & \text{if } M_x > 1.5 \text{ and } A = M_x - 1.17 < 2.5, \\ \frac{0.92E}{A} \left(\frac{t}{R}\right)^2 & \text{if } 2.5 < A < 0.208Rt, \\ 0.836C_P^{-1.061} E \left(\frac{t}{R}\right)^3 & \text{if } 0.208 < C_P = \frac{A}{R/t} < 2.85, \\ 0.275E \left(\frac{t}{R}\right)^3 & \text{if } C_P > 2.85. \end{cases} \quad (51)$$

Constraint on general shell buckling

$$\gamma_b p \frac{R}{t} \leq \eta_G \sigma_{UG}, \quad (52)$$

where the plasticity reduction factor η_G is calculated in function of $\delta_G = \sigma_{UG}/f_y$ with the same formulae as in the case of η_L – see equation (44):

$$\sigma_{UG} = \frac{\alpha_G}{1.2} p_{eG} \frac{R}{t} K_G. \quad (53)$$

Here $\alpha_G = 0.8$ is the imperfection factor, K_G is defined by equation (42)₂, and a factor of 1.2 is recommended to avoid the mode interaction (coupled instability):

$$p_{eG} = \frac{E \frac{t}{R} \lambda_G^4}{(n^2 - 1)(n^2 + \lambda_G^2)^2} + \frac{EI_{er}(n^2 - 1)}{L_r R_C^2 R}, \quad (54)$$

where

$$\lambda_G = \frac{\pi R}{L_b} = \frac{1850\pi}{15000} = 0.3875,$$

n is the value which gives the minimum value of p_{eG} , $n_{min} = 2$, $n_{max} = 10$. For our case $n = 2$ is used.

The cost function includes the material, fabrication and painting costs:

$$K = K_M + K_F + K_P. \quad (55)$$

The material cost is

$$K_M = k_M \rho V, \quad (56)$$

k_M [\$\$/kg] is the material cost factor and V is the volume of the structure:

$$V = 2\pi R t L_b + n_r \left[4\pi \delta_r h_r^2 \left(R - \frac{h_r}{2} \right) + 2\pi \delta_r h_r^2 (R - h_r) \right], \quad (57)$$

where n_r is the number of ring-stiffeners.

For a fabrication phase it is

$$K_F = k_F \left(\Theta_{dW} \sqrt{\kappa \rho V} + 1.3 C_W a_W^n L_W \right), \quad (58)$$

where k_F (\$\$/min) is the fabrication cost factor, $\Theta_{dW} = 3$ is the difficulty factor expressing the complexity of a structure regarding assembly, the first member calculates time for assembly and tacking, κ is the number of structural parts to be assembled,

the second member calculates the time of welding and additional works (changing the electrode, deslagging, chipping). The additional works are considered by a factor of 1.3. L_W is the weld length, a_W is the weld size, C_W and n are given for different welding technologies and weld type (butt or fillet).

The fabrication cost function is formulated according to the fabrication sequence as follows.

- (1) Welding of a shell segment from 3 parts without stiffeners with GMAW-C butt welds, number of structural parts to be assembled is 3

$$K_{F1} = 3\sqrt{3\rho V_S} + 1.3x0.2245x10^{-3}t^2x3L_S, \quad (59)$$

where $L_S = 3000$ mm, $V_S = 2R\pi tL_S$.

- (2) Welding of a ring-stiffener from 3 plate parts with 2 fillet welds of GMAW-C (gas metal arc welding with CO₂), weld size $a_W = 0.7t_r$

$$K_{F2} = 3\sqrt{3\rho V_r} + 1.3x0.3394x10^{-3}a_W^2x4\pi(R - h_r), \quad (60)$$

where $V_r = 4\pi\delta_r h_r^2 \left(R - \frac{h_r}{2}\right) + 2\pi\delta_r h_r^2 (R - h_r)$.

- (3) Welding of $n_r/5$ stiffeners to a shell segment with 2 fillet welds of size $a_W = 0.7t_r$, GMAW-C

$$K_{F3} = 3\sqrt{\left(\frac{n_r}{5} + 1\right)\rho V_3} + 1.3 \times 0.3394 \times 10^{-3} a_w^2 x 4\pi R n_r / 5, \quad (61)$$

where $V_3 = V_S + V_r n_r / 5$.

- (4) Welding of 5 stiffened shell segments together with butt welds GMAW-C

$$K_{F4} = 3\sqrt{5\rho 5V_3} + 1.3 \times 0.2245 \times 10^{-3} t^2 \times 8R\pi \quad (62)$$

The total material cost is

$$K_M = k_M \rho 5V_3. \quad (63)$$

The total fabrication cost is

$$K_F = k_F (5K_{F1} + n_r K_{F2} + 5K_{F3} + K_{F4}). \quad (64)$$

The painting cost is

$$K_P = k_P \left[2R\pi L_b + 2R\pi (L_b - n_r h_r) + 2\pi (R - h_r) h_r + 4\pi \left(R - \frac{h_r}{2} \right) \right]. \quad (65)$$

In the numerical example the following cost factors are used: $k_M = 1.0$ \$/kg, $k_F = 1.0$ \$/min and $k_P = 28.8 \times 10^{-6}$ \$/mm².

The results of the optimum design are as follows: $n_r = 15$, $h_r = 160$, $t = 10$ mm and the total minimum cost is $K = 38964$ \$.

Comparing the ring-stiffened design with an *unstiffened* one, it is calculated that, for the unstiffened version a shell thickness of $t = 34$ mm is required. In the case considered here, where $M_x = 59.81$, $A = 58.64$, $C_P = 1.1094$, $p_{el} = 0.9761$ MPa and $1.5 \times 0.5 = 0.75 < 0.8 \times 0.9761 = 0.78$ MPa is satisfactory. The costs of the unstiffened version are as follows: $K_{F1} = 2140$ \$, $K_{F4} = 9916$ \$, $K_F = 20616$ \$, $K_M = 46535$ \$, $K_P = 10043$ \$, the total cost is $K = 77194$ \$. This is $100(77194-38964)/38964 = 98\%$ higher than that of the stiffened version.

It can be concluded that, in the case of cylindrical shells subject to external pressure, ring-stiffening is economic, since the shell is very sensitive to buckling due to external pressure.

5. Ring-stiffened cylindrical shells subject to axial compression or bending

According to DNV design rules (Det Norske Veritas [4]) the constraint on local shell buckling is expressed by

$$\sigma_{\max} \leq \sigma_{cr} = \frac{f_y}{\sqrt{1 + \lambda^4}} \quad (66)$$

$$\lambda^2 = \frac{f_y}{\sigma_E}, \quad \sigma_E = (1.5 - 50\beta) C \frac{\pi^2 E}{10.92} \left(\frac{t}{L_r} \right)^2 \quad (67)$$

$$L_r = \frac{L}{n + 1} . \quad (68)$$

The factor of $(1.5-50\beta)$ in equation (51) expresses the effect of initial radial shell deformation caused by the shrinkage of circumferential welds and can be calculated as follows (Farkas [7], Farkas & Jármai [1]).

The maximum radial deformation of the shell caused by the shrinkage of a circumferential weld is

$$u_{\max} = 0.64 A_T \sqrt{R/t}, \quad (69)$$

where $A_T t$ is the area of specific strains near the weld. According to our results (Farkas & Jármai [13])

$$A_T t = \frac{0.3355 Q_T \alpha_0}{c_0 \rho} . \quad (70)$$

For steels it is

$$A_T t = 0.844 \times 10^{-3} Q_T \quad (A_T t, \text{ in mm}^2 \quad Q_T \text{ in J/mm}), \quad (71)$$

$$Q_T = \eta_0 \frac{UI}{v_W} = C_A A_W . \quad (72)$$

For manually arc welded butt welds

$$Q_T = 60.7 A_W \quad (A_W \text{ in mm}^2) . \quad (73)$$

Here

$$A_W = \begin{cases} 10t & \text{if } t \leq 10 \text{ mm} , \\ 3.05t^{1.45} & \text{if } t > 10 \text{ mm} . \end{cases} \quad (74)$$

Introducing a reduction factor of β for which

$$0.01 \leq \beta = \frac{u_{\max}}{4\sqrt{Rt}} \leq 0.02 \quad (75)$$

the imperfection factor for shell buckling strength should be multiplied by $(1.5 - 50\beta)$.

$$\text{For } \beta \leq 0.01, \quad \beta = 0.01; \quad \text{for } \beta \geq 0.02 \quad \beta = 0.02. \quad (76)$$

$$\text{For } t > 9 \text{ mm } 1.5 - 50\beta = 1.$$

Furthermore

$$C = \psi \sqrt{1 + \left(\frac{\rho_0 \xi}{\psi}\right)^2}, \quad Z = 0.9539 \frac{L_r^2}{Rt}. \quad (77)$$

In the case of bending it is

$$\psi = 1, \quad \xi = 0.702Z, \quad \rho_0 = 0.5 \left(1 + \frac{R}{300t}\right)^{-0.5}. \quad (78)$$

In the case of axial compression

$$\psi = 1, \quad \xi = 0.702Z, \quad \rho_0 = 0.5 \left(1 + \frac{R}{150t}\right)^{-0.5}. \quad (79)$$

It can be shown that the critical buckling stress does not depend on the distance of ring stiffeners (L_r).

If

$$\rho_0 \xi > 10, \quad C \approx \rho_0 \xi = 0.702 \times 0.9539 \rho_0 \frac{L_r^2}{Rt} \quad (80)$$

and

$$\sigma_E = 0.702 \times 0.9539 \rho_0 \frac{\pi^2 Et}{10.92R} \quad (81)$$

does not depend on L_r .

From equation (80) we obtain

$$L_r > 3.8644 \sqrt{\frac{Rt}{\rho_0}}. \quad (82)$$

E.g. for $R = 1800$, $t = 18$ mm in the case of axial compression $\rho_0 = 0.3873$; $L_r > 1117$ mm, in the case of bending $\rho_0 = 0.4330$; $L_r > 1057$ mm. Therefore it can be concluded that the shell thickness can be decreased only if $L_r < 1000$ mm. This means a very dense stiffening, the welding cost of which is very high and the stiffened shell is uneconomic. The fact that the buckling strength does not depend on the shell length is first derived by Timoshenko and Gere [14].

Ring-stiffening cannot be economic for axially compressed or bent cylindrical shells, since the shell is not very sensitive to buckling for such loads, its stiffness against buckling is large. Ring-stiffening can be used to ensure the accurate cylindrical shape of the shell. In this case the designer can select a realistic domain of the number of ring-stiffeners and can search for the optimum stiffener number in this region minimizing the cost function (Farkas et al. [15]), but this minimal cost will be higher than that of an unstiffened shell.

6. A stringer-stiffened cylindrical shell loaded by bending

The shell is a supporting bridge for a belt-conveyor, simply supported with a given span length of $L = 60$ m and radius of $R = 1850$ mm (Figures 6, 7 and 8). The intensity of the factored uniformly distributed vertical load is $p = 26.0$ N/mm + self mass. Factored live load is 20.0 N/mm, dead load (belts, rollers, service-walkway) is 6.0 N/mm. For self mass a safety factor of 1.35 is used, which is prescribed by

Eurocode 3 (1992). The safety factor for variable load is 1.5. Outside stringers are made of half-rolled I-section (Universal Beam sections). The yield stress of the steel is $f_y = 355$ MPa.

Inside stiffeners are uneconomic, since their moment of inertia in the calculation of central deflection is much lower than that of outside ones. Instead of rolled I-section stiffeners it is better to use half-rolled I-sections, since welding the flange to the curved shell surface is difficult.

Variables: shell thickness t , number and cross-sectional area of longitudinal stiffeners (stringers) n_s, A_s .

Constraints

(1) *Shell buckling (unstiffened curved panel buckling)*

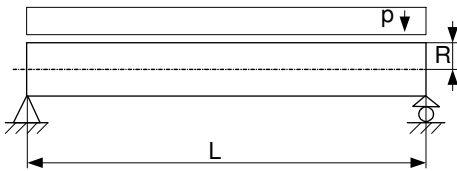


Figure 6. A simply supported cylindrical shell subject to uniformly distributed normal load

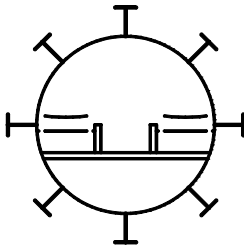


Figure 7. Cross-section of a belt conveyor bridge with two belt conveyors and a service walkway in the middle

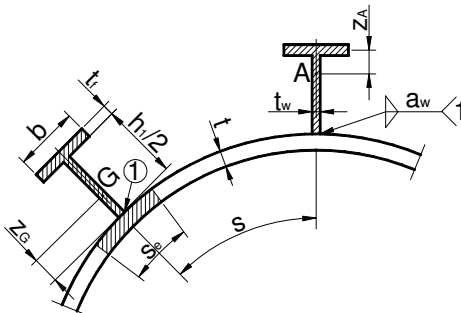


Figure 8. Part of the stiffened shell

$$\sigma_a = \frac{M}{R^2 \pi t_e} \leq \sigma_{cr} = \frac{f_y}{\sqrt{1 + \lambda^4}} \quad (83)$$

$$\lambda^2 = \frac{f_y}{\sigma_E}; \quad t_e = t + \frac{A_s}{2s}; \quad s = \frac{2R\pi}{n_s} \quad (84)$$

$$M = \frac{pL^2}{8}; \quad p = 26.0 + 1.35\rho(2R\pi t_e); \quad \rho = 7.85 \times 10^{-5} \text{ N/mm}^3 \quad (85)$$

$$\sigma_E = C(1.5 - 50\beta) \frac{\pi^2 E}{12(1 - \nu^2)} \left(\frac{t}{s}\right)^2 \quad (86)$$

$$C = 4\sqrt{1 + \left(\frac{\rho_e \xi}{4}\right)^2}; \quad Z = \frac{s^2}{Rt} \sqrt{1 - \nu^2} \quad (87)$$

$$\rho_e = 0.5 \left(1 + \frac{R}{150t}\right)^{-0.5}; \quad \xi = 0.702Z. \quad (88)$$

Note that the calculation of β is detailed in Section 5.

(2) *Stringer panel buckling*

$$\sigma_a = \frac{M}{R^2 \pi t_e} \leq \sigma_{crp} = \frac{f_y}{\sqrt{1 + \lambda_p^4}} \quad (89)$$

$$\lambda_p^2 = \frac{f_y}{\sigma_{Ep}}; \quad \sigma_{Ep} = C_p \frac{\pi^2 E}{10.92} \left(\frac{t}{L}\right)^2 \quad (90)$$

$$C_p = \psi_p \sqrt{1 + \left(\frac{0.5\xi_p}{\psi_p}\right)^2}; \quad Z_p = 0.9539 \frac{L^2}{Rt} \quad (91)$$

$$\xi_p = 0.702Z_p; \quad \gamma_s = 10.92 \frac{I_{sef}}{st^3} \quad (92)$$

$$\psi_p = \frac{1 + \gamma_s}{1 + \frac{A_s}{2s_e t}}. \quad (93)$$

Since DNV rules give the effective shell part s_e by too complicated an iteration, we use the simpler ECCS (1988) rules:

$$s_E = 1.9t \sqrt{\frac{E}{f_y}} \quad (94)$$

If $s_E < s$, $s_e = s_E$; if $s_E > s$, $s_e = s$.

I_{sef} is the moment of inertia of a cross section containing the stiffener and a shell part of width s_e

$$\begin{aligned} I_{sef} = s_e t \left(\frac{t}{2} + z_G\right)^2 + \frac{s_e t^3}{12} + \frac{t_w}{12} \left(\frac{h_1}{2}\right)^3 + \\ + \frac{h_1 t_w}{2} \left(\frac{h_1}{4} - z_G\right)^2 + \frac{bt_f^3}{12} + bt_f \left(\frac{h_1 + t_f}{2} - z_G\right)^2 \end{aligned} \quad (95)$$

$$z_G = \frac{h_1^2 t_w / 8 + h_1 b t_f / 2}{h_1 t_w / 2 + b t_f + s_e t}. \quad (96)$$

- (3) *Deflection constraint.* The moment of inertia is calculated here approximately by the formula of $\pi R^3 t_e$, while the exact expression is given by equation (132).

$$w_{\max} = \frac{5p_0 L^4}{384E\pi R^3 t_e} \leq w_{\text{allow}} = \frac{L}{\phi}; \quad \phi = 500 - 1000 \quad (97)$$

$$p_0 = 20/1.5 + 6.0/1.35 + \rho 2R\pi t_e = 17.78 + \rho 2R\pi t_e. \quad (98)$$

The selected UB rolled I-sections are given in Table 1.

Table 1. Characteristics of the selected UB rolled I-sections

UB Profile	h mm	b mm	t_w mm	t_f mm	A mm ²	$I_y \times 10^{-4}$ mm ⁴
152 × 89 × 16	152.4	88.7	4.5	7.7	2032	834
168 × 102 × 19	177.8	101.2	4.8	7.9	2426	1356
203 × 133 × 25	203.2	133.2	5.7	7.8	3187	2340
254 × 102 × 25	257.2	101.9	6.0	8.4	3204	3415
305 × 102 × 28	308.7	101.8	6.0	8.8	3588	5366
356 × 127 × 39	353.4	126.0	6.6	10.7	4977	10172
406 × 140 × 46	403.2	142.2	6.8	11.2	5864	15685
457 × 152 × 60	454.6	152.9	8.1	13.3	7623	25500
533 × 210 × 92	533.1	209.3	10.1	15.6	11740	55230
610 × 229 × 113	607.6	228.2	11.1	17.3	14390	87320
686 × 254 × 140	683.5	253.7	12.4	19.0	17840	136300
762 × 267 × 173	762.2	266.7	14.3	21.6	22040	205300
838 × 292 × 194	840.7	292.4	14.7	21.7	24680	279200
914 × 305 × 224	910.4	304.1	15.9	23.9	28560	376400

The characteristic data of the UB rolled I-sections can approximately be expressed by the main parameter of section height h (approximately equalling the first number of the profile name) as follows:

$$A_S = 1093.24394022488 + 0.0336839947h^2, \quad (99)$$

$$t_f = \sqrt{34.552565817 + 0.0006518757864h^2}, \quad (100)$$

$$b = \sqrt{4676.099669 + 0.11159269h^2}, \quad (101)$$

$$t_w = \sqrt{16.154183 + 4.228419 \times 10^{-5} h^2 \ln h}. \quad (102)$$

The cost function

Fabrication sequence:

- (1) Fabrication of 20 shell elements of length 3 m without stiffeners. For one shell element 2 axial butt welds are needed (GMAW-C) (K_{F1}). The cost of forming a shell element into the cylindrical shape is also included (K_{F0}).
- (2) Welding of an unstiffened shell unit from 4 shell segments of 3m length with 3 circumferential butt welds (K_{F2}).

- (3) Welding the n_s stiffeners to the unit with $2n_s$ fillet welds of size a_w and length 12 m (K_{F3}), $a_w = 0.3t_w$, $a_{wmin} = 3$ mm.
- (4) Welding the 5 units together with 4 butt welds and butt welds connecting the half UB stiffeners (K_{F4}).

The material cost is

$$K_M = k_{M1} 5 \rho_1 V_2, \quad (103)$$

$$V_2 = 4V_1 + n_S \frac{A_s L}{2 \times 5}, \quad V_1 = 3000 \times 2R\pi t. \quad (104)$$

According to data obtained from a Hungarian manufacturing company (Jászberényi Aprítógépgyár, Crushing Machine Factory, Jászberény), K_{F0} can be expressed in function of shell thickness and diameter as follows (valid for $t = 4 - 40$ mm and $2R = 1500 - 3500$ mm, for width of 3000 mm)

$$K_{F0} = k_F \Theta e^\mu, \quad \mu = 6.8582513 - 4.527217t^{-0.5} + 0.009541996 (2R)^{0.5}, \quad (105)$$

$$K_{F1} = k_F \left(\Theta \sqrt{\kappa \rho_1 V_1} + 1.3 \times 0.152 \times 10^{-3} t^{1.9358} \times 6000 \right), \quad (106)$$

$$\Theta = 2; \kappa = 2; \rho_1 = 7.85 \times 10^{-6} \text{kg/mm}^3,$$

$$K_{F2} = k_F \left(\Theta \sqrt{4x4\rho_1 V_1} + 1.3x0.152x10^{-3}t^{1.9358}6R\pi \right), \quad (107)$$

$$k_F = 1.0 \$/\text{min}, \quad k_{M1} = 1.0 \$/\text{kg},$$

where Θ is a difficulty factor expressing the complexity of the assembly and κ is the number of elements to be assembled.

$$K_{F3} = k_F \left(\Theta \sqrt{(n_s + 1) \rho_1 V_2} + 1.3 \times 0.3394 \times 10^{-3} a_W^2 2Ln_s/5 \right), \quad (108)$$

$$K_{F4} = k_F \left(\Theta \sqrt{5 \times 5 \rho_1 V_2} \right) + k_F 1.3x0.152x10^{-3} \left(8R\pi t^{1.9358} + n_S \frac{h_1}{2} t_w^{1.9358} + n_S b t_f^{1.9358} \right), \quad (109)$$

$$h_1 = h - 2t_f. \quad (110)$$

The cost of painting is

$$K_P = k_P \left(4R\pi L + n_s \frac{A_L L}{2} \right); \quad k_P = 14.4 \times 10^{-6} \$/\text{mm}^2, \quad (111)$$

$$A_L = 2h_1 + 4b. \quad (112)$$

The total cost is

$$K = K_M + 20K_{F1} + 20K_{F0} + 5K_{F2} + 5K_{F3} + K_{F4} + K_P. \quad (113)$$

In order to compare the stiffened shell with the unstiffened one, the constraints of an *unstiffened shell* are given as follows.

(1) *Shell buckling*

$$\sigma_b = \frac{M}{R^2 \pi t} \leq \sigma_{cr} = \frac{f_y}{\sqrt{1 + \lambda^4}}, \quad (114)$$

$$\lambda^2 = \frac{f_y}{\sigma_E}, \quad (115)$$

$$\sigma_E = C(1.5 - 50\beta) \frac{\pi^2 E}{10.92} \left(\frac{t}{L}\right)^2, \quad (116)$$

$$C = \sqrt{1 + (\rho_e \xi)^2}; \quad Z = \frac{L^2}{Rt} 0.9539, \quad (117)$$

$$\rho_e = 0.5 \left(1 + \frac{R}{300t}\right)^{-0.5}; \quad \xi = 0.702Z. \quad (118)$$

(2) *Vertical deflection*

$$w_{\max} = \frac{5p_0 L^4}{384E\pi R^3 t} \leq w_{\text{allow}} = \frac{L}{\phi}. \quad (119)$$

The cost function

Fabrication sequence:

- (1) Fabrication of 20 shell elements of length 3 m without stiffeners. For one shell element 2 axial butt welds are needed (GMAW-C) (K_{F1}). The cost of forming a shell element into the cylindrical shape is also included (K_{F0}).
- (2) Welding the 20 units together with 19 butt welds (K_{F2}).

The material cost is

$$K_M = k_{M1} 20\rho_1 V_1, \quad (120)$$

$$V_1 = 3000x2R\pi t, \quad (121)$$

$$K_{F0} = k_F \Theta e^\mu; \quad \mu = 6.8582513 - 4.527217t^{-0.5} + 0.009541996(2R)^{0.5}, \quad (122)$$

$$K_{F1} = k_F \left(\Theta \sqrt{\kappa \rho_1 V_1} + 1.3 \times 0.152 \times 10^{-3} t^{1.9358} \times 6000 \right), \quad (123)$$

$$\Theta = 2; \quad \kappa = 2; \quad \rho_1 = 7.85x10^{-6} \text{kg/mm}^3,$$

$$K_{F2} = k_F \left(\Theta \sqrt{20x20\rho_1 V_1} + 1.3 \times 0.152 \times 10^{-3} t^{1.9358} 38R\pi \right), \quad (124)$$

$$k_F = 1.0 \$/\text{min}, \quad k_{M1} = 1.0 \$/\text{kg}.$$

The cost of painting is

$$K_P = k_P (4R\pi L); \quad k_P = 14.4x10^{-6} \$/\text{mm}^2. \quad (125)$$

The total cost is

$$K = K_M + 20K_{F1} + 20K_{F0} + K_{F2} + K_P. \quad (126)$$

A numerical example using manual calculation

Assuming that the deflection constraint is active, i.e. selecting a low allowable deflection with a value of $\phi = 1000$, it is possible to determine the required thickness

of an *unstiffened* shell. From the deflection constraint – see equation (119) – one obtains an equation for the required thickness

$$t \geq \frac{5L^3\phi}{384E\pi R^3} (17.78 + \rho 2R\pi t) . \quad (127)$$

For $L = 60$ m, $R = 1850$ mm, $E = 2.1 \times 10^5$ MPa, $\phi = 1000$, $\rho = 7.85 \times 10^{-5}$ N/mm³

$$t \geq 0.6733 (17.78 + 0.9125t) . \quad (128)$$

Solving this equation we get $t = 32$ mm.

Checking this unstiffened shell for buckling we obtain the following values – see equations (114-118): $p = 65.42$ N/mm, $M = 29.439 \times 10^9$ Nmm, $\sigma_{\max} = 85.56$ MPa, $Z = 58.01 \times 10^3$, $\xi = 40.72 \times 10^3$, $\rho_e = 0.4578$, $C = 18642$, $\sigma_E = 1006$ MPa, $\sigma_{cr} = 334.8 > 85.56$ MPa, OK.

The cost calculation of the unstiffened shell results in the following values – see equations (120-126): $V_1 = 1.1159 \times 10^9$ mm³, $K_M = 175195$ \$, $K_{F0} = 1528$ \$, $K_{F1} = 1159$ \$, $K_{F2} = 39517$ \$, $K_P = 20086$ \$, the total cost is $K = 288538$ \$.

Calculation of a stringer-stiffened shell with the same deflection constraint. Equation (128) results in a formula for t_e

$$t_e \geq 0.6733 (17.78 + 0.9125t_e) \quad (129)$$

which gives $t_e = 32$ mm. t_e contains all the three unknowns (t , n_s , A_s)

$$t_e = t + \frac{n_s A_s}{4R\pi} \quad (130)$$

since we use for a stiffener only the half cross-section of a rolled I-section ($A_s/2$).

For the minimum cost solution we need a mathematical algorithm, but, to show the cost savings achieved by decrease of the unstiffened shell thickness of 32 mm, we use a manual calculation and take $t = 10$ mm. If we select a rolled I-section of UB 914 \times 305 \times 289 ($A_s = 36830$ mm²), then the required number of stiffeners from equation (130) is $n_s = 10$.

The selected UB section has the following dimensions: $h = 926.6$, $h_1 = 862.6$, $b = 307.7$, $t_w = 19.5$, $t_f = 32$ mm, the half surface for the calculation of painting cost is $A_L/2 = 1506$ mm²/mm.

Note that this UB profile is not included in Table 1.

Checking the stringer-stiffened shell for buckling using equations (83-88).

$p = 38.318$ N/mm, $M = 172.43 \times 10^8$ Nmm, $\sigma_{\max} = 62$ MPa, $s = 1162$ mm, $Z = 69.62$, $\xi = 48.87$, $\rho_e = 0.3346$, $C = 16.83$, $\sigma_E = 237$ MPa, $\sigma_{cr} = 197 > 62$ MPa, OK.

Check of stringer panel buckling using equations (89-96) .

$s_e = 642$ mm, $z_0 = 264.9$ mm, $I_{sef} = 7.476 \times 10^8$ mm⁴, $\gamma_s = 7025.6$, $\psi = 1409.3$, $\rho_e = 0.5$, $Z = 185.6 \times 10^3$, $\xi = 130310$, $C = 65166$, $\sigma_E = 343.6$ MPa, $\sigma_{cr} = 247 > 62$ MPa, OK.

Check of deflection. The exact calculation of the moment of inertia for the deflection uses the following formulae (Figure 8):

The distance of the center of gravity for the half UB section is

$$z_A = \frac{h_1 t_w / 2 (h_1 / 4 + t_f / 2)}{h_1 t_w / 2 + b t_f} \quad (131)$$

The moment of inertia of the half UB section is expressed by

$$I_x = b t_f z_A^2 + \frac{t_w}{12} \left(\frac{h_1}{2} \right)^3 + \frac{h_1 t_w}{2} \left(\frac{h_1}{4} - z_A \right)^2 \quad (132)$$

The moment of inertia of the whole stiffened shell cross-section is

$$I_{x0} = \pi R^3 t + I_x \sum_{i=1}^{n_s} \sin^2 \left(\frac{2\pi i}{n_s} \right) + \left(\frac{h_1 t_w}{2} + b t_f \right) \left(R + \frac{h_1 + t_f}{2} - z_A \right)^2 \sum_{i=1}^{n_s} \sin^2 \left(\frac{2\pi i}{n_s} \right) \quad (133)$$

In our case $z_A = 106.7$ mm, $I_x = 3.83 \times 10^8$ mm⁴, $I_{x0} = I_x + (1.989 + 4.400)10^{11} = 6.393 \times 10^{11}$ mm⁴, $p_0 = 41.36$ N/mm.

The approximate formula for the moment of inertia gives a smaller value of $I_{x0} \approx \pi R^3 t_e = 5.14 \times 10^{11}$ mm⁴ because, with equation (130) $t_e = 25.84$ mm.

The exact deflection is $w_{\max} = \frac{5p_0 L^4}{384 E I_{x0}} = 52 < 60$ mm, OK.

It can be concluded that the approximate formula of I_{x0} gives a value on the safe side. Note that, in the case of inside half UB section stiffeners, this approximate formula overestimates the exact value, thus, outside stiffeners are more effective than inside ones.

Cost calculation of the stiffened shell using equations (103-113).

$V_1 = 3.4872 \times 10^8$ mm³, $V_2 = 3.6047 \times 10^9$ mm³, $K_M = 141485$ \$, $K_{F0} = 812.55$ \$, $K_{F1} = 250.3$ \$, $K_{F2} = 1012$ \$, $K_{F3} = 1497$ \$, $K_{F4} = 3241$ \$, $K_P = 33098$ \$, the total cost is $K = 211628$ \$, i.e. stringer stiffening results in 36% cost savings. It should be mentioned that the cutting costs of UB sections can be neglected.

Comparison of the costs for unstiffened and stiffened shells

This comparison is shown in Table 2.

Table 2. Summary of costs (negative difference means cost savings)
(Costs in \$)

Cost	Unstiffened shell	Stiffened shell	Difference %
Material K_M	175195	141485	-24
Forming K_{F0}	30560	16251	-88
Welding $20K_{F1} + K_{F2}$	62697		
Welding $20K_{F1} + 5K_{F2} + 5K_{F3} + K_{F4}$		20794	-201
Painting K_P	20086	33098	64
Total	288538	211628	-36

It can be seen that the cost savings caused by stringer stiffening are significant in forming and welding costs, but painting for an unstiffened shell is 64% cheaper than that for a stiffened one. It can be concluded that the cost factors of fabrication and painting play an important role in the achievable cost savings.

7. Conclusions

The economy of stiffening is characterized by a cost comparison of stiffened and unstiffened structural versions. For this purpose the own cost calculation method is used, which is developed mainly for welded structures. The cost function includes the costs of material, forming of shell elements into cylindrical shape, assembly, welding and painting and is formulated according to the fabrication sequence.

The economy of stiffening depends on type of structure (plate, cylindrical shell), type of stiffening (rings, stringers), stiffener profile (flat, L-, trapezoidal, rolled I-section etc.), loading (axial compression, bending, external pressure), constraints (buckling, deflection). Therefore the cost comparison is performed for the following cases: (a) a longitudinally stiffened plate loaded by axial compression, (b) an orthogonally stiffened square plate with transverse loading, (c) a ring-stiffened shell subject to external pressure, (d) a ring-stiffened shell loaded by axial compression or bending, (e) a stringer-stiffened shell loaded by bending with a deflection constraint.

Summarizing the above cost comparisons it can be concluded that the economy of these structures shows the following differences:

- (1) stiffened plates are always economic, since they are very sensitive to buckling and transverse deflection;
- (2) ring-stiffened cylindrical shells are economic only in the case of external pressure, but for axial compression and bending they are uneconomic and can be used only to guarantee the appropriate cylindrical shape;
- (3) cylindrical shells stiffened outside by stringers are economic for bending with an active deflection constraint, but for axial compression or bending without a deflection constraint they are uneconomic. In order to decrease the welding cost, the stiffeners should have a cross-sectional area as large as possible and should be welded to the shell with welds as small as possible, thus halved rolled I-section stringers are advantageous for this purpose.

Acknowledgement. This research has been supported by the Hungarian Scientific Research Foundation grants OTKA T 38058 and T 37941. Special thanks are due to my colleague Prof. Dr. Károly Jármai co-author of optimum design problems applied in this review article.

References

1. FARKAS, J. and JÁRMAI, K.: *Economic design of metal structures*. Millpress Science Publisher, Rotterdam, 2003.
2. American Petroleum Institute (API) Bulletin 2U. *Bulletin on stability design of cylindrical shells*. 2nd ed. Washington, 2000.
3. European Convention of Constructional Steelwork (ECCS), *Recommendations for Steel Construction. Buckling of steel shells*. No.56. Brussels, 1988.

4. Det Norske Veritas (DNV), *Buckling strength analysis*. Classification Notes No.30.1. Hovik, Norway, 1995.
5. MIKAMI, I. and NIWA, K.: Ultimate compressive strength of orthogonally stiffened steel plates. *J. Struct. Engng ASCE*, **122**(6), (1996), 674-682. Discussion by Bedair, O. and authors' closure. *J. Struct. Engng*, **123**(7), (1997), 1116-1119.
6. *Stahlbau Handbuch, Band 2.*, Köln, Stahlbau-Verlag, 1985.
7. FARKAS, J.: Thickness design of axially compressed unstiffened cylindrical shells with circumferential welds. *Welding in the World*, **46**(11/12), (2002), 26-29.
8. SCHADE, H. A.: Design curves for cross-stiffened plating under uniform bending load. *Trans. Soc. Nav. Arch. and Marine Engrs*, **49**, (1941), 154-182.
9. TIMOSKENKO, S. and WOINOWSKY-KRIEGER, S.: *Theory of Plates and Shells*. 2nd ed. New York, McGraw Hill, 1959.
10. FARKAS, J. and JÁRMAI, K.: *Analysis and Optimum Design of Metal Structures*. Balkema, Rotterdam-Brookfield, 1997.
11. VOLMIR, A. S.: 1967. *Buckling Strength of Deformable Systems*. Moscow, Nauka, 1967. (in Russian)
12. Eurocode 3. *Design of steel structures*. Part 1.1. General rules and rules for buildings. European Prestandard ENV 1993-1-1. CEN European Committee for Standardisation, Brussels, 1992.
13. FARKAS, J. and JÁRMAI, K.: Analysis of some methods for reducing residual beam curvatures due to weld shrinkage. *Welding in the World* **41**(4), (1998), 385-398.
14. TIMOSHENKO, S. P. and GERE, J. M.: *Theory of elastic stability*. 2nd ed. New York, Toronto, London, McGraw Hill, 1961.
15. FARKAS, J., JÁRMAI, K. and VIRÁG, Z.: Optimum design of a belt-conveyor bridge constructed as a welded ring-stiffened cylindrical shell. IIW-Doc. XV-WG9-23-03, XV-1144-03. Bucharest, 2003.

MICROHARDNESS TESTS OF GRADED SiC/EP RINGS: EXPERIMENTAL RESULTS AND FE MODELING

DÁVID FELHŐS, KÁROLY VÁRADI

Institute of Machine Design
Budapest University of Technology and Economics
Műegyetem rkp. 3, 1111 Budapest, Hungary
varadik@goliat.eik.bme.hu

KLAUS FRIEDRICH

Institute for Composite Materials (IVW GmbH.)
Technical University of Kaiserslautern, Erwin-Schrödinger-Strasse
67663 Kaiserslautern, Germany
klaus.friedrich@ivw.uni-kl.de

[Received: January 22, 2005]

Dedicated to István Páczelt on the occasion of his 65th birthday

Abstract. Ring-shaped test specimens were made of gradient-structured SiC/EP composite produced by centrifugation. Compression tests and microhardness measurements were performed on epoxy matrix composites of even distribution of SiC reinforcement particles in various degrees of vol.%. As a result, compression stress-strain curves were obtained for the composites as well as changes of universal hardness in function of the SiC vol.% in order to have data for the material properties of the layers of the functionally grade structures. Microhardness measurements were simulated by 2D axisymmetrical and 3D FE micro-models in order to reveal the impact of reinforcement particles on material behavior, i.e. to explore the stresses and strains in the vicinity of the indented area as well as to find how functionally graded materials improve the wear resistance of composites.

Mathematical Subject Classification: 74M25, 74S05

Keywords: microhardness test, functionally graded material, FE analysis

1. Introduction

Functionally gradient materials (FGM) are characterized by the fact that one component is not evenly dispersed in the other component. One of them, the matrix, is usually a thermosetting or thermoplastic polymer; the other, the reinforcement material is a short fiber, metal or ceramic particle. Due to their good wear characteristics, FG materials are intended to be used for rollers, gears, driving and sliding rings, whose wear characteristics are better than those with identical material composition but made from a composite of even material distribution [1, 2]. Depending on the material composition, characteristics changing with gradient features include mechanical, thermal, electrical, magnetic, optical, or other properties [3].

Microhardness tests provide important features to forecast the wear characteristics of a material. FE calculations are suitable for identifying the stresses in a micro-environment, enabling us to gain a deeper knowledge of the expected behavior of different materials.

The object of our research is an FG composite material containing SiC reinforcement particles distributed in an epoxy matrix. The following models are aimed at exploring the contact, stress, and deformation processes in the micro-environment of the material in the course of microhardness measurements. While modeling microhardness measurements, the behavior of a composite of even material distribution containing pure resin and 20 vol.% SiC particles was studied in order to explore the load transfer mechanism of the reinforcement particles.

2. Experimental

2.1. Materials and processes. In the present study, a SiC/EP composite was examined with the material properties listed in Table 1. The matrix was cured with an amine hardener. The reinforcement particles are of irregular forms with coarse edges (Figure 1).

Table 1. Data of the matrix and reinforcement particles

Name	Producer	Density [g/cm ³]	Elastic modulus [GPa]	Size [μm]
Matrix: High-temperature epoxy resin:	Vantico	1.8	2.654	
Filler: Silicon carbide, SiC	Mineralien-Werke Kuppenhaim GmbH	3.2	455	9

In order to reach an even material distribution within the composite, the particles were distributed in the matrix by a dissolver (Dispermat AE, VMA-Getzmann

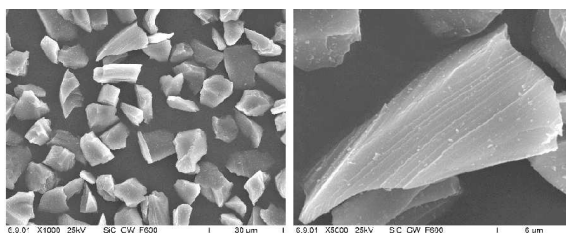


Figure 1. SEM images of SiC reinforcement particles in an epoxy matrix GmbH). A composite containing 5 vol.% of reinforcement particles was used for producing gradient rollers, which were cured in a cylindrical mould. The gradient nature of SiC particle distribution was achieved by centrifugation of the mix at 1000 1/min velocity for 30 minutes (Figure 2).

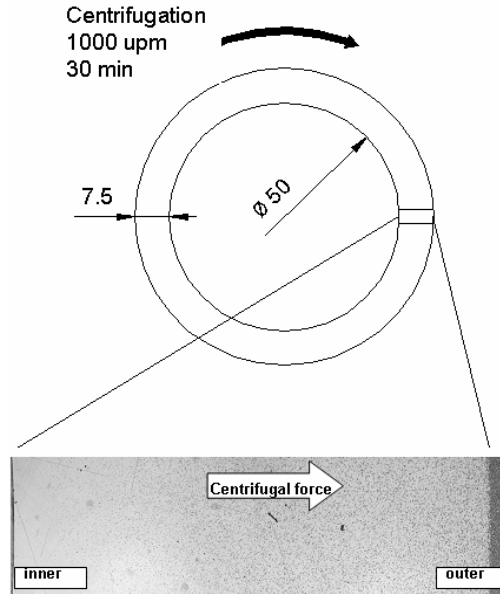


Figure 2. Preparation of FG-structured material

2.2. Microhardness tests. Microhardness tests were performed along the cross-section of the gradient roller (Figure 2) and on test pieces of even SiC distribution in various degrees of vol.%. Measurements were taken by a Shimadzu DUH-202 microhardness measurement device at room temperature, using a Vickers indenter, at 100 MN and 1500 MN of loading force, with an identical loading and unloading velocity of 70 mN/s and 2 sec of follow-up load. The loading force was chosen to be 1500 MN in the course of the measurements performed to identify the material distribution of the gradient roller; a loading force of 100 MN was chosen for the reference measurements of FE models to compare the size of displacements and the largest size of reinforcement particles in order to study the local behavior of specific particles.

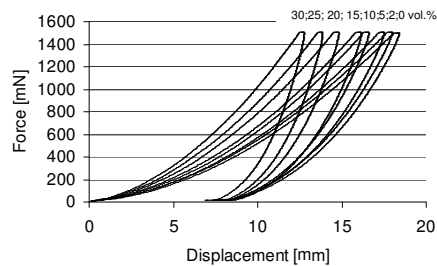


Figure 3. Force vs. displacement curves of microhardness measurements for different vol.% of SiC particles

Due to the high loading force (1500 MN), fairly large indentations were produced (of 90 to 120 μm), so that we could receive an average hardness value characterizing the composite as well as elastic modulus values from the unloading curves of force vs. displacement.

First, measurements were performed on test pieces of even SiC particle distribution for various degrees of vol.%, in order to arrive at a curve of universal hardness in the function of the vol.% of reinforcement particles. Ten measurements were performed for each characteristic vol.% value. The characteristic vol.% series are as follows: 0-, 2-, 5-, 10-, 15-, 20-, 25-, 30-vol.%. Figure 3 shows these curves of force vs. displacement. It can be observed that vol.% values change the results in approximately identical degrees.

Universal hardness HU can be calculated as [4]:

$$HU = \frac{F}{26,43h^2} \text{ [MPa]} \quad (1)$$

where F is the measuring force [N] and h is the depth of the indentation [mm]. Figure 4 shows changes in universal hardness HU in the vol.% of SiC particles.

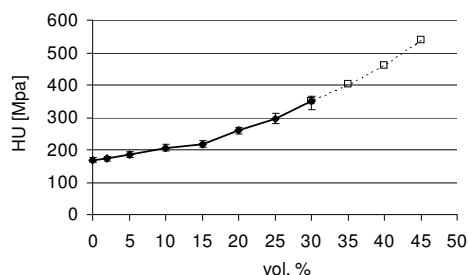


Figure 4. Universal hardness in the function of the SiC vol.%

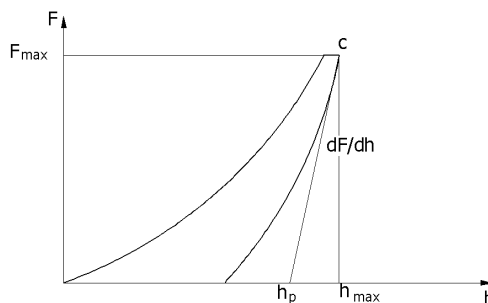


Figure 5. Elastic modulus calculation from the unloading section of the force vs. displacement curve of the hardness measurement

Hardness measurement provides a basis for determining the elastic modulus of a composite containing a given vol.% of SiC. The elastic modulus E can be calculated from the tangent of the unloading curve and the depth of the indentation (Figure 5)

by the following equations:

$$E = \left(\frac{\pi}{A}\right)^{\left(\frac{1}{2}\right)} \frac{S}{2} (1 - \nu^2), \tag{2}$$

$$A = 24.5h^2, \tag{3}$$

$$S = (dF/dh) |_{h_{\max}} \tag{4}$$

where A is the projected area of the indentation, S is the initial tangent of the unloading curve and ν is the Poisson's ratio of the material examined [5].

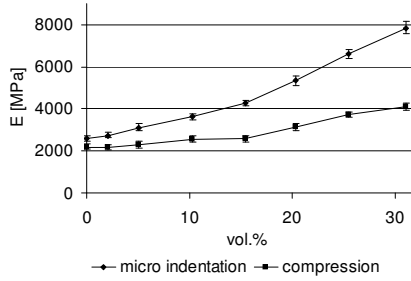


Figure 6. Compression elastic module values resulting from microhardness and compression tests in function of the SiC vol.%

Figure 6 shows the elastic modulus calculated from microhardness measurements for different vol.% of reinforcement particles and also obtained from the compression test. It can be observed that as the vol.% of reinforcement particles increases, the elastic modulus also increases. The higher elastic modulus values of microhardness tests are probably due to the different deformation mechanisms in the cases of microhardness and compression tests. It is likely that for the compression test the matrix can more uniformly deform than the local material structure in the case of microhardness

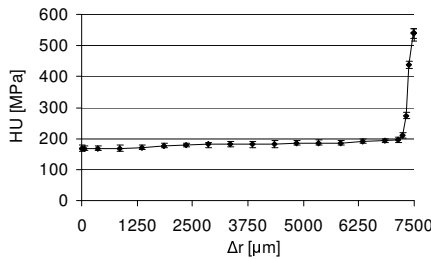


Figure 7. Universal hardness along the cross-section of an FG roller (see Figure 2)

tests. In the latter case the linking of particles, during the load transfer produces a higher local stiffness because mainly a few, partly connected particles transfer the load. Similar tendencies are reported in [1], where the microhardness test produced also higher elastic modulus values than the DMTA test at increasing vol.% of SiC particles.

2.3. Determination of the SiC volume content along the cross-section of a gradient roller. Using the values of universal hardness HU measured at test pieces of uniform particle distribution, a master curve was drawn (Figure 4), in the function of different SiC content. This master curve can be used to predict the SiC content of the layers of the cross-section of the gradient roller from the values of universal hardness HU measured in each layer (Figure 7).

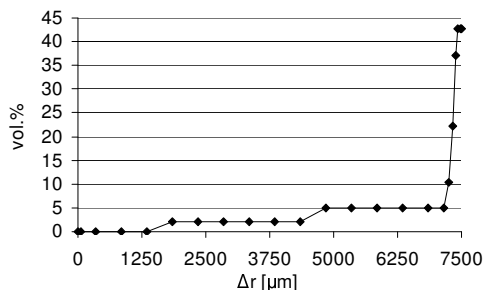


Figure 8. The SiC vol.% along the cross-section of an FG roller. Thus, we can arrive at the vol.% distribution of reinforcement particles in the cross-section of the FG roller (Figure 8). In the course of microhardness measurements along the cross-section of the gradient roller, the gradient nature of the roller can be specified with proper approximation if sufficiently small intervals are selected. A similar indirect method was applied by Watanabe et al. [6] to determine the distribution of aluminum fibers in their ceramic composite of gradient material distribution. In our measurements we observed that reinforcement particles almost entirely moved away from the inner part of the roller, while they came to around in more than 40 vol.% along the outer diameter. Therefore, centrifugation is a procedure suitable for achieving the largest possible vol.% of reinforcement particles.

2.4. Mechanical characteristics of the homogeneous EP/SiC composite. Compression tests were performed on cylindrical test specimens made of the material

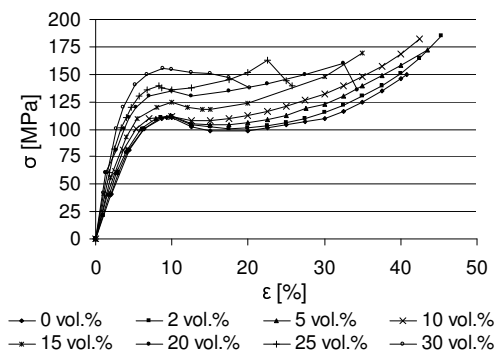


Figure 9. Compression stress-strain curves at characteristic vol.% values

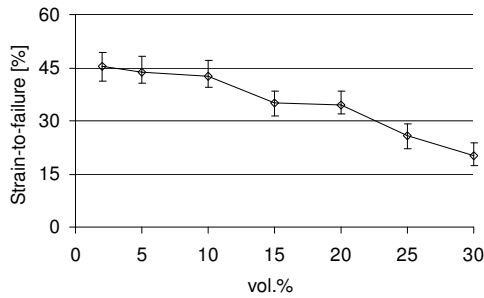


Figure 10. Maximum strain-to-failure values in the function of the SiC vol.%

of the gradient roller, with even material distribution but at varying vol.% values. The compression stress-strain curves of the EP/SiC composites have been required as compression load is characteristic for rollers as well as pressure is the dominant form of load in the course of microhardness tests as well. The compression stress-strain curves in function of the SiC vol.% are presented in Figure 9. Pure resin (0 vol.%) can bear fairly large strains. As regards the compression strength, it can be observed that as the SiC vol.% increases, the compression strength will slightly decrease. The great strain-to-failure ratio of the composite gradually reduces as the SiC vol.% increases (Figure 10).

3. FE modeling and results

3.1. The axisymmetrical FE model. An axisymmetrical model with contact elements was prepared using non-linear material properties.

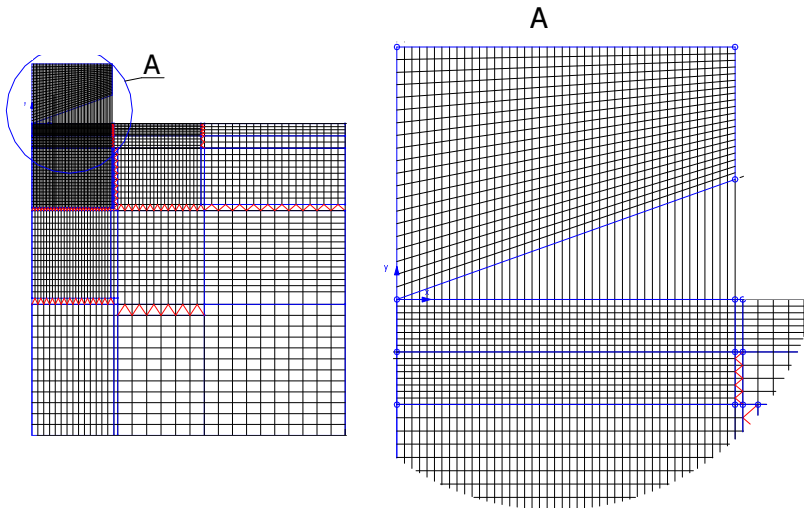


Figure 11. The FE mesh of the axisymmetrical model

Figure 11 shows the FE mesh. Load is introduced at the bottom of the model in the form of pressure, while the nodes at the upper plane of the diamond pyramid are fixed. The plane angle of the Vickers indenter had to be changed because in the axisymmetrical model the indenter is a cone rather than a pyramid. The condition of an equivalent cone angle is to have the same projected area when the indenter is pressed in the same depth. The angle of the cone results in 19.517° . The models include 3903 nodes, 6303 PLANE2D elements, and 56 contact elements. Its dimensions are: $\emptyset 80 \mu\text{m} \times 40 \mu\text{m}$. Calculations for the composite material containing 20 vol.% SiC are non-linear (material law is according to Figure 9), force control driven, applying the Newton-Raphson solution technique. The maximum load applied was 100 MN.

3.2. The 3D FE micro- model. The reinforcement particles as regular micro-cubes are embedded in the matrix, representing 20 vol.% of SiC (Figure 12).

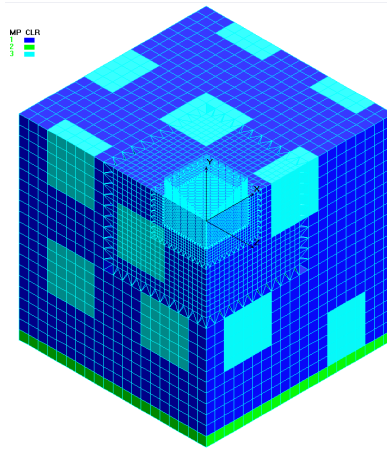


Figure 12. 3D micro-model representing 20 vol.% of SiC

In the model the diamond pyramid is connected to the test specimen by contact elements. Load is introduced from the bottom of the model. Nodes at the top of the indenter are fixed. A non-linear material law was applied for the matrix according to the compression stress-strain curve (Figure 10), while the particles were assumed to be linear elastic. The model contains 50,907 nodes, 59,357 SOLID elements and 1579 contact elements. Its dimensions are: $39.875 \times 39.875 \times 42 \mu\text{m}$. Calculations are non-linear, force control driven, applying the Newton-Raphson solution technique. The CPU time was approx. 16 hours on a P4 machine.

3.3. FE results for the composite containing of 20 vol.% SiC. The axisymmetrical model has a homogeneous material structure. Basic differences can be observed when comparing the stress and strain results of the axisymmetrical and 3D micro-models (Figure 13). The 3D micro-models are only capable of depicting the contact state more accurately between the contacting bodies because of the pyramid shape of the diamond indenter.

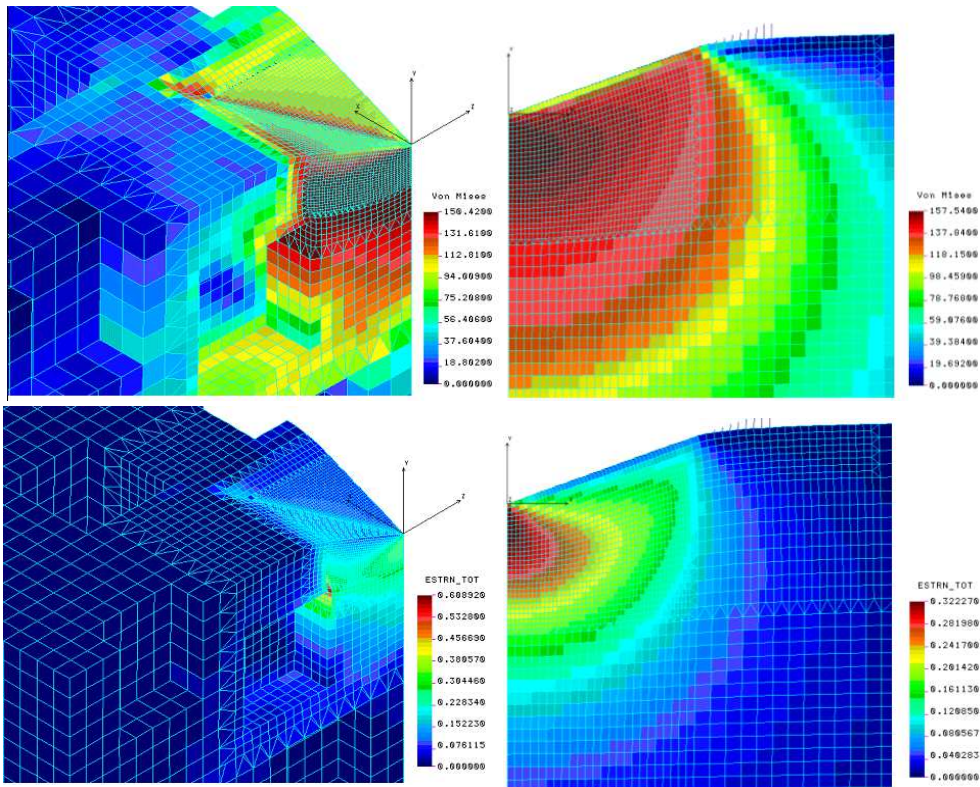


Figure 13. Von Mises equivalent stress (a) and equivalent strain (b) results in the vicinity of the contact area in the case of the 3D and axisymmetrical models

According to the axisymmetrical model the contact pressure distribution (σ_y in Figure 14) is nearly uniform along the contact area. The Von Mises equivalent stress is practically constant due to the extensive plastic deformation in the vicinity of the

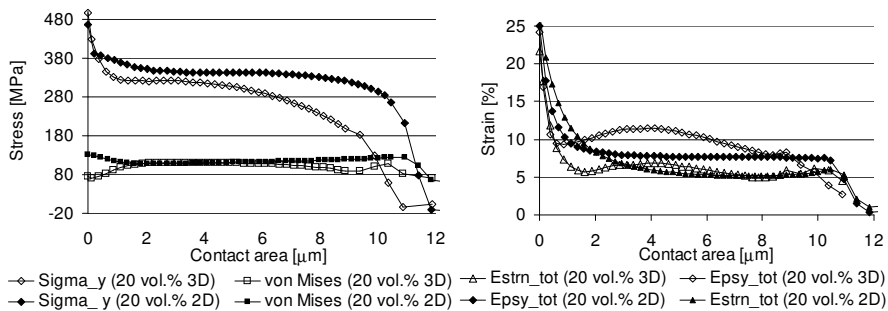


Figure 14. Stress (a) and strain (b) results along the contact area

contact area. As regards the 3D micro-model, a considerable difference can be observed in the stress and strain distribution over the contact area, depending on the fact whether the results represent the side-plane of the diamond pyramid or the edge of the pyramid (“diagonal” in Figure 15).

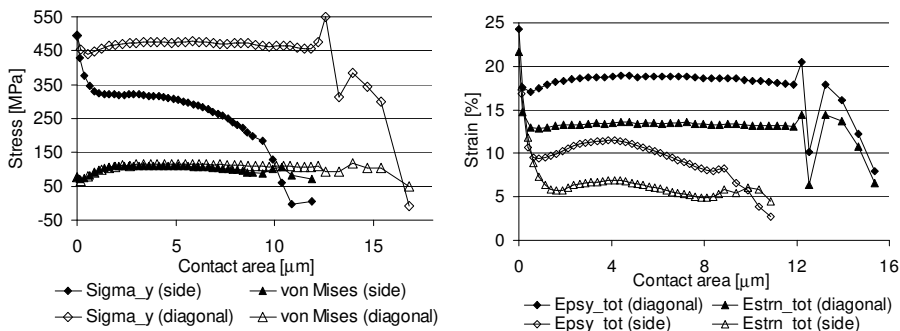


Figure 15. Stress (a) and strain (b) results in the contact area of the 3D micro-model considering the side of the indenter and its edges (called ‘diagonal’)

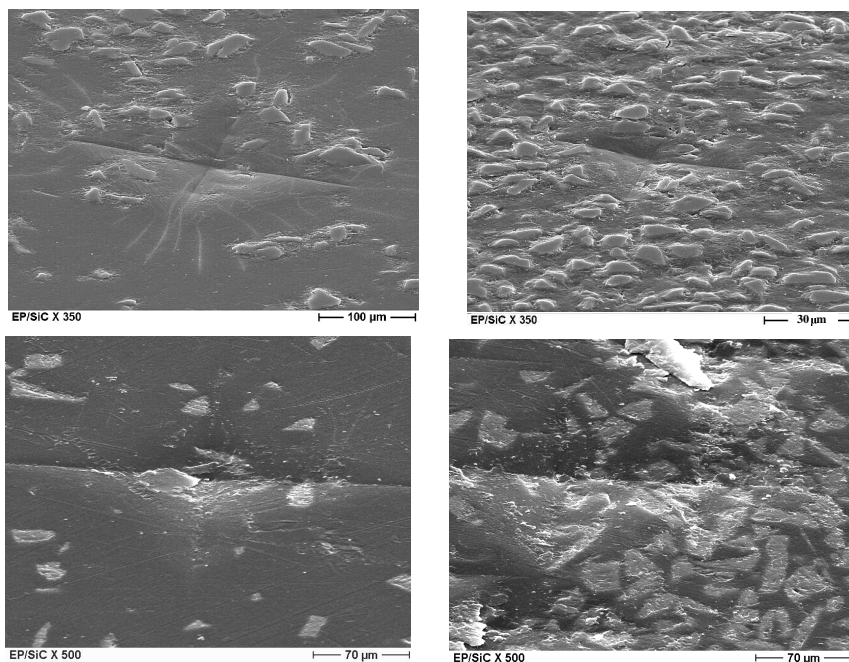


Figure 16. SEM images of microhardness measurement

Larger stresses and strains are produced along the edges of the pyramid, therefore the matrix can be damaged there, as shown by the SEM images (Figure 16). Accordingly, microcracks may be produced in the matrix along the edges.

The 3D micro-model, in Figure 13 clearly shows the behavior of SiC particles in the matrix. The highest stress peak and the largest strain are produced at the edges of the reinforcement particle. Destruction in the surroundings of the highly loaded particles is also proven by the SEM images (Figure 16). This is not transferred to the deeper layers of the material. It can be observed below the contact area that reinforcement particles touch each other at their edges and transmit the load to each other (Figure 17). In such cases, load is transmitted to the matrix through the embedded surface of connecting particles and therefore even less stress and strain is produced therein. In the same time this ‘connection’ produces a stiffer behavior locally (see Section 2.2).

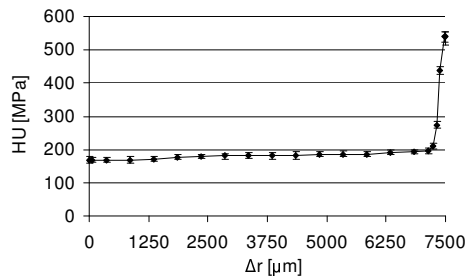


Figure 17. The “linking” of particles during load transfer

Finally, comparing the force vs. displacement curves of the microhardness measurements performed with the force vs. displacement curves taken from the results of the axisymmetrical and 3D FE micro-models, excellent agreement can be found (Figure 18).

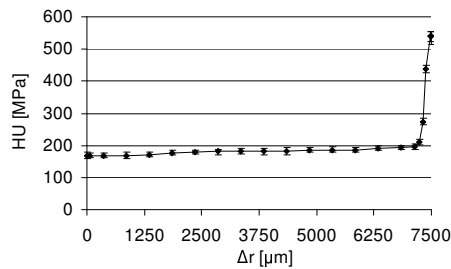


Figure 18. Comparison of the force-displacement results of the measurement and FE models

According to the results of the FE model, it can be assumed that the matrix among reinforcement particles on the surface can crack down or wear off in the wear process, but particles embedded in the matrix relatively deeply and along a larger surface area stay on the surface and produce a wear-resistant surface. This wear-resistance feature can only be produced if the reinforcement particles are located so densely beside each

other on the surface that they are connected to each other and can transfer stress to each other. Therefore this dense configuration can reduce the overloading of single particles.

4. Conclusions

The FE results according to the 2D axisymmetrical and 3D micro-models show a good correlation with the force vs. displacement results of microhardness tests in spite of the fact that in the case of axisymmetrical models a conical indenter is modeled instead of a pyramid one.

Based on the 3D micro-model, a primary stress concentration is generated in the matrix at the edges of the diamond and at the edges of reinforcement particles.

Reinforcement particles distribute load along a larger surface area within the matrix, thereby also improving its wear-resistance. The particles in a large volume fraction produce a nearly uninterrupted structure in the matrix.

According to SEM images as well as calculation results, the matrix is damaged at the surface and at the edges of particles. In the course of the wear process, the matrix among the particles probably wear off from the surface, but well-embedded particles mainly remain at their places and reduce further wear.

References

1. KRUMOVA, M., KLINGSHIRN, C. HAUPERT, F. and FRIEDRICH, K.: Microhardness studies of functionally graded polymer composites. *Compos. Sci. Techn.*, **61**, (2001), 557–563.
2. KLINGSHIRN, C., KOIZUMI, M., HAUPERT F., GIERTZSCH, H. and FRIEDRICH, K.: Structure and wear of centrifuged epoxy-resin/carbon fiber functionally graded materials *J. Mater. Sci. Let.*, **19**, (2000), 263–266.
3. HIRAI, T.: Functionally graded materials in "Materials science and technology: a comprehensive treatment", Cahn, R. W. (ed.). (Weinheim: VCH Verlagsgesellschaft GmbH 1996), 295–337.
4. Deutsche Norm: Prüfung metallischer Werkstoffe, Universelhärteprüfung, Teil 1. Prüfverfahren DIN 50359-1: 1997 – 10.
5. OLIVER, W. C. and PHARR G. M.: An improved technique for determining hardness and elastic modulus using load and displacement sensing indentation experiments. *J. Mater. Res.*, **7**, (1992), 1564–1583.
6. WATANABE, Y. and FUKUI Y.: Fabrication of functionally-graded aluminum materials by the centrifugation method. *Aluminium Transactions*, **2**, (2000), 195-208.

LONG-TERM ANALYSIS OF PRESTRESSED MEMBRANE STRUCTURES

DEZSŐ HEGYI

Department of Mechanics, Materials and Structures
Budapest University of Technology and Economics
Műgyetem rkp. 3-5., K. 323., H-1111 Budapest, Hungary
dizso@silver.szt.bme.hu

KRISZTIÁN HINCZ

Research Group for Computational Structural Mechanics
Hungarian Academy of Sciences and Budapest University of Technology and Economics
Műgyetem rkp. 3-5., K. 323., H-1111 Budapest, Hungary
hinczk@freestart.hu

[Received: June 24, 2004]

Abstract. Our research can be divided into two different areas according to our main objectives. On the one hand, we made experiments to learn as much as possible about the long-term behavior of the PVC-coated polyester textile; the most commonly used material type for the construction of tents in Hungary. On the other hand, we developed a procedure for the numerical analysis of prestressed membrane structures on the basis of a visco-elastic material model. In this paper we report about our first experimental and computational results.

Mathematical Subject Classification: 74K25

Keywords: Membrane structure, creep, long-term analysis

1. Introduction

Prestressed tents are statically in- and overdeterminate structures. They can carry the external loads only with prestress. If the level of prestress decreases, then the stiffness of the structure decreases. It means not only larger deformations, but a higher risk of fluttering as well. If the level of prestress is extremely low, then an ordinary wind can destroy the structure. If the prestress decreases to zero in one direction, it results in undesired wrinkles.

After the erection of membrane structures the relaxation of the material is a general experience. Thus the structure has to be post-tensioned some days after construction and sometimes after the first snowy winter again.

The relaxation of the PVC-coated polyester textile is well-known, but the literature does not deal with the effect of relaxation on the static behavior and usability of the structure. In our research we bring into focus the long-term behavior of the material and its effect on the structure.

2. Creep test of the PVC-coated polyester textile

2.1. Aim of the tests. The aim of the material tests is to determine the time-dependent material law for the PVC coated polyester textile. In the case of prestressed membrane structures, time dependent deformation cannot be divided into creep (increasing elongation while the stress is constant) and relaxation (decreasing stress while the elongation is constant). In practice the stresses and strains change continuously. We started to make creep tests, because measurements on the relaxation require a higher technical level, therefore they are more expensive.

For the experiments we use material pieces according to the Hungarian and German standards. The width of the specimen is 50 mm; the distance between the attached points is 200 mm (a 100 mm-long part in the middle is analyzed). Till now we have made experiments in four configurations:

- in warp direction under a load of 300, 600 and 900 N,
- in a direction inclined by 45° to the warps under a load of 300 N.

Our experiences can be divided into two parts:

- results about material behavior,
- experiences about the technique of measurements.

2.2. Experiences about the measuring technique. Textiles used for engineering purposes are more sensitive than the common building materials, so we have to plan

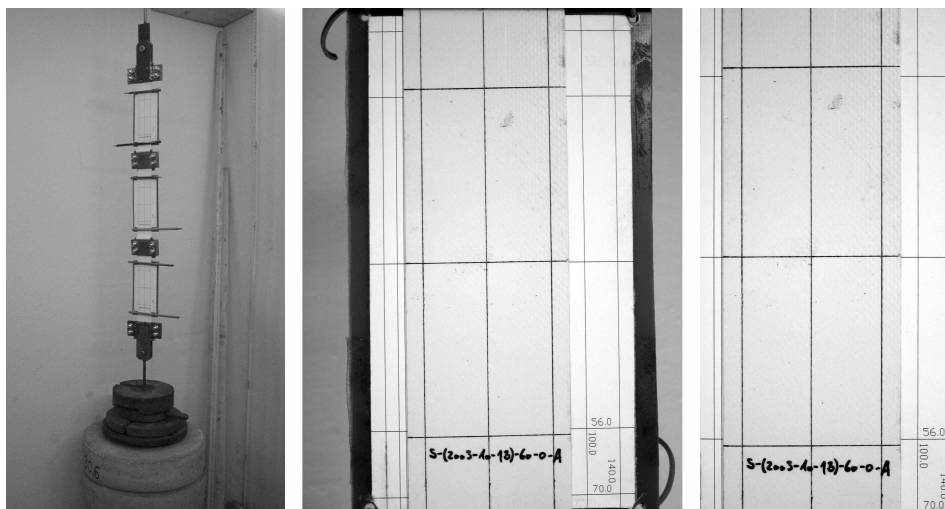


Figure 1. a. Setup of the experiment (on the left); b. Front view of a specimen with the paperboard panel (in the middle); c. Perpendicular view of the specimen (on the right)

the tests with special care. Our intention is to exclude any effects caused by the tools of the measurement and external factors in the course of the experiments. We cannot

fix anything on the material in the measured area without influencing the result, and the measuring tool cannot touch the specimen during the test. Considering the problems mentioned above, we developed a photographic procedure for the creep test of engineering textiles.

The experiment is done in the following steps:

- We suspend the material specimens (Figure 1.a.).
- We fix a small paperboard panel behind every suspended material specimen. The panel is slack and is fixed to the textile over the measured part. The panel is parallel with the textile, and has a calibrated perpendicular network (Figure 1.b.).
- We take front-view pictures of this system.
- We turn the photos to perpendicular view by a photo editor, on the basis of the perpendicular network of the paperboard panel. The aim of this step is to eliminate the angular distortion (from the perpendicular view) of the photos (Figure 1.c.).
- By the calibrated network we can scale the photos, and then we can measure the distance between any two points.

For an accurate measurement we need to care about the followings:

- The camera takes a perspective picture. Since the specimen is not perfectly flat, the perspective distortion can be different from different viewpoints. Thus, we have to take the photos from the same viewpoint.
- The size of the picture is set by the calibration of the paperboard panel. The calibration contains errors. These errors are different on the different panels and are also different in each direction; therefore the same panel is used for one specimen during the whole test. On the other hand, the axis of the panel and the measured specimen need to be parallel.
- We cut a rectangular part of the picture and rotate this part to perpendicular view. According to our experience, the result of the rotation is very sensitive to the determination of the four corner points on the original picture. To eliminate the error of the determination of the corners, we use the reference lengths drawn horizontally and vertically on the paperboard panel. These lengths have to be the same in every picture. Because of the relative errors, it is recommended to use longer reference lengths than the measured length of the specimen.
- The resolution of a picture is determined by the resolution of the CCD of the camera. During the data processing we experienced that we can increase the usability of a picture by increasing the resolution by the help of software.

The accuracy of the measurements could be increased by the following:

- We use a digital camera with 3 mega pixels. With higher resolution we would obtain more information.
- The lenses of the camera cause distortion. With better quality lenses the distortion could be decreased.

- We use an alcoholic pen with a toe of 0.1 mm. The thickness of the line on the material is 0.2-0.3 mm. With thinner lines we could increase the accuracy.

With the available tools, choosing a 10 cm base length on the specimen and a 14 cm x 7 cm perpendicular network on the panel we can measure length with 0.1 mm accuracy. Because of the relative errors the method can be used for the measurement of relative distances.

We take photos about the whole specimen, so we can measure the vertical and horizontal elongations alike. In horizontal direction the length is smaller (5 cm), so the relative error is bigger.

2.3. Experiences about the behavior of the material.

2.3.1. *Time-strain curves.* First we loaded the material with 600N. The time-strain diagram shows the characteristics of the serially connected Maxwell and Kelvin-Voigt material models. The duration of the test was 24 days. On the 17th day we decreased the 600N load to 50N. We regard the time between the 17th and 24th days as the unloading period. Figure 2. contains the time-strain data of the test.

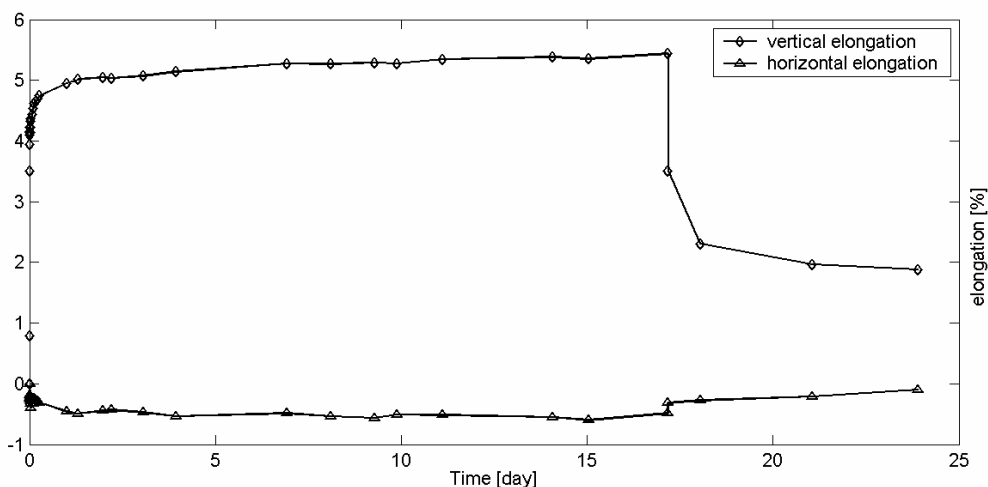


Figure 2. Time-strain data of the test under 600 N

The second and third tests, under 300N and 900N, were disturbed by changing the humidity and temperature.

Figure 3 represents the time-strain-temperature-humidity data of the test under 300N. The duration of the test was 98 days. On the 68th day we decreased the 300N load to 50N.

Figure 4 shows the data of the test under 900N. The duration of the test was 114 days. After 82 days we decreased the load to 90N.

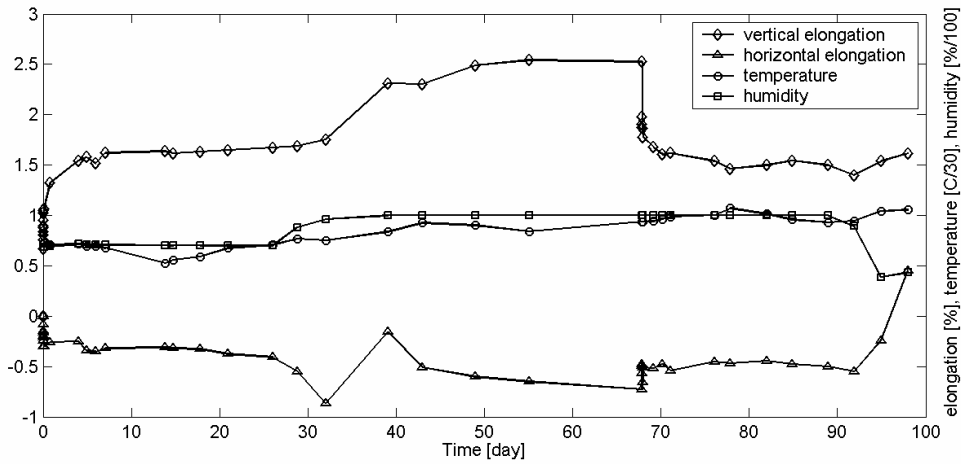


Figure 3. Time-strain data of the test under 300 N

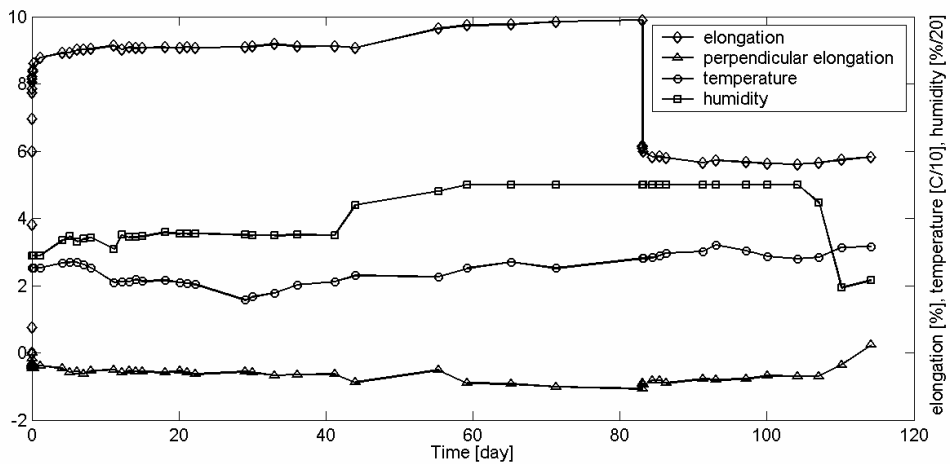


Figure 4. Time-strain data of the test under 900 N

On the basis of the first tests the creep (in the case of loading as well as unloading) can be divided into two periods. In the first period the creep is very fast, in the first hours of the loading the viscous strain achieves the order of magnitude of elastic strain. After the first hours, in the second period of the creep the strain increases much more slowly. We will need very long term tests to determine whether the creep stops or not.

According to [1], in case of large stresses ($\sim 80\%$ of the load bearing capacity) the strain achieves the tear strain in time, but we did not find any information about

similar behavior at lower stress levels. (The allowed stress in membrane structures is never higher than 33% of the load bearing capacity.) If the creep does not stop, it can lead to fracture at a low stress level in a very long time. (This time has to be longer than the lifetime of the structure.)

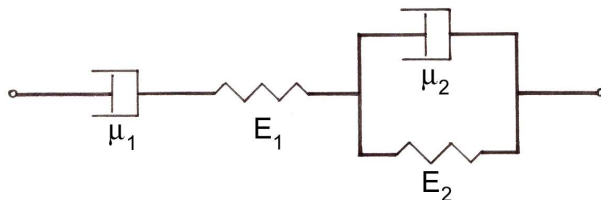


Figure 5. Maxwell and Kelvin-Voigt material models connected in series

There are four parameters to be determined if we want to use serially connected Maxwell and Kelvin-Voigt material models, the elasticity modulus E_1 , E_2 and the creep constant μ_1 , μ_2 .

E_1 can be determined on the basis of the length before loading (l_0) and the first measured length after loading (l_1):

$$E_1 = \frac{l_0}{l_1 - l_0} \Delta\sigma_l, \quad (2.1)$$

or on the basis of the last measured length before unloading (l_{max}) and the first measured length after unloading (l_{max+1}):

$$E_1 = \frac{l_{max+1} - l_{max}}{l_0} \Delta\sigma_u, \quad (2.2)$$

where $\Delta\sigma_l$ and $\Delta\sigma_u$ are the alterations of the stress during loading and unloading. (2.2) gives the following result at three different applied load levels:

$$E_1 = 9.37 \text{ kN/cm (300 N)}, \quad E_1 = 5.98 \text{ kN/cm (600 N)}, \quad E_1 = 4.52 \text{ kN/cm (900 N)}.$$

This method for the determination of E_1 is fairly inaccurate, because it depends on the time between the loading (or unloading) and the first measurement (the first photo). The classical load bearing capacity test would give more accurate result. The tangent of the stress-strain diagram at the current stress level gives the value of E_1 .

The other 3 material constants were determined by regression analysis. The strain in the serially connected Maxwell and Kelvin-Voigt models can be described by:

$$\varepsilon(t) = \frac{\sigma}{E_1} + \frac{\sigma}{\mu_1} t + \frac{\sigma}{E_2} \left(1 - e^{-\frac{E_2}{\mu_2} t}\right). \quad (2.3)$$

For the determination of the material constants, the following function has to be minimized:

$$\varphi(\mu_1, E_2, \mu_2) = \sum_{i=0}^n \left\{ \varepsilon_i - \left[\frac{\sigma}{E_1} + \frac{\sigma}{\mu_1} t_i + \frac{\sigma}{E_2} \left(1 - e^{-\frac{E_2}{\mu_2} t_i}\right) \right] \right\}. \quad (2.4)$$

In the course of the evaluation of the test results we have obtained the following values:

Load N	μ_1 kN*day/cm	E_2 kN/cm	μ_2 kN*day/cm
300	1343.81	8.66	5.95
600	530.04	8.62	0.83
900	6313.96	9.39	3.68

The differences between the viscous constants determined from the 3 experiments are significant. Probably the strong disturbing effects (the change in temperature and humidity) and the unsettled measuring technique caused the unexpected discrepancy in the constants.

On the basis of future test results we will make the material model more accurate or we will use the creep function, which is very common for concrete structures.

2.3.2. The effect the temperature. The membrane material is a kind of plastic, which is sensitive to temperature. According to [1], there is an analogy between the effect of temperature and the progress of time. This means that a rise in temperature speeds up the creep. We can take advantage of this behavior in the future to decrease the length of the experiments, as a kind of extrapolation. It is important that the material has to be in the visco-elastic temperature range, the temperature must not reach the limit of plasticity.

During our tests the temperature was changed between 15.7 °C and 32.1 °C. The effect of the changing temperature is well traceable in the time-strain diagrams. The order of magnitude of the strain corresponding to increasing temperature was equal to the order of magnitude of the viscous strain.

This means that the alteration of the temperature has a significant effect on the behavior of membrane structures. Later it can be interesting to analyze this phenomenon, but in the near future our aim is to make tests on constant temperature and to eliminate the effect mentioned above.

2.3.3. The effect of humidity. Humidity often influences the behavior of plastics. We did not take the effect of humidity into account in the case of the membrane material because the polyester fibres are coated with PVC. In the literature we have not found detailed information about this influence. Some papers consider the effect of humidity to be insignificant [2], some papers mention it as an important factor [3].

During the test under 900 N, the 70 % relative humidity was changed to the extreme level of 99.9 %. The change of humidity had a similar effect on the strain to that of the rise in temperature.

Since membrane structures are often used for covering facilities with high humidity (e.g. swimming pools), it will be interesting to deal with this question in the future. However, during the following tests we would like to eliminate this effect and keep humidity at a constant level as much as possible.

By reason of the significant effect of the changing temperature and humidity, for the following tests we have built a quasi climate chamber, where the temperature and humidity are practically constant. The present tests are going on in this chamber. We expect more accurate results from these experiments.

2.4. Other technical questions.

2.4.1. *The rate of measurements.* On the one hand, we need enough data to draw the time-strain curves, on the other hand, if we have too many photos, they can not be processed, because of the time consuming data processing (about 20 minutes per photo).

During the test the speed of the strain changes significantly. After loading it is very fast and after some hours it becomes much slower. Thus in the first hour of the test we take photos every 10-15 minutes, and then every hour. From the second day it is enough to take pictures in every second or third day. If there are other effects like the change in humidity or temperature, it is better to keep the higher rate (one photo per day).

2.4.2. *Measurements in the direction of the bisector of the warp and fill directions.* The PVC coating plays an important role in the behavior in the direction of the bisector of the warp and weft directions. The stiffness of the matrix is very small, hence the angle deformation and the elongation are very high in this direction. Our test in this direction was not successful. We tried to load the textile with 300 N. The elongation and the perpendicular deformation were about 40 %. After this large deformation, the elongation belonged to the fibre, and not to the matrix material.

The material became curved, so it was not possible to make orthogonal photos.

We have to find a way to measure the long time shear deformation because it may have a significant effect on the stress distribution of tent structures.

3. Numerical analysis of the visco-elastic behavior of membrane structures

The other direction of our research is the numerical analysis of the long-term behavior of prestressed membrane structures on the basis of a visco-elastic material model.

A finite element program has been developed in the previous years for the design and static analysis of prestressed membrane structures [4], [5]. The procedure is based on the Dynamic Relaxation Method (DRM) [6].

The procedure developed contains four main modules. With the aid of the first module we can determine the theoretical shape, the equilibrium shape that corresponds to the boundary conditions and to a hydrostatic stress-field or to constant principal projected stresses. The second module prepares the cutting pattern by flattening the theoretical shape. The third module determines the construction shape, the equilibrium shape that corresponds to the boundary conditions, the material constants and the cutting pattern, taking into account the real warp and fill directions in the material. Usually the difference between the theoretical and construction shapes is insignificant, but the corresponding stress fields are considerably different. With the help of the fourth module we can analyze the behavior of the structure under static loads on the basis of the construction shape. The hyperbolic surface of the tent is approximated by a finite element network of planar, triangular, and orthotropic membrane elements.

DRM is a step by step method and we use it for the determination of the different equilibrium shapes of the membrane structures. The main idea of the DRM is that we follow up the fictitious motion of the structure from the initial shape to the equilibrium shape in Δt time steps. During the determination of the construction shape and the statical analysis, every triangular element of the finite element network is linked to a corresponding triangular (stress-free) part of the cutting pattern. The stresses and strains in warp and weft directions are calculated in every iteration step on the basis of the current coordinates and the stress-free size of the elements. The stresses are reduced to the nodes and these forces are summed for every node. These unbalanced nodal forces accelerate the fictitious masses, placed to every node of the finite element network, at the beginning of the procedure. If we use suitable damping, this fictitious motion converges to the equilibrium shape. We stop the iteration if the maximum of the unbalanced nodal forces (F_{max}) is smaller than an allowed value (F_p).

For the analysis of the long-term behavior of prestressed tent structures, we improve this program on the basis of a visco-elastic material model. The first task is the analysis of the prestress level and the stress distribution in time, leaving the external forces out of consideration. The diminution of the prestress in time is an important question because it results in a smaller stiffness of the structure and in a higher risk of fluttering.

Our task is to determine the equilibrium shapes and stress fields in t^k moments on the basis of the construction shape and the corresponding stress field (initial prestress in $t = t^0$ moment). (This time we do not deal with the determination of the construction shape.) To find the equilibrium shape we use the DRM, but there is a big difference in the determination of the construction shape and the determination of the equilibrium shape at the t^k moment. In the first case we can calculate the stresses directly from the strains of the triangular membrane elements; we suppose that the strains are totally elastic. In the second case we need one more inner iteration cycle for the calculation of the viscous and elastic parts of the strains. Since our method for the determination of the construction shape has been published before [4], [5], this time we demonstrate only the inner iteration cycle (the determination of the stresses) in detail.

We use serially connected Maxwell and Kelvin-Voigt material models (Figure 5) according to the first results of the material tests. The procedure developed uses the following material constants:

$E_{1,w}, \mu_{1,w}, E_{2,w}, \mu_{2,w}$ constants in warp direction,

$E_{1,f}, \mu_{1,f}, E_{2,f}, \mu_{2,f}$ constants in fill (weft) direction,

since we do not have measured data about the time dependence of G, ν_{wf}, ν_{fw} parameters for the present time, we consider them constants in time. In addition to the material constants, we assume that the construction shape with the initial stress field belongs also to the input.

We use the following marking for the stresses (σ) and strains (ε):

- the first upper index (k) is the time index, it means the number of past time steps from the beginning of the analysis,

- the second upper index (i) is the current number of the iteration step in the inner iteration cycle, if there is no second index, the value is accepted for the t^k time step,
- the first lower index is the sign of direction, warp (w) or fill (f),
- the second lower index is for the element of the material model (E_1, μ_1, E_2, μ_2). The index 2 means the equal strains of the two elements in the Kelvin-Voigt model, ($\varepsilon_{w,2} = \varepsilon_{w,E_2} = \varepsilon_{w,\mu_2}$, $\varepsilon_{f,2} = \varepsilon_{f,E_2} = \varepsilon_{f,\mu_2}$).

In the course of the determination of the equilibrium shape in time t^k , the elongations of the triangular elements are calculated on the basis of the current coordinates and the stress-free sizes of the elements, in every iteration step of the DRM. Since the angle between the sides of the elements and the warp direction in the material is known, the strains in warp (ε_w^k) and fill (ε_f^k) directions and the shear strain (γ_{wf}^k) can be calculated.

According to the material model, the $\varepsilon_w^k, \varepsilon_f^k$ strains can be divided into 3 parts:

$$\varepsilon_w^k = \varepsilon_{w,\mu_1}^k + \varepsilon_{w,E_1}^k + \varepsilon_{w,2}^k, \quad (3.1)$$

$$\varepsilon_f^k = \varepsilon_{f,\mu_1}^k + \varepsilon_{f,E_1}^k + \varepsilon_{f,2}^k. \quad (3.2)$$

At the same time the stress is equal in the three elements of the material model:

$$\sigma_w^k = \sigma_{w,\mu_1}^k = \sigma_{w,E_1}^k = \sigma_{w,2}^k, \quad (3.3)$$

$$\sigma_w^k = \dot{\varepsilon}_{w,\mu_1}^k \mu_{1,w} = \dot{\varepsilon}_{w,E_1}^k E_{1,w} = \dot{\varepsilon}_{w,2}^k \mu_{2,w} + \dot{\varepsilon}_{w,2}^k E_{2,w}. \quad (3.4)$$

We suppose that in time t^0 :

$$\varepsilon_{w,\mu_1}^0 = \varepsilon_{w,\mu_2}^0 = \varepsilon_{f,\mu_1}^0 = \varepsilon_{f,\mu_2}^0 = 0. \quad (3.5)$$

In the following we give the formulae only in warp direction. By changing index w to f in the equations, we can get the formulae for fill direction.

The viscous strains are calculated from the average value of the stresses in the (t^{k-1}, t^k) time interval:

$$\frac{\varepsilon_{w,\mu_1}^k - \varepsilon_{w,\mu_1}^{k-1}}{\Delta t_v} \mu_{1,w} = \frac{\sigma_w^{k-1} + \sigma_w^k}{2}, \quad (3.6)$$

$$\frac{\varepsilon_{w,2}^k - \varepsilon_{w,2}^{k-1}}{\Delta t_v} \mu_{2,w} + \frac{\varepsilon_{w,2}^k + \varepsilon_{w,2}^{k-1}}{2} E_{2,w} = \frac{\sigma_w^{k-1} + \sigma_w^k}{2}, \quad (3.7)$$

where Δt_v is the length of the time interval between the analysed moments.

On the basis of the above-mentioned formulae, the iteration cycle for the determination of the stresses in the triangular elements contains the following steps (in moment t^k , for one given shape of the DRM iteration):

- Initially ($i = 1$) the normal stresses in every element are given equal to the stresses in the same element in the equilibrium shape corresponding to moment t^{k-1}

$$\sigma_w^{k,i} = \sigma_w^{k-1}. \quad (3.8)$$

- The shear stress is calculated on the basis of

$$\tau_{wf} = G \gamma_{wf}. \quad (3.9)$$

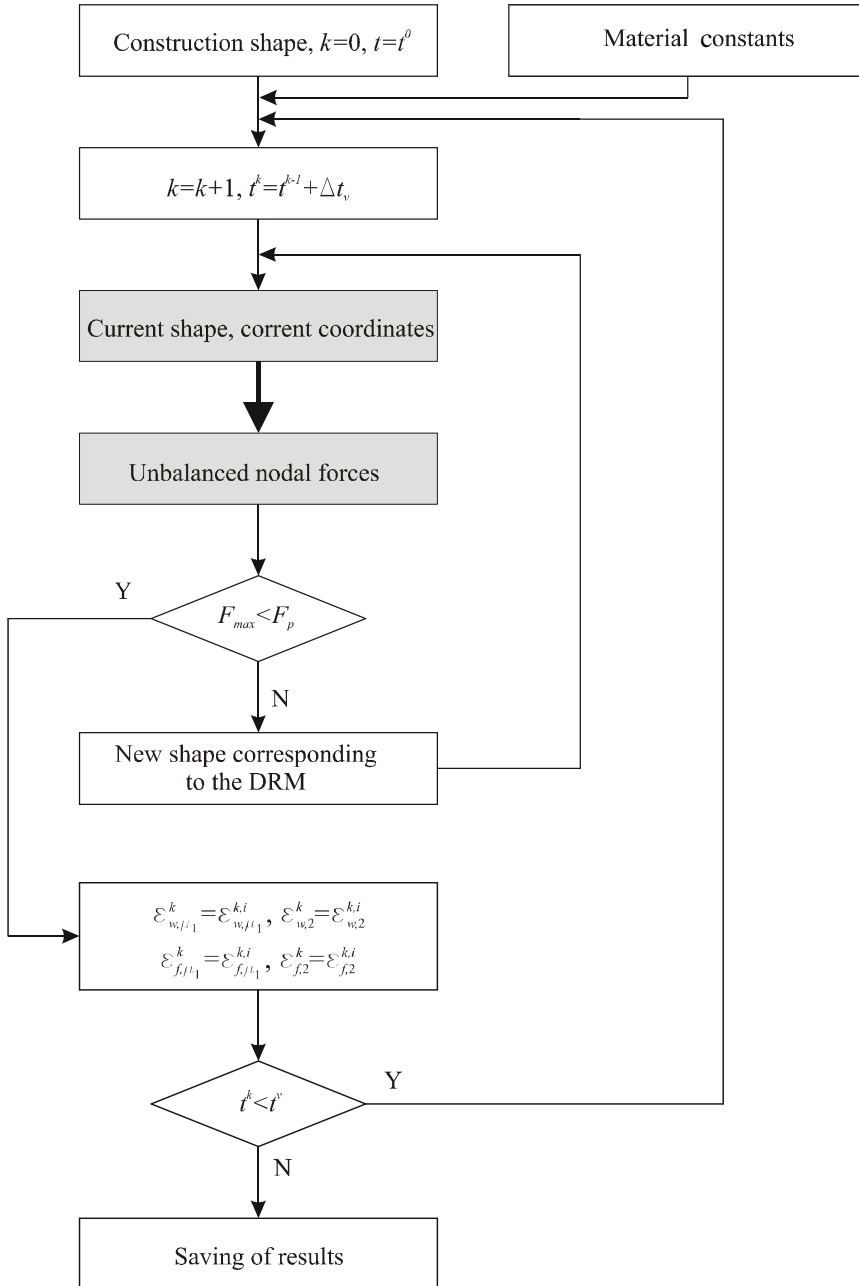


Figure 6. Main flowchart of the DRM, the thick arrow meaning the inner iteration

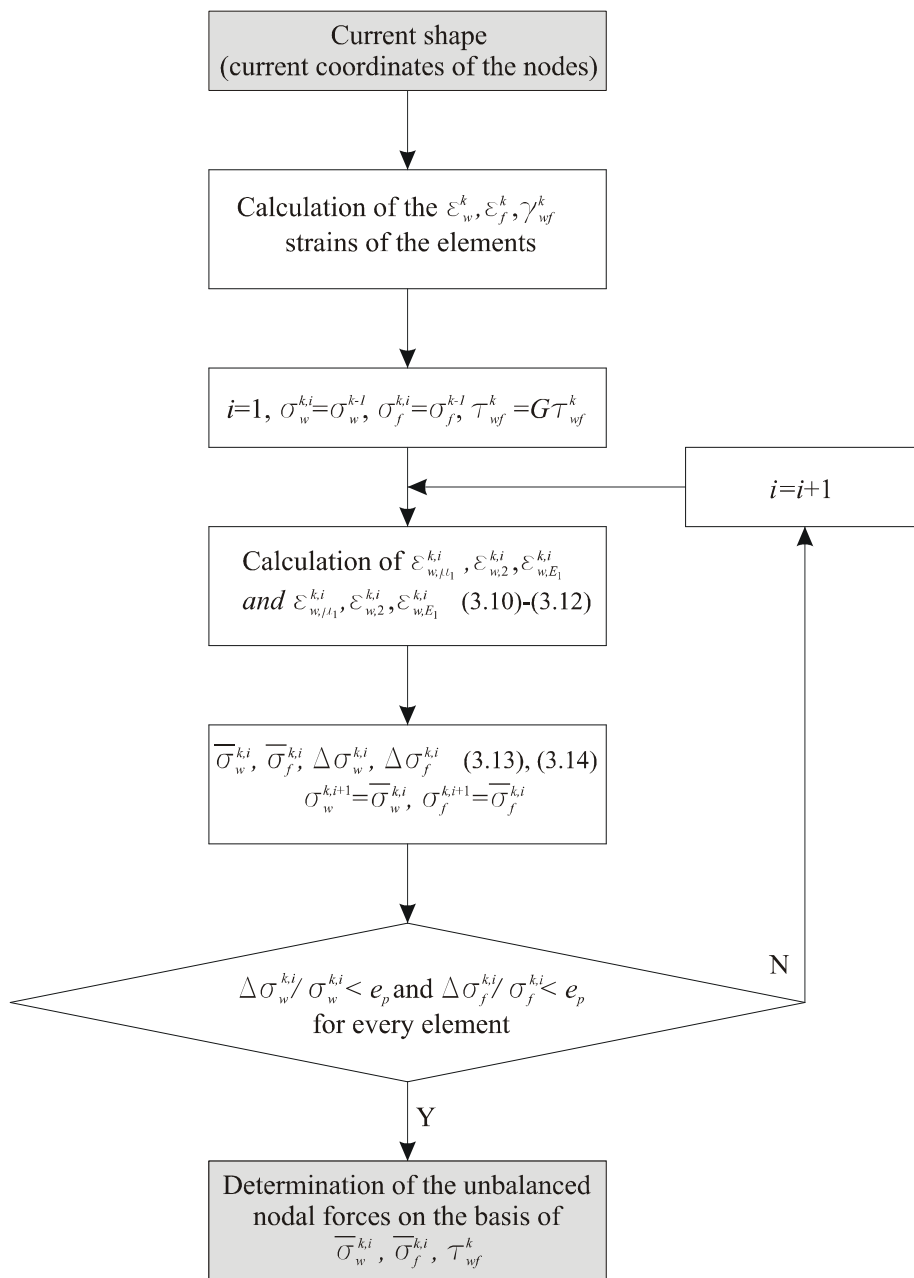


Figure 7. Inner iteration, determination of the stresses, strains and unbalanced nodal forces on the basis of the current coordinates

- According to (3.6), the strain of the piston in the Maxwell element can be calculated by

$$\varepsilon_{w,\mu_1}^{k,i} = \varepsilon_{w,\mu_1}^{k-1} + \Delta t_v (\sigma_w^{k-1} + \sigma_w^{k,i}) / (2\mu_{1,w}), \quad (3.10)$$

and the strain of the Kelvin-Voight element, according to (3.7), can be described by:

$$\varepsilon_{w,2}^{k,i} = \left(\frac{\sigma_w^{k-1} + \sigma_w^{k,i}}{2} + \frac{\varepsilon_{w,2}^{k-1} \mu_{2,w}}{\Delta t_v} - \frac{\varepsilon_{w,2}^{k-1} E_{2,w}}{2} \right) / \left(\frac{\mu_{2,w}}{\Delta t_v} + \frac{E_{2,w}}{2} \right). \quad (3.11)$$

With the known values of $\varepsilon_{w,\mu_1}^{k,i}, \varepsilon_{w,2}^{k,i}$, the elastic elongation is

$$\varepsilon_{w,E_1}^{k,i} = \varepsilon_w^k - \varepsilon_{w,\mu_1}^{k,i} - \varepsilon_{w,2}^{k,i}. \quad (3.12)$$

- The stresses are calculated from the strains in warp and weft directions:

$$\bar{\sigma}_w^{k,i} = \frac{1}{1 - \nu_{wf} \nu_{fw}} (E_{1,w} \varepsilon_{w,E_1}^{k,i} + \nu_{wf} E_{1,f} \varepsilon_{f,E_1}^{k,i}). \quad (3.13)$$

- Comparing the

$$\Delta \sigma_w^{k,i} = \frac{\bar{\sigma}_w^{k,i} - \sigma_w^{k,i}}{\sigma_w^{k,i}} \quad (3.14)$$

error of the iteration for every element with an allowed value (e_p), we decide on the continuation of the DRM iteration (if $\Delta \sigma_w^{k,i} < e_p$), or the continuation of the inner iteration cycle (if $\Delta \sigma_w^{k,i} > e_p$) from step (3.10) after

$$\sigma_w^{k,i+1} = \bar{\sigma}_w^{k,i} \quad (3.15)$$

and $i=i+1$.

The actual shape is accepted as an equilibrium shape, according to the DRM, if

$$F_{\max} < F_p. \quad (3.16)$$

Then

$$\varepsilon_{w,\mu_1}^k = \varepsilon_{w,\mu_1}^{k,i}, \quad (3.17)$$

$$\varepsilon_{w,2}^k = \varepsilon_{w,2}^{k,i} \quad (3.18)$$

are stored and increasing k by one the calculation is continued with the next time step of the long term analysis.

The main steps of the long term analysis are shown in Figure 6. The inner iteration loop, the calculation of the stresses and strains are demonstrated in Figure 7.

4. Results of the numerical analysis

4.1. Assumptions for the change in time. In the course of the numerical analysis of different structures, we experienced that the equilibrium shape of the tent, the distribution of the stresses and the $\sigma_w^{\max} / \sigma_w^{avg}, \sigma_f^{\max} / \sigma_f^{avg}$ quotients do not change significantly in time, where

σ_w^{\max} is the maximum stress in warp direction,
 σ_w^{avg} is the average stress in warp direction,

σ_f^{\max} is the maximum stress in fill direction,
 σ_f^{avg} is the average stress in fill direction.

The reason for this (at first sight surprising and perhaps misleading) result is the following. Since so far we have measured data only in warp direction, we used a linear visco-elastic material model with the same material constants in warp and weft directions and did not take into account the time-dependency in the case of constants G , ν_{wf} and ν_{fw} . Because the normal stresses are definitive from the aspect of the equilibrium of the structure, the same linear viscous model in warp and fill direction results that the surface substantially remains in equilibrium while the normal stresses decrease in time.

4.2. Example structure. In Figure 8, the plan view, in Figure 9, the construction shape of an example structure can be seen. The membrane is supported by a 10 m high mast, the diameter of the inner ring is 2 m, and the diameter of the rigid outer edge is 20 m. We used the following constants in the serially connected Maxwell and Kelvin-Voigt material model: $E_1 = 6.62$ kN/cm, $\mu_1 = 2730$ kN*day/cm, $E_2 = 8.89$ kN/cm, $\mu_2 = 3.49$ kN*day/cm (the arithmetical mean value of the results of the experiments). As we mentioned before, in the case of the constants $G = 0.1$ kN/cm, $\nu_{wf}=0.15$ and $\nu_{fw} = 0.15$ we did not take into account the time-dependence.

Figure 10 shows the alteration of three representative values of the stress distribution in the structure. During the first day the stresses decreased by almost 45 %; and by an additional 5 % in the following 59 days. (In practice, a significant part of the viscous strain arises during construction.)

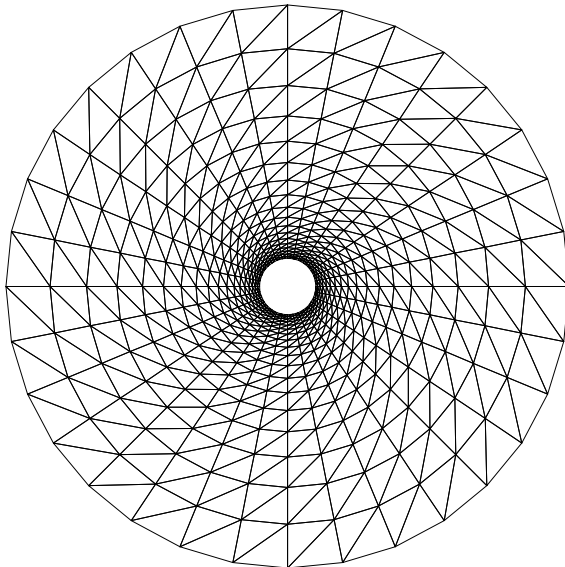


Figure 8. Plan view of the example structure

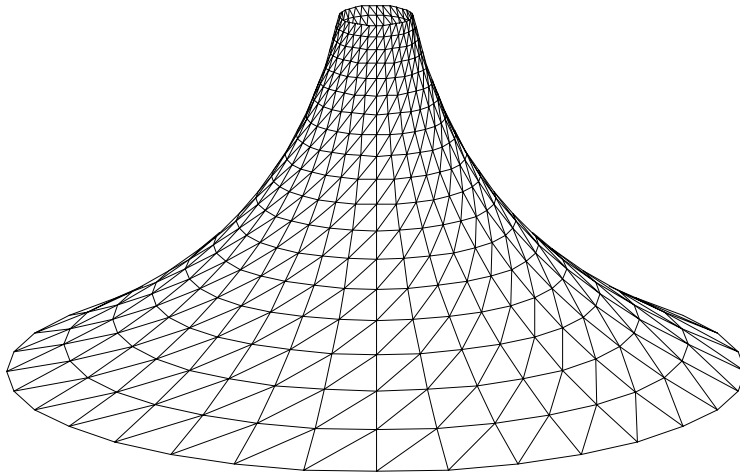


Figure 9. Construction shape of the example structure

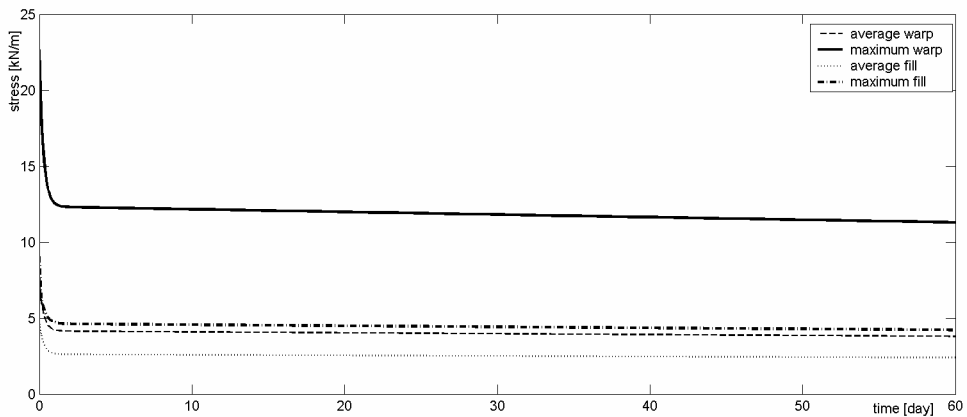


Figure 10. Decreasing of stresses in warp and fill directions in the first 60 days after construction

According to practice, we post-tensioned the structure by lifting the mast. After three days we lifted the mast by 15 cm, after the sixth day we post-tensioned the structure again by lifting the mast by an additional 5 cm. Figure 11 demonstrates

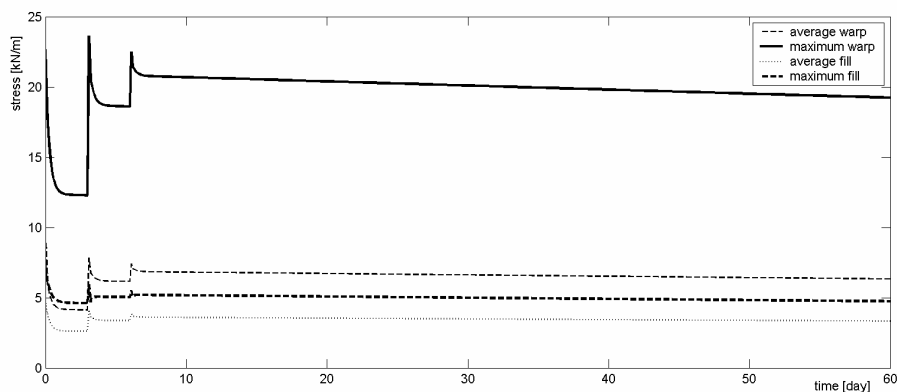


Figure 11. The change of stresses in warp and fill directions in the first sixty days after construction, in the case of post-tension after the 3rd and 6th day

the effect of the post-tension on the stress level. 60 days after construction the stresses are 15% smaller than the initial prestress (without post-tension, the diminution is 50%).

5. Conclusions

We have developed a photographic procedure for the creep test of engineering membrane materials. The first tests of the PVC-coated polyester material show that the long-term deformation can be divided into two parts. In the first hours after loading the strain increases very rapidly but after some hours the creep of the material is much slower. It is important from two aspects: on the one hand our method cannot be used for measuring elastic elongation (the photos cannot be taken quickly enough); on the other hand, the construction shape is the result of both the elastic and plastic deformations.

During the experiments, the temperature and the humidity changed considerably and this had a significant effect on the strains. In future tests we will try to eliminate these effects and we use a quasi-climate chamber. Later it may be interesting to analyze these effects.

The most important experience of the tests is that the creep of the PVC-coated polyester is significant, we cannot neglect the relaxation of the membrane and we have to use a visco-elastic material model for the long-term static analysis of membrane structures.

With this aim, simultaneously with the tests, we have developed a computer program for the numerical analysis of the long-term behavior of prestressed membrane structures. With the aid of the first version of this program, the decreasing stress level (according to the relaxation of the material) and the effect of post-tension can be analyzed. The result of the long-term analysis of a simple structure is demonstrated.

References

1. KNUDSON, W. C.: Recent advances in the field of long span tension structures. *Eng. Struct.* **13**, (1991), 164-177.
2. HOLLAWAY, L. C.: *Polymers and polymer composites in constructions*. Thomas Telford Ltd, London, 1990.
3. LEONARD, J. W.: *Tension Structures*, McGraw-Hill Book Company, New York, 1988.
4. GÁSPÁR, Zs. and HINCZ, K.: Formfinding and Static Analysis of Tents, IASS-2001, *Theory, Design and Realization of Shell and Spatial Structures*. Proceedings CD, Nagoya, Japan, 2001.
5. HINCZ, K.: Determination of the cutting patterns of prestressed tent structures. *Revista Portuguesa de Engenharia de Estruturas*, **47**, (2000) 45-49.
6. DAY, A. S.: An Introduction to Dynamic Relaxation. *The Engineer*, **219**, (1965), 218-221.

PARTICLE SWARM METHOD AS A NEW TOOL FOR STRUCTURAL OPTIMIZATION

KÁROLY JÁRMAI

Department of Materials Handling and Logistics, University of Miskolc
3515 Miskolc-Egyetemváros, Hungary

altjar@uni-miskolc.hu

[Received: March 25, 2004]

Dedicated to István Páczelt on the occasion of his 65th birthday

Abstract. A new and promising optimization technique is introduced: the particle swarm optimization (PSO). In this evolutionary technique the social behavior of birds is imitated. The technique is modified in order to be efficient in technical applications. It calculates discrete optima, uses dynamic inertia reduction and craziness at some particles. The efficiency of the technique is shown in the optimum design of a stringer-stiffened shell under bending and compression. The PSO is built into an interactive program system, where several optimization techniques are employed. The program system includes multiobjective optimization techniques as well. Results show that PSO is a reliable and robust technique to find optima with highly non-linear constraints. In the cost calculation 2D and 3D curve fitting is employed to determine the production time.

Mathematical Subject Classification: 74P10

Keywords: particle swarm method, structural optimization

1. Introduction

The optimum design process has the following three main phases:

- preparation: selection of candidate structural versions defining the main characteristics to be changed, formulation of design constraints and cost function,
- solution of the constrained function minimization problem by using efficient mathematical methods,
- evaluation of results by designers, comparison of optimised versions, formulation of design rules, incorporation in expert systems.

These phases show that structural optimization has the following three main parts: cost function, design constraints, and mathematical method.

In this paper we focus on the mathematical technique and show its application.

There is a great number of methods available for single objective optimization as it was described in Farkas & Jármai [1]. Methods without derivatives include: Complex [2], Flexible Tolerance, and Hillclimb. Methods with first derivatives include: Sequential Unconstrained Minimization Technique (SUMT), Davidon-Fletcher-Powell,

etc. Methods with second derivatives include: Newton, SQP. There are also other classes of techniques like optimality criteria methods, or the discrete methods like Backtrack, the entropy-based method [3, 4]. Multicriteria optimization is used when several objectives are important to find the compromise solution [5].

The general formulation of a single-criterion non-linear programming problem is the following:

minimize

$$f(x) \quad x = \{x_1, x_2, \dots, x_N\} \quad (1.1)$$

subject to

$$g_j(x) \leq 0, \quad j = 1, 2, \dots, P \quad (1.2)$$

$$h_i(x) = 0, \quad i = P + 1, \dots, P + M \quad (1.3)$$

$f(x)$ is a multivariable non-linear function, $g_j(x)$ and $h_i(x)$ are non-linear inequality and equality constraints, respectively.

In the last two decades some new techniques have appeared, e.g. the evolutionary techniques, the genetic algorithm [6], the differential evolution technique [7, 8], the particle swarm algorithm [9], and the ant colony technique [10, 11].

Some other high performance techniques such as leap-frog with the analogy of potential energy minimum [12, 13, 14], similar to the FEM technique, have also been developed.

2. The particle swarm algorithm

2.1. Preliminary remarks. A number of scientists have created computer simulations of various interpretations of the movement of organisms in a bird flock or fish school [15]. The Particle Swarm Optimization (PSO) algorithm was first introduced



Figure 1. Bird swarm

by Kennedy [16]. The algorithm models the exploration of a problem space by a population of individuals; the success of each individual influences their searches and those of their peers. In our implementation of the PSO, the social behavior of birds is imitated. Individual birds exchange information about their position, velocity and fitness, and the behavior of the flock is then influenced to increase the probability of migration to regions of high fitness [9]. A bird swarm is visible in Figure 1.

Particle swarm optimization has its roots in two main component methodologies. Perhaps more obvious are its ties to artificial life in general, and to bird flocking, fish schooling, and swarming theory in particular. It is also related, however, to evolutionary computation, and has ties to both genetic algorithms and evolutionary programming. Particle Swarm optimizers are similar to genetic algorithms in that they have some kind of fitness measure and start with a population of potential solutions (none of which are likely to be optimal), and attempt to generate a population containing fitter members.

In theory at least, individual members of the school can profit from the discoveries and previous experience of all other members of the school during the search for food. This advantage can become decisive, outweighing the disadvantages of competition for food items, whenever the resource is unpredictably distributed in patches. Social sharing of information among conspecifics offers an evolutionary advantage: this hypothesis was fundamental to the development of particle swarm optimization.

Millonas [15] developed his models for applications in artificial life, and articulated five basic principles of swarm intelligence. The first one is the proximity principle: the population should be able to carry out simple space and time computations. The second one is the quality principle: the population should be able to respond to quality factors in the environment. The third one is the principle of diverse response: the population should not perform its activities along excessively narrow channels. The fourth one is the principle of stability: the population should not change its mode of behavior every time the environment changes. The fifth one is the principle of adaptability: the population must be able to change its behavior mode when it is worth the computational price.

Basic to the paradigm are n -dimensional space calculations carried out over a series of time steps. The population is responding to the quality factors pBest and gBest (gBest is the overall best value, pBest is the best value for a particle). The allocation of responses between pBest and gBest ensures a diversity of response. The population changes its state (mode of behavior) only when gBest changes, thus adhering to the principle of stability. The population is adaptive because it does change when gBest changes.

The method is derivative free, and by its very nature the method is able to locate the global optimum of an objective function. Constrained problems can simply be accommodated using penalty methods.

2.2. Description of the Particle Swarm Algorithm. The system is initialized with a population of random potential solutions. Each potential solution is assigned a randomized ‘velocity’ and is called a particle. (It has position in the space, i.e. it

is a point in the solution space and it has a velocity. So it is analogous to a particle in physics which flies around in 3-D space.)

These particles are then 'flown' through the (hyper) space of potential solutions.

Each particle keeps track of the coordinates in the hyperspace for which it has achieved the best solution and its best fitness (call it pBest) so far.

In the 'global' version of the optimiser gBest is the overall best value with its location. This particle is the leader.

At each time step the 'velocity' of each particle is changed (accelerated) towards its pBest and gBest fellows. This acceleration is weighted by a random term. The idea is that all the particles swarm towards where the current best solutions are. The random factor prevents the swarm getting stuck in the wrong place – insects around a light.

A new position in the solution space is calculated for each particle by adding the new velocity value to each component of the particle's position vector.

The user specifies an acceleration constant and a maximum velocity.

Eventually, the swarm of potential solutions hovers around the best solution position. In the case of a neural net, this best 'particle' would be the optimum set of weights. (The weights are the particle's coordinates in the weight hyperspace.)

This method of search is a rival of the Genetic Algorithm in finding reasonable solutions to NP-hard problems.

For a given particle, in the N dimension search space:

let $x = (x_1, \dots, x_N)$ be its current position,

let $v = (v_1, \dots, v_N)$ be its current velocity,

let $p_i = (p_{i,1}, \dots, p_{i,N})$ be the best position it has found so far,

let $p_g = (p_{g,1}, \dots, p_{g,N})$ be the best position found so far in its neighborhood.

In other words for each particle the following information is available:

- (a) It has a position and a velocity,
- (b) It knows its position, and the objective function value for this position,
- (c) It knows its neighbors, best previous position and objective function value (variant: current position and objective function value),
- (d) It remembers its best previous position.

From now on, to put (b) and (c) in a common frame, we consider that the 'neighborhood' of a particle includes this particle itself.

At each time step, the behavior of a given particle is a compromise between three possible choices: (1) Following its own way, (2) Going towards its best previous position, (3) Going towards the best neighbor's best previous position, or towards the best neighbor (variant).

Define the new velocity by

$$v_d = (v_1^d, \dots, v_d^d, \dots, v_N^d) , \quad (2.1)$$

with

$$v_d^d = c_1 v_d + \text{rand}(0, c_2) (p_{i,d} - x_d) + \text{rand}(0, c_3) (p_{g,d} - x_d) , \quad (2.2)$$

define the new position by

$$x_d = x + v_d . \quad (2.3)$$

For $d = 1$ to N

$$v_d = v_d + \varphi_1(p_{i,d} - x_d) + \varphi_2(p_{g,d} - x_d) , \quad (2.4)$$

where φ_1 and φ_2 are said to be 'random positive numbers', without indicating *when* the randomness occurs: *inside* the d -loop (case 1), or *before* the d -loop (case 2). Unfortunately, several authors do use case 1, but nevertheless conclude that the new velocity vector is globally defined by

$$v_d = c_1 v + \text{rand}(0, c_2)(p_i - x) + \text{rand}(0, c_3)(p_g - x) , \quad (2.5)$$

which is true only for case 2. In this case, all the possible vectors are in the same plane, as in case 1 they define a complete volume in the search space.

There are different versions of Particle Swarm Optimization algorithms, but they can all be seen from an information point of view: what kind of information each particle has access to, and how it uses it (Shi & Eberhard 1998a,b).

2.3. The three methods.

2.3.1. *Random search rPSO*. The dimensionality of the search space H is N . It is supposed that H is finite, so that for each dimension k there is a minimum value $x_{min,k}$ and a maximum one $x_{max,k}$. At a time step, the particle uses no (variable) information at all.

2.3.2. *Constricted version cPSO*. At each time step, the pieces of variable information a given particle knows and can transmit are:

- its current position $x(t)$ and the corresponding objective function value,
- its best position found so far, $p_i(t)$, and the corresponding objective function value.

2.3.3. *Adaptive version aPSO*. At each time step, the pieces of variable information a given particle knows and can transmit are:

- its current position $x(t)$ and the corresponding objective function value,
- its best position found so far, $p_i(t)$, and the corresponding objective function value,
- its previous position (to estimate its improvement),
- its neighborhood size,
- the swarm size (global information).

To summarize, depending on the algorithm, each particle knows:

- no (variable) information at all (rPSO),
- only local information (cPSO),
- a bit more local information and some global information (swarm size) (aPSO).

Previously, the PSO algorithm was applied to analytical test functions, mostly univariate or bivariate without constraints [17]. In addition, multimodal problem generators were described by Kennedy & Spears [17]. Kennedy [18] used the PSO as an optimization paradigm that simulates the ability of human societies to process knowledge. The algorithm models the exploration of a problem space by a population of individuals; individuals' successes influence their searches and those of their peers. There

were attempts to improve the efficiency of the PSO by hybridising the algorithm with various other search methods [18, 19].

Lately, the PSO was successfully applied to the optimum shape and size design of structures by Fourie & Groenwold [20, 21, 22]. An operator, namely craziness, was re-introduced, together with the use of dynamic varying maximum velocities and inertia. An attempt was also made to optimize the parameters associated with the various operators in the case of generally constrained non-linear mathematical programming problems [23].

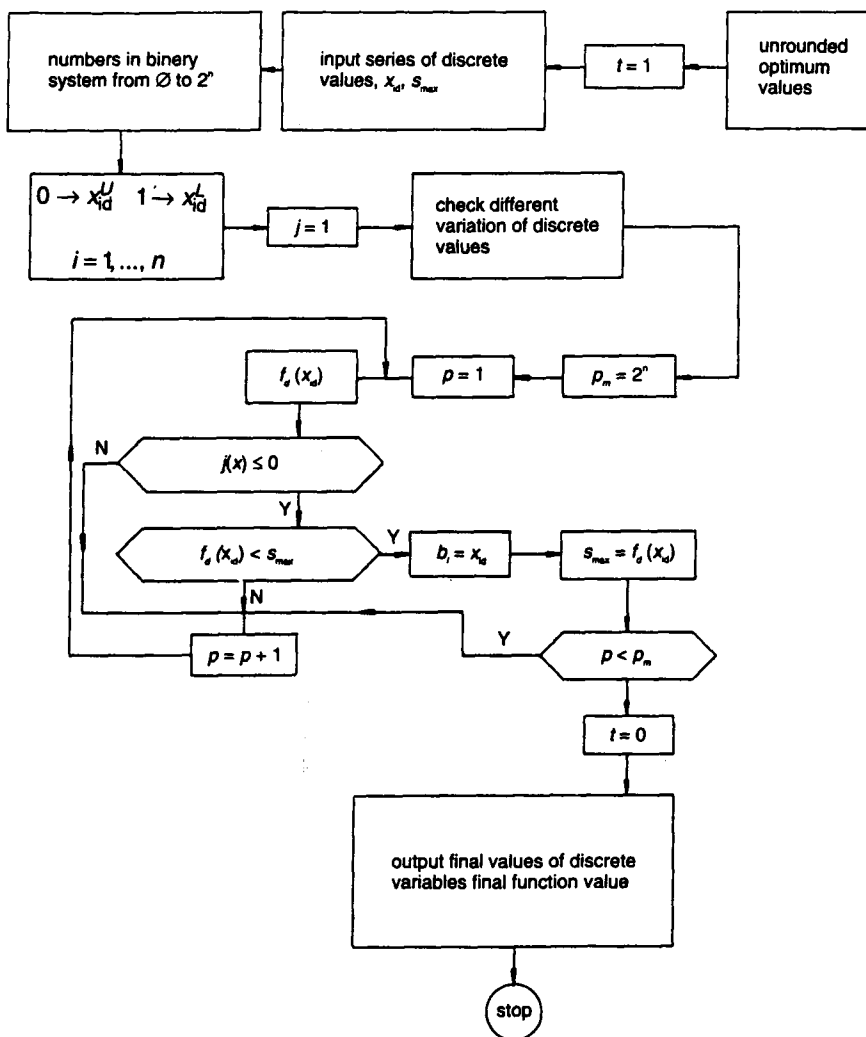


Figure 2. Flow chart of secondary discretization

3. Discretization after continuous optimization

To make the search more practicable it is advisable to use discrete member sizes. After continuous optimization a secondary search is necessary to find discrete optimum sizes in such a way that not only the explicit and implicit constraints are satisfied but the merit function takes its minimum as well. It is assumed that the optimum discrete sizes are near the optimal continuous ones [24].

Starting from the optimum continuous values, the secondary search chooses the nearest discrete sizes for each continuous size from the series of discrete values. The number of chosen discrete sizes for one continuous size can be two, three or more. The possible variations can be obtained using binary, ternary or larger systems. In our numerical example we use the binary system, two discrete sizes, upper and lower, belonging to one continuous value. In a binary system the figure zero means the upper discrete size, the figure one means the lower one. The first $2n$ number in a binary system gives all possible variations. Each variation is tested, whether the explicit and implicit constraints are satisfied, and the optimal values minimizing the merit function are determined. The flow chart of secondary discretization can be seen in Figure 2.

The number 0000 means the lower discrete values of all variables, the number 1111 means the upper discrete values of all variables. The other numbers in the binary system are the variants of the possible discrete solution. The solution is the tested variant that gives the minimum objective function value.

4. Stringer stiffened cylindrical shell loaded by axial compression and bending

4.1. Aim and variables. The aim of the optimization is to find the minimum value of the cost function due to non-linear constraints. The variables are: the height of stiffener h_s , number of stiffener n_s and the thickness of the shell t .

4.2. Constraints.

4.2.1. Shell buckling (unstiffened curved panel buckling) DNV (1995)[25]. The stresses caused by compression and bending are as follows

$$\sigma_a + \sigma_b = \frac{N_F}{2R\pi t_e} + \frac{H_F L}{R^2 \pi t_e} \leq \sigma_{cr} = \frac{f_y}{\sqrt{1 + \lambda^4}}, \quad (4.1)$$

where N_F is the compression force in N, H_F is the bending force in N, L is the length of the shell in mm, R is the radius of the shell in mm, t_e is the reduced shell thickness in mm and f_y is the yield stress in MPa.

Slenderness λ can be calculated making use of the equations

$$\lambda^2 = \frac{f_y}{\sigma_a + \sigma_b} \left(\frac{\sigma_a}{\sigma_{Ea}} + \frac{\sigma_b}{\sigma_{Eb}} \right); \quad t_e = t + \frac{A_s}{s}; \quad s = \frac{2R\pi}{n_s} \quad (4.2)$$

$$\sigma_{Ea} = C_a (1.5 - 50\beta) \frac{\pi^2 E}{10.92} \left(\frac{t}{s} \right)^2 \quad (4.3)$$

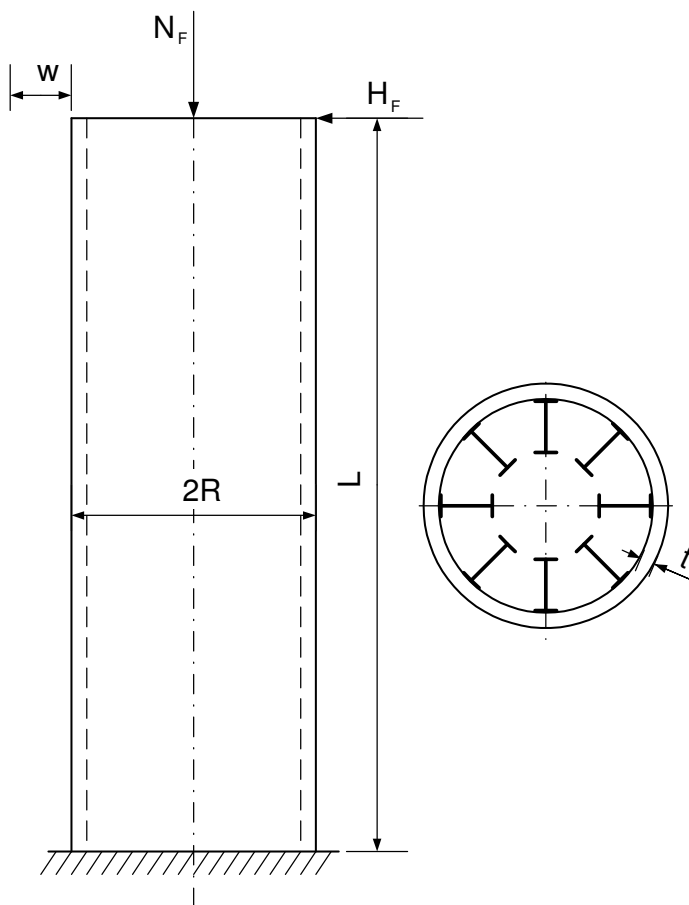


Figure 3. Stringer-stiffened shell

$$C_a = 4\sqrt{1 + \left(\frac{\rho_a \xi}{4}\right)^2}; \quad Z = \frac{s^2}{Rt} 0.9539 \quad (4.4)$$

$$\rho_a = 0.5 \left(1 + \frac{R}{150t}\right)^{-0.5}; \quad \xi = 0.702Z \quad (4.5)$$

$$\sigma_{Eb} = C_b (1.5 - 50\beta) \frac{\pi^2 E}{10.92} \left(\frac{t}{s}\right)^2 \quad (4.6)$$

$$C_b = 4\sqrt{1 + \left(\frac{\rho_b \xi}{4}\right)^2}; \quad \rho_b = 0.5 \left(1 + \frac{R}{300t}\right)^{-0.5}. \quad (4.7)$$

Note that the residual welding distortion factor is $1.5 - 50\beta = 1$ when $t > 9$ mm.

4.2.2. Stringer panel buckling.

$$\sigma_a + \sigma_b \leq \sigma_{crp} = \frac{f_y}{\sqrt{1 + \lambda_p^4}}, \quad (4.8)$$

$$\lambda_p^2 = \frac{f_y}{\sigma_{Ep}}, \quad \sigma_{Ep} = C_p \frac{\pi^2 E}{10.92} \left(\frac{t}{L} \right)^2, \quad (4.9)$$

$$C_p = \psi_p \sqrt{1 + \left(\frac{0.5 \xi_p}{\psi_p} \right)^2}, \quad Z_p = 0.9539 \frac{L^2}{Rt}, \quad (4.10)$$

$$\xi_p = 0.702 Z_p, \quad \gamma_s = 10.92 \frac{I_{sef}}{st^3}, \quad (4.11)$$

$$\psi_p = \frac{1 + \gamma_s}{1 + \frac{A_s}{s_e t}}; \quad (4.12)$$

according to ECCS [26]

$$s_E = 1.9t \sqrt{\frac{E}{f_y}}, \quad \text{where} \quad s_e = \begin{cases} s_E & \text{if } s_E < s \\ s & \text{if } s_E > s \end{cases}. \quad (4.13)$$

I_{sef} is the moment of inertia of a cross-section containing the stiffener and a shell part of width s_e . For a stiffener of rolled I-section

$$I_{sef} = I_y + A_S \left(\frac{h+t}{2} - z_G \right)^2 + s_e t z_G^2 \quad (4.14)$$

and

$$z_G = \frac{A_S (h+t)}{2(A_S + s_e t)}. \quad (4.15)$$

Horizontal displacement

$$w_h = \frac{ML^2}{3E\pi R^3 t_e} \leq w_{allow} = \frac{L}{\phi}, \quad (4.16)$$

$$M = H_F L / \gamma_M, \quad \gamma_M = 1.5; \quad H_F = 0.1 N_F. \quad (4.17)$$

The limit for displacement is $\phi = 600$.

Numerical data: $N_F = 68000$ kN, $f_y = 355$ MPa, $R = 1850$ mm, $L = 15$ m.

The main parameters of the PSO are as follows:

Probability of craziness (% i.e: 0 - 100) CRAZY = 1.5

Cognitive learning coefficient $0.5 - 2C1 = 2.0$

Social learning coefficient $C2 = 1.4$

Dynamic inertia scale factor. Beta =1 standard PSO alpha BETA = 0.98

Starting value of omega (linear inertia scale factor) OMEGA = 1.0

Minimum allowable fitness FMIN = $-1.0E10$

No-improvement termination criterion (iterations) TITER = 10

Maximum allowed number of function evaluations MAXNF = 10000

Update dynamic inertia criterion (# function evaluations) UPDT = 20

Velocity update factor (1 is normal PSO) VF = 0.985

Minimum allowable omega value MINOMGA = 0.2

Level of craziness of a completely crazy particle, CRTYPE = 1
 Moderately craze population CRTYPE = 2
 Standard velocity rule VRTYPE = 1
 Nico's rule $R2 = (1 - R1)$ original VRTYPE = 2
 Random placement BTYPE = 1
 Biased placement (minimum on the boundary) BTYPE = 2
 Perform max. velocity check VCHK = 1
 Don't have velocity check VCHK = 2

4.3. Curve fitting. Cost calculations are founded on industrial data. The main parameter is the time of a specific manufacturing element. This time (in min.) multiplied by the specific fabrication cost (\$/min) gives the cost (in \$). Data given by factories are discrete values and for the optimization we need functions. A curve-fitting program is needed to find the best function for the approximation of the given data. We have used 2D and 3D curve fittings made by the TableCurve 2D [27] and 3D [28] software. We would like to show the efficiency of curve-fitting approximations for the stiffener parameters and the plate forming time calculations.

TableCurve 2D's built-in library includes thousands of equations, a wide array of linear and nonlinear models for any application from simple linear equations to high order Chebyshev polynomials. It contains a 38-digit precision math emulator for properly fitting high order polynomials and rationals. TableCurve 2D speeds up programming by generating actual function code and test routines for all fitted equations in FORTRAN, C, Basic, Pascal and VBA for Excel.

TableCurve 3D's surface fitting contains in addition to standard least squares minimization, three different robust estimations: least absolute deviation, Lorentzian minimization and Pearson VII Limit minimization. Its built-in equation set includes a wide array of linear and nonlinear models for any application:

- Linear equations,
- Polynomial and rational functions,
- Logarithmic and exponential functions,
- Non-linear peak functions,
- Non-linear transition functions,
- Non-linear exponential and power equations,
- User-defined functions (up to 15).

It contains 453,697,387 built-in equations. Data input is up to 16,384 points in data table, 16.4 million points can be filtered into table using an averaging digital import filter. Visualization: up to 90,000 vertices can be plotted, resulting in ultra-high 3D surface resolution.

Stiffeners are rolled universal I-beams (UB), their properties are given in the catalogue of Profil Arbed [28].

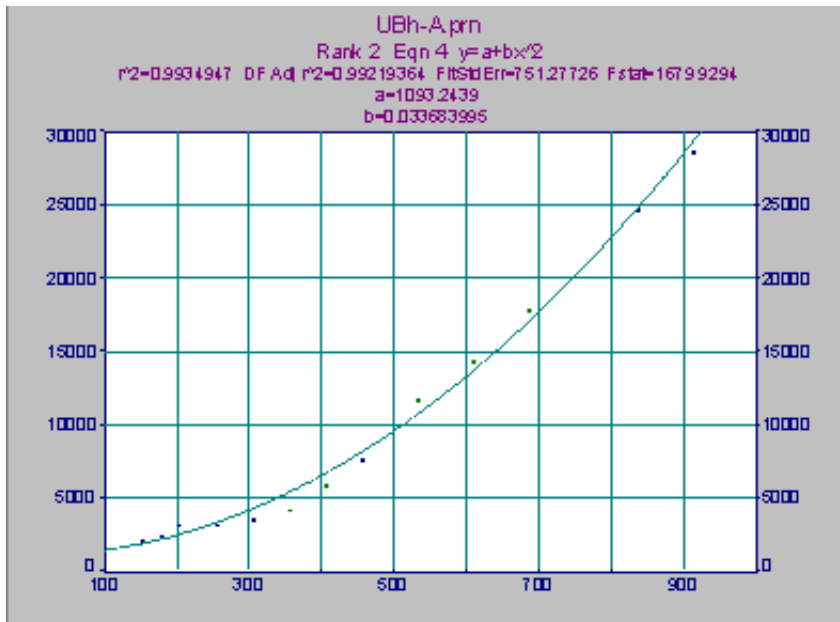
All parameters of the UB section are calculated in function of the height of the profile.

The cross sectional area is calculated in the following way. Table 1 shows the given data for A and h_s .

Table 1. Data for A and h_s

h (mm)	A (mm ²)	h (mm)	A (mm ²)
152	2032	457	7623
178	2426	533	11740
203	3197	610	14390
254	3204	686	17840
305	3588	838	24680
356	4213	914	28560
406	5864		

TableCurve 2D gives several approximations. The one we have chosen is shown in Figure 4.

Figure 4. Curve fitting of A in the function of h_s

$$A = a + bh_s^2 \quad (4.18)$$

where the accuracy of the approximation is $r^2 = 0.99349$, $a = 1093.2439$ and $b = 0.0336839$.

The moment of inertia is as follows

$$\ln(I_y) = a + \frac{b}{\ln(h_s)}. \quad (4.19)$$

Here $r^2 = 0.99984798$, $a = 45.0061779$, $b = -156.528802$.

The web thickness of a stiffener can be approximated in the following way

$$t_f = \sqrt{a + bh_s^2}, \quad (4.20)$$

where $r^2 = 0.98995121$, $a = 34.55256581$ and $b = 0.000651875$.

The flange width of stiffener can be calculated by

$$b_f = \sqrt{a + bh_s^2}, \quad (4.21)$$

where $r^2 = 0.954195679$, $a = 4676.099669$ and $b = 0.111592698$.

Time of plate forming into cylindrical shape (T) can be calculated in function of radius (R) and the plate thickness (t). The forming time is given as a 3D function

$$\ln(T) = a + \frac{b}{t^{0.5}} + cR^{0.5} \quad (4.22)$$

and given in details in equation (4.25).

The industrial data of the Hungarian manufacturing company (Jászberényi Aprítógépgyár, Crushing Machine Factory, Jászberény) are given in Table 2.

Table 2. Plate forming time T (min) in the function of radius R (mm) and thickness t (mm)

t	R	T									
4	1500	145.4	10	1500	348.8	20	1500	485.0	30	1500	611.0
4	1700	151.0	10	1700	352.2	20	1700	490.3	30	1700	619.1
4	2000	161.4	10	2000	366.6	20	2000	507.3	30	2000	643.4
6	1500	211.0	10	2300	379.2	20	2300	525.3	30	2300	666.8
6	1700	220.5	10	2500	386.4	20	2500	536.1	30	2500	687.5
6	2000	229.0	10	3000	401.8	20	3000	556.5	30	3000	713.0
6	2300	236.2	10	3500	420.0	20	3500	579	30	3500	744.0
6	2500	244.3	15	1500	414.2	25	1500	561	40	1500	681.0
8	1500	280.5	15	1700	417.7	25	1700	569.1	40	1700	689.1
8	1700	286.2	15	2000	432.9	25	2000	593.4	40	2000	713.4
8	2000	297.2	15	2300	446.4	25	2300	616.8	40	2300	736.8
8	2300	303.5	15	2500	455.4	25	2500	637.5	40	2500	757.3
8	2500	312.5	15	3000	472.4	25	3000	663	40	3000	783.0
8	3000	325.0	15	3500	490.5	25	3500	694	40	3500	814
8	3500	336.5									

4.4. Cost function. The cost function includes the material, fabrication and painting costs [30]. The fabrication costs are calculated by the time of the process.

The fabrication sequence is the following:

Fabrication of 5 shell elements of length 3 m without stiffeners. For one shell element 2 axial butt welds are needed (GMAW-C) (K_{F1}). The cost of forming of a shell element into the cylindrical shape is also included (K_{F0}).

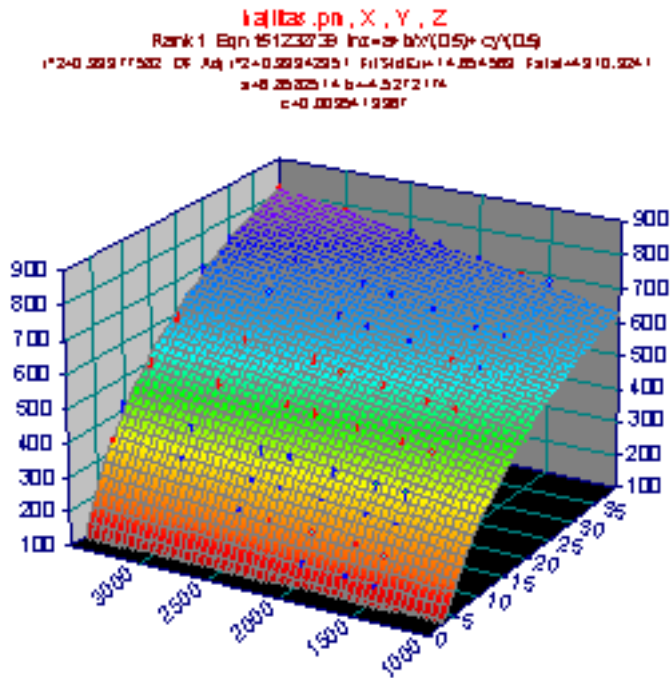


Figure 5. Curve fitting of plate forming time (T) in function of radius ($1500 < R < 3500$) and thickness ($4 < t < 40$)

Welding of the whole unstiffened shell from 5 elements with 4 circumferential butt welds (K_{F2}).

The preparation of longitudinal stiffeners depends on the type of stiffener. When rolled I profiles are used, no preparation cost should be considered.

Welding of n_s stiffeners into the shell with double-sided GMAW-C fillet welds. Number of fillet welds is $2n_s$. (K_{F3}).

4.4.1. *The material cost is for the shell and the stiffeners.*

$$K_M = k_{M1}5\rho V_1 + k_{M2}\rho n_s A_s L \quad (4.23)$$

where V_1 is the volume of the shell, t is shell thickness, $V_1 = 3000 \times 2R\pi t$; $\rho = 7.85 \times 10^{-6} \text{ kgmm}^{-3}$.

The shell and stiffener material costs can be different, but we use approximately the following values: $k_{M1} = 1.0 \text{ \$/kg}$, $k_{M2} = 1.0 \text{ \$/kg}$.

4.4.2. *The fabrication cost can be expressed as.*

$$K_f = k_f \sum_i T_i, \quad (4.24)$$

where K_f [\$] is the fabrication cost, k_f [\$/min] is the corresponding fabrication cost factor, T_i [min] are production times. It is assumed that the value of k_f is constant for a given manufacturer. If not, it is possible to apply different fabrication cost factors simultaneously in Equation (4.24).

The corresponding fabrication cost is as follows: $k_F = 1.0$ \$/min.

4.4.3. *Plate forming cost to reach the necessary curvature.*

$$K_{F0} = k_F \Theta e^\mu; \quad \mu = 6.8582513 - 4.527217t^{-0.5} + 0.009541996 (2R)^{0.5} \quad (4.25)$$

Butt welding cost for one shell element

$$K_{F1} = k_F \left[\Theta \sqrt{\kappa \rho V_1} + 1.3 \times 0.1520 \times 10^{-3} t^{1.9358} (2 \times 3000) \right], \quad (4.26)$$

where Θ is a difficulty factor expressing the complexity of the assembly and κ is the number of elements to be assembled

$$\kappa = 2; V_1 = 2R\pi t \times 3000; \quad \Theta = 2. \quad (4.27)$$

Welding cost of the whole unstiffened shell

$$K_{F2} = k_F \left(\Theta \sqrt{25\rho V_1} + 1.3 \times 0.1520 \times 10^{-3} t^{1.9358} \times 4 \times 2R\pi \right). \quad (4.28)$$

Cost of welding of stiffeners into the shell

$$K_{F3} = k_F \left(\Theta \sqrt{(n_s + 1) \rho V_2} + 1.3 \times 0.3394 \times 10^{-3} a_W^2 2Ln_s \right). \quad (4.29)$$

The fillet weld size $a_w = 0.5t$, $a_{wmin} = 3$ mm.

$$V_2 = 5V_1 + n_s A_s L. \quad (4.30)$$

The cost of painting is

$$K_P = k_P (4R\pi L + (2h + 3b)n_s L); \quad k_P = 14.4 \times 10^{-6} \$/mm^2. \$/mm^2. \quad (4.31)$$

The total cost is

$$K = K_M + 5K_{F1} + 5K_{F0} + K_{F2} + K_{F3} + K_P. \quad (4.32)$$

5. Results

The optimization is made considering 3 unknowns (h_s , n_s , t), 3 non-linear constraints (shell buckling, stringer panel buckling, horizontal displacement). For single-objective optimization the *total cost* (1st) is considered. For multiobjective optimization the different parts of the total cost are also considered as independent cost functions: *material cost of the structure* (2nd), *one shell element butt-welding cost and plate forming cost* (3rd), *welding cost of the whole unstiffened shell and the stiffeners into the shell* (4th), *painting cost* (5th). The discrete value step for h_s is 10 mm, for n_s and t is 1 member, or mm.

Table 3 shows the optima determined by PSO changing the number of particles. It shows that one particle can find an optimum. Increasing the number, the reliability of the technique is better, but the computational time also increases. The ‘best’ solution (in boldface) is the smallest number of particle that finds the minimum.

Table 3. Different optima using different numbers of particles at PSO

Number of particles	Height of stiffener (mm)	Number of stiffener	Thickness of shell (mm)	Cost of the structure (\$)
1	730	18	18	118693
2	730	20	16	116993
3	790	18	16	116975
4	760	19	16	117119
5	760	19	16	117119
10	750	19	16	115841
16	750	20	15	113424
20	750	20	15	113424
30	750	20	15	113424
60	750	20	15	113424
90	780	20	14	115266
120	780	20	14	115266
150	750	20	15	113424
300	780	20	14	115266
500	780	20	14	115266

Changing the limit for the number of stiffeners to $n_s < 30$ instead of 20, the results can be seen on Table 4. In this case the stiffeners get closer, their welding is more difficult, or can be impossible.

Table 4. Different optima using different number of particles at PSO with larger limit for n_s

Number of particles	Height of stiffeners (mm)	Number of stiffeners	Thickness of shell (mm)	Cost of the structure (\$)
3	700	24	13	111385
16	600	34	10	110502
90	630	29	12	112547

The Particle Swarm Optimizer has been built into an interactive decision support program system [24], which contains the following single objective optimization methods

Flexible Tolerance (FT) method of Himmelblau [31],
 Direct Random Search (DRS),
 Hillclimb (HI) method of Rosenbrock [32],
 Davidon-Fletcher-Powell (DFP) method [33],
 Particle Swarm Optimization (PSO) [34, 35].

The efficiencies of these methods are different. All of them use the same objective, constraint subroutines. For a problem like this, which is highly non-linear, several local minima exist. They find different ones. The advantage of Particle Swarm Optimization is that it can find optimum for a nonconvex problem. It has found the minimum cost structure. Table 5 shows the single objective optima.

Table 5. Different optima using different single objective optimization techniques

Method	h_s (mm)	n_s	t (mm)	Cost of the structure (\$)
Flexible tolerance	890	15	16	115871
Direct random search	890	13	22	129496
Hillclimb	890	15	16	115871
Davidon Fletcher Powell	890	13	22	129496
Particle Swarm Optimization	750	19	16	115841

The interactive decision support program system contains several multiobjective optimization methods. They are the following:

Min-max method,
 Global criterion method: type - 1,
 Global criterion method: type - 2,
 Weighted min-max method,
 Weighted global criterion method,
 Pure weighting method,
 Normalized weighting method.

A description of methods is available in Jármai [24]. Weighting coefficients are similar to all five objectives 0.2 each.

The objective functions are as follows:

Total cost of the structure in \$, K (1^{st}),

Material cost of the structure in \$, K_m (2^{nd}),

Cost of forming and welding of shell elements in \$, $5(K_0 + K_1)$ (3^{rd}),

Welding cost of stiffeners in \$, $K_2 + K_3$ (4^{th}),

Painting cost in \$, K_p (5^{th}).

Table 6 shows the different multiobjective optima. The material cost is dominating, being 50-70 % of the total cost. The other three objectives are around 12-25 %. The height of stiffener is nearly the same for all optima; the number of stiffeners and the shell thickness changes in an opposite way due to the necessary stiffness. The greatest conflict is between the total and the painting costs. The painting cost minimum gives the greatest shell thickness t .

Table 6. Multiobjective optima for the stringer stiffened shell

Method	h_s (mm)	n_s	t (mm)	1 st	2 nd	3 rd	4 th	5 th
1 st	880	17	14	116321.5	73565.8	12479.9	15466.7	14809.0
2 nd	890	13	22	129496.9	72627.2	17019.6	27260.2	12589.6
3 rd	890	20	11	118337.9	80464.4	10488.7	10719.9	16664.8
4 th	890	14	20	126678.2	73160.2	15947.7	24398.3	13171.8
5 th	890	11	26	134433.7	71561.2	19104.7	32342.3	11425.3
Min-max	860	17	16	121579.8	73956.7	13693.1	19339.2	14590.5
Global type I	880	19	12	117610.2	77228.8	11180.3	13240.5	15960.5
Global type II	880	16	16	119443.6	73103.0	13693.1	18414.1	14233.3
Weighted Min-max	860	17	16	121579.8	73956.7	13693.1	19339.2	14590.5
Weighted global	880	16	16	119443.6	73103.0	13693.1	18414.1	14233.3
Pure weighting	880	17	14	116321.5	73565.8	12479.9	15466.7	14809.0
Normalized weighting	880	19	12	117610.2	77228.8	11180.3	13240.5	15960.5

6. Conclusions

The particle swarm method is an efficient tool of structural optimization. It can find the global optimum for the problems where the constraints are highly nonlinear, where the feasible region is nonconvex. The algorithm was modified to find discrete values for practical problems. PSO has been built into an interactive program system, which contains other optimization techniques, like Flexible tolerance, Complex, Hillclimb, Davidon-Fletcher-Powell and Direct random search. The efficiency of PSO is shown on a stiffened shell design problem, where there are stringer stiffeners and its loading is compression and bending. The multiobjective optimization gives several optima, considering five objectives, the total cost and the cost elements at the same time. There are conflicts between the objective functions and the different minima of objectives mean different structural sizes and numbers of stiffeners.

Acknowledgement. The research work was supported by the Hungarian Scientific Research Foundation grants OTKA T38058 and T37941. The project was also supported by the Hungarian-South African Intergovernmental S&T Co-operation program. The Hungarian partner is the Ministry of Education, R&D Deputy Undersecretary of State, the South African partner is the Foundation for Research Development. The help of Mr. Derren Wood from the University of Pretoria is gratefully acknowledged in the Particle Swarm Optimization algorithm with the dynamic inertia reduction version.

References

1. FARKAS, J., AND JÁRMAI, K.: *Analysis and optimum design of metal structures*. Balkema Publishers, Rotterdam, Brookfield, ISBN 90 5410 669 7, 1997.
2. BOX, M. J.: A new method of constrained optimization and a comparison with other methods. *Computer Journal*, **8** (1965), 42–52.
3. JARMAI, K.: *Topology optimization of tubular structures*, June 1-6. 1998. 5 lectures, Mechanics and Design of Tubular Structures, Advanced Professional School, Coordinated by J. Farkas & K. Jármai, International Centre for Mechanical Science, CISM; Udine, Italy, in K. Jármai and J. Farkas (eds.), Springer Verlag, Chapter 5. 225-284. ISBN 3-211-83145-2, 1998.
4. FARKAS, J., JÁRMAI, K., SNYMAN, J. A., and GONDOS, GY.: Minimum cost design of ring-stiffened welded steel cylindrical shells subject to external pressure, in Lamas, A., and Simoes da Silva, (eds.) Proc. 3rd European Conf. Steel Structures, Coimbra, 2002, Universidade de Coimbra, 2002, pp. 513-522.
5. OSY CZKA, A.: *Multicriterion optimization in engineering*. Ellis Horwood Limited, Chichester, 1984.
6. GOLDBERG, D. E.: *Genetic algorithms in search, optimization & machine learning*. Addison-Wesley Publ. Company, Inc., 1989.
7. STORN, R.: Constrained optimization. *Dr. Dobb's Journal*, May, (1995), 119-123.
8. STORN, R., AND PRICE, K.: *Differential evolution – simple and efficient adaptive scheme for global optimization over continuous spaces*. Technical Report TR-95-012, ICSI, 1995.
9. KENNEDY, J. and EBERHART, R. C.: Particle swarm optimization, Proceedings of the 1995 IEEE International Conference on Neural Networks, Perth, Australia, IEEE Service Center, Piscataway, NJ, vol. 4., 1995, pp. 1942-1948.
10. DORIGO, M., MANIEZZO, V., AND COLORNI, A.: The ant system: Optimization by a colony of cooperating agents, *IEEE Transactions on Systems, Man, and Cybernetics–Part B*, **26** (1), (1996), 1-13.
11. DORIGO, M., DI CARO, G. and GAMBARDELLA, L. M.: Ant algorithms for discrete optimization. *Artificial Life*, **5** (3), (1999), 137-172.
12. SNYMAN, J. A.: A new and dynamic method for unconstrained minimization. *Appl. Math. Modelling*, **6**, (1982), 449-462.
13. SNYMAN, J. A.: An improved version of the original leap-frog method for unconstrained minimization. *Appl. Math. Modelling*, **7**, (1983), 216-218.
14. SNYMAN, J. A.: The LFOPC leap-frog method for constrained optimization. *Comp. Math. Applic.*, **40**, (2000), 1085-1096.

15. MILLONAS, M. M.: *Swarms, phase transitions, and collective intelligence*. in Langton, C.G., (ed) *Artificial Life III*. Addison Wesley, Reading, MA., 1994.
16. KENNEDY, J.: The particle swarm: social adaptation of knowledge, *Proceedings of the International Conference on Evolutionary Computation*, IEEE, Piscataway NJ, 1977, pp. 303-308.
17. KENNEDY, J. and SPEARS, W. M.: Matching algorithms to problems: an experimental test of the particle swarm and some genetics algorithms on the multimodal problem generator, *Proceedings of the 1998 IEEE International Conference on Evolutionary Computation*, Anchorage, AK (USA), 4-9 May 1998 IEEE, New York, 1998, pp. 78-83.
18. KENNEDY, J.: Stereotyping: Improving Particle Swarm Performance with Cluster Analysis, *Proc. of the 2000 Congress on Evolutionary Computation*, IEEE Service Center, Piscataway, NJ, 2000, pp. 1507-1512.
19. LOVBJERG, M., RASMUSSEN, T. K. and KRINK, T.: Hybrid Particle Swarm Optimiser with Breeding and Subpopulations, *Proceedings of the third Genetic and Evolutionary Computation Conference (GECCO-2001)*, 2001, pp 469-476.
20. FOURIE, P. C. and GROENWOLD, A. A.: Particle swarm in size and shape optimisation, *International Workshop on Multidisciplinary Design Optimization*, 7-10, Aug. 2000, Pretoria, South Africa, *Proceedings*, 2000, pp. 97-106.
21. FOURIE, P. C. and GROENWOLD, A. A.: Particle Swarms in Topology Optimization, *World Congress on Structural and Multidisciplinary Optimization*, Liaoning Electronic Press, *Proceedings on CD file Paper No. 113*, 2002, 6 p.
22. BOLTON, H. P. J., SCHUTTE, J. F. and GROENWOLD, A. A.: Multiple Parallel Local Searches in Global Optimization, *Recent advances in parallel virtual machine and message passing interface*, Balatonfüred, Hungary, in Dongarra, J., Kacsuk, P. and Podhorszki, N. (eds.), 2000, pp. 88-95.
23. KOVÁCS, GY., GROENWOLD, A., A., JÁRMAI, K. and FARKAS, J.: Analysis and optimum design of fiber reinforced composite structures. *Structural and Multidisciplinary Optimization*, (2004) (under publication)
24. JÁRMAI, K.: Single- and multicriteria optimization as a tool of decision support system. *Computers in Industry*. Elsevier Applied Science Publishers, **11**(3), (1989) 249-266.
25. DET NORSKE VERITAS (DNV): *Buckling strength analysis*. Classification Notes No.30.1., Hovik, Norway, 1995.
26. ECCS European Recommendations for Steel Construction, *Buckling of steel shells*. No.56. (1988), European Convention for Constructional Steelwork, Brussels
27. *TableCurve 2D*: Users' manual, Systat Software Inc., 2003.
28. *TableCurve 3D*: Users' manual Systat Software Inc., 2003.
29. *Profil Arbed Sales program*, Structural shapes. Arcelor Long Commercial, 2001.
30. JÁRMAI, K. and FARKAS, J.: Cost calculation and optimization of welded steel structures. *Journal of Constructional Steel Research*, **50**, (1999), 115-135.
31. HIMMELBLAU, D. M.: *Applied nonlinear programming*. Mc Graw-Hill Book Co., New York, 1971.
32. ROSENBROCK, H. H.: An automatic method for finding the greatest or least value of a function. *Computer Journal*, **3**, (1960), 175-184.

33. RAO, S. S.: *Optimisation theory and applications*. Wiley Eastern Limited, New Delhi, 1984.
34. FARKAS, J. and JÁRMAI, K.: *Economic Design of Metal Structures*. Millpress, Rotterdam, ISBN 90 77017 99 2, 2003.
35. JÁRMAI, K., FARKAS, J. and VIRÁG, Z.: Minimum cost design of ring-stiffened cylindrical shells subject to axial compression and external pressure, 5th World Congress on Structural and Multidisciplinary Optimization, Lido di Jesolo, Italy, Schöenfeld & Ziegler, Italian Polytechnic Press, Milano, ISBN 88-88412-18-2, Proceedings, 2003, pp. 63-64.

TENSORS OF FINITE ROTATIONS AND SMALL STRAINS ON THE MIDDLE SURFACE OF A SHELL

IMRE KOZÁK

Department of Mechanics, University of Miskolc
3515 Miskolc-Egyetemváros, Hungary
mechkoz@uni-miskolc.hu

[Received: June 9, 2004]

Dedicated to István Páczelt on the occasion of his 65th birthday

Abstract. On the middle surface of the shell, the displacements as well as the rotations of the base vectors are finite, the strains are, however, considered to be infinitesimally small. The rotation of the base vectors is described by three rotation tensors that define three special, geometrically well identified rotations. This paper derives the three-dimensional Green-Lagrange strain tensor and the symmetric right Jaumann strain tensor on the middle surface.

Mathematical Subject Classification: 74K25

Keywords: non-linear shell theory, finite rotations, small strains, middle surface

1. Introduction

Shell theories are two-dimensional theories that have an approximate nature with respect to the three-dimensional theories of solid bodies. This approximate nature arises from the special geometry of shells and from the description of the deformation and boundary conditions of the shell-like body, which are usually expressed through different hypotheses and neglections.

Topics related to the theories of shells seem to be always topical, especially from the point of view of the numerical analysis of shell problems. This is well demonstrated by the following two citations: "*Shell structures may be called the prima donnas of structures.*" by Chapelle and Bathe (1998, [1]), and "*The modelling of shell structures represents a challenging task since the early developments of the finite element method.*" by Valente et al. (2003, [2]).

The topic of this paper is related to the kinematics of non-linear shell theories in which the middle surface of the shell has a distinguished role. This is expressed through the description of both the deformation of the middle surface and the deformations along the normal to the middle surface.

The main goal of the present paper is to derive the Green-Lagrange and the Jaumann strain tensors on the middle surface of the shell. The derivation is based on the non-linear theory of three-dimensional deformation of continuum mechanics and on the introduction of kinematical hypotheses.

In the investigations it is assumed that the middle surface of the shell is sufficiently smooth, quantities defined on it are continuous and continuously differentiable with respect to the surface parameters as many times as required.

The independent variables on the middle surface of the shell in this paper are the displacements, the rotation tensors (including the drilling rotation, i.e. the rotation about the normal to the middle surface), and the transverse normal strain, which represent seven independent parameters in all.

The primary goal is to derive the three-dimensional deformation gradient tensor and the three-dimensional Green-Lagrange strain tensor *on the middle surface of the shell* with the assumption that the displacements as well as the rotations of the base vectors are finite, the strains at the points of the middle surface and across the thickness of the shell are, however, infinitesimally small.

The finite rotations of the base vectors on the middle surface are described by three rotation tensors. These tensors define three *special rotations* which are geometrically well identified. Two rotation tensors describe the finite rotation of the base vectors (including the drilling rotation) in such a case when the middle surface normal to, and the tangential base vectors of, the reference middle surface are mapped into the middle surface normal to, and the tangential base vectors of the deformed middle surface. The third rotation tensor describes an infinitesimal rotation of the already deformed base vectors, ensuring that the transverse shear strains be, according to our primary goals, infinitesimally small.

Considering the above assumptions, the secondary goal is to derive the three-dimensional, symmetric right Jaumann strain tensor *on the middle surface of the shell*, utilizing the polar decomposition of the three-dimensional deformation gradient tensor.

The third goal is to present, in an exemplary manner, the derivation of the three-dimensional deformation gradient tensor and the Green-Lagrange strain tensor *at an arbitrary point of the shell*, making use of the previous results and from the point of view of shell theories based on the Reissner-Mindlin hypothesis.

In the majority of shell theories applying finite rotations to describe the deformation of the shell, the rotation tensors are defined, just like in this paper, on the middle surface. In those theories the middle surface strains can be finite or infinitesimally small. The transverse shear strains are usually taken into account, which is not, however, the case for transverse normal strains. In what follows, a brief review of shell theories without completeness is given from the point of view of finite rotations.

The concept of finite rotation tensor to develop a nonlinear shell theory has been introduced by Simmonds and Danielson [3],[4]. Wriggers and Gruttmann [5] discuss a finite element model for shells subjected to finite rotations. A detailed analysis on the

role of drilling rotations in non-linear shell theories has been given in the significant papers by Ibrahimbegovich [6], Ibrahimbegovich and Frey [7],[8]. Pietraszkiewicz [9],[10] has developed a general, geometrically non-linear shell theory using the drilling rotations.

Wisniewski [11] investigated the rotation tensor with respect to the derivation of the Green-Lagrange strain tensor, obtained directly from the deformation gradient tensor, and the Jaumann strain tensor, obtained through the polar decomposition of the deformation gradient tensor.

Brank et al. [12],[13], Ibrahimbegovich et al. [14], Brank and Ibrahimbegovich [15], Ibrahimbegovich et al. [16], Lee and Lee [17] derived geometrically exact shell theories without using the drilling rotations.

Atluri et al. [18] pointed out that the use of the drilling rotation as an independent variable in shell structures with faceted joints has special significance.

Campello et al. [19] applied a geometrically exact six-parameter non-linear shell theory to develop a shell finite element.

Bertóti [20] developed a three-dimensional non-linear shell theory using the equilibrated stress field and the rotation field.

Aside from the above aspects, the possibilities and requirements of the application of the finite element method are not investigated in this paper. In this respect we refer to the papers by Parisch [21], Basar and Ding [22], Bischoff and Ramm [23], Sansour and Kollmann [24], as well as the papers by Bucleam and Bathe [25] and Bathe et al. [26].

Section 2 introduces the notation and gives a summary of the basic relations applied in the paper, among them the representation of the rotation tensor using the Rodrigues formula. Section 3 introduces important assumptions with respect to the rotation of the base vectors and the measures of strains on the middle surface, then defines three rotation tensors and gives their geometric interpretations. Making use of the above results, Section 4 derives the three-dimensional deformation gradient tensor, the Green-Lagrange strain tensor and the symmetric right Jaumann strain tensor obtained through the polar decomposition of the deformation gradient tensor. Section 5 presents, as an example, the derivation of the three-dimensional deformation gradient tensor and the Green-Lagrange strain tensor at arbitrary points of the shell, employing the Reissner-Mindlin hypothesis.

2. Notations. Fundamental relations

2.1. Both invariant and indicial notations of tensor analysis are used. Scalar variables are denoted by italic normal letters. When *invariant notation* is applied, vector variables are denoted by upright boldface letters, tensor variables by italic boldface letters. The dyadic (tensorial) product has no special sign (e.g. $\mathbf{a}^1 \mathbf{a}_1$), the scalar product is denoted by a dot (e.g. $\mathbf{R} \cdot \mathbf{a}_1$), the vector product is denoted by a cross sign (e.g. $\mathbf{a}_1 \times \mathbf{a}_2$). When *indicial notation* is applied, the range of Latin indices is

1, 2, 3, the range of Greek indices is 1, 2. The usual summation convention is applied over the repeated indices. A comma followed by an index in the right subscript denotes partial differentiation, whereas a semicolon indicates covariant differentiation. The so called *marking indices* are underlined and they do not have the range 1, 2, 3 (e.g. $e_{\underline{s}}^m$). The unit tensor is denoted by \mathbf{I} , δ_i^k is the Kronecker delta, ϵ_{klm} is the covariant permutation tensor and e_{klm} is the covariant permutation symbol. The transpose of a tensor is denoted by a "T" in the right superscript (e.g. \mathbf{R}^T).

2.2. Let the shell, as a three-dimensional solid body, be denoted by (B) in the *reference configuration*, and by (\bar{B}) in the *deformed configuration*. The reference configuration is assumed to be stress- and deformation-free. The middle surface of the shell and its surface element in (B) are denoted by (S_o) and (dS_o) , whereas in (\bar{B}) they are denoted by (\bar{S}_o) and $(d\bar{S}_o)$.

A *convected* (x^1, x^2, x^3) coordinate system is employed, where x^1, x^2 are the surface coordinates on the middle surface (S_o) . The coordinate line x^3 is perpendicular to (S_o) in (B) and $x^3 = 0$ on both (S_o) and (\bar{S}_o) . In (\bar{B}) x^3 is not necessarily straight and perpendicular to (\bar{S}_o) .

Total Lagrangian description is applied throughout this paper.

Quantities and geometrical forms in the deformed configuration are distinguished by a bar, in the reference configuration they have no special sign.

On (S_o) and (\bar{S}_o) (at $x^3 = 0$), the value of a quantity defined at an arbitrary point of coordinate x^3 is denoted by a sign "o" in the right subscript, i.e.,

$$\mathbf{u} = \mathbf{u}(x^1, x^2, x^3), \quad \text{but} \quad \mathbf{u}_o = \mathbf{u}(x^1, x^2, x^3 = 0).$$

Quantities defined only at $x^3 = 0$ are written without the sign "o", e.g.,

$$\mathbf{a}_\alpha = \mathbf{a}_\alpha(x^1, x^2), \quad \text{or} \quad \bar{\mathbf{n}} = \bar{\mathbf{n}}(x^1, x^2).$$

2.3. The middle surface of the shell together with the basic geometrical quantities are shown in Figure 1 (see also Subsection 5.1 and Figure 4).

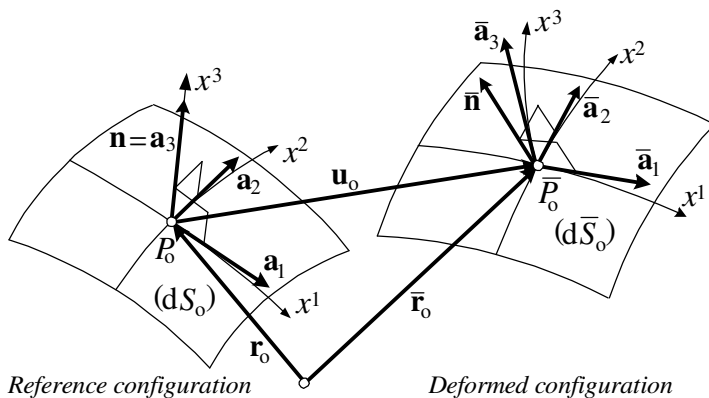


Figure 1.

At point P_o of the *middle surface* (S_o) in the *reference configuration*, the unit normal vector is denoted by \mathbf{n} , $|\mathbf{n}| = 1$, the position vector is $\mathbf{r}_o(x^1, x^2)$, the covariant base vectors are $\mathbf{a}_\alpha = \mathbf{r}_{o,\alpha}$ and $\mathbf{a}_3 = \mathbf{n}$, the metric tensor is $a_{kl} = \mathbf{a}_k \cdot \mathbf{a}_l$ ($a_{\alpha 3} = 0$, $a_{33} = 1$) and its determinant is denoted by a , the curvature tensor of the middle surface is $b_{\kappa\lambda} = -\mathbf{a}_\kappa \cdot \mathbf{a}_{3,\lambda}$, the contravariant base vectors are \mathbf{a}^m , and the inverse of the metric tensor is $a^{mn} = \mathbf{a}^m \cdot \mathbf{a}^n$ ($a^{\mu 3} = 0$, $a^{33} = 1$). The following relations hold:

$$\mathbf{a}_3 = \frac{\mathbf{a}_1 \times \mathbf{a}_2}{|\mathbf{a}_1 \times \mathbf{a}_2|} = \mathbf{n}, \quad |\mathbf{a}_3| = 1, \quad a = \det a_{\alpha\beta} = a_{11}a_{22} - a_{12}a_{21}, \quad (2.1)$$

$$|\mathbf{a}_1 \times \mathbf{a}_2|^2 = (\mathbf{a}_1 \times \mathbf{a}_2) \cdot (\mathbf{a}_1 \times \mathbf{a}_2) = a, \quad \mathbf{a}^\alpha = a^{\alpha\beta} \mathbf{a}_\beta, \quad \mathbf{a}^3 = \mathbf{a}_3. \quad (2.2)$$

At point (\bar{P}_o) of the *middle surface* (\bar{S}_o) in the *deformed configuration*, the unit normal vector is $\bar{\mathbf{n}}$, $|\bar{\mathbf{n}}| = 1$, the position vector is $\bar{\mathbf{r}}_o(x^1, x^2)$, the covariant base vectors are $\bar{\mathbf{a}}_\alpha = \bar{\mathbf{r}}_{o,\alpha}$ and $\bar{\mathbf{a}}_3$ (it is assumed that $\bar{\mathbf{a}}_3 \neq \bar{\mathbf{n}}$), the surface part of the metric tensor is $\bar{a}_{\alpha\beta} = \bar{\mathbf{a}}_\alpha \cdot \bar{\mathbf{a}}_\beta$ and its determinant is denoted by \bar{a} , the curvature tensor of the middle surface is $\bar{b}_{\kappa\lambda} = -\bar{\mathbf{a}}_\kappa \cdot \bar{\mathbf{n}}_{,\lambda}$. The following relations hold:

$$\bar{\mathbf{n}} = \frac{\bar{\mathbf{a}}_1 \times \bar{\mathbf{a}}_2}{|\bar{\mathbf{a}}_1 \times \bar{\mathbf{a}}_2|}, \quad \bar{a} = \det \bar{a}_{\alpha\beta} = \bar{a}_{11}\bar{a}_{22} - \bar{a}_{12}\bar{a}_{21}, \quad (2.3)$$

$$|\bar{\mathbf{a}}_1 \times \bar{\mathbf{a}}_2|^2 = (\bar{\mathbf{a}}_1 \times \bar{\mathbf{a}}_2) \cdot (\bar{\mathbf{a}}_1 \times \bar{\mathbf{a}}_2) = [(\bar{\mathbf{a}}_1 \times \bar{\mathbf{a}}_2) \times \bar{\mathbf{a}}_1] \times \bar{\mathbf{a}}_2 = \bar{a}. \quad (2.4)$$

2.4. Let $\mathbf{u}_o(x^1, x^2) = u_o^k \mathbf{a}_k$ be the displacement field on the middle surface (S_o). Then

$$\bar{\mathbf{r}}_o = \mathbf{r}_o + \mathbf{u}_o \quad \text{and} \quad \bar{\mathbf{a}}_\alpha = \bar{\mathbf{r}}_{o,\alpha} = \mathbf{a}_\alpha + \mathbf{u}_{o,\alpha} = (\delta_\alpha^m + u_{o;\alpha}^m) \mathbf{a}_m \quad (2.5)$$

on (\bar{S}_o). The deformation gradient tensor is

$$\mathbf{F}_o = \bar{\mathbf{a}}_k \mathbf{a}^k = \bar{\mathbf{a}}_\kappa \mathbf{a}^\kappa + \bar{\mathbf{a}}_3 \mathbf{a}^3, \quad \mathbf{F}_o \cdot \mathbf{a}_k = \bar{\mathbf{a}}_k, \quad (2.6)$$

i.e.

$$d\bar{\mathbf{r}}_o = \mathbf{F}_o \cdot d\mathbf{r}_o = \mathbf{F}_o \cdot \mathbf{a}_k dx^k = \bar{\mathbf{a}}_k dx^k. \quad (2.7)$$

The Green-Lagrange strain tensor assumes the form

$$\begin{aligned} \mathbf{E}_o &= E_{okl} \mathbf{a}^k \mathbf{a}^l = \frac{1}{2} \left(\mathbf{F}_o^\top \cdot \mathbf{F}_o - \mathbf{I} \right) = \frac{1}{2} [(\bar{\mathbf{a}}_k \cdot \bar{\mathbf{a}}_l) - (\mathbf{a}_k \cdot \mathbf{a}_l)] \mathbf{a}^k \mathbf{a}^l = \\ &= \frac{1}{2} [(\bar{\mathbf{a}}_\kappa \cdot \bar{\mathbf{a}}_\lambda - a_{\kappa\lambda}) \mathbf{a}^\kappa \mathbf{a}^\lambda + (\bar{\mathbf{a}}_\kappa \cdot \bar{\mathbf{a}}_3) \mathbf{a}^\kappa \mathbf{a}^3 + (\bar{\mathbf{a}}_3 \cdot \bar{\mathbf{a}}_\lambda) \mathbf{a}^3 \mathbf{a}^\lambda + (\bar{\mathbf{a}}_3 \cdot \bar{\mathbf{a}}_3 - 1) \mathbf{a}^3 \mathbf{a}^3]. \end{aligned} \quad (2.8)$$

According to (2.3)-(2.5), the unit normal vector to the middle surface (\bar{S}_o) is

$$\bar{\mathbf{n}} = \bar{n}_m \mathbf{a}^m = \frac{1}{\sqrt{\bar{a}}} \bar{\mathbf{a}}_1 \times \bar{\mathbf{a}}_2 = \frac{1}{\sqrt{\bar{a}}} (\mathbf{a}_1 + \mathbf{u}_{o,1}) \times (\mathbf{a}_1 + \mathbf{u}_{o,2}). \quad (2.9)$$

Components of the normal vector $\bar{\mathbf{n}}$ can be expressed by the components of the gradient of displacement vector, $\mathbf{u}_{o,\alpha}$, as:

$$\bar{n}_1 = \bar{\mathbf{n}} \cdot \mathbf{a}_1 = \frac{1}{\sqrt{a}} [(\mathbf{a}_1 + \mathbf{u}_{o,1}) \times (\mathbf{a}_2 + \mathbf{u}_{o,2})] \cdot \mathbf{a}_1 = -\frac{\sqrt{a}}{\sqrt{a}} [(1 + u_{o,2}^2) u_{o,1}^3 - u_{o,1}^2 u_{o,2}^3], \quad (2.10)$$

$$\bar{n}_2 = \bar{\mathbf{n}} \cdot \mathbf{a}_2 = \frac{1}{\sqrt{a}} [(\mathbf{a}_1 + \mathbf{u}_{o,1}) \times (\mathbf{a}_2 + \mathbf{u}_{o,2})] \cdot \mathbf{a}_2 = -\frac{\sqrt{a}}{\sqrt{a}} [(1 + u_{o,1}^2) u_{o,2}^3 - u_{o,2}^2 u_{o,1}^3], \quad (2.11)$$

$$\begin{aligned} \bar{n}_3 = \bar{\mathbf{n}} \cdot \mathbf{a}_3 &= \frac{1}{\sqrt{a}} [(\mathbf{a}_1 + \mathbf{u}_{o,1}) \times (\mathbf{a}_2 + \mathbf{u}_{o,2})] \cdot \mathbf{a}_3 = \\ &= \frac{\sqrt{a}}{\sqrt{a}} (1 + u_{o,1}^2 + u_{o,2}^2 + u_{o,1}^1 u_{o,2}^2 - u_{o,2}^1 u_{o,1}^2). \end{aligned} \quad (2.12)$$

2.5. Any rotation tensor \mathbf{R} ($\mathbf{R}^{-1} = \mathbf{R}^T$; $\det|\mathbf{R}| = 1$), defined at point P_o of the middle surface (S_o) can be given by the Rodrigues-formula:

$$\mathbf{R} = R^k_l \mathbf{a}_k \mathbf{a}^l = \cos \vartheta \mathbf{I} + (1 - \cos \vartheta) \mathbf{e} \mathbf{e} + \sin \vartheta \mathbf{e} \times \mathbf{I}, \quad (2.13)$$

$$R^k_l = \cos \vartheta \delta_l^k + (1 - \cos \vartheta) e^k e_l + \sin \vartheta a^{ks} \varepsilon_{sml} e^m, \quad (2.14)$$

where $\mathbf{e} = \mathbf{e}(x^1, x^2) = e^m \mathbf{a}_m$, $|\mathbf{e}| = 1$ is the unit vector of the axis of rotation and $-\pi \leq \vartheta(x^1, x^2) \leq \pi$ is the angle of rotation. The rotation tensor is a proper orthogonal tensor. There exist other representations of the rotation tensor \mathbf{R} in the specialist literature.

The rotation tensor \mathbf{R} rotates the arbitrary vector \mathbf{c} into the vector

$$\mathbf{R} \cdot \mathbf{c} = \cos \vartheta \mathbf{c} + (1 - \cos \vartheta) (\mathbf{e} \cdot \mathbf{c}) \mathbf{e} + \sin \vartheta \mathbf{e} \times \mathbf{c}, \quad (2.15)$$

while its transpose, \mathbf{R}^T , rotates \mathbf{c} into the vector

$$\mathbf{R}^T \cdot \mathbf{c} = \mathbf{c} \cdot \mathbf{R} = \cos \vartheta \mathbf{c} + (1 - \cos \vartheta) (\mathbf{e} \cdot \mathbf{c}) \mathbf{e} - \sin \vartheta \mathbf{e} \times \mathbf{c}. \quad (2.16)$$

3. Finite rotations and small strains on the middle surface (S_o)

3.1. Let us introduce, in advance, the rotation tensors $\mathbf{R}^*(x^1, x^2)$ and $\bar{\mathbf{R}}_s(x^1, x^2)$ as well as the following fundamental assumptions:

1. let \mathbf{R}^* rotate the base vectors \mathbf{a}_k into vectors $\bar{\mathbf{k}}_k^*$ by a *finite rotation*:

$$\bar{\mathbf{k}}_k^* = \mathbf{R}^* \cdot \mathbf{a}_k, \quad \text{and let} \quad \bar{\mathbf{k}}_3^* = \mathbf{R}^* \cdot \mathbf{a}_3 = \bar{\mathbf{n}}, \quad (3.1)$$

2. let $\bar{\mathbf{R}}_s$ rotate vectors $\bar{\mathbf{k}}_k^*$ into vectors $\bar{\mathbf{k}}_k$ by an *infinitesimal rotation*:

$$\bar{\mathbf{k}}_k = \bar{\mathbf{R}}_s \cdot \bar{\mathbf{k}}_k^* = \bar{\mathbf{R}}_s \cdot \mathbf{R}^* \cdot \mathbf{a}_k, \quad (3.2)$$

3. let the rotated base vectors $\bar{\mathbf{k}}_k$ and the *infinitesimal strain vectors* $\bar{\alpha}_k(x^1, x^2)$ give the base vectors $\bar{\mathbf{a}}_k$:

$$\bar{\mathbf{a}}_k = \bar{\mathbf{k}}_k + \bar{\alpha}_k, \quad (3.3)$$

4. let $\bar{\mathbf{a}}_3 = \varepsilon_{o3} \bar{\mathbf{k}}_3$, i.e., let the base vector $\bar{\mathbf{a}}_3$ be given by

$$\bar{\mathbf{a}}_3 = \bar{\mathbf{k}}_3 + \varepsilon_{o3} \bar{\mathbf{k}}_3, \tag{3.4}$$

where ε_{o3} is the *infinitesimal* stretch in the normal direction to the middle surface,

5. let the rotation tensor $\bar{\mathbf{R}}_s$, defining an infinitesimal rotation, be given by

$$\bar{\mathbf{R}}_s = \mathbf{I} + \vartheta_s \bar{\mathbf{e}}_s \times \mathbf{I}, \tag{3.5}$$

where $|\vartheta_s| \ll 1$ holds for the angle of rotation and the unit vector of the axis of rotation, $\bar{\mathbf{e}}_s$, is perpendicular to $\bar{\mathbf{n}}$:

$$\bar{\mathbf{e}}_s = e_s^\mu \bar{\mathbf{k}}_\mu^* = \mathbf{R}^* \cdot \left(e_s^\mu \mathbf{a}_\mu \right) = \mathbf{R}^* \cdot \mathbf{e}_s; \quad \mathbf{e}_s = e_s^\mu \mathbf{a}_\mu. \tag{3.6}$$

In the following Subsections **3.2-3.6**, we investigate first the rotation tensor \mathbf{R}^* that fulfills condition (3.1)₂, then, in view of the results of this investigation, \mathbf{R}^* is obtained by the (scalar) product of two rotation tensors ($\mathbf{R}^* = \mathbf{R}_2 \cdot \mathbf{R}_1$), and the geometrical interpretation of these two rotation tensors is given. Next, in Subsection **3.7**, the description of the rotation tensor $\bar{\mathbf{R}}_s$ defined in (3.5) is detailed.

3.2. For a given $\bar{\mathbf{n}}$, we are looking for a rotation tensor \mathbf{R}^* (the angle of rotation ϑ^* and the axis of rotation \mathbf{e}^*) that satisfies assumption (1) with equation (3.1)₂:

$$\bar{\mathbf{k}}_3^* = \mathbf{R}^* \cdot \mathbf{a}_3 = \cos \vartheta^* \mathbf{a}_3 + (1 - \cos \vartheta^*) e_3^* \mathbf{e}^* + \sin \vartheta^* \mathbf{e}^* \times \mathbf{a}_3 = \bar{\mathbf{n}} = \bar{n}_p \mathbf{a}^p.$$

The solution satisfies the following scalar equations:

$$\mathbf{a}_p \cdot \mathbf{R}^* \cdot \mathbf{a}_3 = \cos \vartheta^* a_{3p} + (1 - \cos \vartheta^*) e_3^* e_p^* + \sqrt{a} \sin \vartheta^* e_{ps3} e^{*s} = \bar{n}_p,$$

which, after inserting $e_p^* = a_{pq} e^{*q}$, can be written as

$$(1 - \cos \vartheta^*) e_3^* (a_{11} e^{*1} + a_{12} e^{*2}) + \sqrt{a} \sin \vartheta^* e^{*2} = \bar{n}_1, \tag{3.7}$$

$$(1 - \cos \vartheta^*) e_3^* (a_{21} e^{*1} + a_{22} e^{*2}) - \sqrt{a} \sin \vartheta^* e^{*1} = \bar{n}_2, \tag{3.8}$$

$$\cos \vartheta^* + (1 - \cos \vartheta^*) (e_3^*)^2 = \bar{n}_3. \tag{3.9}$$

With components \bar{n}_p given and, in addition, with an e_3^* chosen, equation system (3.7)-(3.9) has a unique solution for ϑ^* , e^{*1} and e^{*2} (the trivial solution of $\vartheta^* = 0$ is not considered). Indeed, from (3.9) it immediately follows that

$$\cos \vartheta^* = \frac{\bar{n}_3 - (e_3^*)^2}{1 - (e_3^*)^2}, \tag{3.10}$$

whereas e^{*1} and e^{*2} can be obtained from the transformed equations (3.7)-(3.8), using the Cramer-rule:

$$\begin{aligned} (1 - \cos \vartheta^*) e_3^* a_{11} e^{*1} &+ [(1 - \cos \vartheta^*) e_3^* a_{12} + \sqrt{a} \sin \vartheta^*] e^{*2} &= \bar{n}_1 \\ [(1 - \cos \vartheta^*) e_3^* a_{21} - \sqrt{a} \sin \vartheta^*] e^{*1} &+ (1 - \cos \vartheta^*) e_3^* a_{22} e^{*2} &= \bar{n}_2 \end{aligned} .$$

The determinant of this equation system is $d = a \left[(1 - \cos \vartheta^*)^2 (e_3^*)^2 + \sin^2 \vartheta^* \right]$, and its solution reads:

$$e^{*1} = \frac{(1 - \cos \vartheta^*) e_3^* \bar{n}_1 - \frac{1}{\sqrt{a}} \sin \vartheta^* \bar{n}_2}{(1 - \cos \vartheta^*)^2 (e_3^*)^2 + \sin^2 \vartheta^*}, \quad e^{*2} = \frac{(1 - \cos \vartheta^*) e_3^* \bar{n}_2 + \frac{1}{\sqrt{a}} \sin \vartheta^* \bar{n}_1}{(1 - \cos \vartheta^*)^2 (e_3^*)^2 + \sin^2 \vartheta^*}. \quad (3.11)$$

Selection of the possible values for e_3^* is restricted by the fact that $-1 \leq \cos \vartheta^* \leq 1$, i.e. after taking into account (3.10),

$$-1 \leq \frac{\bar{n}_3 - (e_3^*)^2}{1 - (e_3^*)^2} \leq 1.$$

This means that, beside the evidently satisfied conditions $|\bar{n}_3| \leq 1$, condition

$$e_3^* \leq \sqrt{\frac{1 + \bar{n}_3}{2}} \quad (3.12)$$

should also be satisfied.

Taking into account the above constraint, for a given normal vector $\bar{\mathbf{n}}$ of the middle surface (\bar{S}_o) and for a given component e_3^* of the rotation axis \mathbf{e}^* , the rotation angle ϑ^* can be determined using (3.10) and the other two components $e^{*\mu}$ of \mathbf{e}^* can then be obtained from (3.11).

3.3. The results of Subsection 3.2 can now be summarized as follows: For a given normal vector $\bar{\mathbf{n}} = \bar{n}^p \mathbf{a}_p = \bar{n}_q \mathbf{a}^q$, $|\bar{\mathbf{n}}| = 1$ of the middle surface (\bar{S}_o), there exists an infinite number of solutions to equation $\mathbf{R}^* \cdot \mathbf{a}_3 = \bar{\mathbf{k}}_3^* = \bar{\mathbf{n}}$ for the rotation tensor \mathbf{R}^* . These solutions differ from each other in one component of the unit vector \mathbf{e}^* of the rotation axis, namely the component e_3^* . After selecting the component $e_3^* = e^{*3}$ of vector \mathbf{e}^* , with satisfied constraint (3.12), equations (3.10) and (3.11) give a unique solution for ϑ^* and for the other two components of \mathbf{e}^* , i.e. for the rotation tensor \mathbf{R}^* . It can be pointed out that this solution satisfies the requirement $|\mathbf{e}^*| = 1$.

It can also be seen that vectors $\mathbf{R}^* \cdot \mathbf{a}_\alpha = \bar{\mathbf{k}}_\alpha^*$, obtained with different rotation tensors \mathbf{R}^* , lie in the tangent plane, perpendicular to the normal $\bar{\mathbf{k}}_3^* = \bar{\mathbf{n}}$ of the middle surface (\bar{S}_o), in such a way that the different vectors $\bar{\mathbf{k}}_\alpha^*$ belonging to e_3^* (to \mathbf{e}^*) can be rotated into each other about vector $\bar{\mathbf{k}}_3^* = \bar{\mathbf{n}}$. This follows from the evidently satisfied equation $\bar{\mathbf{k}}_\alpha^* \cdot \bar{\mathbf{k}}_3^* = \mathbf{a}_\alpha \cdot \mathbf{R}^{*\text{T}} \cdot \mathbf{R}^* \cdot \mathbf{a}_3 = \mathbf{a}_\alpha \cdot \mathbf{a}_3 = 0$.

Another important consequence of equations (3.10) and (3.11) is that for every normal vector $\bar{\mathbf{n}}$, $|\bar{\mathbf{n}}| = 1$, there exists a finite rotation tensor with the axis of rotation lying in the tangent plane to the middle surface (S_o). Let this rotation tensor be denoted by \mathbf{R}_2 (the angle of rotation is ϑ_2 , the unit vector of the rotation axis is \mathbf{e}_2):

$$\mathbf{R}_2 = R_2^k \mathbf{a}_k \mathbf{a}^l = \cos \vartheta_2 \mathbf{I} + (1 - \cos \vartheta_2) \mathbf{e}_2 \mathbf{e}_2 + \sin \vartheta_2 \mathbf{e}_2 \times \mathbf{I}. \quad (3.13)$$

According to relations (3.10) and (3.11):

$$\cos \vartheta_2 = \bar{n}_3, \quad \sin \vartheta_2 = \sqrt{1 - (\bar{n}_3)^2}, \quad (3.14)$$

$$e_2^1 = -\frac{1}{\sqrt{a}} \frac{\bar{n}_2}{\sin \vartheta_2}, \quad e_2^2 = \frac{1}{\sqrt{a}} \frac{\bar{n}_1}{\sin \vartheta_2} = -\frac{\bar{n}_1}{\bar{n}_2} e_2^1. \quad (3.15)$$

3.4. Making use of the results of Subsection **3.3**, the rotation tensor \mathbf{R}^* is obtained first by the product of two rotation tensors: $\mathbf{R}^* = \bar{\mathbf{R}}_n \cdot \mathbf{R}_2$, i.e. we apply two rotations, one after the other, described by expression

$$\bar{\mathbf{k}}_k^* = \mathbf{R}^* \cdot \mathbf{a}_k = \bar{\mathbf{R}}_n \cdot \mathbf{R}_2 \cdot \mathbf{a}_k = \bar{\mathbf{R}}_n \cdot (\mathbf{R}_2 \cdot \mathbf{a}_k), \quad (3.16)$$

where \mathbf{R}_2 is defined by (3.13)-(3.15) and the rotation tensor $\bar{\mathbf{R}}_n$ describes a rotation about the unit normal $\bar{\mathbf{n}}$, being the axis of rotation, with rotation angle ϑ_1 :

$$\bar{\mathbf{R}}_n = \cos \vartheta_1 \mathbf{I} + (1 - \cos \vartheta_1) \bar{\mathbf{n}} \bar{\mathbf{n}} + \sin \vartheta_1 \bar{\mathbf{n}} \times \mathbf{I}. \quad (3.17)$$

The vectors $\bar{\mathbf{k}}_k^* = \mathbf{R}^* \cdot \mathbf{a}_k$, rotated into the tangent plane of the middle surface (\bar{S}_o), can thus be obtained by rotating first the base vectors \mathbf{a}_k into vectors $\mathbf{R}_2 \cdot \mathbf{a}_k$ lying in the tangent plane, then these vectors are being rotated again in the tangent plane about the normal $\bar{\mathbf{n}}$: $\bar{\mathbf{k}}_k^* = \bar{\mathbf{R}}_n \cdot (\mathbf{R}_2 \cdot \mathbf{a}_k)$. The vector \mathbf{a}_3 is rotated only once by $\bar{\mathbf{k}}_3 = \mathbf{R}_2 \cdot \mathbf{a}_3 = \bar{\mathbf{n}}$, because $\bar{\mathbf{R}}_n \cdot \bar{\mathbf{n}} = \bar{\mathbf{n}}$. The geometric interpretation of the described rotations is shown in Figure 2.

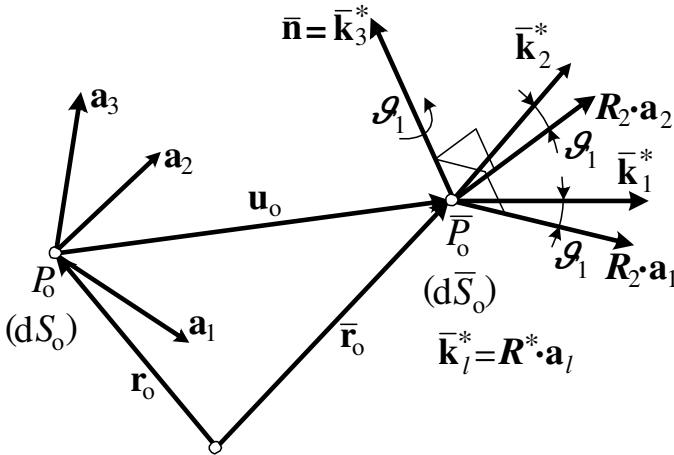


Figure 2.

3.5. The components of the unit normal vector $\bar{\mathbf{n}}$ can be obtained from the gradient $\mathbf{u}_{o,\alpha}$ of the displacement vector of the middle surface (S_o), according to (2.10)-(2.12), and the parameters of the rotation tensor \mathbf{R}_2 can then be computed from (3.14) and

(3.15) as

$$\cos \vartheta_2 = \bar{n}_3 = \frac{\sqrt{a}}{\sqrt{\bar{a}}} (1 + u_{o;1}^1 + u_{o;2}^2 + u_{o;1}^1 u_{o;2}^2 - u_{o;2}^1 u_{o;1}^2), \tag{3.18}$$

$$\sqrt{a} \sin \vartheta_2 e_2^1 = -\bar{n}_2 = \frac{\sqrt{a}}{\sqrt{\bar{a}}} [(1 + u_{o;1}^1) u_{o;2}^3 - u_{o;2}^1 u_{o;1}^3], \tag{3.19}$$

$$\sqrt{a} \sin \vartheta_2 e_2^2 = \bar{n}_1 = -\frac{\sqrt{a}}{\sqrt{\bar{a}}} [(1 + u_{o;2}^2) u_{o;1}^3 - u_{o;1}^2 u_{o;2}^3]. \tag{3.20}$$

3.6. Let us introduce, secondly, the rotation tensor

$$\mathbf{R}_1 = \cos \vartheta_1 \mathbf{I} + (1 - \cos \vartheta_1) \mathbf{a}_3 \mathbf{a}_3 + \sin \vartheta_1 \mathbf{a}_3 \times \mathbf{I} \tag{3.21}$$

on the middle surface (S_o). It can be pointed out (see APPENDIX A) that

$$\mathbf{R}^* = \bar{\mathbf{R}}_n \cdot \mathbf{R}_2 = \mathbf{R}_2 \cdot \mathbf{R}_1, \tag{3.22}$$

i.e. the following relations hold:

$$\bar{\mathbf{k}}_\kappa^* = \mathbf{R}^* \cdot \mathbf{a}_\kappa = \bar{\mathbf{R}}_n \cdot \mathbf{R}_2 \cdot \mathbf{a}_\kappa = \mathbf{R}_2 \cdot \mathbf{R}_1 \cdot \mathbf{a}_\kappa, \quad \bar{\mathbf{k}}_3^* = \mathbf{R}^* \cdot \mathbf{a}_3 = \mathbf{R}_2 \cdot \mathbf{a}_3 = \bar{\mathbf{n}}. \tag{3.23}$$

In view of equation (3.23), the finite rotation of the base vectors \mathbf{a}_κ , given by the rotation tensor \mathbf{R}^* , will be described *in the following by two rotation tensors, \mathbf{R}_2 and \mathbf{R}_1* . Then the base vectors $\bar{\mathbf{k}}_\kappa^* = \mathbf{R}^* \cdot \mathbf{a}_\kappa$, rotated into the tangent plane of the middle surface (\bar{S}_o), can be obtained in two steps: first the base vectors \mathbf{a}_κ are rotated about \mathbf{a}_3 by angle ϑ_1 into vectors $\mathbf{R}_1 \cdot \mathbf{a}_\kappa$ lying in the tangent plane of (S_o), and, next, these vectors are rotated about axis \mathbf{e}_2 , lying in the tangent plane of (S_o), by the angle ϑ_2 as $\bar{\mathbf{k}}_\kappa^* = \mathbf{R}_2 \cdot (\mathbf{R}_1 \cdot \mathbf{a}_\kappa)$. The base vector \mathbf{a}_3 is rotated, however, only once, according to $\bar{\mathbf{k}}_3^* = \mathbf{R}_2 \cdot \mathbf{a}_3 = \bar{\mathbf{n}}$, as $\mathbf{R}_1 \cdot \mathbf{a}_3 = \mathbf{a}_3$. The geometrical interpretation of these rotations is seen in Figure 3.

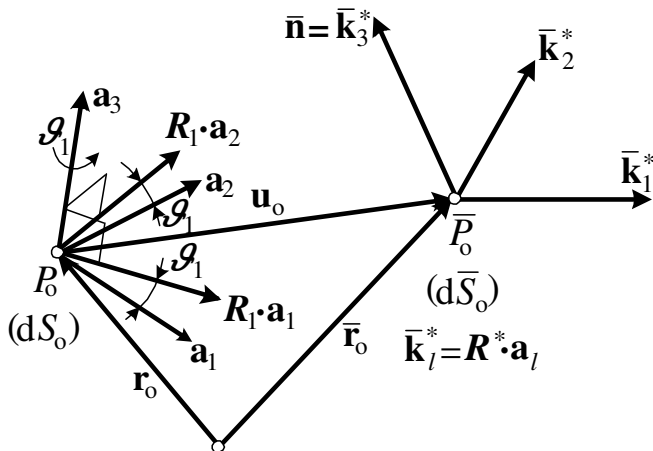


Figure 3.

The parameters of the rotation tensor \mathbf{R}^* can be obtained from the parameters of the rotation tensors \mathbf{R}_1 and \mathbf{R}_2 , defined in (3.21) and (3.13), respectively, according to the following expressions:

$$1 + \cos \vartheta^* = \frac{1}{2} (1 + \cos \vartheta_1) (1 + \cos \vartheta_2),$$

$$\sin \vartheta^* \mathbf{e}^* = \frac{1}{2} [(1 + \cos \vartheta_1) \sin \vartheta_2 \mathbf{e}_2 + (1 + \cos \vartheta_2) \sin \vartheta_1 \mathbf{a}_3 + (\sin \vartheta_2 \mathbf{e}_2) \times (\sin \vartheta_1 \mathbf{a}_3)].$$

3.7. The rotation tensor $\overline{\mathbf{R}}_s$, describing an infinitesimal rotation, is defined by equations (3.5) and (3.6). According to (3.2), the rotated base vectors $\overline{\mathbf{k}}_k$ and $\overline{\mathbf{k}}_k^*$ can be related to each other through

$$\overline{\mathbf{k}}_k = \overline{\mathbf{R}}_s \cdot \overline{\mathbf{k}}_k^* = \overline{\mathbf{k}}_k^* + \vartheta_s \overline{\mathbf{e}}_s \times \overline{\mathbf{k}}_k^* = \mathbf{R}^* \cdot \mathbf{a}_k + \vartheta_s e_s^\mu (\mathbf{R}^* \cdot \mathbf{a}_\mu) \times (\mathbf{R}^* \cdot \mathbf{a}_k), \quad (3.24)$$

and, in view of equation (B.1) of APPENDIX B, we have

$$\overline{\mathbf{k}}_k = \overline{\mathbf{R}}_s \cdot \overline{\mathbf{k}}_k^* = \mathbf{R}^* \cdot (\mathbf{a}_k + \vartheta_s \mathbf{e}_s \times \mathbf{a}_k) = \mathbf{R}^* \cdot \mathbf{R}_s \cdot \mathbf{a}_k = \mathbf{R} \cdot \mathbf{a}_k, \quad (3.25)$$

where

$$\mathbf{R}_s = \mathbf{I} + \vartheta_s \mathbf{e}_s \times \mathbf{I}; \quad \mathbf{R} = \mathbf{R}^* \cdot \mathbf{R}_s = \mathbf{R}_2 \cdot \mathbf{R}_1 \cdot \mathbf{R}_s. \quad (3.26)$$

The resultant rotation tensor $\mathbf{R} = \mathbf{R}_2 \cdot \mathbf{R}_1 \cdot \mathbf{R}_s$ has three independent parameters, since \mathbf{R}_2 [and the two components of its vector $\vartheta_2 = \vartheta_2 \mathbf{e}_2$, ($\vartheta_2 = |\vartheta_2|$)] is uniquely defined by the displacement field \mathbf{u}_o , according to (3.18)-(3.20) (zero parameter in number), \mathbf{R}_1 is described, according to (3.21), by the rotation angle ϑ_1 (1 parameter), and \mathbf{R}_s is described, according to (3.25), by the two components of the vector $\vartheta_s = \vartheta_s \mathbf{e}_s$ ($\vartheta_s = |\vartheta_s|$) (2 parameters).

The above equations can be supplemented by the following relations for the rotated base vectors $\overline{\mathbf{k}}_k^*$: from (3.23)₂ and (2.3) we have:

$$\overline{\mathbf{a}}_\kappa \cdot \overline{\mathbf{k}}_3^* = \overline{\mathbf{a}}_\kappa \cdot \overline{\mathbf{n}} = 0, \quad (3.27)$$

and from (3.6) and (3.27) we have:

$$(\overline{\mathbf{e}}_s \times \overline{\mathbf{k}}_\kappa^*) \cdot \overline{\mathbf{a}}_\lambda = 0, \quad \text{since} \quad (\overline{\mathbf{e}}_s \times \overline{\mathbf{k}}_\kappa^*) \parallel \overline{\mathbf{n}}. \quad (3.28)$$

4. The deformation gradient, the Green-Lagrange and the Jaumann strain tensors on the middle surface (S_o)

4.1. The deformation gradient tensor and its transpose are defined in (2.6) as

$$\mathbf{F}_o = \overline{\mathbf{a}}_k \mathbf{a}^k = \overline{\mathbf{a}}_\kappa \mathbf{a}^\kappa + \overline{\mathbf{a}}_3 \mathbf{a}^3 \quad \text{and} \quad \mathbf{F}_o^T = \mathbf{a}^k \overline{\mathbf{a}}_k = \mathbf{a}^\kappa \overline{\mathbf{a}}_\kappa + \mathbf{a}^3 \overline{\mathbf{a}}_3,$$

where the base vectors $\overline{\mathbf{a}}_\kappa$ and $\overline{\mathbf{a}}_3$ are given, respectively, by expressions (3.3) and (3.4).

The detailed Green-Lagrange strain tensor is given by (2.8). When the different products of the base vectors of the middle surface (\overline{S}_o), appearing in equation (2.8) and later on, are computed, it will be taken into account that the strain vectors $\overline{\boldsymbol{\alpha}}_k$,

the angle of rotation ϑ_s as well as the stretch ε_{o3} are infinitesimally small, according to the assumptions introduced in Subsection 3.1. Then we can write:

$$\begin{aligned} \bar{\mathbf{a}}_\kappa \cdot \bar{\mathbf{a}}_\lambda &= (\bar{\mathbf{k}}_\kappa + \bar{\boldsymbol{\alpha}}_\kappa) \cdot (\bar{\mathbf{k}}_\lambda + \bar{\boldsymbol{\alpha}}_\lambda) = \bar{\mathbf{k}}_\kappa \cdot \bar{\mathbf{k}}_\lambda + \bar{\mathbf{k}}_\kappa \cdot \bar{\boldsymbol{\alpha}}_\lambda + \bar{\boldsymbol{\alpha}}_\kappa \cdot \bar{\mathbf{k}}_\lambda + \bar{\boldsymbol{\alpha}}_\kappa \cdot \bar{\boldsymbol{\alpha}}_\lambda \approx \\ &\approx a_{\kappa\lambda} + \bar{\mathbf{k}}_\kappa \cdot \bar{\boldsymbol{\alpha}}_\lambda + \bar{\boldsymbol{\alpha}}_\kappa \cdot \bar{\mathbf{k}}_\lambda, \end{aligned} \quad (4.1)$$

$$\bar{\mathbf{a}}_\kappa \cdot \bar{\mathbf{a}}_3 = (1 + \varepsilon_{o3}) \bar{\mathbf{a}}_\kappa \cdot \bar{\mathbf{k}}_3 \approx \bar{\mathbf{a}}_\kappa \cdot \bar{\mathbf{k}}_3, \quad (4.2)$$

$$\bar{\mathbf{a}}_3 \cdot \bar{\mathbf{a}}_3 = (1 + \varepsilon_{o3})^2 \bar{\mathbf{k}}_3 \cdot \bar{\mathbf{k}}_3 \approx 1 + 2\varepsilon_{o3}. \quad (4.3)$$

In obtaining (4.1) and (4.3), equation (B.2) of APPENDIX B has been utilized.

Taking into account (3.24) and (3.28), the product $\bar{\mathbf{k}}_\kappa \cdot \bar{\boldsymbol{\alpha}}_\lambda$ appearing in (4.1) can be written in a different way:

$$\begin{aligned} \bar{\mathbf{k}}_\kappa \cdot \bar{\boldsymbol{\alpha}}_\lambda &= \bar{\mathbf{k}}_\kappa \cdot (\bar{\mathbf{a}}_\lambda - \bar{\mathbf{k}}_\lambda) = \bar{\mathbf{k}}_\kappa \cdot \bar{\mathbf{a}}_\lambda - a_{\kappa\lambda} = \left(\bar{\mathbf{k}}_\kappa^* + \vartheta_s \bar{\mathbf{e}}_s \times \bar{\mathbf{k}}_\kappa^* \right) \cdot \bar{\mathbf{a}}_\lambda - a_{\kappa\lambda} = \\ &= \bar{\mathbf{k}}_\kappa^* \cdot \bar{\mathbf{a}}_\lambda - a_{\kappa\lambda} = \mathbf{a}_\kappa \cdot \mathbf{R}^{*\text{T}} \cdot (\mathbf{a}_\lambda + \mathbf{u}_{o,\lambda}) - a_{\kappa\lambda}. \end{aligned} \quad (4.4)$$

The product $\bar{\mathbf{a}}_\kappa \cdot \bar{\mathbf{a}}_3$ of (4.2) can also be modified using (3.24), (3.27) and equation (B.1) of APPENDIX B:

$$\begin{aligned} \bar{\mathbf{a}}_\kappa \cdot \bar{\mathbf{a}}_3 &\approx \bar{\mathbf{a}}_\kappa \cdot \bar{\mathbf{k}}_3 = \bar{\mathbf{a}}_\kappa \cdot \left(\bar{\mathbf{k}}_3^* + \vartheta_s \bar{\mathbf{e}}_s \times \bar{\mathbf{k}}_3^* \right) = (\bar{\mathbf{k}}_\kappa + \bar{\boldsymbol{\alpha}}_\kappa) \cdot \left(\vartheta_s \bar{\mathbf{e}}_s \times \bar{\mathbf{k}}_3^* \right) \approx \\ &\approx \bar{\mathbf{k}}_\kappa^* \cdot \left(\vartheta_s \bar{\mathbf{e}}_s \times \bar{\mathbf{k}}_3^* \right) = \mathbf{a}_\kappa \cdot \mathbf{R}^{*\text{T}} \cdot \mathbf{R}^* \cdot (\vartheta_s \mathbf{e}_s \times \mathbf{a}_3) = \vartheta_s \mathbf{a}_\kappa \cdot (\mathbf{e}_s \times \mathbf{a}_3) = \vartheta_s \sqrt{a} e_{\kappa\mu 3} e_{\underline{s}}^\mu. \end{aligned} \quad (4.5)$$

4.2. The components of the Green-Lagrange strain tensor on the middle surface (S_o) are thus the following:

$$\begin{aligned} E_{o\kappa\lambda} &= \mathbf{a}_\kappa \cdot \mathbf{E}_o \cdot \mathbf{a}_\lambda = \frac{1}{2} (\bar{\mathbf{a}}_\kappa \cdot \bar{\mathbf{a}}_\lambda - a_{\kappa\lambda}) \approx \\ &\approx \frac{1}{2} \left[\mathbf{a}_\kappa \cdot \mathbf{R}^{*\text{T}} \cdot (\mathbf{a}_\lambda + \mathbf{u}_{o,\lambda}) + (\mathbf{a}_\kappa + \mathbf{u}_{o,\kappa}) \cdot \mathbf{R}^* \cdot \mathbf{a}_\lambda \right] - a_{\kappa\lambda}, \end{aligned} \quad (4.6)$$

$$E_{o\kappa 3} = E_{o3\kappa} = \mathbf{a}_\kappa \cdot \mathbf{E}_o \cdot \mathbf{a}_3 = \frac{1}{2} \bar{\mathbf{a}}_\kappa \cdot \bar{\mathbf{a}}_3 \approx \frac{1}{2} \vartheta_s \mathbf{a}_3 \cdot (\mathbf{a}_\kappa \times \mathbf{e}_s) = \frac{1}{2} \vartheta_s \sqrt{a} e_{\kappa\mu 3} e_{\underline{s}}^\mu, \quad (4.7)$$

$$E_{o33} = \mathbf{a}_3 \cdot \mathbf{E}_o \cdot \mathbf{a}_3 = \frac{1}{2} (\bar{\mathbf{a}}_3 \cdot \bar{\mathbf{a}}_3 - 1) \approx \varepsilon_{o3}. \quad (4.8)$$

Components E_{okl} are infinitesimal.

It is noted that to compute the components $E_{o\kappa\lambda}$, only the displacement field \mathbf{u}_o and the rotation tensor $\mathbf{R}^* = \mathbf{R}_2 \cdot \mathbf{R}_1$ are needed. On the other hand, components $E_{o\kappa 3}$ depend on the rotation tensor \mathbf{R}_s (on the rotation vector $\boldsymbol{\vartheta}_s = \vartheta_s \mathbf{e}_s$), and component E_{o33} depends only on the stretch ε_{o3} .

4.3. The surface part $\bar{a}_{\alpha\beta} = \bar{\mathbf{a}}_\alpha \cdot \bar{\mathbf{a}}_\beta$ of the metric tensor at point \bar{P}_o can be written using (2.8) as follows:

$$\bar{a}_{\alpha\beta} = 2E_{o\alpha\beta} + a_{\alpha\beta}.$$

Taking into account that the strain components $E_{\alpha\beta}$ are infinitesimally small, the approximate value of the determinant of the metric tensor in (2.3)₂ is:

$$\bar{a} = \det \bar{a}_{\alpha\beta} = \bar{a}_{11}\bar{a}_{22} - \bar{a}_{12}\bar{a}_{21} \approx a. \quad (4.9)$$

4.4. The curvature tensor of the middle surface (\bar{S}_o) reads:

$$\bar{b}_{\kappa\lambda} = -\bar{\mathbf{a}}_{\kappa} \cdot \bar{\mathbf{n}}_{,\lambda} = -(\bar{\mathbf{k}}_{\kappa} + \bar{\boldsymbol{\alpha}}_{\kappa}) \cdot \bar{\mathbf{k}}_{3,\lambda} \approx -\bar{\mathbf{k}}_{\kappa} \cdot \bar{\mathbf{k}}_{3,\lambda}. \quad (4.10)$$

4.5. The symmetric right Jaumann strain tensor, \mathbf{H}_o , can be obtained using the polar decomposition of the deformation gradient tensor:

$$\begin{aligned} \mathbf{F}_o &= \mathbf{R} \cdot (\mathbf{H}_o + \mathbf{I}), \\ \mathbf{H}_o &= H_{okl} \mathbf{a}^k \mathbf{a}^l = \frac{1}{2} \left(\mathbf{R}^T \cdot \mathbf{F}_o + \mathbf{F}_o^T \cdot \mathbf{R} \right) - \mathbf{I}. \end{aligned} \quad (4.11)$$

In view of (3.3) and (4.1), the components of this tensor are given by

$$\begin{aligned} H_{o\kappa\lambda} &= \mathbf{a}_{\kappa} \cdot \mathbf{H}_o \cdot \mathbf{a}_{\lambda} = \frac{1}{2} \left(\mathbf{a}_{\kappa} \cdot \mathbf{R}^T \cdot \mathbf{F}_o \cdot \mathbf{a}_{\lambda} + \mathbf{a}_{\kappa} \cdot \mathbf{F}_o^T \cdot \mathbf{R} \cdot \mathbf{a}_{\lambda} \right) - a_{\kappa\lambda} = \\ &= \frac{1}{2} (\bar{\mathbf{k}}_{\kappa} \cdot \bar{\mathbf{a}}_{\lambda} + \bar{\mathbf{a}}_{\kappa} \cdot \bar{\mathbf{k}}_{\lambda}) - a_{\kappa\lambda} = \frac{1}{2} [\bar{\mathbf{k}}_{\kappa} \cdot (\bar{\mathbf{k}}_{\lambda} + \bar{\boldsymbol{\alpha}}_{\lambda}) + (\bar{\mathbf{k}}_{\kappa} + \bar{\boldsymbol{\alpha}}_{\kappa}) \cdot \bar{\mathbf{k}}_{\lambda}] - a_{\kappa\lambda} \approx \\ &\approx \frac{1}{2} [\bar{\mathbf{k}}_{\kappa} \cdot \bar{\boldsymbol{\alpha}}_{\lambda} + \bar{\boldsymbol{\alpha}}_{\kappa} \cdot \bar{\mathbf{k}}_{\lambda}] \approx \frac{1}{2} (\bar{\mathbf{a}}_{\kappa} \cdot \bar{\mathbf{a}}_{\lambda} - a_{\kappa\lambda}) = E_{o\kappa\lambda}, \end{aligned} \quad (4.12)$$

and, in addition, taking into account (4.5) as well, we obtain:

$$\begin{aligned} H_{o\kappa 3} &= \mathbf{a}_{\kappa} \cdot \mathbf{H}_o \cdot \mathbf{a}_3 = \frac{1}{2} (\bar{\mathbf{k}}_{\kappa} \cdot \bar{\mathbf{a}}_3 + \bar{\mathbf{a}}_{\kappa} \cdot \bar{\mathbf{k}}_3) = \\ &= \frac{1}{2} [(1 + \varepsilon_{o3}) \bar{\mathbf{k}}_{\kappa} \cdot \bar{\mathbf{k}}_3 + \bar{\mathbf{a}}_{\kappa} \cdot \bar{\mathbf{k}}_3] \approx \frac{1}{2} \bar{\mathbf{a}}_{\kappa} \cdot \bar{\mathbf{a}}_3 = E_{o\kappa 3}, \end{aligned} \quad (4.13)$$

$$H_{o33} = \mathbf{a}_3 \cdot \mathbf{H}_o \cdot \mathbf{a}_3 - 1 = \frac{1}{2} (\bar{\mathbf{k}}_3 \cdot \bar{\mathbf{a}}_3 + \bar{\mathbf{a}}_3 \cdot \bar{\mathbf{k}}_3) - 1 = (1 + \varepsilon_{o3}) \bar{\mathbf{k}}_3 \cdot \bar{\mathbf{k}}_3 - 1 = \varepsilon_{o3} \approx E_{o33}. \quad (4.14)$$

It can be concluded, that using the assumptions (neglections) introduced in the previous sections, the Green-Lagrange and the Jaumann strain tensors are identical on the middle surface (S_o).

5. The deformation gradient and the Green-Lagrange strain tensor at an arbitrary point of the reference configuration (B)

5.1. Let P denote an arbitrary point on the normal (on the coordinate line x^3) to the middle surface (S_o) of the reference configuration (B). The base vectors and the metric tensor at point P are:

$$\mathbf{r} = \mathbf{r}(x^1, x^2, x^3) = \mathbf{r}_o + \mathbf{a}_3 x^3, \quad (5.1)$$

$$\mathbf{g}_{\kappa} = \mathbf{r}_{,\kappa} = \mathbf{r}_{o,\kappa} + \mathbf{a}_{3,\kappa} x^3 = \mathbf{a}_{\kappa} - \mathbf{a}_{\alpha} b_{\kappa}^{\alpha} x^3 = (\delta_{\kappa}^{\alpha} - b_{\kappa}^{\alpha} x^3) \mathbf{a}_{\alpha}, \quad \mathbf{g}_3 = \mathbf{r}_{,3} = \mathbf{a}_3 = \mathbf{n}, \quad (5.2)$$

$$g_{\kappa\lambda} = \mathbf{g}_{\kappa} \cdot \mathbf{g}_{\lambda} = a_{\kappa\lambda} - 2b_{\kappa\lambda} x^3 + b_{\kappa\alpha} b_{\lambda}^{\alpha} (x^3)^2, \quad g_{\kappa 3} = 0, \quad g_{33} = 1. \quad (5.3)$$

The contravariant base vectors are denoted by \mathbf{g}^m , the inverse of the metric tensor is $g^{mn} = \mathbf{g}^m \cdot \mathbf{g}^n$ ($g^{\mu 3} = 0, g^{33} = 1$). If the shifter is denoted by μ_k^m , $\mu_k^\mu = \delta_k^\mu - b_{\kappa}^\mu x^3$, $\mu_3^\mu = 0, \mu_3^3 = 1$ and its inverse is $\bar{\mu}_k^m$, then the following relations hold:

$$\mathbf{g}_k = \mu_k^m \mathbf{a}_m, \quad \mathbf{g}^m = \bar{\mu}_k^m \mathbf{a}^k. \tag{5.4}$$

Let \bar{P} denote an arbitrary point on the coordinate line x^3 of the deformed configuration (\bar{B}). The position vector of point \bar{P} and the base vectors at \bar{P} are:

$$\bar{\mathbf{r}} = \bar{\mathbf{r}}(x^1, x^2, x^3) = \bar{\mathbf{r}}_0 + \bar{\mathbf{h}}, \quad \bar{\mathbf{g}}_\kappa = \bar{\mathbf{r}}_{0,\kappa} + \bar{\mathbf{h}}_{,\kappa} = \bar{\mathbf{a}}_\kappa + \bar{\mathbf{h}}_{,\kappa}, \quad \bar{\mathbf{g}}_3 = \bar{\mathbf{h}}_{,3}, \tag{5.5}$$

where $\bar{\mathbf{h}} = \bar{\mathbf{h}}(x^1, x^2, x^3)$. The geometrical setting with an enlarged scale in the thickness direction is shown in Figure 4. Geometrically non-linear shell theories differ from each other in the assumptions for the form of $\bar{\mathbf{h}}$ (for instance, in shell theories based on the Kirchhoff-Love hypothesis, $\bar{\mathbf{h}} = \bar{\mathbf{n}}x^3$).

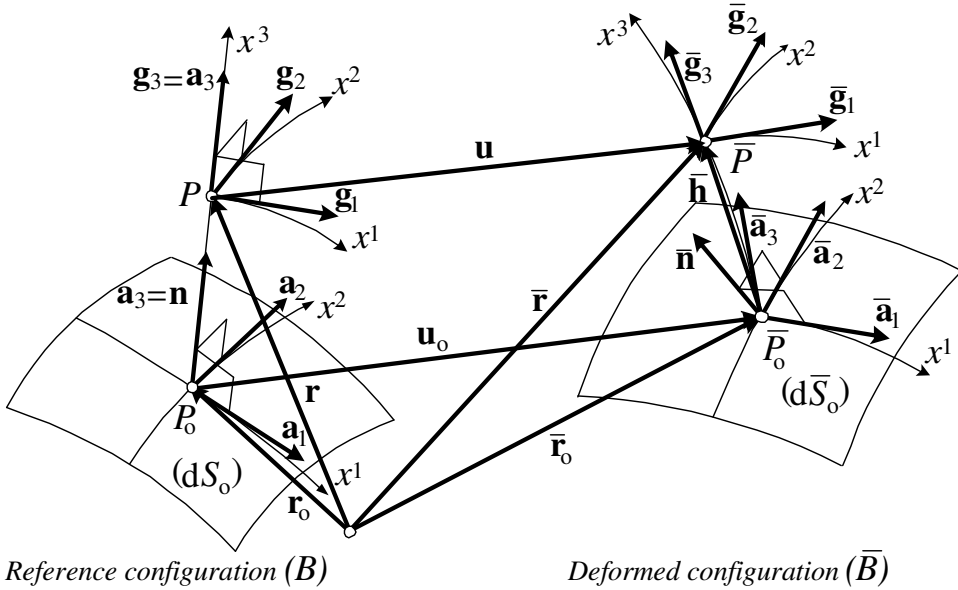


Figure 4.

As a continuation of Sections 3 and 4, the following part of this section derives the deformation gradient and the Green-Lagrange strain tensor at an arbitrary point P of the configuration (B), considering the relatively simple hypothesis of Reissner-Mindlin:

$$\bar{\mathbf{h}} = \bar{\mathbf{k}}_3 x^3 = \mathbf{R}^* \cdot (\mathbf{a}_3 + \vartheta_s \mathbf{e}_s \times \mathbf{a}_3) x^3. \tag{5.6}$$

5.2. The deformation gradient and its transpose at the arbitrary point P are:

$$\mathbf{F} = \bar{\mathbf{g}}_k \mathbf{g}^k = \bar{\mathbf{g}}_\kappa \mathbf{g}^\kappa + \bar{\mathbf{g}}_3 \mathbf{g}^3, \quad \mathbf{F}^T = \mathbf{g}^k \bar{\mathbf{g}}_k = \mathbf{g}^\kappa \bar{\mathbf{g}}_\kappa + \mathbf{g}^3 \bar{\mathbf{g}}_3. \tag{5.7}$$

At point \bar{P} , the base vectors can be written on the basis of equations (5.5)_{2,3} and (5.6) as

$$\bar{\mathbf{g}}_\kappa = \bar{\mathbf{a}}_\kappa + \bar{\mathbf{h}}_{,\kappa} = \bar{\mathbf{k}}_\kappa + \bar{\alpha}_\kappa + \bar{\mathbf{k}}_{3,\kappa} x^3, \quad \bar{\mathbf{g}}_3 = \bar{\mathbf{h}}_{,3} = \bar{\mathbf{k}}_3, \quad (5.8)$$

where

$$\bar{\mathbf{k}}_{3,\kappa} = [\mathbf{R}^* \cdot (\mathbf{a}_3 + \vartheta_s \mathbf{e}_s \times \mathbf{a}_3)]_{,\kappa} = \mathbf{R}^*_{,\kappa} \cdot (\mathbf{a}_3 + \vartheta_s \mathbf{e}_s \times \mathbf{a}_3) + \mathbf{R}^* \cdot (\mathbf{a}_3 + \vartheta_s \mathbf{e}_s \times \mathbf{a}_3)_{,\kappa}. \quad (5.9)$$

5.3. The Green-Lagrange strain tensor at the arbitrary point P is given by

$$\begin{aligned} \mathbf{E} &= E_{kl} \mathbf{g}^k \mathbf{g}^l = \frac{1}{2} (\mathbf{F}^\top \cdot \mathbf{F} - \mathbf{I}) = \frac{1}{2} [(\bar{\mathbf{g}}_k \cdot \bar{\mathbf{g}}_l) - (\mathbf{g}_k \cdot \mathbf{g}_l)] \mathbf{g}^k \mathbf{g}^l = \\ &= \frac{1}{2} [(\bar{\mathbf{g}}_\kappa \cdot \bar{\mathbf{g}}_\lambda - g_{\kappa\lambda}) \mathbf{g}^\kappa \mathbf{g}^\lambda + (\bar{\mathbf{g}}_\kappa \cdot \bar{\mathbf{g}}_3) \mathbf{g}^\kappa \mathbf{g}^3 + (\bar{\mathbf{g}}_3 \cdot \bar{\mathbf{g}}_\lambda) \mathbf{g}^3 \mathbf{g}^\lambda + (\bar{\mathbf{g}}_3 \cdot \bar{\mathbf{g}}_3 - 1) \mathbf{g}^3 \mathbf{g}^3]. \end{aligned} \quad (5.10)$$

Assume that beside the strain vectors $\bar{\alpha}_\kappa$ and the angle of rotation ϑ_s , the derivative $\vartheta_{s,\kappa}$ is also infinitesimally small. Then, using the transformations of Subsection 4.1, the scalar product of the base vectors of configuration (\bar{B}), appearing in (5.10), can be written as

$$\begin{aligned} \bar{\mathbf{g}}_\kappa \cdot \bar{\mathbf{g}}_\lambda &= (\bar{\mathbf{k}}_\kappa + \bar{\alpha}_\kappa + \bar{\mathbf{k}}_{3,\kappa} x^3) \cdot (\bar{\mathbf{k}}_\lambda + \bar{\alpha}_\lambda + \bar{\mathbf{k}}_{3,\lambda} x^3) \approx \\ &\approx a_{\kappa\lambda} + \bar{\mathbf{k}}_\kappa \cdot \bar{\alpha}_\lambda + \bar{\alpha}_\kappa \cdot \bar{\mathbf{k}}_\lambda + (\bar{\mathbf{k}}_\kappa \cdot \bar{\mathbf{k}}_{3,\lambda} + \bar{\mathbf{k}}_{3,\kappa} \cdot \bar{\mathbf{k}}_\lambda) x^3 + \bar{\mathbf{k}}_{3,\kappa} \cdot \bar{\mathbf{k}}_{3,\lambda} (x^3)^2, \end{aligned} \quad (5.11)$$

$$\bar{\mathbf{g}}_\kappa \cdot \bar{\mathbf{g}}_3 = \bar{\mathbf{g}}_3 \cdot \bar{\mathbf{g}}_\kappa = (\bar{\mathbf{a}}_\kappa + \bar{\mathbf{k}}_{3,\kappa} x^3) \cdot \bar{\mathbf{k}}_3 = \bar{\mathbf{a}}_\kappa \cdot \bar{\mathbf{k}}_3 \approx \vartheta_s \mathbf{a}_\kappa \cdot (\mathbf{e}_s \times \mathbf{a}_3), \quad (5.12)$$

$$\bar{\mathbf{g}}_3 \cdot \bar{\mathbf{g}}_3 = \bar{\mathbf{k}}_3 \cdot \bar{\mathbf{k}}_3 = 1. \quad (5.13)$$

Making use of (3.24), the scalar product $\bar{\mathbf{k}}_\kappa \cdot \bar{\mathbf{k}}_{3,\lambda}$ in (5.11) can be approximated as

$$\bar{\mathbf{k}}_\kappa \cdot \bar{\mathbf{k}}_{3,\lambda} = (\bar{\mathbf{k}}_\kappa^* + \vartheta_s \bar{\mathbf{e}}_s \times \bar{\mathbf{k}}_\kappa^*) \cdot (\bar{\mathbf{k}}_{3,\lambda}^* + \vartheta_s \bar{\mathbf{e}}_s \times \bar{\mathbf{k}}_{3,\lambda}^*) \approx \bar{\mathbf{k}}_\kappa^* \cdot \bar{\mathbf{k}}_{3,\lambda}^*,$$

and then we can write:

$$\begin{aligned} \bar{\mathbf{k}}_\kappa \cdot \bar{\mathbf{k}}_{3,\lambda} &\approx -\bar{b}_{\kappa\lambda} \approx \bar{\mathbf{k}}_\kappa^* \cdot \bar{\mathbf{k}}_{3,\lambda}^* \approx \mathbf{a}_\kappa \cdot \mathbf{R}^{*\top} \cdot (\mathbf{R}^*_{,\lambda} \cdot \mathbf{a}_3 + \mathbf{R}^* \cdot \mathbf{a}_{3,\lambda}) = \\ &= \mathbf{a}_\kappa \cdot \mathbf{R}^{*\top} \cdot \mathbf{R}^*_{,\kappa} \cdot \mathbf{a}_3 + \mathbf{a}_\kappa \cdot \mathbf{a}_{3,\lambda}, \end{aligned} \quad (5.14)$$

$$\begin{aligned} \bar{\mathbf{k}}_{3,\kappa} \cdot \bar{\mathbf{k}}_{3,\lambda} &\approx \bar{b}_{\kappa\mu} \bar{b}_{\lambda}^\mu \approx \bar{\mathbf{k}}_{3,\kappa}^* \cdot \bar{\mathbf{k}}_{3,\lambda}^* \approx (\mathbf{R}^*_{,\kappa} \cdot \mathbf{a}_3 + \mathbf{R}^* \cdot \mathbf{a}_{3,\kappa}) \cdot (\mathbf{R}^*_{,\lambda} \cdot \mathbf{a}_3 + \mathbf{R}^* \cdot \mathbf{a}_{3,\lambda}) = \\ &= \mathbf{a}_3 \cdot \mathbf{R}^{*\top}_{,\kappa} \cdot \mathbf{R}^*_{,\lambda} \cdot \mathbf{a}_3 + \mathbf{a}_3 \cdot \left(\mathbf{R}^{*\top}_{,\kappa} \cdot \mathbf{R}^* \cdot \mathbf{a}_{3,\kappa} + \mathbf{R}^{*\top}_{,\lambda} \cdot \mathbf{R}^* \cdot \mathbf{a}_{3,\kappa} \right) + \mathbf{a}_{3,\kappa} \cdot \mathbf{a}_{3,\lambda}, \end{aligned} \quad (5.15)$$

In obtaining (5.12), (4.6) has also been used.

5.4. In view of the previous results, the following are the scalar components of the Green-Lagrange strain tensor:

$$\begin{aligned} E_{\kappa\lambda} &= \mathbf{g}_\kappa \cdot \mathbf{E} \cdot \mathbf{g}_\lambda = \frac{1}{2} (\bar{\mathbf{g}}_\kappa \cdot \bar{\mathbf{g}}_\lambda - g_{\kappa\lambda}) \approx \frac{1}{2} [a_{\kappa\lambda} + \bar{\mathbf{k}}_\kappa \cdot (\bar{\alpha}_\lambda - \bar{\mathbf{k}}_\lambda) + (\bar{\alpha}_\kappa - \bar{\mathbf{k}}_\kappa) \cdot \bar{\mathbf{k}}_\lambda] + \\ &+ \frac{1}{2} [\mathbf{a}_\kappa \cdot \mathbf{R}^{*\top} \cdot \mathbf{R}^*_{,\lambda} \cdot \mathbf{a}_3 + \mathbf{a}_\lambda \cdot \mathbf{R}^{*\top} \cdot \mathbf{R}^*_{,\kappa} \cdot \mathbf{a}_3 - 2b_{\kappa\lambda}] x^3 + \frac{1}{2} [\mathbf{a}_3 \cdot \mathbf{R}^{*\top}_{,\kappa} \cdot \mathbf{R}^*_{,\lambda} \cdot \mathbf{a}_3 + \\ &+ \mathbf{a}_3 \cdot \mathbf{R}^{*\top}_{,\kappa} \cdot \mathbf{R}^* \cdot \mathbf{a}_{3,\lambda} + \mathbf{a}_3 \cdot \mathbf{R}^{*\top}_{,\lambda} \cdot \mathbf{R}^* \cdot \mathbf{a}_{3,\kappa} + b_{\kappa}^\mu b_{\mu\lambda}] (x^3)^2 - \frac{1}{2} g_{\kappa\lambda}, \end{aligned}$$

i.e.,

$$E_{\kappa\lambda} = E_{0\kappa\lambda} + E_{1\kappa\lambda}x^3 + E_{2\kappa\lambda}(x^3)^2, \quad (5.16)$$

$$E_{\perp\kappa\lambda} = -(\bar{b}_{\kappa\lambda} - b_{\kappa\lambda}) = \frac{1}{2} \left[\mathbf{a}_{\kappa} \cdot \mathbf{R}^{*\text{T}} \cdot \mathbf{R}^*_{,\lambda} \cdot \mathbf{a}_3 + \mathbf{a}_{\lambda} \cdot \mathbf{R}^{*\text{T}} \cdot \mathbf{R}^*_{,\kappa} \cdot \mathbf{a}_3 \right], \quad (5.17)$$

$$E_{2\kappa\lambda} = \frac{1}{2} \left(\bar{b}_{\kappa}^{\mu} \bar{b}_{\mu\lambda} - b_{\kappa}^{\mu} b_{\mu\lambda} \right) = \frac{1}{2} \left[\mathbf{a}_3 \cdot \mathbf{R}^{*\text{T}}_{,\kappa} \cdot \mathbf{R}^{*\text{T}}_{,\lambda} \cdot \mathbf{a}_3 + \mathbf{a}_3 \cdot \mathbf{R}^{*\text{T}}_{,\kappa} \cdot \mathbf{R}^* \cdot \mathbf{a}_{3,\lambda} + \mathbf{a}_3 \cdot \mathbf{R}^{*\text{T}}_{,\lambda} \cdot \mathbf{R}^* \cdot \mathbf{a}_{3,\kappa} \right], \quad (5.18)$$

and, furthermore,

$$E_{\kappa 3} = E_{3\kappa} = \mathbf{g}_{\kappa} \cdot \mathbf{E} \cdot \mathbf{g}_3 = \frac{1}{2} \bar{\mathbf{g}}_{\kappa} \cdot \bar{\mathbf{g}}_3 \approx \frac{1}{2} \vartheta_s \mathbf{a}_3 \cdot (\mathbf{a}_{\kappa} \times \mathbf{e}_s) = \frac{1}{2} \vartheta_s \sqrt{a} e_{\kappa\mu 3} e_{\underline{s}}^{\mu} \approx E_{0\kappa 3}, \quad (5.19)$$

$$E_{33} = \mathbf{g}_3 \cdot \mathbf{E} \cdot \mathbf{g}_3 = \frac{1}{2} (\bar{\mathbf{g}}_3 \cdot \bar{\mathbf{g}}_3 - g_{33}) \approx 0. \quad (5.20)$$

It is noted that the scalar components of the Green-Lagrange strain tensor obtained above at the arbitrary point P are related to the contravariant basis $\mathbf{g}^k \mathbf{g}^l$. Naturally, these components can also be written in the contravariant basis $\mathbf{a}^k \mathbf{a}^l$, using the inverse shifter μ_k^{-1m} .

5.5. To summarize the above results it is worth mentioning that when the above shell kinematics based on the Reissner-Mindlin hypothesis is employed, we obtain that $E_{33} \approx 0$ and $E_{\kappa 3} \approx E_{0\kappa 3}$, i.e. neither the change in the thickness, nor the variation of the transverse shear deformations across the thickness of the shell can be taken into account.

6. Concluding remarks

This paper investigates the middle surface of a shell in connection with the kinematical description of nonlinear shell theories. It is assumed that on the reference middle surface the displacements and the rotations of the base vectors are finite, whereas the strains are infinitesimal. A convected coordinate system attached to the middle surface is employed.

On the deformed middle surface, the tangential base vectors and, therefore, the unit normal are uniquely determined by the displacement field. To describe the rotation of the base vectors on the middle surface in the deformation process, this paper applies three rotation tensors.

There exist an infinitely large number of rotation tensors that rotate the unit normal vector and the tangential base vectors of the reference surface into the unit normal vector and tangent base vectors of the deformed middle surface. In this paper, one of the rotation tensors describing the above mentioned rotation (\mathbf{R}_2) is chosen in such a way that *the axis of the rotation lies in the tangent plane of the reference middle surface*. Such a rotation tensor is uniquely defined by the displacement field of the middle surface. The second rotation tensor ($\bar{\mathbf{R}}_n$) defined in the paper rotates

the tangent base vectors obtained by rotation (\mathbf{R}_2) in the tangent plane of deformed middle surface about its normal. This rotation is usually called drilling rotation in the specialist literature. Both rotations mentioned are finite and yield a single rotation ($\mathbf{R}^* = \overline{\mathbf{R}}_n \cdot \mathbf{R}_2$). The axis of the third rotation tensor ($\overline{\mathbf{R}}_s$) lies in the tangent plane of the deformed middle surface and performs an infinitesimally small rotation on the base vectors obtained after the previous two rotations. The resultant rotation tensor thus describes three, geometrically well identified (two finite and an infinitesimal) rotations and can be given by the product of the three rotation tensors ($\mathbf{R} = \overline{\mathbf{R}}_s \cdot \mathbf{R}^* = \overline{\mathbf{R}}_s \cdot \overline{\mathbf{R}}_n \cdot \mathbf{R}_2$). All the three rotation tensors are transformed onto the reference middle surface in the paper ($\mathbf{R} = \mathbf{R}^* \cdot \mathbf{R}_s = \mathbf{R}_2 \cdot \mathbf{R}_1 \cdot \mathbf{R}_s$). The transverse shear strains on the middle surface are obtained from the third, infinitesimally small rotation, whereas the description of the transverse normal strain requires the introduction of another parameter.

After describing the rotations of the base vectors, the complete three-dimensional deformation gradient tensor, the Green-Lagrange strain tensor as well as the symmetric right Jaumann strain tensor on the middle surface of the shell are determined, using the three-dimensional theory of deformation of solids. Due to the assumptions (neglections) introduced by the paper, the Green-Lagrange and the Jaumann strain tensors are identical on the middle surface.

The shell theory presented by this paper to investigate the middle surface of the shell leads hence to a seven-parameter shell model. These parameters consist of the three components of the displacement vector of the middle surface, one parameter of the rotation tensor $\overline{\mathbf{R}}_n$, two parameters of the rotation tensor $\overline{\mathbf{R}}_s$, and the seventh parameter is the transverse normal strain.

Acknowledgement. The support provided by the Hungarian National Research Foundation within the framework of the project OTKA T 046834 is gratefully acknowledged.

References

1. CHAPELLE, D. and BATHE, K.: Fundamental considerations for finite element analysis of shell structures. *Int. J. Num. Meths. Engng.*, **66**, (1998), 19–36.
2. VALENTE, R. F., JORGE, R. N., CARDOSO, R., DE SA, J. C., and GRACIO, J.: On the use an enhanced transverse shear strain shell element for problem involving large rotation. *Computational Mech.*, **30**, (2003), 286–196.
3. SIMMONDS, J. and DANIELSON, D.: Nonlinear shell theory with a finite rotation vector. *Proceedings, Kon. Ned. Ak. Wet., Series B.*, **73**, (1970), 460–478.
4. SIMMONDS, J. and DANIELSON, D.: Nonlinear shell theory with finite rotation and stress-function vectors. *J. Appl. Mech.*, **29**, (1972), 1085–1090.
5. WRIGGERS, P. and GRUTTMANN, F.: Thin shells with finite rotations formulated in biot stresses: theory and finite element formulation. *Int. J. Num. Meths. Engng.*, **36**, (1993), 2049–2071.
6. IBRAHIMBEGOVICH, A.: Stress resultant geometrically nonlinear shell theory with drilling rotations. part i. a consistent formulation. *Comput. Methods Appl. Mech. Engrg.*, **118**, (1994), 265–284.

7. IBRAHIMBEGOVICH, A. and FREY, F.: Stress resultant geometrically nonlinear shell theory with drilling rotations. part ii. computational aspects. *Comput. Methods Appl. Mech. Engrg.*, **118**, (1994), 285–308.
8. IBRAHIMBEGOVICH, A. and FREY, F.: Stress resultant geometrically nonlinear shell theory with drilling rotations. part iii. linearized kinematics. *Int. J. Num. Meths. Engrng.*, **37**, (1994), 3659–3683.
9. PIETRASZKIEWICZ, W.: Geometrically nonlinear theories of thin elastic shells. *Advances in Mechanics*, **12**, (1989), 51–130.
10. PIETRASZKIEWICZ, W.: On using rotations as primary variables in the non-linear theory of thin irregular shells. In D. G. D. Durban and J. Simmonds (eds.), *Advances in the mechanics of plates and shells*, pp. 245–258, Kluwer Academic Publisher, 2001.
11. WISNIEWSKI, K.: A shell theory with independent rotations for relaxed Biot stress and right stretch tensor. *Computational Mechanics*, **21**, (1998), 101–122.
12. BRANK, B., PERIC, D., and B.DAMJANICH, F.: On large deformations of thin elasto-plastic shells: implementation of finite rotation model for quadrilateral shell element. *Computers and Structures*, **40**, (1997), 689–726.
13. BRANK, B., BRISGHIELLA, L., PERIC, N. T., and DAMJANICH, F. B.: On non-linear dynamics of shells: implementation of energy-momentum conserving algorithm a finite rotation shell model. *Int. J. Num. Meths. Engrng.*, **42**, (1998), 409–442.
14. IBRAHIMBEGOVICH, A., BRANK, B., and COURTOIS, P.: Stress resultant geometrically exact form of classical shell model and vector-like parametrization of constrained finite rotations. *Int. J. Num. Meths. Engrng.*, **52**, (2001), 1235–1252.
15. BRANK, B. and IBRAHIMBEGOVICH, A.: On the relation between different parametrizations of finite rotations for shell. *Engineering Computations*, **18**, (2001), 950–971.
16. IBRAHIMBEGOVICH, A., MAMOURI, S., and BRANK, B.: Finite rotation shell elements for nonlinear statics and dynamics. In *European Congress on Computational Methods in Applied Sciences and Engineering. ECCOMAS*, 11–14 September 2000, p. 21.
17. LEE, W. and LEE, B.: An effective finite rotation formulation for geometrical non-linear shell structures. *Computational Mechanics*, **27**, (2001), 360–368.
18. ATLURI, S., IURA, M., and SUETAKE, Y.: A consistent theory of, and a variational principle for, thick elastic shells undergoing finite rotations. In D. G. D. Durban and J. Simmonds (eds.), *Advances in the mechanics of plates and shells*, pp. 17–32, Kluwer Academic Publisher, 2001.
19. CAMPELLO, E., PIMENTA, P., and WRIGGERS, P.: Triangular finite shell element based on a fully nonlinear shell formulation. *Computational Mechanics*, **31**, (2003), 505–518.
20. BERTÓTI, E.: *Non-linear shell theory in terms of stress-functions and rotations*. Dr.Sc. dissertation, Hungarian Academy of Sciences, 2003. In Hungarian.
21. PARISCH, H.: A continuum based shell theory for nonlinear applications. *Int. J. for Num. Meths. in Engrng.*, **38**, (1995), 1855–1883.
22. BASAR, Y. and DING, Y.: Shear deformation models for large strain shell analysis. *Int. J. Solids Structures*, **34**, (1997), 1687–1708.
23. BISCHOFF, M. and RAMM, E.: Shear deformation shell element for large strains and rotations. *Int. J. Numer. Mech. Engrng.*, **40**, (1997), 4427–4449.

24. SANSOUR, C. and KOLLMANN, F.: Families of 4-node and 9-node finite elements for a finite deformation shell theory. An assesment of hybrid stress, hybrid strain elements. *Computational Mechanics*, **24**, (2000), 435–447.
25. BUCALEM, M. and BATHE, K.-J.: Higher-order MITC general shell elements. *Int. J. Num. Meths. Engng.*, **36**, (1993), 3729–3754.
26. BATHE, K.-J., IOSILEVICH, A., and CHAPELLE, D.: An evaluation of the MITC shell elements. *Computers and Structures*, **75**, (2000), 1–30.

Appendix A.

This appendix contains the proof of equation $\bar{\mathbf{R}}_n \cdot \mathbf{R}_2 = \mathbf{R}_2 \cdot \mathbf{R}_1$, where

$$\begin{aligned}\bar{\mathbf{R}}_n &= \cos \vartheta_1 \mathbf{I} + (1 - \cos \vartheta_1) \bar{\mathbf{n}} \bar{\mathbf{n}} + \sin \vartheta_1 \bar{\mathbf{n}} \times \mathbf{I}, \\ \mathbf{R}_2 &= \cos \vartheta_2 \mathbf{I} + (1 - \cos \vartheta_2) \mathbf{e}_2 \mathbf{e}_2 + \sin \vartheta_2 \mathbf{e}_2 \times \mathbf{I}, \\ \mathbf{R}_1 &= \cos \vartheta_1 \mathbf{I} + (1 - \cos \vartheta_1) \mathbf{a}_3 \mathbf{a}_3 + \sin \vartheta_1 \mathbf{a}_3 \times \mathbf{I}, \\ \bar{\mathbf{n}} &= \mathbf{R}_2 \cdot \mathbf{a}_3 = \cos \vartheta_2 \mathbf{a}_3 + \sin \vartheta_2 \mathbf{e}_2 \times \mathbf{a}_3.\end{aligned}$$

Since the arbitrary vector \mathbf{c} can be written in terms of three orthogonal unit vectors $\mathbf{e}_2 \times \mathbf{a}_3$, \mathbf{e}_2 , \mathbf{a}_3 as $\mathbf{c} = c_1 \mathbf{e}_2 \times \mathbf{a}_3 + c_2 \mathbf{e}_2 + c_3 \mathbf{a}_3$, it is to be pointed out that

$$\bar{\mathbf{R}}_n \cdot \mathbf{R}_2 \cdot (\mathbf{e}_2 \times \mathbf{a}_3) = \mathbf{R}_2 \cdot \mathbf{R}_1 \cdot (\mathbf{e}_2 \times \mathbf{a}_3), \quad (\text{A.1})$$

$$\bar{\mathbf{R}}_n \cdot \mathbf{R}_2 \cdot \mathbf{e}_2 = \mathbf{R}_2 \cdot \mathbf{R}_1 \cdot \mathbf{e}_2, \quad (\text{A.2})$$

$$\bar{\mathbf{R}}_n \cdot \mathbf{R}_2 \cdot \mathbf{a}_3 = \mathbf{R}_2 \cdot \mathbf{R}_1 \cdot \mathbf{a}_3. \quad (\text{A.3})$$

Indeed, the transformations can be detailed on the one hand as

$$\begin{aligned}\bar{\mathbf{R}}_n \cdot \mathbf{R}_2 \cdot (\mathbf{e}_2 \times \mathbf{a}_3) &= \bar{\mathbf{R}}_n \cdot [\cos \vartheta_2 (\mathbf{e}_2 \times \mathbf{a}_3) - \sin \vartheta_2 \mathbf{a}_3] = \\ &= \cos \vartheta_1 [\cos \vartheta_2 (\mathbf{e}_2 \times \mathbf{a}_3) - \sin \vartheta_2 \mathbf{a}_3] + \\ &+ (1 - \cos \vartheta_1) [\sin \vartheta_2 (\cos \vartheta_2 \mathbf{a}_3 + \sin \vartheta_2 \mathbf{e}_2 \times \mathbf{a}_3) - \sin \vartheta_2 (\cos \vartheta_2 \mathbf{a}_3 + \sin \vartheta_2 \mathbf{e}_2 \times \mathbf{a}_3)] + \\ &+ \sin \vartheta_1 (\cos^2 \vartheta_2 \mathbf{e}_2 + \sin^2 \vartheta_2 \mathbf{e}_2),\end{aligned}$$

$$\begin{aligned}\bar{\mathbf{R}}_n \cdot \mathbf{R}_2 \cdot \mathbf{e}_2 &= \bar{\mathbf{R}}_n \cdot \mathbf{e}_2 = \\ &= \cos \vartheta_1 \mathbf{e}_2 + \sin \vartheta_1 [\cos \vartheta_2 (\mathbf{e}_2 \times \mathbf{a}_3) + \sin \vartheta_2 \mathbf{a}_3],\end{aligned}$$

$$\bar{\mathbf{R}}_n \cdot \mathbf{R}_2 \cdot \mathbf{a}_3 = \bar{\mathbf{R}}_n \cdot \bar{\mathbf{n}} = \bar{\mathbf{n}},$$

and, on the other hand, as

$$\begin{aligned}\mathbf{R}_2 \cdot \mathbf{R}_1 \cdot (\mathbf{e}_2 \times \mathbf{a}_3) &= \mathbf{R}_2 \cdot [\cos \vartheta_1 (\mathbf{e}_2 \times \mathbf{a}_3) + \sin \vartheta_1 \mathbf{e}_2] = \\ &= \cos \vartheta_2 [\cos \vartheta_1 (\mathbf{e}_2 \times \mathbf{a}_3) + \sin \vartheta_1 \mathbf{e}_2] + \\ &(1 - \cos \vartheta_2) \sin \vartheta_1 \mathbf{e}_2 - \sin \vartheta_2 \cos \vartheta_1 \mathbf{a}_3,\end{aligned}$$

$$\begin{aligned}\mathbf{R}_2 \cdot \mathbf{R}_1 \cdot \mathbf{e}_2 &= \mathbf{R}_2 \cdot [\cos \vartheta_1 \mathbf{e}_2 + \sin \vartheta_1 (\mathbf{a}_3 \times \mathbf{e}_2)] = \\ &= \cos \vartheta_2 [\cos \vartheta_1 \mathbf{e}_2 + \sin \vartheta_1 (\mathbf{a}_3 \times \mathbf{e}_2)] + \\ &+ (1 - \cos \vartheta_2) \cos \vartheta_1 \mathbf{e}_2 + \sin \vartheta_2 \sin \vartheta_1 \mathbf{a}_3,\end{aligned}$$

$$\mathbf{R}_2 \cdot \mathbf{R}_1 \cdot \mathbf{a}_3 = \mathbf{R}_2 \cdot \mathbf{a}_3 = \bar{\mathbf{n}},$$

i.e. conditions (A.1)-(A.3) hold.

Appendix B.

The positions of the base vectors with respect to each other do not change when they are rotated. Hence, the following relations hold (for example):

$$\bar{\mathbf{k}}_m^* \times \bar{\mathbf{k}}_k^* = (\mathbf{R}^* \cdot \mathbf{a}_m) \times (\mathbf{R}^* \cdot \mathbf{a}_k) = \mathbf{R}^* \cdot (\mathbf{a}_m \times \mathbf{a}_k), \quad (\text{B.1})$$

$$\begin{aligned} \bar{\mathbf{k}}_m \cdot \bar{\mathbf{k}}_k &= (\mathbf{R}_{\underline{s}} \cdot \bar{\mathbf{k}}_m^*) \cdot (\mathbf{R}_{\underline{s}} \cdot \bar{\mathbf{k}}_k^*) = \\ &= \bar{\mathbf{k}}_m^* \cdot \bar{\mathbf{k}}_k^* = (\mathbf{R}^* \cdot \mathbf{a}_m) \cdot (\mathbf{R}^* \cdot \mathbf{a}_k) = \mathbf{a}_m \cdot \mathbf{a}_k = a_{mk}. \end{aligned} \quad (\text{B.2})$$

COMPATIBILITY PATHS OF AN INFINITELY DEGENERATE MECHANISM

ANDRÁS LENGYEL², ZSOLT GÁSPÁR^{1,2}

¹HAS Research Group for Computational Structural Mechanics

²Department of Structural Mechanics

Budapest University of Technology and Economics

H-1521 Budapest, Műegyetem rkp. 3., Hungary

lengyel@eik.bme.hu, gaspar@ep-mech.me.bme.hu

[Received: January 14, 2004]

Abstract. The kinematic determinacy of a bar-and-joint mechanism is dependent on the topology and the metric properties of the structure. Special arrangements can result in singularities, such as bifurcation points on the compatibility paths. The analysis of a special four-bar linkage yields an infinitely degenerate bifurcation point. Modifications in plane and in space are investigated in order to produce the most general perturbations of the system. The compatibility path can be perturbed to have a shape of arbitrary finite order or to result in compatible states in an arbitrary finite number.

Mathematical Subject Classification: 53A17, 58K35

Keywords: kinematic determinacy, bifurcation points, compatibility path

1. Introduction

A mechanism consisting of rigid bars with a prescribed length and a given topology is called a mechanism with a single degree-of-freedom if it typically has compatible positions where, applying a suitable displacement to a suitable element, the displacement of the other elements can be uniquely determined. Compatibility paths form a set of points which belong to compatible positions in the space of the state variables chosen to define the position of the mechanism. The compatibility paths usually consist of lines which can intersect one another (bifurcation points).

Bifurcation points arise from special geometric configurations. If a mechanism is created with a special geometry, it may have certain positions where the number of instantaneous kinematic degrees-of-freedom increases. At these points the mechanism can change shape and continue its motion along a different path.

Bifurcations of compatibility paths have been studied by several researchers. Tarnai [1] and Litvin [2] have shown mechanisms producing asymmetric bifurcations. Lengyel and You [3] discussed further examples and compared this phenomenon to the well-known equilibrium bifurcations of elastic structures. They made further examinations

with the aid of the elementary catastrophe theory [4]. Their method was based on the analogy between equilibrium and compatibility equations.

In paper [5] we proposed a general classification of the points of the compatibility paths. With the aid of an energy function we showed a connection between singularities and catastrophe types in Thom's theorem [6]. A catastrophe point is a singularity of the system where a small change of the parameter(s) may cause significantly different behavior according to the perturbation. Consequently the number of solutions of the governing equations may change, i.e. in this case the number of possible compatible states. Hence at catastrophe points one may apply small perturbations to the original layout of the system so that a different number of states is obtained [5]. The maximum number of the compatible configurations forms the basis of the classification of the singular points.

In paper [5] we also showed a degenerate planar mechanism that produced infinite compatible positions at the critical value of the control parameter. This paper examines the mechanism and presents a perturbation that reduces the degeneracy to arbitrary finite order. The layout of the paper is as follows. The second part introduces the basic structure. The third part defines the geometrical modifications of the system and the mathematical formulation is given in the fourth.

2. Basic structure

Consider a special four-bar linkage with all bars having unit length shown in Figure 1a. The compatibility paths of the mechanism consist of straight lines plotted in the coordinate system

$$(\alpha, \beta)$$

as shown in Figure 1b [4, 5]. Each value of β corresponds to a certain position of node B on the perimeter of a unit circle centered at O_B . Geometrically possible positions

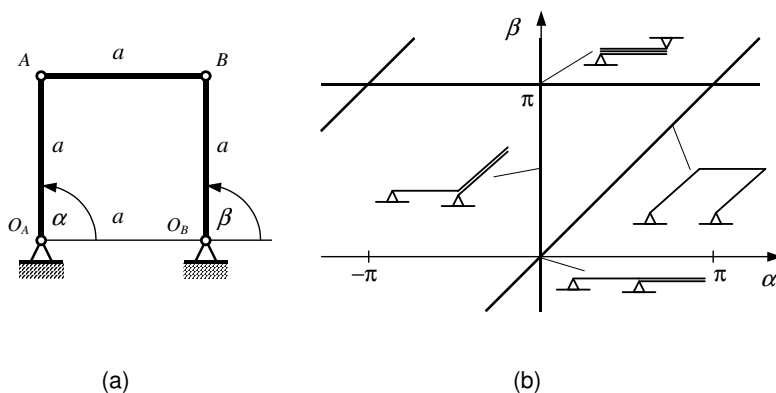


Figure 1. Four-bar mechanism (a) basic structure (b) compatibility path

of node A must be at a unit distance from both O_A and B , and hence compatible configurations of the mechanism are obtained at the intersections of a unit circle centered at O_A (set S_1) and another one centered at B (set S_2).

The behaviour of the points of the compatibility paths is determined by the properties of the intersections, which can be further studied by examining the transversality of the sets [7]. Let X and Y be affine subspaces of \mathbb{R}^n of dimensions s, t , respectively, where \mathbb{R} denotes the set of real numbers. They meet transversely if either their intersection $X \cap Y$ is empty or its dimension is $s + t - n$ (if this number is non-negative). Two submanifolds of \mathbb{R}^n meet transversely at a given point provided either they do not meet, or their tangent affine hyperplanes meet transversely.

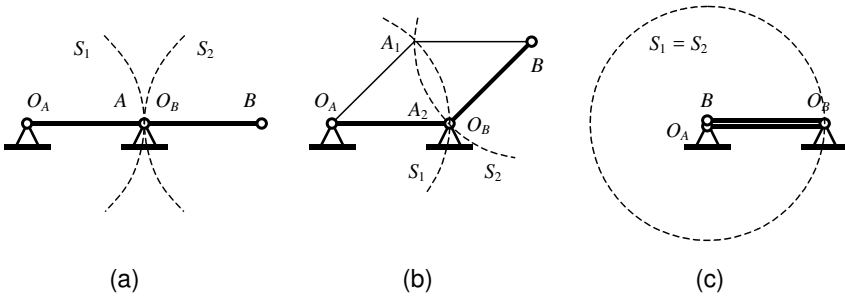


Figure 2. Compatible configurations at different values of parameter β (a) $\beta = 0$ (b) $0 < \beta < \pi$ (c) $\beta = \pi$

At $\beta = 0$ only one compatible configuration exists as the two circles have one common point (see Figure 2a). The tangents are common, hence the intersection is not transverse. At $0 < \beta < \pi$ two intersections are obtained: $\alpha = 0$ and $\alpha = \beta$ (see Figure 2b). Here the two sets meet transversely because the tangents are not parallel. At $\beta = \pi$ node B and O_A coalesce and the two circles become the same (see Figure 2c). This is again a non-transverse intersection. Here all values of α correspond to compatible configurations. Thus at the bifurcation point

$$(\alpha = 0, \beta = \pi)$$

there is an infinitely degenerate compatibility path.

A small perturbation of the system modifies the sets S_1 and S_2 and, consequently, the number of compatible positions of the mechanism. The first of the three cases above is non-transverse. A small perturbation of the geometry, such as imperfections of lengths of the bars or of positions of supports, would make the circles detach or intersect at two points transversely (Figure 3a). In the second case the circles meet at two points transversely and the transversality is unchanged by a small perturbation (Figure 3b). In the third case the two circles coalesce and a small perturbation can reduce the number of intersections to two, one, or none (Figure 3c). The three cases are denoted by dashed, dotted and dashdot lines, respectively.

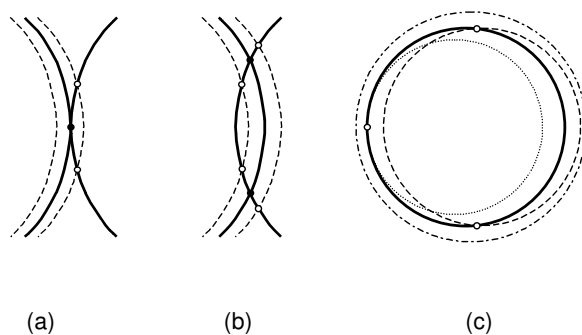


Figure 3. Transversality of intersections of two circles

Planar imperfections can modify the behaviour to produce one or two compatible configurations or none. Our goal is to create a non-transverse intersection that can be modified by a suitable small perturbation so that the number of compatible configurations is any arbitrarily chosen number. In order to obtain this, we introduce a spatial structure.

3. Spatial configuration

Consider the mechanism in Figure 1a with unchanged topology but with spherical joints applied at nodes O_A , A and B . Also keep the revolute joint at O_B . The mechanism has two independent degrees-of-freedom by means of these modifications. Sets S_1 and S_2 become unit spheres in the

$$(X, Y, Z)$$

coordinate system shown in Figure 4a. The two spheres typically meet at transverse points forming a circle $C_1 = S_1 \cap S_2$. At point $\beta = \pi$ the two spheres coalesce and all points are non-transverse intersections (Figure 4b): $C_1 = S_1 = S_2$.

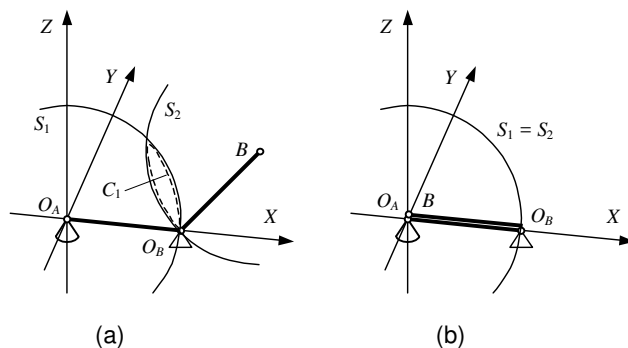


Figure 4. Spatial configuration (a) $0 < \beta < \pi$ (b) $\beta = \pi$

In order to obtain a mechanism with a single degree-of-freedom, the number of degree-of-freedom has to be reduced by introducing an additional support. Let now node A be supported by a roller allowing it to move on a given smooth surface

$$S_3 = S_3(X, Y)$$

(Figure 6). Hence now the motion of node A is restricted to the intersection set $C_2 = S_1 \cap S_3$, i.e. the common points of the sphere S_1 and the surface S_3 , which is a curve on the surface of sphere S_1 . Compatible positions can be obtained only at points which are on curve C_1 as well because A has to be on S_2 , the circle centered at B . The set of compatible positions is now defined as

$$P = C_1 \cap C_2 = S_1 \cap S_2 \cap S_3 .$$

Now in case of $\beta = \pi$ it is possible to apply appropriate imperfections to the structure so that the set of intersections is reduced to a required finite number. Let

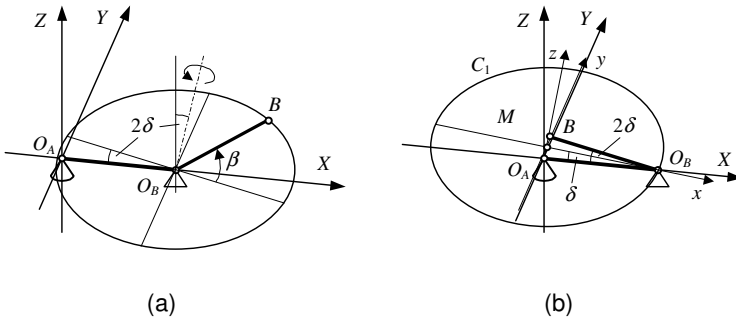


Figure 5. Imperfection of joint O_B (a) tilting angle (b) intersection circle

us do this in a number of steps as follows. First let the axis of rotation of joint O_B be tilted from Z by a small angle 2δ anticlockwise in plane (X, Z) as is shown in Figure 5a. Node B at $\beta = \pi$ is out of the plane (X, Y) :

$$B(1 - \cos 2\delta, 0, \sin 2\delta) .$$

Hence the intersection of the two spheres is a circle: $C_1 = S_1 \cap S_2$. It is centered at M , the middle point of section $O_A B$ and is fitting to point O_B (Figure 5b), hence its plane is tilted from (X, Y) by angle δ . It is then possible to define the surface S_3 so that C_1 and C_2 meet non-transversely at O_B and they produce a required number of intersections.

In order to do that, let us define the final shape of C_2 in a few steps. First construct S_3 so that C_2 be equal to C_1 . Then rotate points $P \in C_2$ around axis MO_B by an angle which is not constant but proportional to the n th order of the sine of the arc length $O_B P$. It adds an n th order perturbation to circle C_2 . The first perturbation term is shown in Figure 7a. If a suitable linear combination of these terms of various orders is applied, then an oscillating curve is obtained which has n intersections with

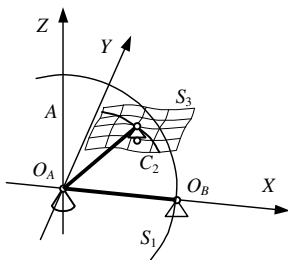


Figure 6. Perturbation of motion A

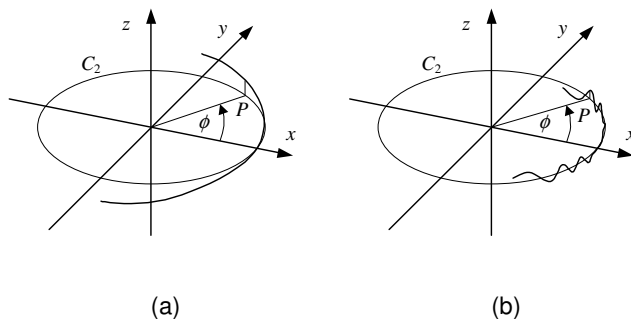


Figure 7. Perturbation (a) single term (b) combination

C_1 in the vicinity of O_B (Figure 7b). If the highest order term is the n th, a maximum of n intersections can be obtained by suitable imperfections. These are the only points referring to compatible configurations of the mechanism.

4. Transformations

The mathematical formulation of the principles above is as follows. C_1 is a circle centered at

$$M((1 - \cos 2\delta)/2, 0, \sin 2\delta/2)$$

with radius $r = \cos \delta$. A local

$$(x, y, z)$$

coordinate system is created so that x and y cover the plane of C_1 and x is aligned with MO_B as shown in Figure 5b. In this local system the points of the circle $c \in C_1$ can be defined as

$$c = (r \cos \varphi, r \sin \varphi, 0)^T$$

where angle φ measures the $O_B P$ arc length. An i th order rotational perturbation around axis x mentioned above is given by the transformation matrix:

$$T_i = \begin{bmatrix} 1 & 0 & 0 \\ 0 & \cos(p_i \sin^i \varphi) & -\sin(p_i \sin^i \varphi) \\ 0 & \sin(p_i \sin^i \varphi) & \cos(p_i \sin^i \varphi) \end{bmatrix}, \tag{1}$$

where p_i is a suitable constant and i is a positive integer number. A linear combination of these terms gives the final shape of the curve C_2 in the local (x, y, z) coordinate system:

$$\mathbf{c}_2^{xyz} = \sum_i \mathbf{T}_i \mathbf{c} = \sum_i \begin{bmatrix} 1 & 0 & 0 \\ 0 & \cos(p_i \sin^i \varphi) & -\sin(p_i \sin^i \varphi) \\ 0 & \sin(p_i \sin^i \varphi) & \cos(p_i \sin^i \varphi) \end{bmatrix} \begin{bmatrix} r \cos \varphi \\ r \sin \varphi \\ 0 \end{bmatrix}. \tag{2}$$

In the global coordinate system (X, Y, Z) a rotation and a translation yield the equation

$$\mathbf{c}_2^{XYZ} = \mathbf{T} \mathbf{c}_2^{xyz} + \mathbf{v}, \tag{3}$$

where the rotational matrix \mathbf{T} and the translation vector \mathbf{v} define the transformation from (x, y, z) to (X, Y, Z) :

$$\mathbf{T} = \begin{bmatrix} \cos \delta & 0 & \sin \delta \\ 0 & 1 & 0 \\ -\sin \delta & 0 & \cos \delta \end{bmatrix}, \quad \mathbf{v} = \begin{bmatrix} (1 - \cos 2\delta) / 2 \\ 0 \\ (\sin 2\delta) / 2 \end{bmatrix}. \tag{4}$$

5. Conclusions

In this paper we have examined how the compatibility of an infinitely degenerate mechanism can be modified by suitable imperfections of the geometry. Discrete geometric imperfections of the structure, e.g. a constant error of the length of the bars or of the position of the supports can only add a limited (second order) variation to the degenerate compatibility path as not more than two possible compatible positions can be obtained at a certain value of the parameter. Therefore, in order to exploit the potential of the degeneracy of the geometry, a spatial modification has been introduced incorporating a continuum perturbation of the system. Forcing the motion of node A on a smooth continuous surface above the coordinate plane allows us to define a compatibility path of arbitrary shape in the neighborhood of the bifurcation point.

Acknowledgement. The authors acknowledge the financial support of The European Science Exchange Programme extended by The Royal Society. The work of the first author was also supported by University Graduate Scholarship at St Edmund Hall, University of Oxford and the Hungarian Grant OTKA D45978. The second author thanks for the support of the Hungarian Grant FKFP 0308/2000 and OTKA T031931.

References

1. TARNAI T.: Rigidity and kinematic bifurcation of structures. 40th Anniversary Congress of the International Association for Shell and Spatial Structures 1, B 2.81-B 2.90, CEDEX, 1999.

2. LITVIN, F. L.: Application of theorem of implicit function system existence for analysis and synthesis of linkages. *Mechanism and Machine Theory*, **15**, (1980), 115-125.
3. LENGYEL, A. and YOU, Z.: Analogy between bifurcations in stability of structures and kinematics of mechanisms. *Mechanics based design of structures and machines*, **31**(4), (2003), 491-507.
4. LENGYEL, A. and YOU, Z.: Bifurcations of SDOF mechanisms using catastrophe theory. *International Journal of Solids and Structures*, **41**(2), (2004), 559-568.
5. LENGYEL, A. and GÁSPÁR, Z.: Classification of compatibility paths of SDOF mechanisms. Submitted to *International Journal of Solids and Structures* for publication.
6. THOM, R.: *Structural Stability and Morphogenesis*. Benjamin-Addison Wesley, New York, 1975. (Translation of R. Thom, *Stabilité Structurelle et Morphogénèse*. Benjamin, New York, 1972.)
7. POSTON, T. AND STEWART, I.: *Catastrophe Theory and its Applications*. Pitman, London, 1978.

THREE-COMPONENT DISCRETELY-FIBROUS COMPOSITES UNDER MATRIX MICRODAMAGING

LIDIYA V. NAZARENKO

Department of Wave Propagation, Institute of Hydromechanics
03680 Kyiv, Ukraine
lnazarenko@yandex.ru

[Received: February 8, 2005]

Abstract. In the present paper a model for the nonlinear deformations in stochastic composites under microdamaging is developed for three-component composites providing that the microdamage is accumulated in the matrix. The composite is treated as an isotropic matrix strengthened by two different types of spheroidal inclusions with transversally-isotropic symmetry of elastic properties. It is assumed that the loading process leads to accumulation of damage in the matrix. Fractured microvolumes are modeled by a system of randomly distributed quasispherical pores. The porosity balance equation and relations for determining the effective elastic modules for the case of transversally-isotropic components are taken as basic relations. The fracture criterion is assumed to be given as the limit value of the intensity of average shear stresses occurring in the undamaged part of the material. Based on the analytical and numerical approach the algorithm for determination of nonlinear deformative properties of such a material is constructed. The nonlinearity of composite deformations is caused by finiteness of component deformations. Using the numerical solution, the nonlinear stress-strain diagrams for three-component concrete for the case of uniaxial tension are obtained.

Mathematical Subject Classification: 74R99, 74M99

Keywords: stochastic composites, microdamaging, anisotropic components

1. Introduction

Deformation of composites may become nonlinear with increase in macrostrains or macrostresses. Physical nonlinearity of macrostress - macrostrain relations is due to the nonlinearity of physical deformations in the components or microdamages manifesting itself as micropores or microcracks. In this paper the nonlinear effective deformation properties of a composite attributed to the growth of microdamage in the deformed components are considered.

The idea on accumulation of scattered microscopic cavities occurring in a material under a load, resulting in a decrease in the effective (bearing) cross-sectional area, is based on the theory of material damage. The corresponding research is based on the introduction of a so-called 'damage' parameter with the associated evolutionary equation postulated in [1, 2]. Constants entering this equation are determined

from long-term strength or creep tests. Such a formal approach is essentially equivalent to replacing time by another parameter (damage), which depends on time in a certain way so that it cannot provide knowledge or conceptions, supplementing the experiment, about the nature of the process, especially about structural changes in the material or the specific mechanism of the process. Moreover, any identification of damage with time will not encompass the extensive class of phenomena of short-period damage, manifested in the experimentally observed one-to-one dependence of the content of submicroscopic cracks on the given deformation, for example as it was shown in [3]. This also leaves aside the fundamental question on the structure of the relationship between damage and the physical and mechanical properties of a material.

The above indicates that a rational approach to the description of damage to a material and the phenomena accompanying it can be based only on the simulation of damage by specific structural microscopic elements in the form of the system of microcracks or micropores and on the construction of appropriate equations for the mechanics of a macroscopically inhomogeneous medium, allowing for the interaction of the processes of damage and deformation of the material. Such an informal approach applies to short-term damage of materials. The damage process is simulated by formation of a system of randomly distributed micropores, which are empty or are filled with destroyed material, in those microscopic volumes where microscopic destruction (microdestruction) occurs. The destruction criterion is taken in the form of the ultimate value of the intensity of shear stresses averaged over the undamaged part of the material or the Schleicher-Nadai criterion. The yield strength is assumed to be the random function of the coordinates, the single-point distribution of which is described by the power-law or Weibull distribution. The effective deformative properties and the stress-strain state of the material are determined from stochastic equations of the elasticity theory [4] - [6], which allow for the random nature of the arrangement of microdestruction. An equation of porosity balance is formulated for determining the porosity, which changes as a consequence of microdestruction. This fact makes it possible to describe the combined process of deformation and microdamage with allowance for their interaction, which leads to the nonlinear relationships between macrostresses and macrodeformations.

Microdestructions occur in the weakest microvolumes of a material under high-level loads, which reduces the bearing section of the material and leads to a redistribution of microstresses, and hence to nonlinear relationships between macrostresses and macrodeformations. The essence of this mechanism is described in [3] using the simplest working scheme for a material, in the form of the system of parallel, linearly elastic rods having a randomly distributed yield strength and acted upon by a uniform tensile load. The successive destruction of some of the rods under load results in a nonlinear deformation of a pattern.

The deformation and microdestruction of actual materials are considerably more complex processes, due primarily to the three-dimensional character of the stress-strain state and the random arrangement of the local microdestructions. The structural inhomogeneity of elastic properties, typical of composite materials, introduces

additional complications. Experimental research [3] shows that during uniaxial stretching of polymer materials, submicrocracks develop with ratios of transverse to longitudinal dimensions ranging from 0.4 to 1.3. If we will assume that the part of the material in the vicinity of a disk-shaped crack does not carry a load along the major axis, as well as the disorientation of submicrocracks is not uniform and the stress state is complex due to the non-uniformity of the structure, then there are every reasons to simulate an individual act of microdestruction by a quasi-spherical pore. We take the limiting value of intensity of shear stresses in the microvolume as the condition for the appearance of individual microdestruction. Nor does invariance of the microdestruction criterion provide a basis for assuming a certain orientation for the individual microdestruction. We assume the arrangement of individual pieces of microdestruction in the material to be random, satisfying the criteria of statistical uniformity and isotropy.

The model of short-term microdamaging of composites of the stochastic structure, taking into account the distribution of material strength, is proposed by Khoroshun in [7]. This model is developed in papers [8, 9] for composite materials with isotropic components provided that microdestructions occur in the matrix or inclusions. The approach has received development in paper [10] for anisotropic materials, and then for composites with anisotropic components in [11]. The present work is devoted to the investigation of macrodeformations in three-component composites representing an isotropic matrix, randomly reinforced by two types of unidirectional spheroidal inclusions with various elastic properties and geometrical parameters. It is assumed that the accumulation of microdamage occurs in the matrix.

2. Mechanical model

Let us consider the representative volume V of a composite material subjected to uniform macrodeformations $\langle \varepsilon_{\alpha\beta} \rangle$. The composite is treated as an isotropic matrix strengthened by stochastically distributed unidirectional spheroids with various elastic constants and various geometrical parameters. Such a type of composite is shown in Figure 1. We suppose that the physical and mechanical properties of the material of inclusions have transversally-isotropic symmetry. It is assumed that the matrix shows initial microdamage, which is modelled by a system of randomly distributed micropores of quasispherical shape. The effective deformative properties and the stress-strain state of such a composite is determined on the basis of the stochastic equations of the elasticity theory by the method of conditional moment functions stated in [5].

Under homogeneous loading, the stresses and strains appearing in the representative volume will form statistically homogeneous random fields satisfying the ergodicity condition. In this case we can replace the operation of averaging over the representative volume by the operation of averaging over an ensemble of realizations. Then the macroscopic stresses $\langle \sigma_{ij} \rangle$ and strains $\langle \varepsilon_{\alpha\beta} \rangle$ of such a material will be related by Hooke's law:

$$\langle \sigma_{ij} \rangle = \lambda_{ij\alpha\beta}^{**} \langle \varepsilon_{\alpha\beta} \rangle, \quad (i, j, \alpha, \beta = 1, 2, 3). \quad (2.1)$$

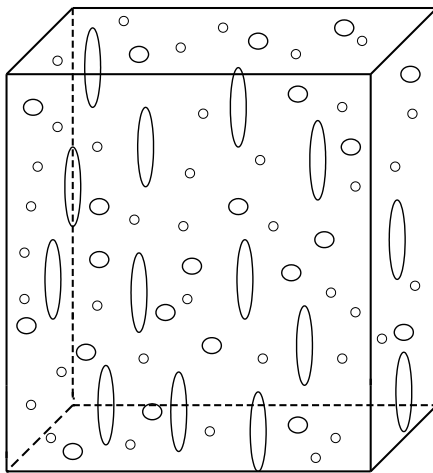


Figure 1. Type of the composite under consideration.

Here $\lambda_{ij\alpha\beta}^{**}$ is the tensor of effective elastic constants for the given composite which is determined in three steps. In the first step the elastic modules of the matrix weakened by micropores (microdamage) is determined on the basis of the results presented in paper [12]

$$\lambda_{ij\alpha\beta}^p = \lambda_{ij\alpha\beta}^p \left(\lambda_{ij\alpha\beta}^{[3]}, p_0 \right). \quad (2.2)$$

Here $\lambda_{ij\alpha\beta}^p$ is the tensor of elastic modules of a porous matrix, which depends on the elastic constants of matrix material $\lambda_{ij\alpha\beta}^{[3]}$ and the initial porosity p_0 of matrix. Then using the results, obtained in paper [6] for transversally-isotropic composites of stochastic structure, we can calculate the effective elastic modules of a two-component composite with porous matrix and spheroidal inclusions

$$\lambda_{ij\alpha\beta}^* = \lambda_{ij\alpha\beta}^* \left(\lambda_{ij\alpha\beta}^{[1]}, \lambda_{ij\alpha\beta}^p, c_1, t_1 \right), \quad (2.3)$$

as the function of elastic module tensors of inclusions $\lambda_{ij\alpha\beta}^{[1]}$ and porous matrix $\lambda_{ij\alpha\beta}^p$, volume content of inclusions in matrix c_1 and their geometrical parameters t_1 , which are characterized by the ratio of the spheroid semi-axes. In the last step we calculate the effective elastic properties of the composite material with a porous matrix stochastically reinforced by spheroidal fibres of two types which have different elastic properties and geometrical parameters:

$$\lambda_{ij\alpha\beta}^{**} = \lambda_{ij\alpha\beta}^{**} \left(\lambda_{ij\alpha\beta}^*, \lambda_{ij\alpha\beta}^{[2]}, c_2, t_2 \right), \quad (2.4)$$

where $\lambda_{ij\alpha\beta}^{[2]}$ is the elastic module tensor of the material of inclusions of the second type, and c_2 and t_2 are their volume content and the ratio of the spheroid semi-axes. Considering equations (2.2) - (2.4), it is possible to make the conclusion that the

effective elastic properties of such a composite $\lambda_{ij\alpha\beta}^{**}$ certainly depend on the elastic constants of components and geometrical parameters of fibers, and also on the initial porosity of matrix p_0

$$\lambda_{ij\alpha\beta}^{**} = \lambda_{ij\alpha\beta}^{**} \left(\lambda_{ij\alpha\beta}^{[1]}, \lambda_{ij\alpha\beta}^{[2]}, \lambda_{ij\alpha\beta}^{[3]}, c_1, c_2, p_0, t_1, t_2 \right). \tag{2.5}$$

For the known effective elastic modules of such a composite, it is possible to calculate the matrix macrostrains $\langle \varepsilon_{\alpha\beta} |_3 \rangle$ using consecutively the relations obtained in paper [11] for two-component composites:

$$\begin{aligned} \langle \varepsilon_{\alpha\beta} |_3 \rangle = & \left(I_{\alpha\beta kl} + (1 - c_2) \left(c_2 \lambda_{\alpha\beta kl}^{[2]} + (1 - c_2) \lambda_{\alpha\beta kl}^* - \lambda_{\alpha\beta kl}^{**} \right) \left(\lambda_{kl\gamma\rho}^{[2]} - \lambda_{kl\gamma\rho}^* \right)^{-1} \right) * \\ & * \left(I_{\gamma\rho mn} + c'_3 \left(\langle \lambda_{\gamma\rho mn} \rangle - \lambda_{\gamma\rho mn}^* \right) \lambda_{mnij}^{[4]-1} \right) \langle \varepsilon_{ij} \rangle, \end{aligned} \tag{2.6}$$

in which

$$\langle \lambda_{\gamma\rho mn} \rangle = c'_1 \lambda_{\gamma\rho mn}^{[1]} + c'_3 \lambda_{\gamma\rho mn}^{[3]}; \quad \lambda_{mnij}^{[4]} = \lambda_{mnij}^{[1]} - \lambda_{mnij}^{[3]}, \tag{2.7}$$

where

$$(i, j, k, l, m, n, \alpha, \beta, \gamma, \rho = 1, 2, 3).$$

Here c_3 is the volume content of the binding in a composite, and c'_1 and c'_2 are defined by the following ratios:

$$c'_1 = \frac{c_1}{c_1 + c_3}, \quad c'_3 = \frac{c_3}{c_1 + c_3}, \quad c_1 + c_2 + c_3 = 1. \tag{2.8}$$

Macrostrains and macrostresses in a matrix are related to each other by Hooke's law:

$$\langle \sigma_{ij} |_3 \rangle = \lambda_{ij\alpha\beta}^{[3]} \langle \varepsilon_{\alpha\beta} |_3 \rangle. \tag{2.9}$$

At the same time, stresses averaged over the matrix skeleton $\langle \sigma_{ij}^{3p} \rangle$ are connected with average stresses over all the matrix $\langle \sigma_{ij} |_3 \rangle$ by the following dependence:

$$\langle \sigma_{ij}^{3p} \rangle = \frac{1}{1 - p_0} \langle \sigma_{ij} |_3 \rangle. \tag{2.10}$$

Thus, on the basis of expressions (2.6)-(2.10) stresses averaged over the matrix skeleton $\langle \sigma_{ij}^{3p} \rangle$ are connected with macrostrains by means of the relationships:

$$\begin{aligned} \langle \sigma_{\alpha\beta}^{3p} \rangle = & \frac{1}{1 - p_0} \lambda_{\alpha\beta mn}^{[3]} * \\ & * \left(I_{\alpha\beta kl} + (1 - c_2) \left(c_2 \lambda_{\alpha\beta kl}^{[2]} + (1 - c_2) \lambda_{\alpha\beta kl}^* - \lambda_{\alpha\beta kl}^{**} \right) \left(\lambda_{kl\gamma\rho}^{[2]} - \lambda_{kl\gamma\rho}^* \right)^{-1} \right) * \\ & * \left(I_{\gamma\rho mn} + c'_3 \left(\langle \lambda_{\gamma\rho mn} \rangle - \lambda_{\gamma\rho mn}^* \right) \lambda_{mnij}^{[4]-1} \right) \langle \varepsilon_{ij} \rangle. \end{aligned} \tag{2.11}$$

Let us take the strength condition for the microvolume of the undestroyed part of a matrix as the Huber-Mises criterion [3]:

$$I_\sigma^3 = \left(\langle \sigma_{ij}^{3p} \rangle', \langle \sigma_{ij}^{3p} \rangle' \right) = k_3, \tag{2.12}$$

where $\langle \sigma_{ij}^{3p} \rangle'$ is the deviator of stresses averaged over a matrix skeleton, and k_3 is the corresponding limit value of microstrength of the matrix, being a stochastic function of coordinates. One-point distribution function $F(k_3)$ of random variable k_3 can be described by the exponential distribution function in a semi-infinite domain, i.e. the Weibull distribution:

$$F(k_3) = \begin{cases} 0 & \text{if } k_3 < k_0, \\ 1 - \exp(-n(k_3 - k_0)^\alpha) & \text{if } k_3 \geq k_0. \end{cases} \quad (2.13)$$

Here k_0 is the lower limit value of the intensity of the averaged tangential stresses over the matrix skeleton where destruction in some microvolumes begins; n and α are the factors chosen from a condition of the best approximation of strength distribution which is determined experimentally for each material.

If the stresses of the matrix skeleton $\langle \sigma_{ij}^{3p} \rangle$ are known, the function $F(I_\sigma^3)$ determines, according to formulas (2.12), (2.13), the relative content of the destroyed microvolumes in a matrix. If the destroyed microvolumes are modeled by the pores, it is possible to write down the balance porosity equation:

$$p = p_0 + F(I_\sigma^3) (1 - p_0), \quad (2.14)$$

where p_0 is the initial porosity of the matrix. According to the formula (2.11), stresses of matrix skeleton $\langle \sigma_{ij}^{3p} \rangle$ can be expressed as a function of macrostrains of all composite $\langle \varepsilon_{\alpha\beta} \rangle$. These equations enable us to determine the current porosity of matrix p , generated by microdestructions, from nonlinear algebraic equations (2.12) - (2.14), as a dependence on macrostrains. Thus, we obtain the nonlinear dependence of macrostresses on macrostrains (2.2) - (2.14), caused by the matrixes microdestructions, with regard to strength distribution of a material.

3. Iterative scheme of equation solution

On the basis of the proposed model and the constructed solutions for the effective properties and stress-strain state of the elastic material, reinforced by two types of spheroidal inclusions with various elastic properties and geometrical parameters it is possible to investigate the accumulation of damage and the nonlinear deformation caused by microdamaging of transversally-isotropic composite under uniform macrodeformations. For given uniform macrostrains $\langle \varepsilon_{\alpha\beta} \rangle$ the matrix microdamaging, characterized by porosity p , is determined from the nonlinear system of equations (2.12) - (2.14). The solution of such a system of nonlinear equations can be obtained on the basis of the following iterative scheme.

Matrix porosity $p^{(n)}$ for the n -th approximation is determined as the function of the limiting value of averaged tangential stresses of a binding skeleton for the n -th approximation $I_\sigma^{3(n)}$. The averaged tangential stresses of the skeleton are related to the current porosity of a matrix in the $(n-1)$ -th approximation $p^{(n-1)}$ via equations (2.5), (2.11).

Thus, on the basis of equations (2.13), (2.14) we can write

$$p^{(n)} = p_0 + F \left(I_\sigma^{3(n)} \right) (1 - p_0) , \tag{3.1}$$

where

$$F \left(I_\sigma^{3(n)} \right) = \begin{cases} 0 & \text{if } I_\sigma^{3(n)} < k_0 , \\ 1 - \exp \left(-n \left(I_\sigma^{3(n)} - k_0 \right)^\alpha \right) & \text{if } I_\sigma^{3(n)} \geq k_0 . \end{cases} \tag{3.2}$$

According to expressions (2.6) – (2.12)

$$I_\sigma^{3(n)} = \varphi \left(\lambda_{ij}^{**(n-1)} , p^{(n-1)} , \langle \varepsilon_{\alpha\beta} \rangle \right) , \tag{3.3}$$

while the tensor components of the effective elastic modules for the composite can be determined from formulas (2.5)

$$\lambda_{ij\alpha\beta}^{**(n-1)} = \lambda_{ij\alpha\beta}^{**} \left(\lambda_{ij\alpha\beta}^{[1]} , \lambda_{ij\alpha\beta}^{[2]} , \lambda_{ij\alpha\beta}^{[3]} , c_1 , c_2 , p^{(n-1)} , t_1 , t_2 \right) . \tag{3.4}$$

Hence, equations (3.1)-(3.4) allow us to investigate the effective elastic characteristics of porous transversally isotropic composites as a function of macrodeformations

$$\lambda_{ij\alpha\beta}^{**} = \lim_{n \rightarrow \infty} \lambda_{ij\alpha\beta}^{**(n)} . \tag{3.5}$$

Thus, giving the macrodeformation of the composite, and determining its effective elastic modules, from equations (3.1)-(3.5) it is possible to investigate the macrostresses arising in such a composite.

4. Numerical results and discussion

Using the above method and the relations obtained for determining the current porosity of a matrix material, as an example, we can construct the nonlinear diagram of macrodeformation and investigate the behavior of a concrete representing the cement matrix, strengthened by crushed stones and metal fibres under uniaxial extension

$$\left(\langle \varepsilon_{11} \rangle \neq 0 , \quad \langle \varepsilon_{22} \rangle = 0 , \quad \langle \varepsilon_{33} \rangle = 0 \right) . \tag{4.1}$$

The elastic modulus and Poisson’s ratios of crushed stone, metal and concrete are, respectively, equal to:

$$\begin{aligned} E^{[1]} &= 3 \cdot 10^8 \text{ Pa} , & \nu^{[1]} &= 0.4 , \\ E^{[2]} &= 2000 \cdot 10^8 \text{ Pa} , & \nu^{[2]} &= 0.25 , \\ E^{[3]} &= 300 \cdot 10^8 \text{ Pa} , & \nu^{[3]} &= 0.2 , \end{aligned} \tag{4.2}$$

the volume contents of crushed stone and metal fibres are:

$$c_1 = 0.1 , \quad c_2 = 0.3 , \tag{4.3}$$

and the ratios of the spheroid semi-axes of crushed stone and metal are, respectively:

$$t_1 = 1.0 , \quad t_2 = \infty , \tag{4.4}$$

the lower limit value of the intensity of the averaged tangential stresses over matrix skeleton is equal to:

$$k_0 = 0.8 \cdot 10^8 \text{ Pa} . \tag{4.5}$$

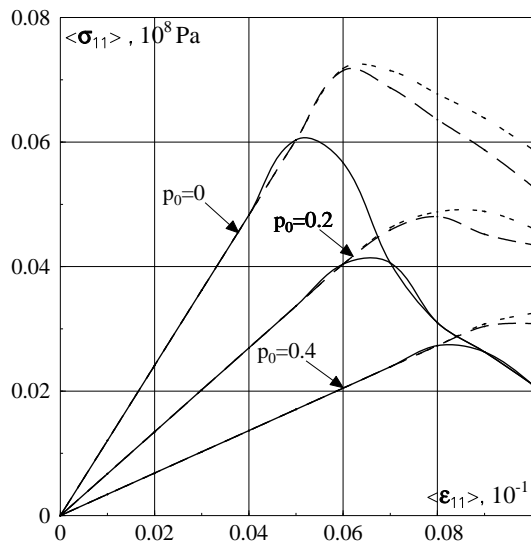


Figure 2. Stress-strain diagrams for various values of initial porosity and parameters characterizing the distribution function of the strength distribution.

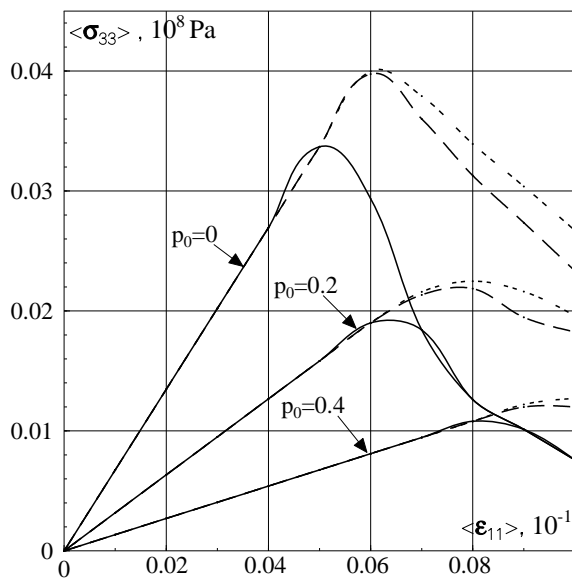


Figure 3. Stress-strain diagrams for various values of initial porosity and parameters characterizing the distribution function of the strength distribution.

In Figures 2–3 the nonlinear diagrams of stress-strain state for macrostresses $\langle \sigma_{11} \rangle$, and $\langle \sigma_{33} \rangle$ depending on macrostrain $\langle \varepsilon_{11} \rangle$ for various values of initial porosity of concrete p_0 ($p_0 = 0; 0.2; 0.4$) and parameters characterizing the distribution function of the strength distribution are represented. On the diagrams the continuous line designates the curves which take into account the strength distribution of a material with parameters $\alpha = 2; n = 60$, the dotted line – the curves which take into account the strength distribution with parameters $\alpha = 2; n = 30$, the dash-dot line – the curves which take into account the strength distribution with parameters $\alpha = 2; n = 10$. For different values of matrix porosity, all three curves coincide up to the moment of the appearance of microdamage. Moreover, varying the parameters n and α , the experimental curve of macrodeformation can be fitted to the theoretical one for every specific material in the best way.

5. Conclusions

Thus, we may conclude that the above method and proposed numerical and analytical procedure based on the methods of conditional moment function and the iterative secant method allows us to investigate the nonlinear behavior of stochastic three-component composites representing an isotropic matrix, strengthened by spheroidal inclusion, under loading. It is assumed that the nonlinearity of composite deformations is caused by matrix microdamage. The numerical analysis demonstrates that the deformative properties of such a composite depend on elastic modules of components, shape and volume concentration of inclusions and initial matrix porosity. It is shown that the strength distribution of a matrix material has significant influence on the stress-strain diagrams of the composite.

References

1. KACHANOV, A.: *Fundamentals of Fracture Mechanics*. Moscow: Nauka, 1974. (in Russian)
2. KUKSENKO, V. and TAMUZH, V.: *Fracture Micromechanics of Polymer Materials*. Riga, Zinatne, 1978. (in Russian)
3. RZHANITSYN, A.: *Analysis of Structural Calculations on Design Reliability*. Moscow, Stroyizdat, 1978. (in Russian)
4. KHOROSHUN, L.: *Methods of the theory of random functions in problems on the macroscopic properties of microinhomogeneous media*. Prikl. Mekh., **2**, (1978), 3-17.
5. KHOROSHUN, L.: *The method of conditional moments in the mechanics of composites*. Prikl. Mekh., **4**, (1988), 3-13.
6. KHOROSHUN, L., MASLOV., B., SHIKULA., E. and NAZARENKO, L.: *Statistical Mechanics and Effective Properties of Materials*. Vol. **3** of the 12-volume series *Mechanics of Composites*, Kiev, Naukova Dumka, 1993. (in Russian)
7. KHOROSHUN, L.: Principles of the micromechanics of material damage. 1. Short-term damage. *International Applied Mechanics*, **10**, (1998), 1035-1041.
8. KHOROSHUN, L. and SHIKULA., E.: Deformation of composite material for micro destruction. *International Applied Mechanics*, **6**, (1996), 52-58.

9. KHOROSHUN, L. and SHIKULA., E.: Effect of the spread of strength characteristics of the binder on the deformation of laminar fibrous composite. *International Applied Mechanics*, **7**, (1998), 39-45.
10. NAZARENKO., L.: The influence of the micro destruction on the deformative properties of anisotropic materials. *Dopovidy NAS of Ukraine*, **10**, (1999), 63-67.
11. KHOROSHUN, L. and NAZARENKO., L.: Model of short-term damaging of transversally isotropic materials. *International Applied Mechanics*, **1**, (2001), 74-83.
12. NAZARENKO., L.: Elastic properties of materials with ellipsoidal pores. *International Applied Mechanics*, **1**, (1996), 46-53.

INVESTIGATION OF THE ENERGY CHARACTERISTICS OF A LAYERED BEAM-DAMPER

YAROSLAV A. ZHUK AND IGOR K. SENCHENKOV

Thermoelasticity Department, Timoshenko Institute of Mechanics

03057 Kyiv, Ukraine

zhuk@inmech.kiev.ua

[Received: January 31, 2004]

Abstract. Coupled thermomechanical behaviour of inhomogeneous viscoplastic structures under cyclic loading is investigated for the problem of harmonic bending and dissipative heating of a three-layered beam. Two problem statements are used. One is based on the generalized thermomechanically consistent flow theory (rigorous problem statement) and another one is the approximate scleronomic model implementation (approximate problem statement). Aluminium alloy and steel are chosen as the materials of layers. Two possible configurations of beam are studied. The first one is a composition with aluminium outer layers and a steel inner layer. The second one has the opposite combination of layers. A comparison of the results obtained for the rigorous and approximate problem statements is performed. The following quantities are compared: amplitudes of mechanical field characteristics, heating temperature and energies dissipated and stored in the material. A good agreement between the results is reached. A comparative estimation of beam loss coefficients for different configurations is also performed.

Mathematical Subject Classification: 74H99

Keywords: computational modeling, plastic deformation, thermomechanical properties

1. Introduction

The forced-vibration analysis of structures and their elements occupies an important place in the mechanics of deformable systems. This research area attracts great interest because of the need of deeper theoretical analysis (especially of nonlinear systems) and purely practical requirements in various fields of engineering. Under intensive loading there are several factors that determine the behavior of multilayer structures. Among them are the nonlinearity of material properties, the heterogeneity of the stress-strain state (which is due to the layered structure) and the coupling of the mechanical and thermal fields. In particular, intensive loading may cause plastic deformation in the elements of damping systems [1],[2], building structures [3], test specimens in low-cycle fatigue tests [4], etc. This may result in elevated temperatures due to dissipative heating. Heating, in turn, may change the strength characteristics of the structure, deteriorate its performance, and, under adverse conditions, even cause

its failure. The heterogeneity of the stress-strain state is an additional complicating factor of the problem.

The present work is devoted to the energy absorption and dissipation aspects of the problem considered for multi-layered structures. The main aim is to determine the part of energy that can be safely absorbed/dissipated by a three-layered beam. One of the basic issues for such investigations is to determine the energy dissipation characteristics. The usual procedure lies in obtaining such energetic quantities as stored and dissipated energies and the loss coefficient for the case of cyclic loading.

The number of structural members subjected to cyclic loading is vast. There are different technological structures, elements of power equipment, dampers etc. (Chiba and Kobayashi [1]) among these structural elements. Some of them can deform plastically. It can cause significant heating due to the internal dissipation of mechanical energy and a change in the functional characteristics of elements under longterm cyclic loading. The investigation of this class of structures and processes demands the implementation of material models that take into account properly both the mechanical and thermal aspects of the state of the members. In the authors' opinion, generalized flow theories are most promising from this point of view. Within the framework of these theories, the thermodynamics of irreversible processes is used to derive the correct system of constitutive equations and heat conductivity equation (see, for example, Chan, Lindholm et al. [5], Bodner and Lindenfeld [6], Bodner and Partom [7], Chaboche [8], Lubliner [9]). A refined, thermodynamically consistent model of coupled thermo-viscoplastic material behavior was elaborated on the basis of the Bodner-Partom's one, by Bodner and Lindenfeld [6], Senchenkov and Zhuk [10], and Senchenkov, Zhuk et al. [11]. This model describes isotropic and anisotropic hardening by means of one scalar and one tensor variable. A more general variant of the model which employs the spectrum of hardening parameters was developed in works by Bodner and Lindenfeld [6], Senchenkov and Zhuk [10] and Senchenkov, Zhuk et al. [11] for the case of significant non-linear hardening. The alternative approach that assumes stored free energy can be chosen in the form of significant non-linear functions of internal variables and was also applied by Bodner and Lindenfeld [6] and Senchenkov, Zhuk et al. [11]. On the basis of the model developed, the approximate scleronomic model of coupled thermomechanical behaviour of elastic-viscoplastic bodies was elaborated by Senchenkov and Zhuk [10], Senchenkov, Zhuk et al. [11], [12]. This model was formulated in terms of amplitudes of mechanical field variables, averaged over the period temperature and complex mechanical moduli (see also Zhuk, Chervinko et al. [13]). In the present paper original 'rigorous' and approximate models are applied to investigate coupled thermomechanical behaviour of structurally inhomogeneous viscoplastic bodies under harmonic loading. Quasi-static vibration and dissipative heating of a three-layered beam subjected to harmonic bending at its ends are under consideration. Set of mechanical field variables and heating temperatures obtained as a result of the implementation of both models are compared. Some aspects of storage and dissipation of energy under cyclic bending that has a particular interest for vibration damping, are investigated as well.

2. Problem statement

The problem of vibration and dissipative heating of a three-layered viscoplastic beam $|x| \leq a$, $|y| \leq b$ under kinematic harmonic bending applied at its ends is studied for the plane stress state (Fig.1). It is assumed that the inner and outer layers are fabricated from different viscoplastic materials. Ideal thermal and mechanical contact is assumed on the boundaries between layers. In accordance with Senchenkov and Zhuk [10] and Senchenkov, Zhuk et al. [11], the problem statement consists of Cauchy's relations

$$\epsilon = \frac{1}{2} [\nabla \mathbf{u} + (\nabla \mathbf{u})^T], \quad (2.1)$$

the equation of quasi-static equilibrium (2.2), the energy balance equation (2.3), constitutive equations of material behavior and initial and thermomechanical conditions on the outer boundary (2.4)-(2.6)

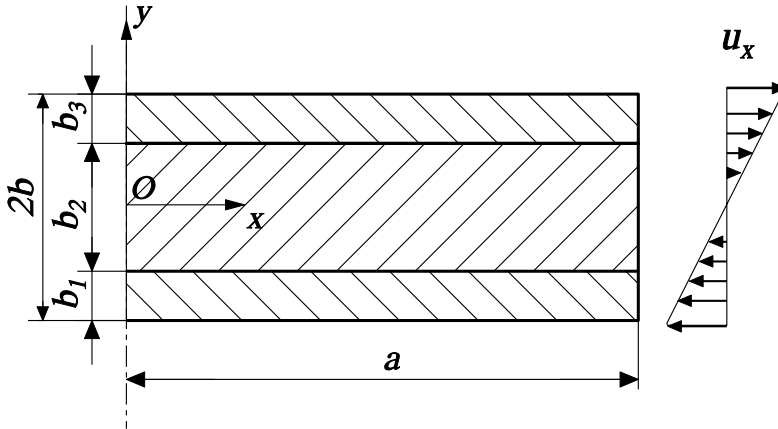


Figure 1. Three-layer beam-damper geometry.

$$\nabla \cdot \boldsymbol{\sigma} = 0 \quad \text{in } V, \quad (2.2)$$

$$c_V \dot{\theta} + 3\alpha\theta K_V (\text{tr } \dot{\epsilon} - 3\alpha\dot{\theta}) - D' - k\Delta\theta = r, \quad (2.3)$$

$$\theta(0) = \theta_0, \quad (2.4)$$

$$u_x = \pm \hat{\epsilon} y \sin \omega t, \quad \sigma_{xy} = 0, \quad |x| = a; \quad \sigma_{yy} = \sigma_{xy} = 0, \quad |y| = b, \quad (2.5)$$

$$-k\nabla\theta = \gamma(\theta - \theta_0), \quad |x| = a, \quad |y| = b. \quad (2.6)$$

It is assumed that the thermo-viscoplastic behaviour of materials is described by the Bodner-Partom model (Bodner and Lindenfeld [6], Bodner and Partom [7]). Its energetization and thermodynamic analysis were performed by Senchenkov and Zhuk [10] and Senchenkov, Zhuk et al. [11]. It was accepted for this model that the total strain is a sum of elastic, inelastic and thermal parts

$$\epsilon = \epsilon^e + \epsilon^p + \epsilon^\theta, \quad (2.7)$$

$$\boldsymbol{\epsilon}^\theta = \mathbf{I} \int_{\theta_0}^{\theta} \alpha(\theta') d\theta'. \quad (2.8)$$

The model also incorporates Hooke's law for elastic strain (2.9), the flow law (2.10) and the evolution equation for parameters of isotropic and anisotropic hardening (2.11), (2.12)

$$s = 2G(\mathbf{e} - \boldsymbol{\epsilon}^p), \quad \text{tr } \boldsymbol{\sigma} = 3K_V \text{tr}(\boldsymbol{\epsilon} - \boldsymbol{\epsilon}^\theta), \quad (2.9)$$

$$\dot{\boldsymbol{\epsilon}}^p = \frac{D_0}{\sqrt{J_2}} \exp\left[-\frac{1}{2} \left(\frac{Z^2}{3J_2}\right)^n\right] \mathbf{s}; \quad Z = K + D, \quad (2.10)$$

$$\dot{K} = m_1(K_1 - K)\dot{W}_p - A_K K_1 \left(\frac{K - K_2}{K_1}\right)^{r_K}, \quad (2.11)$$

$$\dot{\boldsymbol{\beta}} = m_2(D_1 \mathbf{u} - \boldsymbol{\beta})\dot{W}_p - A_D K_1 \left[\frac{(\boldsymbol{\beta} : \boldsymbol{\beta})^{1/2}}{K_1}\right]^{r_D} \mathbf{V} \quad (2.12)$$

where

$$J_2 = \mathbf{s} : \mathbf{s}/2, \quad \dot{W}^p = \boldsymbol{\sigma} : \dot{\boldsymbol{\epsilon}}^p, \quad \mathbf{u} = \mathbf{s}/(\mathbf{s} : \mathbf{s})^{1/2}, \quad \mathbf{V} = \boldsymbol{\beta}/(\boldsymbol{\beta} : \boldsymbol{\beta})^{1/2}, \quad D = \boldsymbol{\beta} : \mathbf{u}.$$

The following notations were used in equations (2.1)-(2.12): \mathbf{u} is the displacement vector; $\boldsymbol{\epsilon}$ and $\boldsymbol{\sigma}$ are the tensors of total strain and stress; $\boldsymbol{\epsilon}^e$, $\boldsymbol{\epsilon}^p$ and $\boldsymbol{\epsilon}^\theta$ are the elastic, inelastic and thermal components of the strain tensor, respectively; \mathbf{e} and \mathbf{s} are the deviators of strain and stress tensors; K and $\boldsymbol{\beta}$ are the parameters of isotropic and anisotropic hardening; θ is the temperature; G and K_V are the shear and bulk moduli, respectively; D' is the rate of energy dissipation; k is the heat conductivity coefficient; c_V is the heat capacity for constant volume; α is the thermal expansion coefficient; r is the power of thermal sources; γ is the heat transfer coefficient; θ_0 is the temperature of environment. The constants D_0 , D_1 , K_0 , K_1 , K_2 , m_1 , m_2 , A_K , A_D , r_K , r_D and n are the model parameters. In accordance with the model formulation, coefficients D_0 , D_1 , K_1 , m_1 , m_2 , r_K and r_D are temperature independent as opposed to K_0 , K_2 , A_K , A_D , K_V and G that depend on temperature. In equations (2.1)-(2.12) \mathbf{I} denotes the unit tensor of appropriate rank; $\mathbf{a} : \mathbf{b}$ is a convolution of tensors \mathbf{a} and \mathbf{b} ; $\text{tr } \mathbf{a}$ is a trace of the tensor \mathbf{a} ; $(\dot{\cdot}) = \partial(\cdot)/\partial t$ and Δ is Laplacian operator.

The numerical integration of problem (2.1)-(2.12) is significantly complicated by the necessity of taking into account the total prehistory of deformation in the case of multiple cycle loading.

3. Thermodynamic analysis of the model

The formulation of the coupled thermo-viscoplasticity problem requires the model of material behaviour to be consistent with the thermodynamics of irreversible processes. In this section the thermodynamic analysis of the Bodner-Partom model will be performed.

The Helmholtz energy ψ is taken as a thermodynamic potential

$$\psi = U - \eta\theta, \quad \psi = \psi(\boldsymbol{\epsilon}, \theta, \alpha_k), \quad (3.1)$$

where U is internal energy; η is entropy; α_k is the set of internal variables.

The energy equation takes the form

$$\dot{U} - \boldsymbol{\sigma} : \dot{\boldsymbol{\epsilon}} + \text{div } \mathbf{h} = r \tag{3.2}$$

where \mathbf{h} is heat flux.

Taking into account equation (3.2), the second law of thermodynamics in Planck form reduces to a dissipative inequality

$$\boldsymbol{\sigma} : \dot{\boldsymbol{\epsilon}} = \dot{\psi} - \eta\dot{\theta} \geq 0. \tag{3.3}$$

Employing the standard thermodynamic procedure, the defining equations may be established on the basis of equations (3.2) and (3.3), making use of equation (2.8)

$$\boldsymbol{\sigma} = \frac{\partial \psi}{\partial \boldsymbol{\epsilon}}, \quad \eta = -\frac{\partial \psi}{\partial \theta}, \quad A_k = \frac{\partial \psi}{\partial \alpha_k}, \quad k = \overline{1, N}. \tag{3.4}$$

Here, A_k are the thermodynamic forces conjugated with the variables (thermodynamic displacements) α_k . The dissipative inequality then takes the form

$$\boldsymbol{\sigma} : \dot{\boldsymbol{\epsilon}}^p - A_k \dot{\alpha}_k = D' \geq 0. \tag{3.5}$$

According to equation (3.5), D' is the difference between the plastic power and the rate of variation of hidden stored energy \dot{W}_s

$$\dot{W}_s = A_k \dot{\alpha}_k. \tag{3.6}$$

It follows from equation (3.5) that only a part of the plastic work is converted into heat. Its portion that is phenomenologically related to hardening is stored in the material. This energy is associated with the additional stored energy due to the dislocation kinetics and also with the changes in the surface energy of the pores.

The following evolution equations for the internal variables should be added to equation (3.4)

$$\dot{\alpha}_k = \bar{\alpha}_k(\boldsymbol{\epsilon}, \theta, \alpha_j), \quad k, j = \overline{1, N}. \tag{3.7}$$

Let us assume that the body occupies the region V bounded by surface S with the external normal \mathbf{n} . Taking account of equations (3.1), (3.4) and (3.5), equation (3.2) transforms into

$$\theta \dot{\eta} = \text{div } \mathbf{h} + D' + r, \quad \text{in } V. \tag{3.8}$$

In order to obtain the Bodner-Partom model from the general model, we determine the appropriate form of equation (3.1) and (3.7). In the generalized models the thermodynamic forces A_k are associated with the hardening parameters. In particular, for the Bodner-Partom model A_k are equivalent to the set $\{K, \beta\}$. The conjugate internal variables are denoted by δ and α .

According to Senchenkov and Zhuk [10] and Senchenkov, Zhuk et al. [11], the following expression can be written for the free energy

$$\psi = G(\mathbf{e} - \boldsymbol{\epsilon}^p) : (\mathbf{e} - \boldsymbol{\epsilon}^p) + \frac{1}{2} K_V [\text{tr}(\boldsymbol{\epsilon} - \boldsymbol{\epsilon}^p) - 3 \boldsymbol{\epsilon}^p]^2 + \frac{m_1 K_1^2 \delta^2}{2c} + \frac{m_2 D_1^2 (\boldsymbol{\alpha} : \boldsymbol{\alpha})}{2d} - \int_{\theta_0}^{\theta} dx \int_{\theta_0}^{\theta} \frac{c_V(y)}{y} dy. \tag{3.9}$$

Here $c_V(\theta)$ is the isochoric specific heat; c and d are dimensionless constants.

As follows from equations (2.11), (2.12) and (3.7), the evolution equations for the thermodynamic forces are specified in the mechanical model, whereas the equations for thermodynamic displacements are employed in the thermodynamic analysis. Obviously, these equations must be consistent. Determining the thermodynamic forces from equation (3.4) by means of equation (3.9) and then differentiating both sides of the resulting equations with respect to time, we find that

$$\dot{K} = \frac{d}{dt} \left(\frac{\partial \psi}{\partial \delta} \right) = \frac{m_1 K_1^2}{c} \dot{\delta}, \quad \dot{\beta} = \frac{d}{dt} \left(\frac{\partial \psi}{\partial \alpha} \right) = \frac{m_2 D_1^2}{d} \dot{\alpha}. \quad (3.10)$$

It is readily seen that substitution of the evolution equations obtained by Senchenkov, Zhuk et al. [11]

$$\dot{\delta} = c(1 - K/K_1) \dot{W}_p/K_1 - cA_K K (K_1 m_1)^{-1} [(K - K_2)/K_1]^{r_K}, \quad (3.11)$$

$$\dot{\alpha} = d(\mathbf{u} - \beta/D_1) \dot{W}_p/D_1 - dA_D (D_1^2 m_2)^{-1} [(\beta : \beta)^{1/2}/K_1]^{r_D} \beta / (\beta : \beta)^{1/2} \quad (3.12)$$

into equation (3.10) yields equations (2.11) and (2.12). Making use of equations (3.5) and (3.11), (3.12), one can find the following expression for the dissipation rate

$$D' = \boldsymbol{\sigma} : \dot{\boldsymbol{\epsilon}}_p - \boldsymbol{\beta} : \dot{\boldsymbol{\alpha}} - K \dot{\delta} = \dot{W}_p - \dot{W}_s, \quad (3.13)$$

$$\dot{W}_s = \dot{W}_{s\beta} + \dot{W}_{sK} = \boldsymbol{\beta} : \dot{\boldsymbol{\alpha}} + K \dot{\delta}. \quad (3.14)$$

In equation (3.14), the accumulation rate of stored energy \dot{W}_s is divided into parts associated with anisotropic $\dot{W}_{s\beta}$ and isotropic \dot{W}_{sK} hardening.

The analysis of equations (2.11), (2.12), (3.13) and (3.14) shows that the coefficients c and d in equations (3.9), (3.11) and (3.12) do not appear in the equations of the mechanical model described in Section 2. However, they are thermodynamically significant: they determine the portion of the plastic work converted into heat.

Equation (2.9) for $\boldsymbol{\sigma}$ and the equation for η are found by differentiating the free energy in equation (3.9) according to equation (3.4). To eliminate cumbersome computations for entropy, we assume that thermo-mechanical characteristics of the material and coefficients in equation (3.9) do not depend on temperature. After simple transformations, we write equation (3.8) in the form

$$c_{V0} \dot{\theta} + 3\alpha_0 \theta K_V (\text{tr } \dot{\boldsymbol{\epsilon}} - 3\alpha_0 \dot{\theta}) - D' - k \Delta \theta = r, \quad (3.15)$$

where c_{V0} and α_0 are, respectively, the specific heat and linear thermal expansion coefficients correspondingly to the reference temperature $\theta = \theta_0$; the dissipative function D' is determined by equations (3.11)-(3.13).

The formulation of the coupled problem derived here is valid for arbitrary deformation processes in materials satisfying the Bodner-Partom equations.

4. Approximate scleronomic model of coupled thermomechanical behaviour of viscoplastic bodies

An approximate scleronomic model that incorporates complex characteristics concept was elaborated for the particular case of proportional harmonic loading. It is assumed that for the harmonic excitation of material element

$$\mathbf{e}(t) = \mathbf{e}'(t) \cos \omega t - \mathbf{e}''(t) \sin \omega t, \quad \mathbf{s}(t) = \mathbf{s}'(t) \cos \omega t - \mathbf{s}''(t) \sin \omega t \quad (4.1)$$

the corresponding response is also close to harmonic. As a result, the complex amplitudes of total and plastic strain deviators $\tilde{\mathbf{e}} = \mathbf{e}' + i\mathbf{e}''$ and $\tilde{\mathbf{\epsilon}}^p = \mathbf{\epsilon}^p + i\mathbf{\epsilon}^{p''}$ as well as the amplitude of stress deviator $\tilde{\mathbf{s}} = \mathbf{s}' + i\mathbf{s}''$ are related by means of the complex shear modulus $\tilde{G}_N, \tilde{G}'_N = G'_N + iG''_N$ and plasticity coefficient $\tilde{\kappa}_N, \tilde{\kappa}'_N = \kappa'_N - i\kappa''_N$ in each cycle as follows

$$\tilde{\mathbf{s}} = 2\tilde{G}_N\tilde{\mathbf{e}}; \quad \tilde{\mathbf{\epsilon}}^p = \tilde{\kappa}_N\tilde{\mathbf{e}}, \quad N = 1, 2, \dots \quad (4.2)$$

where \tilde{G} and $\tilde{\kappa}$ are the functions of tensor of strain amplitude intensity e_0 , frequency ω and temperature θ , N is the cycle number. In the general case $\tilde{G} = \tilde{G}(e_0, \omega, \theta)$, $\tilde{\kappa} = \tilde{\kappa}(e_0, \omega, \theta)$, where $e_0 = \mathbf{e}' : \mathbf{e}' + \mathbf{e}'' : \mathbf{e}''$.

The imaginary parts of characteristics are determined from the condition of equality of dissipated energies over the period

$$G''_N = \langle D' \rangle_N \omega e_0^2, \quad \kappa''_N = G''_N / G, \quad (4.3)$$

and real parts are obtained from the condition of equivalence of generalized cyclic diagrams $\sigma_{aN} = \sigma_{aN}(e_0, \omega)$ and $\epsilon_{aN}^p = \epsilon_{aN}^p(e_0, \omega)$, which relates amplitudes of the equivalent plastic strain ϵ_{aN}^p and stress σ_{aN} in the N^{th} cycle

$$\begin{aligned} G'_N(e_0, \omega) &= \left[\frac{\sigma_{aN}^2(e_0, \omega)}{4e_0^2} - G''_N{}^2(e_0, \omega) \right]^{1/2}, \\ \kappa'_N(e_0, \omega) &= \left[\frac{\epsilon_{aN}^p{}^2(e_0, \omega)}{e_0^2} - \kappa''_N{}^2(e_0, \omega) \right]^{1/2} \end{aligned} \quad (4.4)$$

where $\langle \cdot \rangle = \frac{1}{T} \int_{(N-1)T}^{NT} (\cdot) dt, T = \frac{2\pi}{\omega}$.

Dissipation and cyclic diagrams are calculated by means of straight numerical integration of the Bodner-Partom model equations for the case of torsion of a hollow thin-walled cylinder.

By averaging energy equation (2.3) over the period of vibration and neglecting thermoelastic effects one can obtain

$$c_V \langle \dot{\theta} \rangle - k \Delta \langle \theta \rangle - \langle D' \rangle_N = 0, \quad (4.5)$$

where $\langle \theta \rangle$ is the averaged temperature.

The averaged dissipation function is determined as $\langle D' \rangle_N = \langle \dot{W}_p \rangle_N$.

The equation of quasi-static equilibrium takes the form

$$\nabla \cdot \tilde{\sigma} = 0. \quad (4.6)$$

The following mechanical boundary conditions (2.5) and thermal boundary and initial conditions (2.6), (2.4) should be added to equations (4.2)-(4.6)

$$\tilde{u}_x = \mp i \hat{\epsilon} y, \quad \tilde{\sigma}_{xy} = 0, \quad |x| = a; \quad \tilde{\sigma}_{yy} = \tilde{\sigma}_{xy} = 0, \quad |y| = b, \quad (4.7)$$

$$-k \nabla \langle \theta \rangle = \gamma (\langle \theta \rangle - \theta_0), \quad |x| = a, \quad |y| = b, \quad (4.8)$$

$$\langle \theta \rangle = \theta_0, \quad t = 0 \quad (4.9)$$

where $\hat{\epsilon}$ is loading parameter.

The approximate scleronomic model of the thermomechanical non-steady behaviour of viscoplastic bodies is given by equations (4.2)-(4.6). The approximate problem statement for the thermo-mechanical behaviour of viscoplastic bodies consists of the equations mentioned with incorporation of equations (4.5), (4.6) and conditions (4.7)-(4.9).

5. Material properties

Aluminium alloy and steel were chosen as the materials of layers. Their mechanical properties and generalized model constants are given in Table 1. Stabilized complex moduli ($N \rightarrow \infty$) of the approximate model for both materials are plotted in Figure 2. Curves 1 and 2 show the dependence of G'/G on strain intensity for aluminium alloy and steel, respectively. Similar dependencies for G''/G are depicted by curves 3 and 4.

Table 1. Mechanical properties and generalized model constants used.

Parameter	Aluminium alloy	Steel
$\rho, \text{kg/m}^3$	2640	7820
$c_p, \text{J/kg} \cdot ^\circ\text{K}$	921.0	485.9
$E \cdot 10^{-5}, \text{MPa}$	0.816	2.12
ν	0.34	0.30
$k, \text{W/m} \cdot ^\circ\text{K}$	90.00	30.98
$\alpha \cdot 10^{-6}, 1/^\circ\text{K}$	23.0	12.0
n	2.06	1.00
D_0, s^{-1}	10^4	10^4
D_1, MPa	80	0
K_0, MPa	323.6	3145
K_1, MPa	647.4	4000
K_2, MPa	35	0
m_1, MPa^{-1}	0.182	0.300
m_2, MPa^{-1}	3.7	0.0

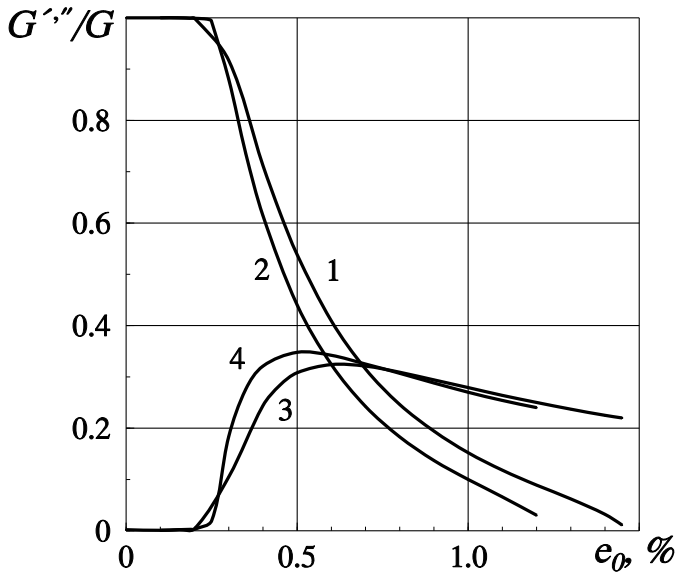


Figure 2. Stabilized complex moduli of approximate model for aluminium alloy and steel.

6. Solution technique

The technique of numerical solution for the rigorous problem statement is designed as a double iterative process. The first (internal) process is formed by the numerical integration of the evolution equations. The second iterative process is related to the quasi-static equilibrium equation and heat conductivity equation integration. The implicit Euler's method is used for the integration of evolution equations. A simple integration technique is employed for the solution of the non-linear transcendental system of equations, which arises at each time step. The Steffensen-Eytken's technique is used to accelerate the process convergence. The initial iteration is calculated by means of square extrapolation of values from three previous time steps. The equilibrium and heat conductivity problems are solved by means of FEM. Quadrilateral eight-node elements with four Gauss points are used. The plastic strain is incorporated into fictive mass forces and is not varied under the variation procedure. A time step correction technique is applied. The rates of convergence of internal and external iterative processes are used as a criterion of step changing. The solution convergence is estimated by the values of maximum stress and plastic strain. The technique developed by Senchenkov, Zhuk et al. [11] and [12] is used to find the solution of the approximate problem. The main difference from the technique incorporated for solving the rigorous problem lies in the absence of an internal iterative process designed for the evolution equation integration. There is only an external iterative process for each time step.

7. Numerical results and discussion

There were two main aims of the calculations performed. The first one is the determination of basic regularities of coupled thermo-mechanical processes in inhomogeneous viscoplastic bodies. The second one is the estimation of applicability of the approximate technique derived for the solution of the class of problems mentioned. The geometry of the beam was chosen as follows: $a = 0.15$ m, $b = 0.15 \cdot 10^{-1}$ m, $b_1 = b_3 = 0.3 \cdot 10^{-2}$ m, $b_2 = 0.24 \cdot 10^{-1}$ m, where b_i , $i = 1, 2, 3$ are the layer thicknesses. Two possible configurations were studied. The first one has the composition aluminium-steel-aluminium (ASA) and the second one has the opposite, SAS, composition. The excitation frequency is 1Hz.

A comparison of results was performed for the following set of thermo-mechanical characteristics: 1) ranges of the equivalent stress and plastic strain $\sigma_{1,2}^a$, $\epsilon_{1,2}^a$ at the points $x = 0.3 \cdot 10^{-1}$ m, $y = 0.146 \cdot 10^{-1}$ m (corresponds to subscript 1) and $x = 0.3 \cdot 10^{-1}$ m, $y = 0.1 \cdot 10^{-1}$ m (corresponds to subscript 2) that belong to the 1st and 2nd layers respectively; 2) the plastic power \bar{D}' averaged over the volume of the body; 3) the maxima of the mean value of the energy W_e stored in the volume V for one period and the heating temperature $\langle \theta \rangle$ at the point $x = 0.0$ m, $y = 0.15 \cdot 10^{-1}$ m. The expressions for these quantities for the rigorous model are given by

$$\begin{aligned} \begin{bmatrix} \sigma_{xxaN} \\ \epsilon_{xxaN}^p \end{bmatrix} &= \frac{1}{2} \left\{ \max_{T_N} \begin{bmatrix} \sigma_{xx}(t) \\ \epsilon_{xx}^p(t) \end{bmatrix} - \min_{T_N} \begin{bmatrix} \sigma_{xx}(t) \\ \epsilon_{xx}^p(t) \end{bmatrix} \right\}, \\ \bar{D}' &= \frac{1}{VT} \int_V \int_{(N-1)T}^{NT} \mathbf{s} : \dot{\epsilon}^p dt dV, \\ \bar{W}_e &= \frac{1}{V} \max_{T_N} \int_V \left[\frac{1}{18K_V} (\text{tr } \boldsymbol{\sigma})^2 + \frac{1}{4G} \mathbf{s} : \mathbf{s} \right] dV. \end{aligned} \quad (7.1)$$

The same quantities for the approximate model should be calculated as follows:

$$\begin{aligned} \sigma_{xxaN} &= |\tilde{\sigma}_{xxN}|, \quad \epsilon_{xxaN}^p = |\tilde{\epsilon}_{xxN}^p|, \\ \bar{D}' &= \frac{\omega}{2V} \int_V \text{Im}(\tilde{\mathbf{s}}_N : \tilde{\boldsymbol{\epsilon}}_N^{p*}) dV, \\ \bar{W}_e &= \frac{1}{V} \int_V \left[\frac{1}{18K_V} (\text{tr } |\tilde{\boldsymbol{\sigma}}_N|)^2 + \frac{1}{4G} \tilde{\mathbf{s}}_N : \tilde{\mathbf{s}}_N^* \right] dV, \end{aligned} \quad (7.2)$$

where N denotes the number of cycles. Results of the numerical calculation for configuration ASA are shown in Table 2 for loading value $\hat{\epsilon} = 0.1 \cdot 10^{-1}$. The upper rows correspond to the solution of the rigorous problem, while the lower rows represent the solution for the approximate one. The good agreement between two approaches should be emphasized. The following errors of the approximate solution were detected: 2% for stored energy, 3% for dissipated energy, 2% for equivalent stress, 8% for equivalent plastic strain and 3% for heating temperature in the stage of stabilized process. Maximum errors were detected in the starting cycles. They can be explained

Table 2. Results of numerical calculation for configuration ASA

N	$\bar{D}'_N,$ MPa/s	$\bar{W}_{eN},$ MPa	$\Delta s_{1N},$ MPa	$\Delta e_{1N},$ %	$\Delta s_{2N},$ MPa	$\Delta e_{2N},$ %	$\langle \theta \rangle,$ °C
1	3,608	0,759	152,4	0,627	438,7	0,316	21,77
	3,740	0,715	137,7	0,632	415,0	0,317	21,60
2	4,691	0,860	180,9	0,548	459,2	0,288	23,51
	4,807	0,870	175,9	0,554	454,8	0,292	23,30
5	4,656	0,917	193,1	0,528	461,1	0,291	29,02
	4,788	0,935	192,6	0,522	460,3	0,289	27,70
10	4,625	0,924	193,3	0,542	461,1	0,299	35,95
	4,761	0,940	192,9	0,521	460,3	0,289	34,40
15	4,613	0,925	193,3	0,555	461,1	0,305	42,54
	4,752	0,941	192,9	0,521	460,3	0,289	41,00
20	4,611	0,926	193,3	0,568	461,1	0,312	49,06
	4,748	0,941	192,9	0,521	460,3	0,289	47,50

by larger errors in complex characteristics values in the beginning due to unclosed hysteresis loops.

The good agreement of the results mentioned provides possibility for approximate model application for investigation of the temperature evolution and stabilization process. The results of calculation are shown in Figure 3 for heat transfer coefficient $\gamma = 20 \text{ W/m}^2 \cdot \text{K}$. The good agreement of results both in time and spatial coordinates should be emphasized.

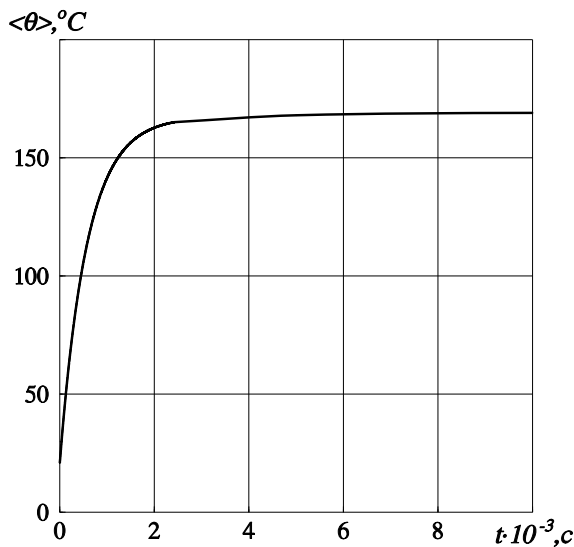


Figure 3. Temperature evolution in time at the point with coordinates $x = 0.0 \text{ m}$, $y = 0.15 \cdot 10^{-1} \text{ m}$

The results of strain-stress state investigation for configurations ASA and SAS are shown in Figures 4,5 and Figures 6,7 respectively. Lines 1 and 2 show equivalent stress range distribution along cross-section $y = 0$ for the rigorous and approximate problem statement, respectively. Curves 3 and 4 have the same meaning for the equivalent plastic strain range distribution. They almost coincide for the chosen scale. A comparison of the two configurations shows that the maximum stress over the cross-section is reached in steel layer for SAS composition. There is a jump in the equivalent strain range distribution on the contact surfaces for both configurations. Plastic strain intensity ranges are distributed continuously. They have maxima at the external surfaces of the beam. Steady-state temperature distribution over cross-section $y = 0$ is shown by line 5 in Figure 5. It is characterized by a high level of homogeneity that can be explained by the high heat conductivity of layer materials. In the case of rubber-metal or polymer structures the situation may be different.

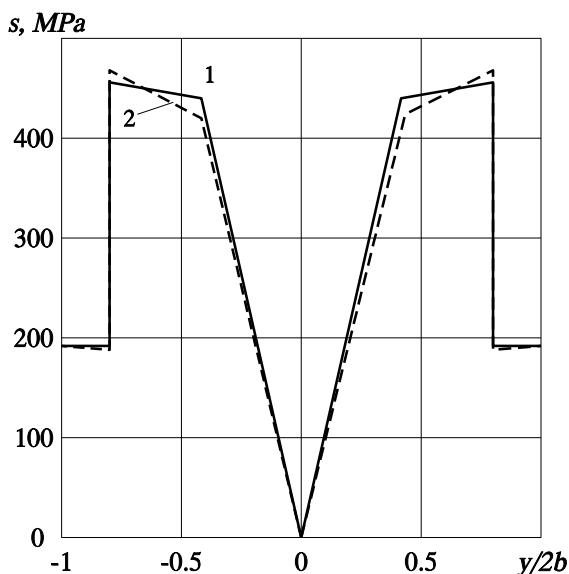


Figure 4. Comparison of the equivalent stress distribution through the thickness provided by the rigorous and approximate problem statements for the ASA beam configuration.

The good agreement between the stored and dissipated energy values for rigorous and approximate problem statements provides a reason for applying the approximate technique to estimate the element damping properties. The following energy characteristics were considered for a comparison of the damping abilities of ASA and SAS beam compositions: \bar{D}' , \bar{W}_e and loss coefficient

$$\psi_L = \frac{2\pi \int_V \bar{D}'(\mathbf{x}) dV}{\omega \int_V \max_T \bar{W}(\mathbf{x}) dV}.$$

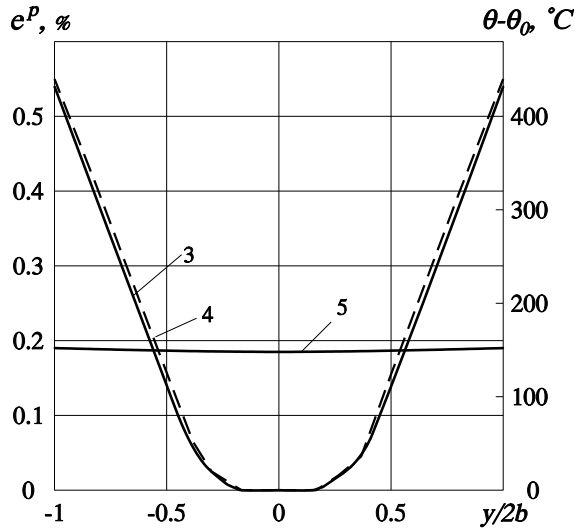


Figure 5. Comparison of the equivalent strain distribution through the thickness provided by the rigorous and approximate problem statements for the ASA beam configuration. Steady temperature distribution over the cross-section $y = 0$

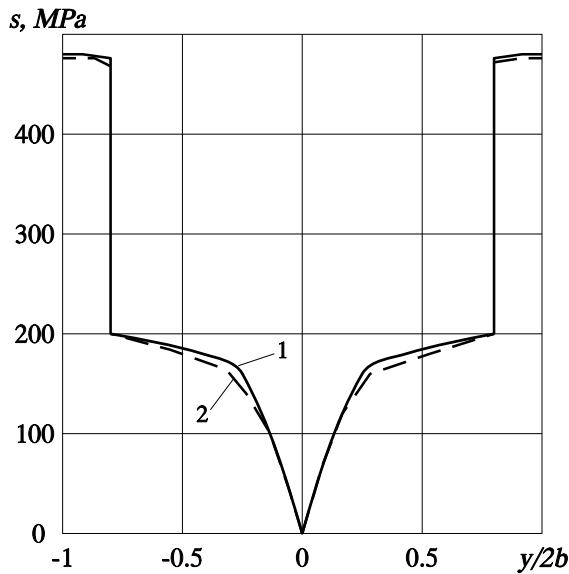


Figure 6. Comparison of the equivalent stress distribution through the thickness provided by the rigorous and approximate problem statements for the SAS beam configuration

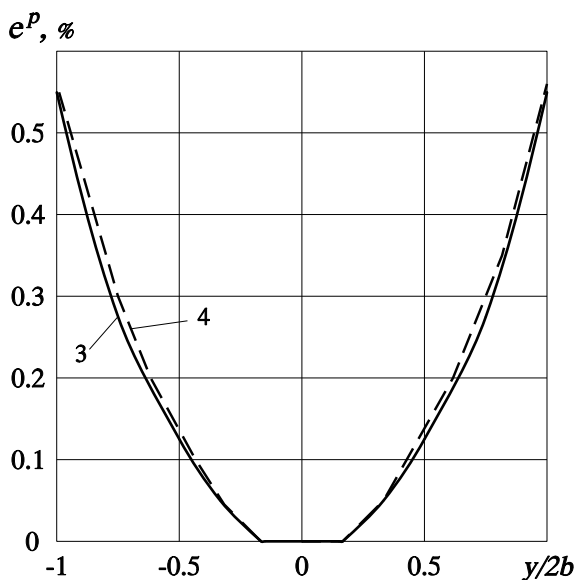


Figure 7. Comparison of the equivalent strain distribution through the thickness provided by the rigorous and approximate problem statements for the SAS beam configuration

Table 3. Energy characteristics of the beam-damper for the 7th cycle

Composition	ψ_L	\bar{D}' , MPa/s	$\bar{W}_{e,}$ MPa
ASA	5,04	4,65	0,922
SAS	8,02	4,76	0,593

Table 4. Energy characteristics of the damper layers for the 7th cycle

Composition	$\psi_{L1,3}$	ψ_{L2}	$\bar{D}'_{1,3}$, MPa/s	\bar{D}'_2 , MPa/s	$\bar{W}_{e1,3}$, MPa	\bar{W}_{e2} , MPa
ASA	9,85	4,01	0,672	3,30	0,07	0,82
SAS	11,53	3,76	1,779	1,19	0,15	0,32

Results for the 7th cycle (steady vibrations regime) are presented in Tables 3 and 4. Indexes denote the number of layer.

8. Conclusions

There is a good agreement between the solutions provided by the rigorous and approximate problem statements. The configuration SAS is characterized by a higher loss coefficient. It means that a composition with a thick enough internal layer of 'soft' material covered by thin layers of 'hard' one is more suitable for damping of forced vibration for loading under consideration. Both rigorous and approximate models can

be applied for solving the vibration and dissipative heating problem for inhomogeneous structures such as multi-layered beam-dampers. But it should be emphasized that in the case of harmonic loading, integration of the approximate statement requires two orders less time than the rigorous one.

References

1. CHIBA, T. and KOBAYASHI, N.: Dynamic Characteristics of Pipe Systems Supported with Viscoelastic and Elasto-Plastic Dampers. *Transactions of the ASME, Journal of Applied Mechanics*, **57**, (1990), 409-421.
2. SHIBA, K., MASE, S., YABE, Y. and TAMURA, K.: Active/passive vibration control systems for tall buildings. *Smart Materials and Structures*, **7**, (1998), 588-598.
3. AIZAWA, S., KANIZAWA, T. and HIGASINO, M.: Case studies of smart materials for civil structures. *Smart Materials and Structures*, **7**, (1998), 617-626.
4. BUI, H.D., EHRLACHER A. and NGUYEN, Q.S.: *Thermomechanical coupling in fracture mechanics (in Thermomechanical Couplings in Solids. H.D. Bui and Q.S. Nguyen (Eds), Elsevier, 1987, 327-342.*
5. CHAN, R., LINDHOLM, U., BODNER, S. and WALKER, K.: High temperature inelastic deformation under uniaxial loading: theory and experiment. *Transactions of the ASME, Journal of Engineering Materials and Technology*, **111**, (1989), 345-353.
6. BODNER, S.R. and LINDENFELD, A.: Constitutive modeling of the stored energy of cold work under cyclic loading. *The European Journal of Mechanics, A / Solids*, **14**, (1995), 333-348.
7. BODNER, S. and PARTOM, Y.: Constitutive equations for elastoviscoplastic strain hardening material. *Transactions of the ASME, Journal of Applied Mechanics*, **42**, (1975), 385-389.
8. CHABOCHE, J.-L.: Cyclic viscoplastic constitutive equations. Part 1: A thermodynamic consistent formulation. *Transactions of the ASME, Journal of Applied Mechanics*, **60**, (1993), 813-821.
9. LUBLINER, J.: On the structure of the rate equations of materials with internal variables. *Acta Mechanica*, **17**, (1973), 109-119.
10. SENCHENKOV, I. and ZHUK, Y.: Thermoviscoplastic Deformation of Materials. *International Applied Mechanics*, **33**, (1997), 122-128.
11. SENCHENKOV, I., ZHUK, Y. and TABIEVA, G.: Thermodynamically consistent modification of generalized thermoviscoplastic models. *International Applied Mechanics*, **34**, (1998), 53-60.
12. ZHUK, Y. and SENCHENKOV, I.: Approximate model of thermomechanically coupled inelastic strain cycling. *International Applied Mechanics*, **39**, (2003), 300-306.
13. ZHUK, Y., CHERVINKO, O. and TABIEVA, G.: Planar flexural vibration and dissipative heating of laminated rectangular plates. *International Applied Mechanics*, **38**, (2002), 837-844.

NUMERICAL SIMULATION OF THE DYNAMICS OF A NONLOCAL, INHOMOGENEOUS, INFINITE BAR

OLAF WECKNER

Massachusetts Institute of Technology
Department of Mechanical Engineering
Cambridge, MA 02139, USA
olaf@weckner.de

ETIENNE EMMRICH

Technische Universität Berlin
Institut für Mathematik
Straße des 17. Juni 135, 10623 Berlin, Germany
emmrich@math.tu-berlin.de

[Received: January 31, 2005]

Abstract. In this paper, we develop an efficient numerical method based on Gauß-Hermite quadrature to calculate the one-dimensional dynamic response of a nonlocal, peridynamic bar composed of (inhomogeneous) linear material. The principal *physical* characteristic of the peridynamic theory is the presence of long-range forces leading to nonlinear dispersion relations while the principal *mathematical* characteristic is the presence of a stationary Barbashin operator in the integro-differential equation of motion. We calculate two examples corresponding to continuous and discontinuous, Riemann-like initial conditions. As the analytical solutions for these examples are known, they serve as validation problems for the proposed numerical scheme.

Mathematical Subject Classification: 74H15, 65R20, 45K05

Keywords: integro-differential equation, quadrature, Barbashin operator, long-range forces, nonlocal, peridynamic

1. Introduction

In the classical *local* theory of elasticity, the equation of motion is a partial differential equation (PDE). However, if *nonlocal* effects have to be considered, it can¹ become an integro-differential equation (IDE), see Silling [2], Kunin [3] and Rogula [4]. For an infinite, homogeneous, linear microelastic bar, this ‘peridynamic’ equation of motion

¹There are numerous approaches to model nonlocality which do not necessarily involve integro-differential equations, see e.g. Chen et al. [1] for a comparison of different microcontinuum theories and their relation to atomistic models.

is given by

$$\begin{aligned} \rho_0 \partial_t^2 u(x, t) &= \int_{-\infty}^{+\infty} C(\hat{x} - x) [u(\hat{x}, t) - u(x, t)] d\hat{x} + b(x, t), \\ (x, t) &\in \mathbb{R} \times (0, T) \end{aligned} \quad (1.1)$$

where ρ_0 is the constant density, $u(x, t)$ the displacement field for the material point x at time t , C the stiffness distribution density or ‘micromodulus’ function and b the external force density. If C is a suitable generalized function, (1.1) coincides with the wave equation of local elasticity, see Section 3 for explicit examples. A dispersion analysis of (1.1) gives the angular frequency ω as a function of the wavenumber k :

$$\omega(k) = \left(\int_{-\infty}^{+\infty} [1 - \cos(k \hat{x})] \frac{C(\hat{x})}{\rho_0} d\hat{x} \right)^{1/2}. \quad (1.2)$$

The phase velocity $v_p(k) := \omega(k)/k$ can, in principle, be found experimentally, see e.g. Graff [5]. It can then be used to determine the micromodulus function C according to (1.2). Therefore the nonlocal model (1.1) provides an analytical description of the dynamics of a system characterized by its nonlinear² dispersion relation. Weckner & Abeyaratne [6] derived analytical solutions by means of Fourier-transforms which serve as validation problems for the numerical method presented in this paper. For the more general IDE

$$\partial_\tau^2 \eta(\zeta, \tau) = \int_{-\infty}^{+\infty} \kappa(\zeta, \xi) \eta(\xi, \tau) d\xi + \chi(\zeta) \eta(\zeta, \tau) + \varphi(\zeta, \tau) \quad (1.3)$$

the authors have shown the existence of a unique mild solution η subject to initial conditions $\eta_0(\zeta) := \eta(\zeta, 0)$, $\nu_0(\zeta) := \partial_\tau \eta(\zeta, 0)$ in the function space of Bochner-integrable abstract functions with values in $L^\infty(\mathbb{R})$, the space of essentially bounded functions, see Emmrich & Weckner [7]. The solution η can be interpreted as the normalized displacement of an inhomogeneous bar. In general, all quantities denoted by Greek letters are dimensionless (except ρ_0 , ω). In agreement with Weckner & Abeyaratne [6], the jump conditions were derived: the Lagrangian location of a discontinuity is shown to remain stationary, which is important for the numerical method presented.

2. Discretization

In order to discretize (1.3), we use the Gauß-Hermite quadrature which is exact for any polynomial $\Phi(\xi) \in P_r(\xi)$ of degree $r \leq 2n - 1$:

$$\int_{-\infty}^{+\infty} e^{-\xi^2} \Phi(\xi) d\xi \approx \sum_{k=1}^n \sigma_k^{(n)} \Phi(\xi_k^{(n)}). \quad (2.1)$$

Here, $\xi_k^{(n)}$, $k = 1, \dots, n$, are the roots of the Hermite polynomials

$$H^{(n)}(\xi) := \frac{(-1)^n}{(2^n n! \sqrt{\pi})^{1/2}} e^{\xi^2} \frac{d^n}{d\xi^n} (e^{-\xi^2})$$

²The wave equation of classical elasticity theory corresponds to a linear dispersion relation.

which we arrange such that $\xi_k^{(n)} < \xi_{k+1}^{(n)}$; the weights $\sigma_k^{(n)}$ are defined by $\sigma_k^{(n)} := \int_{-\infty}^{+\infty} e^{-\xi^2} L_k^{(n)}(\xi) d\xi$ with the Lagrange polynomials $L_k^{(n)}(\xi) := \prod_{j=1, j \neq k}^n \frac{\xi - \xi_j^{(n)}}{\xi_k^{(n)} - \xi_j^{(n)}}$. We set $\Phi(\xi; \zeta, \tau) = e^{\xi^2} \kappa(\zeta, \xi) \eta(\xi, \tau)$ for the approximation of the improper integral in (1.3). The method of collocation then leads to the following set of ordinary differential equations (ODEs)

$$\ddot{\eta}_j^{(n)}(\tau) = \sum_{k=1}^n \sigma_k^{(n)} e^{\xi_k^{(n)2}} \kappa(\xi_j^{(n)}, \xi_k^{(n)}) \eta_k^{(n)}(\tau) + \chi(\xi_j^{(n)}) \eta_j^{(n)}(\tau) + \varphi(\xi_j^{(n)}, \tau), \quad (2.2)$$

where $\eta_j^{(n)}(\tau)$, $j = 1, \dots, n$, are approximations for $\eta(\xi_j^{(n)}, \tau)$. Introducing the notation $\underline{\eta}(\tau) := (\eta_j^{(n)}(\tau))$, $\underline{\Gamma} := (\Gamma_{j,k}) = (-\sigma_k^{(n)} e^{\xi_k^{(n)2}} \kappa(\xi_j^{(n)}, \xi_k^{(n)}) - \chi(\xi_k^{(n)}) \delta_{j,k})$, $\underline{\varphi}(\tau) := (\varphi(\xi_j^{(n)}, \tau))$, where $\delta_{j,k}$ is the Kronecker symbol, one can rewrite the discretized equation of motion (2.2) as

$$\ddot{\underline{\eta}}(\tau) + \underline{\Gamma} \underline{\eta}(\tau) = \underline{\varphi}(\tau). \quad (2.3)$$

Note that the stiffness-matrix $\underline{\Gamma}$ is *not* symmetric. Fourier-transformation leads to $\underline{\Pi}(\mu) \underline{\tilde{\eta}}(\mu) = \underline{\tilde{\varphi}}(\mu)$ with the dynamical stiffness-matrix $\underline{\Pi}(\mu) = \underline{\Gamma} - \mu^2 \underline{\mathbb{1}}$ and the identity matrix $\underline{\mathbb{1}}$.

The solution of the homogeneous problem, $\underline{\Gamma} \underline{\tilde{\eta}}^h(\mu) = \lambda \underline{\tilde{\eta}}^h(\mu)$, is

$$\underline{\tilde{\eta}}^h(\tau) = \sum_{j=1}^n \left(\alpha_j \hat{\eta}_j \cos(\mu_j \tau) + \beta_j \hat{\eta}_j \sin(\mu_j \tau) \right) \quad (2.4)$$

with the semi-simple eigenvalues of the stiffness matrix $\lambda_j = \mu_j^2$ and the corresponding eigenvectors $\hat{\eta}_j$. The $2n$ constants (α_j, β_j) are determined by the initial conditions by solving the set of linear equations

$$\underline{\eta}(\tau = 0) = (\eta_0(\xi_j^{(n)})) = \sum_{j=1}^n \alpha_j \hat{\eta}_j, \quad \dot{\underline{\eta}}(\tau = 0) = (\nu_0(\xi_j^{(n)})) = \sum_{j=1}^n \beta_j \mu_j \hat{\eta}_j. \quad (2.5)$$

Therefore, one can solve the discretized equation of motion (2.2) in two ways: either one uses a time step integration scheme (such as Runge-Kutta or Newmark) or one uses an eigenvalue solver to obtain (2.4) and then solves the above set of linear equations (2.5). The advantage of the second strategy is that the semi-analytical solution allows one to calculate the displacement $\underline{\eta}(\tau^*)$ for *any* time τ^* without having to calculate the solution for $\tau < \tau^*$ in advance. In both cases, we find an approximation of the displacement *field* $\eta(\zeta, \tau^*)$ at time τ^* for the *discrete*, not equidistant points $\zeta = \xi_j^{(n)}$ which can then be interpolated to obtain an approximation for an *arbitrary* point $\zeta \in [\xi_1^{(n)}, \xi_n^{(n)}]$. One has to pay special attention to the interpolation of the

numerical results near displacement discontinuities. But since the stationary position of all discontinuities is known in advance, this can easily be done.

3. Examples

In order to demonstrate the presented numerical method, we calculate two examples for the homogeneous solution of (1.1) that have been already investigated in detail in Weckner & Abeyaratne [6]. This allows us to validate our numerical results and also discuss its limits.

3.1. Gaussian initial displacement. We consider the initial conditions $u_0(x) = Ue^{-(x/L)^2}$, $v_0(x) \equiv 0$ and the micromodulus function $C(x) = \frac{4E}{\ell^3\sqrt{\pi}} e^{-(x/\ell)^2}$ with Young's modulus E and a length scale parameter ℓ . For $\ell \rightarrow 0$, (1.1) becomes the wave equation of local elasticity theory:

$$\rho_0 \partial_t^2 u(x, t) = E \partial_x^2 u(x, t) + b(x, t) . \tag{3.1}$$

Therefore, ℓ can be seen as a degree of nonlocality. With the normalization $\zeta := x/L$, $c_0 := \sqrt{E/\rho_0}$, $\tau := tc_0/L$, $\eta := u(L\zeta, L\tau/c_0)/U$, $\lambda := \ell/L$, the equation of motion (1.1) can be rewritten as (1.3) with $\kappa(\zeta, \xi) := L^3C(L(\zeta - \xi))/E$, $\chi(\zeta) := -4\lambda^{-2}$, $\varphi \equiv 0$. The solution of this initial value problem is

$$\eta(\zeta, \tau; \lambda) = \frac{1}{\sqrt{\pi}} \int_0^\infty \cos(\alpha \zeta) e^{-\alpha^2/4} \cos\left(\tau \sqrt{\frac{1 - e^{-\alpha^2\lambda^2/4}}{\lambda^2/4}}\right) d\alpha , \tag{3.2}$$

see Weckner & Abeyaratne [6]. Expanding (3.2) in a Taylor series around $\lambda = 0$, one obtains the well-known d'Alembert-solution:

$$\lim_{\lambda \rightarrow 0} u(\zeta, \tau; \lambda) = U \frac{e^{-(\zeta-\tau)^2} + e^{-(\zeta+\tau)^2}}{2} . \tag{3.3}$$

We choose $n = 49$ for the quadrature method (2.1) and $\lambda = 3/4$ for the normalized



Figure 1. Roots of Hermite polynomials, $n = 49$

length scale parameter. The location of the roots $\xi_k^{(49)}$ of the Hermite polynomials is shown in Figure 1.

The numerical time integration of (2.2) was carried out with the software Mathematica that uses the Livermore Solver LSODE for solving ODEs. The results are compared with the exact solution given by (3.2).³

³In order to evaluate (3.2), we again use Mathematica. For the following discussion we assume that the (spatial) numerical integration of (3.2) and the (temporal) numerical integration of (2.2) are exact within the resolution of the line thickness. This can be verified by increasing the working precision which does not change the presented numerical and graphical results, respectively.

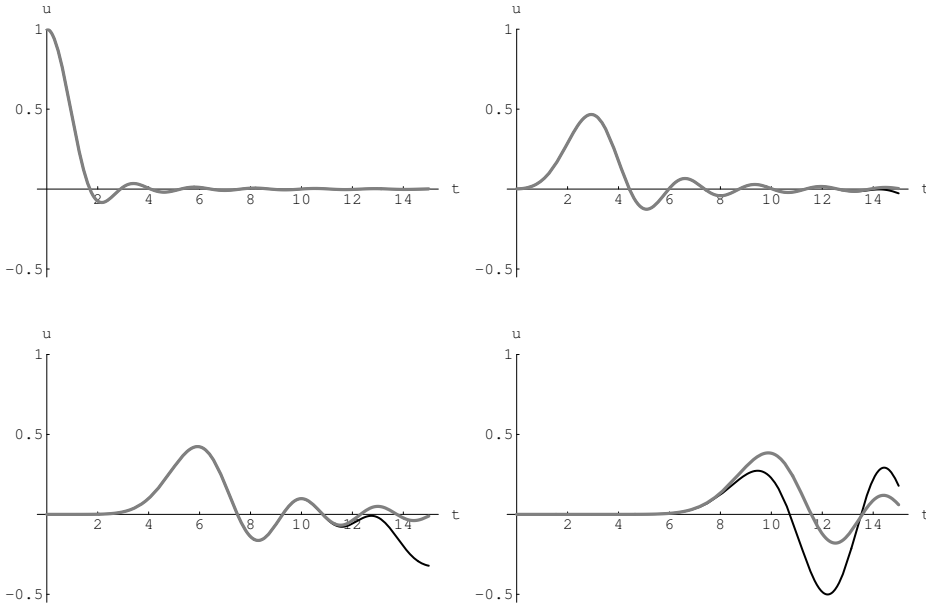


Figure 2. Plots of the displacement $\eta_k(\tau)$ for fixed points: numerical (black line) and analytical results (grey line) of Example 3.1

Figure 2 presents a plot of the displacement $\eta_k^{(n)}(\tau)$ as a function of time for the fixed points $\xi_{25}^{(49)}, \xi_{33}^{(49)}, \xi_{41}^{(49)}, \xi_{49}^{(49)}$ marked by circles in Figure 1. Figure 3 shows the spatially interpolated displacement field $\eta(\zeta, \tau_k)$ for the fixed times $\tau_k = k, k = 0, \dots, 11$, using piecewise cubic polynomials. Since the system is symmetric with respect to the axis $\zeta = 0$, we only plot the half-plane $\zeta \geq 0$. Both figures show that the numerical results agree well with the analytical results for all the points $\zeta \in [\xi_1^{(49)} \approx -9.1, \xi_{49}^{(49)} \approx 9.1]$ if we limit the time of observation to $\tau < 6$. The difference between the analytical and the (interpolated) numerical solution is shown in Figure 4 whereas the spatial L^2 -norm of the error as a function in time is shown in Figure 5.

Increasing the number of integration points extends both the spatial and temporal observation interval. The valid temporal observation period can also be extended if we restrict our attention to points closer to the origin: the displacement of the particle located at the origin $0 = \eta_{25}^{(49)}$ is correct until $\tau \approx 14$.

For $\tau > 14$, the analytical solution and our numerical approximation do not agree any more for *any* particle. This is caused by the reflection of elastic waves at the numerically induced artificial boundary. The type of boundary conditions introduced in this example is dictated by the quadrature method used. In future research, it would be interesting to study the problem of wave reflection in Peridynamics in more detail which to the knowledge of the authors has not been previously pursued. It might be

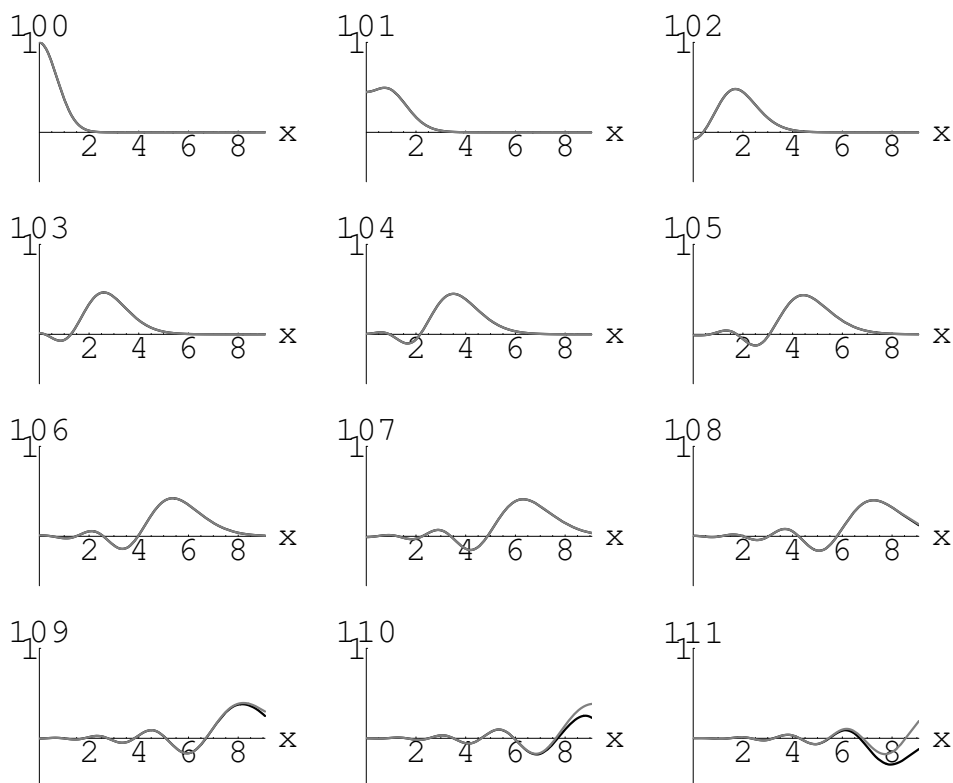


Figure 3. Snapshots of the spatially interpolated displacement field $\eta(\zeta, \tau_k)$ for fixed times $\tau_k = k, k = 0, \dots, 11$: numerical (black line) and analytical results (grey line) of Example 3.1

possible to introduce absorbing, non-reflecting boundary conditions to further improve the above results.

3.2. A Riemann-like problem. In this example, we look at a bar initially at rest with a piecewise constant velocity field involving a jump at the origin: $v_0(x) = v_-h(-x) + v_+h(x)$ where $h(\cdot)$ denotes the unit step function. The aim is to investigate how well the presented numerical method copes with discontinuous initial conditions. The material considered is⁴ $C(x) = \frac{E}{\pi\ell^3} \frac{2\sin(x/\ell) - 2(x/\ell)\cos(x/\ell)}{(x/\ell)^3}$ corresponding to a continuous piecewise linear dispersion relation (1.2). According to Weckner &

⁴We again choose the stiffness distribution such that for $\ell \rightarrow 0$ the equation of motion (1.1) becomes the wave equation (3.1).

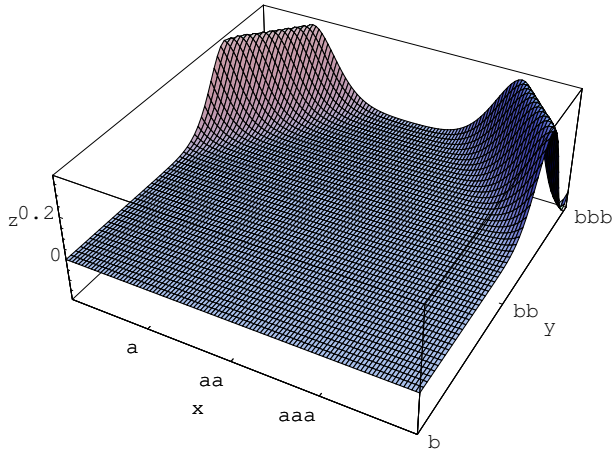


Figure 4. Error between the exact displacement field $\eta(\zeta, \tau)$ and the numerical one for Example 3.1 with $\zeta \in [\xi_1^{49} \approx -9.1, \xi_{49}^{49} \approx 9.1]$ and $\tau < 15$

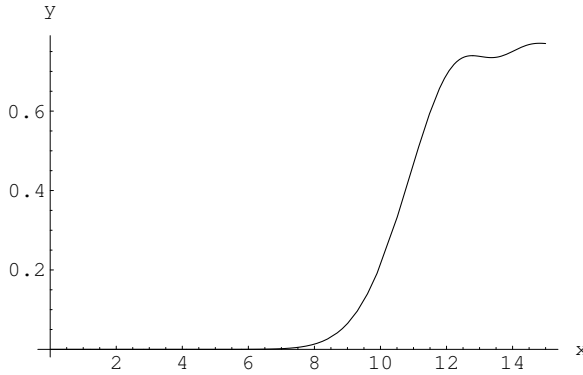


Figure 5. L^2 -norm of the error between the exact displacement field $\eta(\zeta, \tau)$ and the numerical one for Example 3.1 for $\tau < 15$

Abeyaratne [6], the resulting displacement field is:

$$\begin{aligned} \eta(\zeta, \tau) = & \frac{V_+ + V_-}{2} \tau \\ & + \frac{V_+ - V_-}{4\pi} [(\zeta + \tau) \text{Si}(\zeta + \tau) - (\zeta - \tau) \text{Si}(\zeta - \tau) \\ & + \sin(\tau) (\pi \text{sgn}(\zeta) - 2 \sin(\zeta) - 2 \text{Si}(\zeta))], \end{aligned} \tag{3.4}$$

with $\zeta := x/\ell$, $c_0 := \sqrt{E/\rho_0}$, $\tau := c_0 t/\ell$, $\eta(\zeta, \tau) := \frac{u(\zeta\ell, \tau\ell/c_0)}{\ell}$, $V_{\pm} := v_{\pm}/c_0$. $\text{Si}(\cdot)$ is the integral sine function and $\text{sgn}(\cdot)$ is the sign function.

For the numerical simulation, we choose $n = 49$, $V_+ = -V_- = 1$. In Figure 6, the analytical solution (3.2) is drawn as a grey line whereas the numerical solution is drawn as a dashed, black line. As in the previous Example 3.1, the numerical results agree well with the analytical results for a finite time and spatial interval.

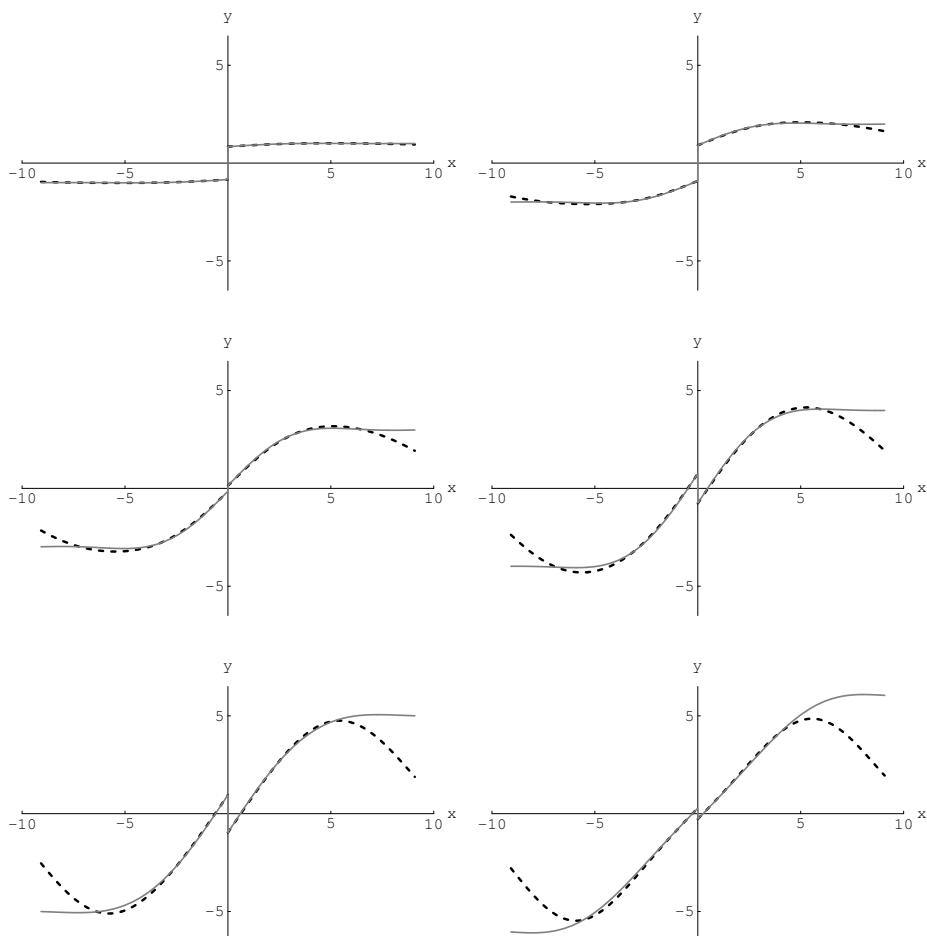


Figure 6. Snapshots of the spatially interpolated displacement field $\eta(\zeta, \tau_k)$ for fixed times $\tau_k = k$, $k = 0, \dots, 6$: numerical (dashed, black line) and analytical results (grey line) of Example 3.2

4. Conclusions

As the two Examples 3.1 and 3.2 show, the numerical method presented can efficiently be used to calculate approximate solutions of the IDE (1.1), even in the case of discontinuous initial data. An agreement with the exact solution, however, can only be expected in a finite spatial domain up to a finite time. This is due to the approximation of the improper integral by a finite sum which can be interpreted as the introduction of artificial boundaries.

Changing the (possibly inhomogeneous) material properties can easily be implemented by redefining the functions $\kappa(\zeta, \xi)$ and $\varphi(\zeta)$ accordingly. Future work will concentrate on extending the presented method to problems in two and three dimensions and to the nonlinear case.

Acknowledgement. This work was supported by a fellowship of the first author within the Postdoc-Programme of the German Academic Exchange Service (DAAD).

References

1. CHEN, Y., LEE, J., and ESKANDARIAN, A.: Atomistic viewpoint of the applicability of microcontinuum theories. *Int. J. Solids Structures*, **41**, 2004, 2085–2097.
2. SILLING, S. A.: Reformulation of elasticity theory for discontinuities and long-range forces. *J. Mech. Phys. Solids*, **48**, 2000, 175–209.
3. KUNIN, I. A.: *Elastic Media with Microstructure I*. Springer-Verlag, Berlin, 1982.
4. ROGULA, D. (ed.): *Nonlocal Theory of Material Media*. Springer-Verlag, Wien, 1982.
5. GRAFF, K. F.: *Wave Motion in Elastic Solids*. Dover Publications, New York, 1991.
6. WECKNER, O. and ABEYARATNE, R.: The effect of long-range forces on the dynamics of a bar. *J. Mech. Phys. Solids* **53**, 2005, 705–728.
7. EMMRICH, E. and WECKNER, O.: Analysis and numerical approximation of an integro-differential equation modelling non-local effects in linear elasticity. *Math. Mech. Solids*, online, December, 2005, DOI No. 10.1177/1081286505059748.

CALENDAR OF EVENTS

2006

January 2-6, 2006: Mérida, Yucatán, México

NINTH PAN AMERICAN CONGRESS OF APPLIED MECHANICS (PACAM IX)

Web: <http://www.mae.ncsu.edu/pacamix/>

Prof. Guillermo Monsivais Galindo, Instituto de Fisica de la UNAM

UNAM, Mexico City, MEXICO

E-mail: monsi@fisica.unam.mx

May 8, 2006 - May 10, 2006: Skiatthos, Greece

6TH INTERNATIONAL CONFERENCE ON ADVANCES IN FLUID MECHANICS

Professor M. Rahman, Dalhousie University, Canada;

Professor C. Brebbia, Wessex Institute of Technology, UK

E-mail: enquires@wessex.ac.uk

Web: <http://www.wessex.ac.uk>

Phone: 44 (0) 238 029 3223; Fax: 44 (0) 238 029 2853;

June 29 - July 1, 2006: Debrecen, Hungary

2ND HUNGARIAN CONFERENCE ON BIOMECHANICS

2nd Hungarian Conference on Biomechanics
June 30th - July 1st 2006
Debrecen, Hungary

Planned programme:

Thursday, 29 June
morning: Femoral neck Osteosynthesis course
afternoon: Formal Dedicatory of the Laboratory of Biomechanics of University of Debrecen

Friday, 30 June
morning: Lectures
afternoon: Lectures
Programme for Accompanying Persons
evening: Reception

Saturday, 1 July
morning: Lectures
afternoon: BMT general assembly

Categories of Subjects:

1. BIOMECHANICS (basically medical related subjects)
2. BioMECHANICS (basically engineer-related subjects)
3. ETHICAL DEONTOLOGY (reports and round table discussion)
4. MIXED SUBJECTS
5. INTELLECTUAL FLEA MARKET (search of research partners)

More information and registration:
www.asszisztencia.hu

July 2 - 6, 2006: Vienna, Austria

13TH INTERNATIONAL CONGRESS ON SOUND AND VIBRATION, ICSV13

Vienna University of Technology

E-mail: office@icsv13.tuwien.ac.at

Web: <http://icsv13.tuwien.ac.at>

Phone: (+43 1) 588 01-20211; Fax: (+43 1) 588 01-20297, 20299;

July 3-7, 2005: Alexandroupolis, Greece

16TH EUROPEAN CONFERENCE OF FRACTURE ECF16

Web: <http://ecf16.civil.duth.gr/menu/welcome.php>

M.S. Konsta-Gdoutos, School of Engineering

Democritus University of Thrace

GR-67100, Xanthi, GR, Alexandroupolis, Greece

E-mail: mkonsta@civil.duth.gr

Phone: +30-25410-79651, 79658, Fax: +30-25410-79652

August 28-September 1, 2006: Budapest, Hungary

6TH EUROPEAN SOLID MECHANICS CONFERENCE

Web: <http://esmc2006.mm.bme.hu/>

Prof. Dr. Gábor Stépán, Budapest University of Technology and Economics

Department of Applied Mechanics, 1521 Budapest, P.O. Box 91, Hungary

E-mail: esmc2006@mm.bme.hu

Phone: +36 1 463 1369, Fax: +36 1 463 3471

November 5 - 9, 2006: Hannover, Germany

IUTAM SYMPOSIUM ON COMPUTATIONAL CONTACT MECHANICS

Chairman: Prof. P. (Peter) Wriggers

IUTAM Representative: Prof. J. (Jean) Salençon

E-mail: wriggers@ibnm.uni-hannover.de

Phone: +49 511 762 3220; Fax: +49 511 762 5496

2007

April 23 - 28, 2007: Tbilisi, Georgia

IUTAM SYMPOSIUM ON RELATION OF SHELL, PLATE, BEAM AND 3D MODELS

Chairman: Prof. G. (George) Jaiani

IUTAM Representative: Prof. D.H. (Dick) van Campen

Email: jaiani@viam.hepi.edu.ge

Phone: +995 32 305995

June 11 - 14, 2007: Shanghai, China

FIFTH INTERNATIONAL CONFERENCE ON NONLINEAR MECHANICS (ICNM-V)

Shanghai Institute of Applied Math. and Mech., Shanghai University, P.O.,

Box 189, 149 Yanchang Road

E-mail: icnm5@mail.shu.edu.cn

Phone: 86-21-56331451; Fax: 86-21-36033287

Notes for Contributors

to the Journal of Computational and Applied Mechanics

Aims and scope. The aim of the journal is to publish research papers on theoretical and applied mechanics. Special emphasis is given to articles on computational mechanics, continuum mechanics (mechanics of solid bodies, fluid mechanics, heat and mass transfer) and dynamics. Review papers on a research field and materials effective for teaching can also be accepted and are published as review papers or classroom notes. Papers devoted to mathematical problems relevant to mechanics will also be considered.

Frequency of the journal. Two issues a year (approximately 80 pages per issue).

Submission of Manuscripts. Submission of a manuscript implies that the paper has not been published, nor is being considered for publication elsewhere. Papers should be written in standard grammatical English. Two copies of the manuscript should be submitted on pages of A4 size. The text is to be 130 mm wide and 190 mm long and the main text should be typeset in 10pt CMR fonts. Though the length of a paper is not prescribed, authors are encouraged to write concisely. However, short communications or discussions on papers published in the journal must not be longer than 2 pages. Each manuscript should be provided with an English Abstract of about 50–70 words, reporting concisely on the objective and results of the paper. The Abstract is followed by the Mathematical Subject Classification – in case the author (or authors) give the classification codes – then the keywords (no more than five). References should be grouped at the end of the paper in numerical order of appearance. Author's name(s) and initials, paper titles, journal name, volume, issue, year and page numbers should be given for all journals referenced.

The journal prefers the submission of manuscripts in \LaTeX . Authors should prefer the $\mathcal{AMS}\text{-}\text{\LaTeX}$ article class and are not recommended to define their own \LaTeX commands. Visit our home page for further details concerning the issue how to edit your paper.

For the purpose of refereeing, two copies of the manuscripts should initially be submitted in hardcopy to an editor of the journal. The eventual supply of an accepted-for-publication paper in its final camera-ready form (together with the corresponding files on an MS-DOS diskette) will ensure more rapid publication. Format requirements are provided by the home page of the journal from which sample \LaTeX files can be downloaded:

<http://www.uni-miskolc.hu/home/web/pumns/mechanics>

These sample files can also be obtained directly (via e-mail) from a member of the Editorial Board, Gy. Szeidl (Gyorgy.SZEIDL@uni-miskolc.hu), upon request.

Twenty offprints of each paper will be provided free of charge and mailed to the correspondent author.

The Journal of Computational and Applied Mechanics is abstracted in Zentralblatt für Mathematik and in the Russian Referativnij Zhurnal.

Responsible for publication: Rector of the Miskolc University

Published by the Miskolc University Press under the leadership of Dr. József PÉTER

Responsible for duplication: works manager Mária KOVÁCS

Number of copies printed: 200

Put to the Press on February 27, 2006

Number of permission: TU 2006-300-ME

HU ISSN 1586–2070

A Short History of the Publications of the University of Miskolc

The University of Miskolc (Hungary) is an important center of research in Central Europe. Its parent university was founded by the Empress Maria Teresia in Selmecebánya (today Banská Štiavnica, Slovakia) in 1735. After the first World War the legal predecessor of the University of Miskolc moved to Sopron (Hungary) where, in 1929, it started the series of university publications with the title *Publications of the Mining and Metallurgical Division of the Hungarian Academy of Mining and Forestry Engineering* (Volumes I.-VI.). From 1934 to 1947 the Institution had the name Faculty of Mining, Metallurgical and Forestry Engineering of the József Nádor University of Technology and Economic Sciences at Sopron. Accordingly, the publications were given the title *Publications of the Mining and Metallurgical Engineering Division* (Volumes VII.-XVI.). For the last volume before 1950 – due to a further change in the name of the Institution – *Technical University, Faculties of Mining, Metallurgical and Forestry Engineering, Publications of the Mining and Metallurgical Divisions* was the title.

For some years after 1950 the Publications were temporarily suspended.

After the foundation of the Mechanical Engineering Faculty in Miskolc in 1949 and the movement of the Sopron Mining and Metallurgical Faculties to Miskolc, the Publications restarted with the general title *Publications of the Technical University of Heavy Industry* in 1955. Four new series - Series A (Mining), Series B (Metallurgy), Series C (Machinery) and Series D (Natural Sciences) - were founded in 1976. These came out both in foreign languages (English, German and Russian) and in Hungarian.

In 1990, right after the foundation of some new faculties, the university was renamed to University of Miskolc. At the same time the structure of the Publications was reorganized so that it could follow the faculty structure. Accordingly three new series were established: Series E (Legal Sciences), Series F (Economic Sciences) and Series G (Humanities and Social Sciences). The latest series, i.e., the series H (European Integration Studies) was founded in 2001. The eight series are formed by some periodicals and such publications which come out with various frequencies.

Papers on computational and applied mechanics were published in the

Publications of the University of Miskolc, Series D, Natural Sciences.

This series was given the name Natural Sciences, Mathematics in 1995. The name change reflects the fact that most of the papers published in the journal are of mathematical nature though papers on mechanics also come out.

The series

Publications of the University of Miskolc, Series C, Fundamental Engineering Sciences

founded in 1995 also published papers on mechanical issues. The present journal, which is published with the support of the Faculty of Mechanical Engineering as a member of the Series C (Machinery), is the legal successor of the above journal.



Contents
Contributed Papers

Gyula BÉDA: Generalized Mindlin's method for the determination of constitutive equations of solids	153–158
Anikó CSÉBFALVI: Evolution methods for discrete minimal weight design of space trusses with stability constraints	159–173
István ECSEDI and Kornél DLUHI: A reciprocal theorem for steady-state heat conduction problems	175–182
József FARKAS: Economy of welded stiffened steel plates and cylindrical shells	183–205
Dávid FELHŐS, Károly VÁRADI and Klaus FRIEDRICH: Microhardness tests of graded SIC/EP rings: experimental results and FE modeling	207–218
Dezső HEGYI and Krisztián HINCZ: Long-term analysis of prestressed membrane structures	219–235
Károly JÁRMAI: Particle swarm method as a new tool for structural optimization	237–256
Imre KOZÁK: Tensors of finite rotations and small strains on the middle surface of a shell	257–276
András LENGYEL and Zsolt GÁSPÁR: Compatibility paths of an infinitely degenerate mechanism	277–284
Lidia NAZARENKO: Three-component discretely-fibrous composites under matrix microdamaging	285–294
Yaroslav A. ZHUK and Igor K. SENCHENKOV: Investigation of energy characteristics of the layered beam-damper	295–309
Olaf WECKNER and Etienne EMMRICH: Numerical simulation of a non-local bar	311–319